Controlling nonlinear optics with dispersion in photonic crystal fibres

John Colin Travers

Femtosecond Optics Group
Photonics Group, Department of Physics
Imperial College London
United Kingdom

March 2008

Thesis submitted for the degree of Doctor of Philosophy of Imperial College London

For Vanessa.

Abstract

Nonlinear optics enables the manipulation of the spectral and temporal features of light. We used the tailorable guidance properties of photonic crystal fibres to control and enhance nonlinear processes with the aim of improving nonlinearity based optical sources. We utilised modern, high power, Ytterbium fibre lasers to pump either single photonic crystal fibres or a cascade of fibres with differing properties. Further extension of our control was realised with specifically tapered photonic crystal fibres which allowed for a continuous change in the fibre characteristics along their length.

The majority of our work was concerned with supercontinuum generation. For continuous wave pumping we developed a statistical model of the distribution of soliton energies arising from modulational instability and used it to understand the optimum dispersion for efficient continuum expansion. A two-fold increase in spectral width was demonstrated, along with studies of the noise properties and pump bandwidth dependence of the continuum. For picosecond pumping we found that the supercontinuum bandwidth was limited by the four wave mixing phase-matching available in a single fibre. A technique to overcome this by using a cascade of fibres with different dispersion profiles was developed. Further improvement was achieved by using novel tapered PCFs to continuously extend the phase-matching. Analysis of this case showed that a key role was played by soliton trapping of dispersive waves and that our tapers strongly enhanced this effect. We demonstrated supercontinua spanning 0.34-2.4 μm with an unprecedented spectral power; up to 5 mW/nm.

The use of long, dispersion decreasing photonic crystal fibres enabled us to demonstrate adiabatic soliton compression at 1.06 μm. From a survey of fibre structures we found that working around the second zero dispersion wavelength was optimal as this allows for decreasing dispersion without decreasing the nonlinearity. We achieved compression ratios of over 15.

Acknowledgments

I am indebted to Prof. Roy Taylor; without his wisdom, guidance, encouragement, humour and seriously tested patience, this work would not have been possible. I must also thank Sergei Popov for his guidance and advice, particularly in my early days. My fellow PhD students deserve a special mention, especially Andrey for providing insightful answers to my persistent questions on every subject. Also Richard and Burly, for putting up with my enthusiasm and, with Andrey, proving to be excellent collaborators and superior drinking partners. I would not have got off to such a good start without the early encouragement and experience of Christiano and David the senior men when I joined the group.

Much of the work in this thesis depended on a collaboration with Prof. Jonathan Knight's group at the University of Bath. In particular, Alexandre Kudlinski and Jim Stone who pulled the tapered PCFs for us.

Many other people have contributed to my completion of this work. My attempts at writing a computer code to model supercontinuum generation were helped and encouraged by Prof. John Dudley in the rare moments I saw him sober. I must also thank Micheal Frosz for getting me started with the use of MPB. The experimental work was made easier with the help of the guys in the workshop, particularly with the components for my beloved FROG. I must particularly thank Paul Brown for his moral support.

While not in the laboratory my fellow flat mates have kept me in order. Thanks Qian (more like disorder), James and Martina. And if it wasn't for Charlie, Gautam, Phil and Vicky, I may have forgotten the outside world.

My family: my brother and Jo, my parents and grandfather, have all encouraged me and provided the support I needed to complete this work, and the years of study that went before it. My life was made more enjoyable and worthwhile with the company and support of Vanessa. Out of her many contributions I must thank her especially for proof reading this entire thesis.

Contents

1 Introduction **13**

1.1 Overview . . . 14
1.2 Motivation from applications . . . 15
1.3 Optical fibres . . . 15
1.3.1 Conventional optical fibre . . . 16
1.3.2 Photonic crystal fibre . . . 19
1.3.3 Ytterbium doped fibre amplifiers and lasers . . . 23
1.3.4 Splicing . . . 26
1.4 Physics and analysis of optical fibres . . . 27
1.4.1 Dispersion . . . 27
1.4.2 Loss . . . 39
1.4.3 Nonlinearity . . . 40
1.4.4 Modelling . . . 42
1.5 Propagation in optical fibres . . . 46
1.5.1 Dispersion . . . 47
1.5.2 Self-phase modulation . . . 48
1.5.3 Solitons . . . 50
1.5.4 Four-wave mixing . . . 52
1.5.5 Raman scattering . . . 54
1.5.6 Soliton fission and dispersive wave generation . . . 55
1.5.7 Supercontinuum generation . . . 57
1.5.8 Other nonlinear effects . . . 60
1.6 A review of early nonlinear fibre optics . . . 61
1.7 Summary . . . 63

2 Continuous wave supercontinuum generation **65**

2.1 Introduction . . . 65
2.2 Literature review of experimental results . . . 66
2.3 Experimental setup . . . 68

2.3.1 Pump sources . . . 68
2.3.2 Fibres . . . 68
2.3.3 Benchmark results . . . 69
2.4 Modelling . . . 70
2.4.1 A comparison of the CW laser models . . . 74
2.5 Physical mechanism . . . 78
2.6 Experimental results . . . 88
2.6.1 Low-water loss PCF . . . 88
2.6.2 Pump spectral bandwidth dependence . . . 92
2.6.3 Noise of CW supercontinua . . . 96
2.6.4 Quasi-CW pumping . . . 97
2.7 Conclusion . . . 98

3 Visible supercontinuum generation with picosecond pump pulses in cascaded PCFs 101
3.1 Introduction . . . 101
3.2 Summary of relevant literature . . . 101
3.3 Pump laser . . . 104
3.4 Experimental setup . . . 105
3.5 Supercontinuum generation in HF1040 . . . 105
3.5.1 Supercontinuum mechanism . . . 108
3.5.2 Phase matching and gain of MI/FWM . . . 109
3.5.3 Limits of supercontinuum generation via FWM . . . 111
3.5.4 Simulations of supercontinuum generation in HF1040 . . . 113
3.6 Pumping fibres with shorter zero dispersion wavelengths . . . 116
3.7 Supercontinuum generation in cascaded PCFs . . . 119
3.8 Further studies of the cascaded supercontinuum generation . . . 122
3.8.1 Properties of HF780 . . . 122
3.8.2 Temporal measurements of the cascaded supercontinuum . . . 125
3.9 Recent developments and future enhancements . . . 129
3.10 Conclusion . . . 129

4 Ultra-violet to mid-infrared supercontinuum generation in tapered PCFs 131
4.1 Introduction . . . 131
4.1.1 A review of tapered optical fibres . . . 131
4.2 Manufacturing and taper properties . . . 135
4.2.1 Manufacturing . . . 135

4.2.2 Properties of the tapers . . . 135
4.3 Results and discussion . . . 141
4.3.1 Experimental setup . . . 141
4.3.2 Optimisation of flatness and visible spectral power . . . 142
4.3.3 Comparison with simulations . . . 145
4.3.4 Understanding the results . . . 146
4.3.5 Optimisation of Blue/UV extent . . . 152
4.3.6 Mid-infrared extent . . . 157
4.4 Limits to short wavelength generation . . . 157
4.4.1 Limits inherent to the nonlinear processes . . . 157
4.4.2 Limits due to loss . . . 158
4.5 Conclusion and future development . . . 160

5 Pulse compression in dispersion decreasing PCFs 163
5.1 Introduction . . . 163
5.2 Pulse compression techniques with optical fibres . . . 163
5.2.1 Fibre-grating compressors . . . 164
5.2.2 Using hollow photonic band-gap PCF for pulse compression . . . 166
5.2.3 Soliton effect compressors . . . 166
5.2.4 Adiabatic soliton compression . . . 168
5.2.5 Combined adiabatic and soliton effect pulse compression . . . 169
5.3 Design of dispersion decreasing PCF . . . 170
5.3.1 Manufacturing technique . . . 170
5.3.2 Controlling the dispersion in a tapered PCF . . . 170
5.4 Experimental results . . . 173
5.4.1 Properties of the dispersion decreasing PCF . . . 173
5.4.2 Experimental setup . . . 175
5.4.3 Results . . . 175
5.5 Future possibilities . . . 179
5.6 Conclusion . . . 180

6 Conclusion and outlook 181

List of publications 185
Journal papers . . . 185
Conference papers . . . 185

References 189

1 Introduction

Nonlinear optics encompasses a wide range of fascinating phenomena which can occur when intense light interacts with matter. In this thesis we use some of these phenomena to achieve the transfer of power from a narrow range of frequencies emitted by our pump lasers to an extremely broad continuum of frequencies spanning from the ultra-violet to the mid-infrared; this process is known as supercontinuum generation. We also use solitons, which arise due to the balance between nonlinear and linear propagation effects, to compress optical pulses.

Although it is nonlinear optics which opens up the possibility for these processes to occur, the linear optical effects of dispersion and attenuation remain dominant in the interaction of light and matter; and it is dispersion, in particular, which determines which nonlinear effects can occur and how strongly. Thus control of dispersion allows us to tailor the observed nonlinear phenomena.

Optical fibres can confine light at high intensity over long distances, and hence nonlinear effects are readily observed. Importantly, the influence of the optical fibre structure on the dispersive properties of the fibre is large and thus control of the nonlinear processes is available. This is especially so since the introduction of photonic crystal fibres (PCFs) over the last decade. These fibres have a cladding made from the inclusion of different materials, often in a periodic pattern. Usually the inclusions are simply air holes in the silica background structure. Such structures have a wide range of exciting guidance properties and enable far greater control of the confined light than conventional fibre. In particular, if the inclusions have a very large refractive index difference from the background (as is the case in air-silica structured fibres) then the waveguide dispersion can be tailored very precisely and strongly and hence great control of nonlinear processes can be achieved.

This thesis is concerned with using the novel dispersion tailoring properties of photonic crystal fibres (PCFs) to control nonlinear effects in advantageous ways. We look especially at extending the bandwidth of high average power pumped supercontinuum generation either to longer wavelengths in the case of continuous wave (CW) pumped supercontinua or to blue and ultra-violet (UV) wavelengths in the case of picosecond pump pulses. We also use dispersion decreasing photonic crystal fibres for soliton pulse compression.

While the fundamental physics of nonlinear fibre optics has been known for some time, photonic crystal fibres and modern fibre laser technology have enabled a qualitative enhancement of the effects and the ability to move into new spectral regions.

1.1 Overview

This thesis is organised as follows. In Chapter 2 we make use of the enhanced nonlinearity of PCF to generate supercontinua with CW fibre lasers as pump sources. We study the mechanism of the CW continuum generation process and look at ways to optimise it. We present experimental results on overcoming the water loss, the relative intensity noise of the supercontinuum and the influence of pump bandwidth. In Chapters 3 and 4 we look at generating extreme broadband supercontinua, concentrating on generating blue and UV light, from a high power picosecond duration fibre laser source. We discuss how optimising the dispersion for four wave mixing processes is critical to the spectral expansion, and the role of solitons and the soliton trapping of dispersive waves in the UV extension process. Experimental results with a cascade of PCFs or using long lengths of tapered PCF are shown to significantly enhance the short wavelength edge of the supercontinuum and also generate long wavelengths into the mid-infrared region. Finally in Chapter 5 we use longer lengths of tapered PCF to achieve adiabatic soliton compression in dispersion decreasing fibres, in a wavelength region where the use of conventional fibre for such compression is impossible.

The rest of this introduction is intended to provide the background material required in later chapters. In the next section we consider how light is guided in a fibre and look specifically at the properties of photonic crystal fibres. In Section 1.3.3 we look at Ytterbium fibre amplifiers and lasers which were used exclusively as the pump sources in this work. Following that, in Section 1.3.4 we briefly discuss splicing between fibres, particularly to PCF. Section 1.4.1 provides a detailed overview of dispersion, the calculation of PCF modes and how structural changes to the fibre can manipulate the dispersion curves. This leads us to Section 1.4.4 where we describe the simulation code used in the analysis of our results. Following that, in Section 1.5 we provide a phenomenological review of the propagation of optical pulses in fibres, looking at some of the linear and nonlinear processes. Finally, in Section 1.6 we review the early development of supercontinuum generation up to the time that the work on this thesis began.

1.2 Motivation from applications

A large part of this thesis was focused on generating enhanced and extended bandwidth supercontinua. This was partially motivated by the numerous applications such sources could be used for. The primary properties of supercontinua include broad bandwidth, high spectral power, spatial coherence, and often short pulse duration. One obvious application is as a replacement for conventional laboratory lamps (i.e. tungsten filaments). Even for this simple, but essential role, numerous advantages are to be found. The orders of magnitude higher spectral power allows for more sensitive measurements, the spatial coherence provides much easier handling of the optics and the short temporal duration allows for time-resolved experiments to be performed. In addition, depending on the pump and fibre parameters, supercontinua can have high coherence properties making them useful, for example, to frequency metrology. Indeed in 2005, the Nobel Prize in Physics was awarded to J. L. Hall and T. W. Hänsch for work on supercontinuum based frequency metrology [Jon00; Hol00]. Alternatively, some applications make explicit use of the lack of coherence in some pump schemes, notably optical coherence tomography (OCT) [Hsi04; Pov05; Har01]. Supercontinua have also been applied to: telecommunications [Smi06], fluorescence lifetime imaging [Dun04], coherent anti-Stokes Raman scattering microscopy [Kan05], gas sensing [ET03], dispersion measurements [Mor95a; GH03], optical communications [Tay87; Mor93; Mor95b], spectroscopy [Lin76; Fre98] and sensors [Kel99].

The last chapter of this thesis concerns soliton compression at 1.06 μm to a pulse duration of less than 50 fs, with potential for even higher compression. Such short pulse sources can be used for a wide variety of applications, for example: the pumping of coherent supercontinua, or the study of ultrafast processes using femtosecond pulses, for which A. H. Zewail was awarded the 1999 Nobel Prize for Chemistry.

1.3 Optical fibres

The fundamental optical element in our work is the optical fibre. This invention was one of the most successful of the 20$^{\text{th}}$ century, impacting the lives of many people as well as leading to new and interesting avenues of scientific inquiry.

Total internal reflection, the basic mechanism of light guidance, was first demonstrated in water jets by D. Colladon and J. Tyndall in the mid 1800s [Hec04], but it took another century for glass optical fibres to be experimentally investigated and most of the early work was dedicated towards image transmission. This work led to the idea of adding a cladding to a fibre by van Hell and L. Curtiss, which paved the way for low loss optical fibres. Telecommunications companies only became interested when the enhanced

bandwidth available at the high optical carrier frequencies was realised [Jr.64]. Pioneering efforts in the 1960s [Kao86], eventually motivated intense research. Over the previous three decades optical fibres have revolutionised communications [Hec04], and in the present decade they are in the process of revolutionising high power laser systems. Their usefulness and success can be attributed to a number of properties, including:

- Extremely low attenuation: when high purity silica is used.
- Good material properties: chemical stability, resistance, and strength.
- Optical confinement over very large distances ($\sim$ 100 km).
- Compactness: fibre is small, can be coiled and packed.
- Robustness: all-fibre systems do not require alignment and are robust against movement.
- High power handling: this stems from the transparency and low intrinsic nonlinearity of silica.
- Efficient laser format: rare earth doped glass fibres are a highly efficient gain medium.

The central focus of optical fibre research since the 1960s has always been for telecommunications but the demands of this field have also led to extensive research efforts in nonlinear fibre optics [Agr01], and fibre lasers and amplifiers. It is the latter two areas which form the basis of this work, but the inheritance from telecommunications in terms of quality optical fibres and high performance packaged technology is significant.

1.3.1 Conventional optical fibre

In 1873 Maxwell published one of the most important, and elegant, contributions to physics, his *Treatise of Electricity and Magnetism* [Max73]. This work lead to the discovery of electromagnetic waves which now pervade many areas of science and technology. In this section we give a brief overview of electromagnetism in the context of guidance in optical fibres. The purpose is to facilitate the discussion of the numerical simulations used throughout this thesis and provide insight into the fundamental physics of dispersion and nonlinear propagation in optical fibres.

From Maxwell's equations it can be shown that the electric field (which dominates the interaction of light and non-magnetic dielectrics like silica glass) obeys the wave equation [Sny83; Buc04]:

$$\nabla^2 \mathbf{E} - \mu_0 \epsilon_0 \partial_t^2 \mathbf{E} = \mu_0 \partial_t^2 \mathbf{P} \tag{1.1}$$

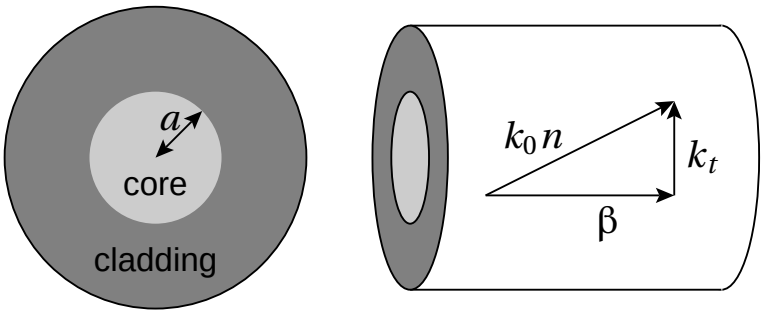


Figure 1.1: The refractive index structure of conventional step index fibre (darker regions have a lower refractive index) and the definition of the propagation constants.

where **P** is the induced polarisation, **E** is the electric field, t is time, μ_0 is the permeability of free space and ϵ_0 is the permitivity of free space. Eqn. 1.1 shows that the time varying polarisation drives the electric field. The incident electric field drives the atomic dipoles causing them to oscillate and re-radiate with some phase delay, through the induced polarisation. The phase delay depends on the locations of the resonant frequencies of the dipoles. We discuss those for silica in Section 1.4.1. For linear propagation, $\mathbf{P} = \epsilon_0 \chi_L \mathbf{E}$ (where χ_L is the linear susceptibility), and by defining the relative permitivity as $\epsilon_r = 1 + \chi_L$ and subsituting for **P** in Eqn. 1.1 we get a wave equation which describes the propagation of the electric field with a phase velocity of c/n, where c is the speed of light and we recover the definition of the refractive index $n = \sqrt{\epsilon_r}$. As χ_L is complex, so is the refractive index. We refer to the real part by n and this defines the magnitude of the propagation vector (or wavevector) in any medium as $k = nk_0 = n\omega/c$. The imaginary part relates to the absorption of the field by the medium which is very small for silica at the frequencies we consider.

Guidance mechanism

Conventional step-index optical fibre, as shown in Fig. 1.1, has a core region, of radius a (usually a few times larger than the wavelength), of slightly higher refractive index than the cladding region. Usually the core is germanium doped silica and the cladding pure fused silica glass, but other dopant combinations are used. Physically, light is guided by total internal reflection at the core-cladding interface. To understand this in more detail we consider the propagation vector of the electric field in the fibre. Due to the axial invariance of optical fibre, we can write the electric (similarly the magnetic) field for a given frequency as:

$$\mathbf{E}(\mathbf{r}, z, t) = \mathbf{E}_m(\mathbf{r}) \exp[-i(\omega t - \beta z)] \tag{1.2}$$

where $\mathbf{E}_m$ is the modal electric field distribution, z is the axial position through the fibre, ω is the angular frequency, $\mathbf{r}$ is the transverse position vector (over the fibre cross section) and β is the axial component of the wavevector and is known as the fibre propagation constant. The definitions of β, along with the magnitude of the propagation vector and the transverse propagation constant, k_t, are also shown in Fig. 1.1. It is implicit in Eqn. 1.2 that β is invariant, regardless of both transverse and axial position in the fibre. In addition, the magnitude of the propagation vector is constant in any material at $k_0 n$ where n is the local refractive index. Therefore we have a constraint on the magnitude of the transverse propagation constant [Zol05]:

$$k_t = \sqrt{k_0^2 n^2 - \beta^2} \tag{1.3}$$

Given that the magnitudes of the total propagation vectors are different in the core and cladding at $k_0 n_{core}$ and $k_0 n_{clad}$ respectively, it may be possible to choose β such that k_t is real in the core, but imaginary in the cladding. In that case the light can be guided in the core and the field in the cladding will decay monotonically from the core.

The above choice of β is necessary, but not sufficient, for a mode to exist. In addition, the field must only change by the phase factor $\exp[i\beta(z_2 - z_1)]$ between two points z_1 and z_2 in the fibre. This can be regarded as a resonance condition. A mode can be considered to be a standing wave of the transverse field distribution over the fibre cross section, similar to a stretched membrane. To determine the values of β (from which the field distributions can be found) we must solve for the eigenmodes of the fibre propagation equation [Sny83]. We discuss how to do this in later sections.

For a conventional step index fibre, the number of fibre modes which exist can be found from the V parameter, or normalised frequency.

$$V = a k_0 \sqrt{n_{core}^2 - n_{clad}^2} \tag{1.4}$$

The number of modes increases with the V parameter. This can be understood from the larger refractive index difference or core size a large V value implies, indicating that it has either tighter confinement, or can accept larger wavelengths. It turns out that for $V < 2.405$ which is the first zero of $J_0(x)$ the 0^{th} order Bessel function of the first kind, the fibre is single-mode and only the fundamental mode propagates. The fundamental mode always exists and for small enough wavelengths, all conventional fibres are multi-mode.

From the above analysis it is clear that to remain single mode the refractive index difference must be small. However, we shall see later that to obtain strong waveguide dispersion, the refractive index difference should be large. In fact, due to this conflict, it is not possible to produce a conventional step index fibre which is both anomalously dispersive and single mode at wavelengths shorter than 1.27 μm - the zero dispersion

wavelength of silica glass. This is one of the major constraints which photonic crystal fibres can overcome, which has led to many intersting advances in nonlinear fibre optics.

1.3.2 Photonic crystal fibre

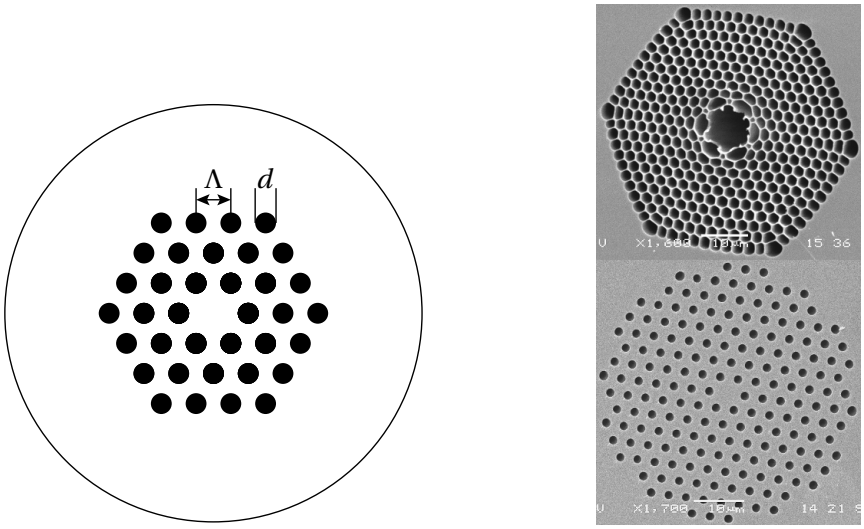
Photonic crystal fibres have caused a renaissance in the nonlinear fibre optics community because they offer great design flexibility in terms of dispersion and nonlinearity, and in the case of hollow core PCF, new ways to guide light and interact with gases and liquids in the fibre format.

History

Photonic crystal fibres were inspired by photonic crystals - structures varying on the scale of optical wavelengths - which have a novel and interesting interaction with light. Photonic crystals rely on a periodic structure to alter their optical properties. The unique properties arise from the photonic bandgap effect. The periodic variations in the refractive index lead to forbidden values of the propagation constant in the crystal. This is analogous to the forbidden regions between electron energy states in a semiconductor crystal. Photonic crystals were originally conceived in bulk form for strong localisation of light [Joh87], or the inhibition of spontaneous emission [Yab87; Yab89]. The idea of constructing two-dimensional photonic crystals in fibre form followed, with the light guided in a hollow core surrounded by a cladding with microscopic air holes running along it. The first PCF to be fabricated, however, was a solid core fibre, but it still had the microstructured cladding [Kni96]. Solid core PCFs are easier to fabricate because they do not require as large air-filling ratios in the cladding as the hollow core fibres, and they do not require a large hollow core to be maintained. The guidance properties are also less sensitive to the exact periodic arrangement of the cladding holes. Hollow core PCFs were first fabricated three years later [Cre99]. It is interesting to also note that photonic bandgaps occur in nature. One example is the coloured reflections from butterfly wings which are caused by the selective reflection of frequencies from microscopic periodic structures in the wings, rather than from material properties, as one might first suspect [Bja03; Rus03].

Structure

The structures of photonic crystal fibres, shown in Fig. 1.2, are usually made from pure fused silica throughout. The cladding structure is made from several rings of air-holes around the core. The holes usually form a triangular lattice as shown. Two parameters describe this structure: the hole diameter d and the centre to centre hole spacing or pitch Λ. Other lattice structures are used and it is also possible to make PCFs with solid or



(a) PCF structure (b) PCF examples

Figure 1.2: The refractive index structure of PCF (a; white is pure silica and black represents the air-holes) and scanning electron micrographs (SEMs) of hollow and solid core fibres (b).

liquid inclusions rather than air-holes. The cores of PCFs are formed from defects in the microstructure. A solid core is usually formed by simply not removing an air-hole from the centre of the structure and so its size depends on the air-hole structure parameters. A hollow core can also be created by making a larger air-hole in the core. Examples of both types of PCF can be seen in Fig. 1.2(b).

The standard manufacturing procedure of PCF has become known as the stack and draw process [Kni96], and is illustrated in Fig. 1.3. A preform is created by stacking silica rods and capillaries into a macroscopic replica of the desired structure. This stack is then fused together into a preform. The preform itself is then drawn into a fibre while applying pressure to the air holes. By controlling the draw speed and pressure the final fibre structure can be influenced and a single preform can produce multiple different fibres. The resulting fibres are extremely robust. This procedure is very versatile and a very wide range of fibre designs have been realised. Including designs involving doped glasses [Lim04]. It should also be noted that fibres with microstructures had been invented in the 1970s in a quest to improve transmission for optical communications [Kai73], but the manufacturing technique was insufficient and the concept of the photonic crystal had not yet been invented. Other manufacturing techniques, such as extrusion, can also be used, particularly for soft glasses.

This manufacturing technique can produce PCFs with pitches ranging from at least 1-10 μm and air-hole ratios (d/Λ) from below 0.1 to over 0.9 [Bja03]. This means that

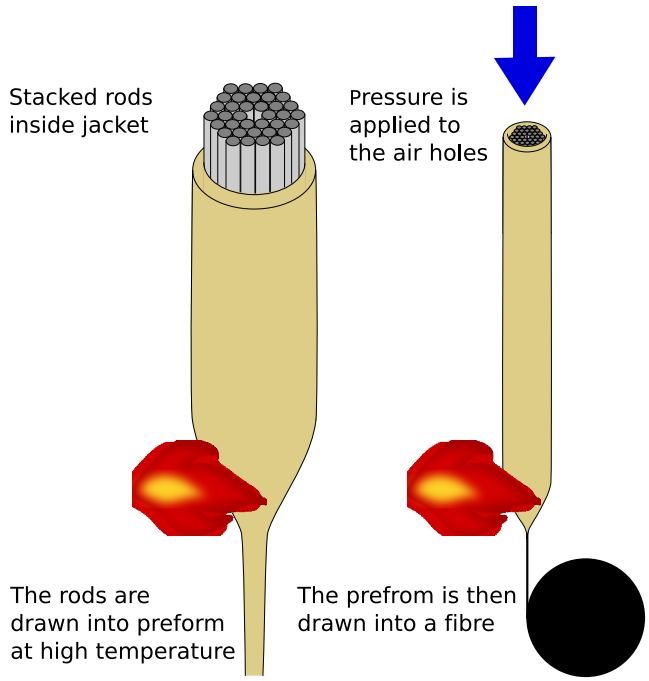


Figure 1.3: Illustration of PCF manufacturing procedure

the refractive index difference can be over 25% compared to a practical limit of ~ 4% for conventional fibre [Rus06]. The high index contrast leads to many of the advantageous properties of PCF.

Guidance mechanism

Similar to step index fibres, light is guided in the core by finding values for β which prevent the existence of real transverse propagation constants in the cladding structure. In the PCF case the photonic bandgap effect is used to achieve this. This originates from the periodicity of the cladding, which prevents transmission of frequencies which destructively interfere due to multiple reflections from the multiple air-silica interfaces. All PCF fibres guide by the photonic bandgap effect [Fer00], but for the solid core PCF an analogy can be drawn with the step index fibres by considering the cladding to have a lower average refractive index than the core. In this case the guidance can be considered to to arise from total internal reflection, as for the conventional fibre [Kni98]. In this regime, the refractive index of the cladding is taken to be the effective index ($n_{eff} = \beta / k_0$) of the fundamental space filling mode, which is defined as the mode which would propagate in an infinite cladding structure with the largest value of β. In fact, when operating in this regime, the cladding need not be perfectly periodic. In addition, an effective V parameter can be defined to allow some of the conventional fibre design concepts to be applied to

solid core PCFs [Mor03], however, although insightful, this is only a crude approximation, and it is usually preferable to solve for the modes of the actual fibre structure. For the hollow core structure no such analogy can be drawn and only the photonic-bandgap concept can explain the light guidance, because the core usually has a significantly lower refractive index than the average cladding index.

Although hollow core PCF can be very interesting and useful, especially as it is possible to fill the core with gases and liquids, leading to some interesting applications, we do not make use of it in this thesis, and so do not discuss it further.

Optical properties

Solid core PCFs can exhibit a range of optical properties not found in conventional fibres. These include:

- Widely variable dispersion properties - including zero dispersion wavelengths shorter than 1.27 μm which is impossible in conventional fibre.
- The endlessly single mode property, where no higher order modes exist at any wavelengths.
- Strong confinement.
- High nonlinearity.
- Strong birefringence - over an order of magnitude higher than conventional birefringent fibres [OB00].

The dispersion properties are discussed in Section 1.4.1, here we review some of the other properties.

The endlessly single mode property is extremely interesting for broadband supercontinuum sources as it means the whole visible supercontinuum can feasibly be maintained in a single mode. It also allows large mode area (and hence low nonlinearity) single mode fibres to be made with applications to high power handling in lasers and amplifiers. This property can be understood by considering the cladding microstructure to be a modal sieve [Rus03]. In this picture, the fundamental mode, which has the largest central lobe of field density, cannot escape between the cladding holes, whereas higher order modes, with smaller lobes can. A more physical understanding comes by noting that the effective cladding refractive index is a strong function of frequency because of the similarity in size of the microstructure to optical wavelengths. This frequency dependence cancels with the frequency dependence included in the V parameter and so it can remain approximately constant, rather than inversely proportional to wavelength, allowing for the

second mode to be cut-off at all frequencies for the correct cladding structures. This property was observed in the first PCF fabricated [Kni96] and later studied in more detail [Bir97]. Theoretical treatments have found that a PCF will be endlessly single mode if $d/\Lambda < 0.43$ [Kuh02b; Mor03].

The strong optical confinement is due to the large refractive index contrast and means that even for large wavelengths, the confinement is still maintained. This results in fibres which can have much higher nonlinearity due to the higher power density, and can also maintain it across a wider wavelength range. The high nonlinearity arises from both the strong confinement and the very small core sizes which can be used. For very high values of d/Λ, i.e. the so called cobweb fibres, which have thin strands of silica (around 100 nm) holding an array of air-holes together around a core, the fibre essentially consists of a single silica strand in air. Thus is has similar extreme nonlinearities and dispersion properties, but with the very significant advantage that the core is protected from the environment which makes these fibres much less lossy and more robust. Values of the nonlinear coefficient γ (see below) can be over three orders of magnitude higher than for conventional optical fibres.

In highly nonlinear conventional fibre (HNLF), high nonlinearity tends to imply a high second mode cut-off wavelength for the single mode regime. This is the same in PCF but the absolute values are different, with HNLF the cut-off is usually above 1.4 μm whereas for PCF cut-offs are closer to the visible spectral region. But it has also been found that the propagation constants between the fundamental and higher order modes in high index difference PCF are very strongly separated; the effective indices are different by more than the core-clad index difference in conventional fibre. This means that coupling between the modes is very weak [Ran00a]. It has been found that exciting the higher order modes in very small core PCF is difficult [Ran00a]. Thus, although the highest nonlinearity is found only in PCFs which are theoretically multi mode, the fibres essentially behave as if they were single mode.

1.3.3 Ytterbium doped fibre amplifiers and lasers

Ytterbium fibre lasers are the dominant high power fibre laser material. Fibre lasers were first suggested in January 1961, [Sni61b], and later that year experimental demonstration was achieved with a flash-lamp pumped neodymium-doped barium crown glass fibre [Sni61a]. Several years later 47 dB gain was measured in a fibre amplifier also based on flash-lamp pumped neodymium-doped glass [Koe64]. This work appears, in retrospect, to be before its time as it pre-dates the development and use of fibres in telecommunication applications and so fibre losses were still very high (~5 dB/m). It was only after the growing interest in optical communications and the subsequent improvements to fibre

technology that fibre lasers saw broad development, and this was mainly due to work on optical amplification for such communication systems.

The first silica-fibre based laser was reported nearly a decade later [Sto73]. A decade later still, a new chemical vapour deposition technique which allowed far easier integration of rare earth ions in fibre cores was developed [Poo85]; this led directly to the first operation of a single-mode rare-earth doped fibre laser [Mea85]. These publications produced renewed interest in fibre laser development, and also rare earth doped fibre amplifiers. Before considering fibre lasers in detail it is worth considering the general advantages of using a wave-guiding structure as the lasing medium as compared to those used in bulk optic lasers. These include [Fra91a]:

- Efficient pumping: no limitations from pump beam divergence.
- Single-mode output: if the fibre core is designed to have a single transverse mode at the lasing wavelength, then the output is necessarily diffraction limited even at very high output powers.
- Thermal advantages: from a simple consideration of fibre geometry (high surface area to volume ratio), most fibre lasers are simply air-cooled.
- Mechanical superiority: fibres can be coiled and packed into very small volumes compared to alternative laser designs.

The main disadvantage of fibre lasers is that they cannot store large amounts of energy, and so the highest energy fibre laser pulses are significantly lower energy than those achievable with bulk lasers.

The Ytterbium (Yb) doped fibre laser is now one of the primary lasers used in industrial settings. Very high average powers are available: over 2 kW CW in a single-mode has been reported [Gap05]. The use of Ytterbium stems from the advantages inherent in its level structure, which is illustrated in Fig. 1.4. For all optical wavelengths there is a ground state manifold ($^2F_{7/2}$) with four Stark levels and an excited state manifold ($^2F_{5/2}$) with three Stark levels. The transitions between sublevels are not fully resolved in silica at room temperature because of strong line broadening, which is predominantly homogeneous [Pas95; Pas97]. Yb^{3+}:silica can be pumped between the lowest Stark level and any of the upper levels, but the absorption is much stronger at the 975 nm transition, so this is mainly used. It should be noted though that this transition is very narrow, and careful pump wavelength control is required. Emission transitions occur between the lowest upper Stark level and all lower levels, but as we are pumping at 975 nm emission to the lowest level is not utilised. Thus the system behaves as a four level laser. The fluorescence decay lifetimes are around 0.8 ms, although this can vary by up to 30% depending on the

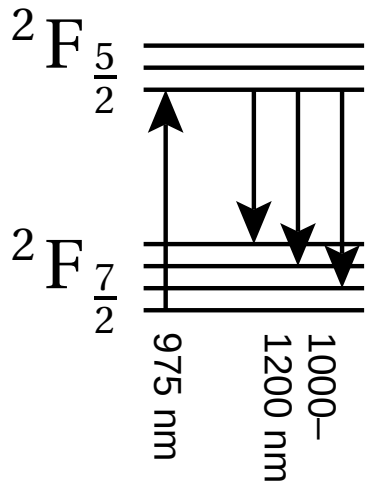


Figure 1.4: The level structure of Yb^{3+} in silica glass.

host [Pas97]. This simple structure leads to a number of benefits compared to other rare earth dopants. These include:

- No excited state absorption of pump or signal due to the absence of higher energy levels.
- No concentration quenching by ion-ion energy transfer, due to the absence of intermediate energy levels.
- Low quantum defect due to the closeness of the pump and emission wavelengths. This leads to good thermal properties.
- No non-radiative decay due to the large energy gap between excited and ground states.
- Very broad absorption, allowing pump flexibility/efficiency.
- Very broad emission, allowing wavelength versatility.

The modern pump scheme makes use of a number of multi-mode pump diodes which are combined by a speciality fused fibre coupler into a multi-mode fibre. This allows very high pump powers to be obtained by simply increasing the number of pump diode modules. The actual gain fibre is double clad, where the multi-mode pump interacts with a single mode gain region which guides the signal. In this way the very high, single transverse mode, output beam quality can be obtained and scaled with pump power. The laser cavity is usually formed with a pair of Bragg gratings at each end of the gain

fibre. Fibre lasers can be operated with active and passive Q-switching or modelocked with a variety of techniques leading to a range of pulse duration, repetition rate and peak powers. In addition, chains of power amplifiers can be spliced to the laser outputs to straightforwardly increase power levels.

The availability of low-cost and high power amplifier and laser technology from Yb systems has opened new possibilities for all-fibre nonlinear optics. The work in this thesis utilises this technology exclusively: all systems were pumped around 1.06 μm. This pump region is optimal, apart from the availability of high quality pump sources, in that it sits mid-way in the silica transparency region. In addition it is the region in which the dispersion of PCF can be most broadly tuned and optimised.

1.3.4 Splicing

Low loss splicing is crucial to reap full benefits from PCFs and fibre lasers, as the full benefits of fibre devices are only realised when no bulk elements are necessary. Gratings, couplers and integrated isolators are key components that facilitate this, but splicing is a necessary requirement to bring all of these elements together. Splicing between standard fibres is routine, with lower than 0.01 dB loss, due to the huge investment in research by the telecommunications industry. But splicing to PCF is more difficult due to structural and guidance differences to standard fibre.

The PCF cladding structure is a less efficient thermal conductor than solid silica. Heating tends to concentrate in the silica bridges between the air-gaps in PCF, leading to hole collapse. Due to this, a way of heating the standard fibre more than the PCF is required. It is particularly important that the holes do not collapse in an uncontrolled way because of the strong dependence of the effective index difference on the fibre geometry. However, controlled hole collapse has been suggested as a technique to match the mode fields at the splice point. In [Læg04] a numerical simulation showed that smoothly (to ensure adiabatic propagation) collapsing the holes could reduce a theoretical loss of 5 dB to 0.5 dB. A simpler alternative to tapering is to use an intermediate fibre with intermediate values of mode field diameter, a technique developed in order to reduce loss when splicing to Erbium amplifiers [Hol90]. It was reported that a loss of 1.45 dB could be reduced to 0.48 dB with the use of two intermediate fibres. We made use of this method to achieve low loss splices to our PCFs.

We used a filament splicer which allows an offset between the heating region and the fibre interfaces. An extensive systematic process of refinement led to a set of parameters for the pre-heating time, the filament current and the time it was applied, which minimised the splice loss. It was found that an initial low power splice to bind the fibres followed by a series of re-heats while monitoring the transmission led to the lowest loss. It was

also found that manually aligning the fibres, so that they were in contact before the splice process, was necessary as the active alignment of the splice software was not sufficiently accurate to deal with the smallest core PCFs.

The intermediate fibre we used was Nufern UHNA3 ultra high numerical aperture fibre. This has a mode field diameter of 2.6 μm at 1.1 μm, and is thus much more closely matched to PCF parameters than the single-mode 1.06 μm fibre which we use to interface with our lasers and isolators, which had a mode field diameter of 7.4 μm. The problem of splicing the intermediate fibre to the single-mode 1.06 μm fibre is solved by the fact that the UHNA3 has core dopants which diffuse to the cladding upon heating, and so the mode field diameter can be expanded and tapered to match that of our standard fibres. Losses of between 0.2 and 0.4 dB were usually achieved for this stage and total splice losses to PCF were usually between 0.8 and 1.5 dB.

1.4 Physics and analysis of optical fibres

In this section we study the physics of dispersion, loss and nonlinearity in optical fibres and techniques for calculating their effects.

1.4.1 Dispersion

Dispersion describes the differing velocity of light at different wavelengths. In single mode optical fibres it is due to two processes. One is the intrinsic material dispersion of the glass which originates from the variation of refractive index with wavelength. The other is due to waveguide dispersion, which is due to the fact that the field of a given mode propagates in both core and cladding regions, which have differing refractive indices. As the mode field distribution changes with wavelength, the proportions in the core and cladding differ and so the resulting mode refractive index, called n_{eff}, is wavelength dependent. The propagation constant β of a fibre mode varies from values close to the cladding wavevector at low frequencies (because the mode is spread out over the cladding) to values close to the wavevector of the core at high frequencies. This variation clearly leads to non-zero derivatives of β and hence to waveguide dispersion. Two facts give rise to the unique dispersion properties of PCFs. Firstly, the index difference between the core and cladding can be very strong, and secondly, the effective index of the cladding can also be very wavelength dependent.

The importance of dispersion

Dispersion is very important to a number of applications, and fundamentally important to nonlinear processes. For example, in telecommunications the fibre dispersion is a

critical parameter dictating the distance which an optical pulse train can propagate before some form of compensation for the pulse spreading must occur. In nonlinear optics dispersion plays a key role. In the wave picture of interactions between different wavelengths propagating through a fibre, the dispersion describes how the phase velocities of the different waves relate to each other, and hence how efficient interactions between them can be. If the waves are not phase matched, then parametric processes tend to be very inefficient. In the particle picture of photon interactions, nonlinear processes between photons of different energies can only occur if momentum is conserved (as well as energy), the momentum conservation is equivalent to the phase matching criteria in the wave picture (easily seen be considering photon velocities). In addition, soliton propagation, which is of great importance to both the supercontinuum generation we discuss in this thesis, and the pulse compression, relies on the precise balance between linear and nonlinear dispersive effects.

Definitions of dispersion parameters

In optical fibres, dispersion is usually characterised by the quantities related to the second derivatives of the refractive index variation with respect to wavelength. This is because it is these quantities which determine the degree of pulse spreading on propagation. The refractive index, or effective mode index is related to β, the propagation constant, by:

$$\beta = k_0 n_{eff}. \tag{1.5}$$

The wavelength dependence of β thus determines the variation of phase velocity with wavelength, of a monochromatic wave. Optical pulses, however, must have a finite bandwidth. The group velocity, v_g, defines the propagation of a packet of monochromatic waves (over an infinitisimal bandwidth). This quantity is related to β via the first derivative with respect to frequency:

$$\beta_1 = \frac{d\beta}{d\omega} = \frac{1}{v_g}. \tag{1.6}$$

Energy is propagated at the group velocity, and in fact, this can be expressed elegantly as in Eqn. 1.7 where the group velocity is related to the modal power flow P_m and the stored energy per unit length in the fibre $\mathcal{W}_m$ [Sny83].

$$v_{gm} = \frac{P_m}{\mathcal{W}_m} \tag{1.7}$$

Due to the different group velocities of different pulses, limitations of the nonlinear interaction length occur due to pulse walk off, where one pulse will be moving slower than another and will be left behind, preventing further interaction. Group velocity also plays a

significant role in soliton trapping of dispersive waves, which we consider in Chapter 4.

The group velocity dispersion is due to the differing group velocities of the components of a particular pulse. If some are moving slower than others, then the pulse will spread in the time domain. As noted above, this parameter is important to telecommunications and also very important to soliton propagation. It is given by the second derivative of β:

$$\beta_2 = \frac{d^2\beta}{d^2\omega} = -\frac{\lambda^2}{2\pi c}D, \tag{1.8}$$

where c is the speed of light in a vacuum and λ is the pulse centre wavelength. D is an engineering unit commonly used because it has practical units of ps nm^{-1} km^{-1} which can be directly related to the amount of pulse spreading (in ps) per bandwidth (in nm) per propagation length (in km). We use both β_2 and D when referring to group velocity dispersion.

Higher order dispersion can also be very important. When the group velocity dispersion is small then third order dispersion becomes the dominating effect. Higher order dispersion can perturb soliton propagation and is also important to the phase matching of nonlinear processes which are separated by large frequency shifts.

Material dispersion

In Section 1.3.1 we saw how the refractive index of a material was related to the linear susceptibility of the material. In this thesis, the only materials used for guiding light are silica, and air (which is effectively dispersionless at optical frequencies). The susceptibility of fused silica is dominated by electronic (atomic) resonances around a wavelength of 0.1 μm and Si-O molecular lattice resonances in the region of 7-15 μm. The wavelength region we are interested in is $\lambda = 0.3 - 2.4$ μm. Due to the dominance of the electronic resonances, the refractive index of silica is decreasing across this region as can be seen in Fig. 1.5. The sharp slope at the short wavelength edge is due to the above mentioned electronic resonances. As the wavelength (or frequency) approaches a resonance, the material absorption dramatically increases, and the refractive index does also. This is because near resonances the dipole oscillators exhibit a larger phase delay which can be understood by considering the intimate relationship between absorption and dispersion expressed in the Kramers-Kronig relations. The lattice absorption is not strong in this region and contributes only to the background value.

The material group velocity dispersion is also shown in Fig. 1.5. There is a zero dispersion point at 1.27 μm which is due to the inflection point in the refractive index curve. The zero dispersion wavelength is very important as it determines the boundary between normal (negative D) and anomalous (positive D) dispersion regions. This is significant as

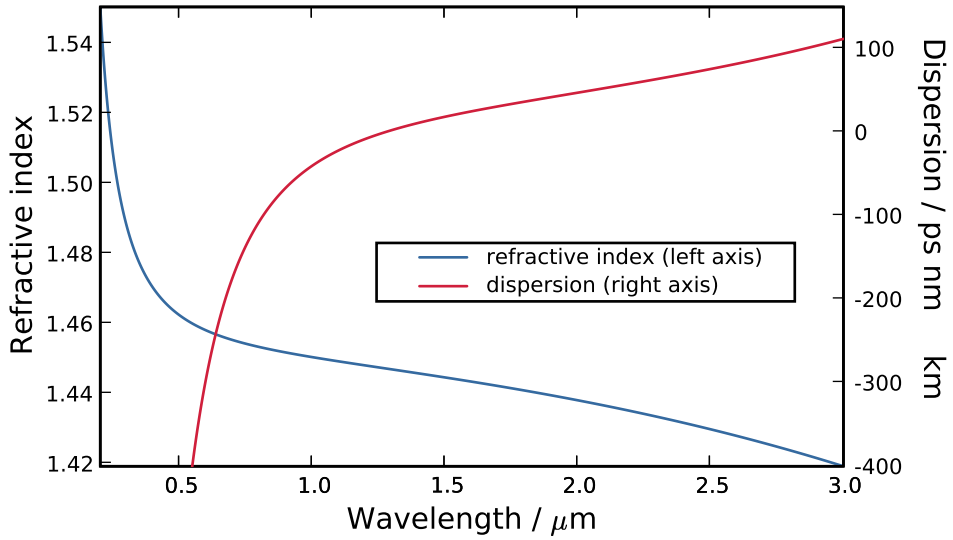


Figure 1.5: The refractive index and material dispersion of pure fused silica.

bright soliton propagation and modulation instability (both essential to our supercontinuum generation) are only possible in the anomalous dispersion region. Overall, the silica dispersion strictly increases with wavelength.

Calculation of dispersion

The calculation of dispersion for a given fibre structure comes down to calculating the propagation constant at a range of wavelengths and then taking derivatives. This can be formulated as an eigenvalue problem with the transverse field as the eigenvector and β as the eigenvalue. To solve this we used two methods. For very complicated structures, such as fibre cross-sections from SEM images, we use a freely available software package which numerically solves Maxwell's equations over arbitrary structures. For simpler, analytical structures, often used when we are looking for PCFs with our desired properties we used an analytical effective index method for its speed and convenience. In the following two subsections we review these methods.

MIT photonic bands

The most accurate technique used in this work was a fully vectorial eigenmode solver of Eqn. 1.9 with Eqn. 1.10 as a constraint and periodic boundary conditions. We used the open source software package called MIT Photonic Bands, which we refer to as MPB

[Joh01].

$$\nabla \wedge \frac{1}{\epsilon} \nabla \wedge \mathbf{H} = -\frac{1}{c^2} \frac{\partial^2}{\partial t^2} \mathbf{H} \tag{1.9}$$

$$\nabla \cdot \mathbf{H} = 0 \tag{1.10}$$

For a given dielectric structure, defined by ϵ the eigenmodes of the magnetic field are found in the frequency domain on a planewave basis using a conjugate gradient method. Apart from β, MPB can also provide the full magnetic and electric fields which can be used for the calculation of the effective mode area, which we discuss in Section 1.4.3. We adapted the MPB software to be able to calculate the eigenmodes directly from SEM images of the fibre cross sections. This technique was used extensively in this thesis.

The MPB software is very accurate, however it makes some assumptions about the problem which are not correct for our purposes, and one should be aware of them when performing calculations with it. Specifically it performs what is called a supercell calculation, where a periodicity is enforced on the structure by periodic boundary conditions. This is ideal for solving for the fundamental space filling mode of the cladding PCF structure, in which case we can solve for just one crystal unit cell leading to efficient computation. But when we have added the core defect we must solve over a number of unit cells (the supercell) so that we can push the infinite number of additional defects (added due to the periodicity) far enough out so they do not interfere with the defect mode calculations. Apart from increasing computation time, some artefacts from coupling between defects may occur, although they can be minimised. In particular, calculations of confinement loss, where the structure begins to leak radiation are impossible with this method, as no light can escape from an infinite structure!

Nevertheless we have found MPB to agree well with experimental dispersion measurements and other software. In particular we have verified the results with another free tool based on the multipole method, which is deemed to be extremely accurate [Kuh02a]. However, this tool could not be used because it requires the inclusions to be perfectly circular ruling out a number of interesting PCF structures.

Vector analytical approach

As noted above, the MPB software can be very accurate, it is also computationally intensive and it is sometimes useful to be able to interactively look at the effects of PCF structure on dispersion and nonlinearity. In such cases we used a vector analytical method which shows good agreement to more accurate numerical methods over a wide range of parameters. Building on the concept of modified total internal reflection described above, we model the PCF with an equivalent step-index fibre, where the air-holes in

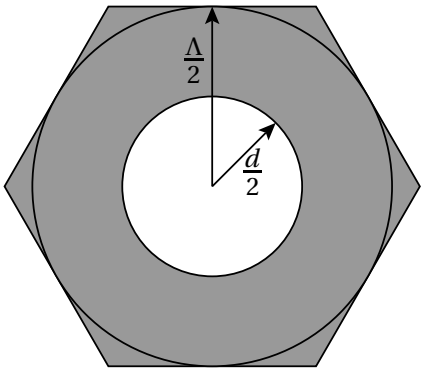


Figure 1.6: The unit cell of the PCF cladding with the air-hole radius and equivalent cell radius defined.

the cladding yield a lower effective refractive index than the pure silica core. To do this we first calculate the effective index of the cladding structure using the concept of the fundamental space filling mode, as mentioned above. This comes down to finding the fundamental eigenmode (that with the largest effective index) of the infinite periodic lattice with the same structure as the PCF cladding. When this is complete we then model the PCF as a step index fibre with a solid core of silica and a cladding with the previously calculated effective index. This approach is much faster than the full numerical solutions to Maxwell's equations, but also considerably more accurate than the traditional scalar approximations [Mid00]. There are two problems to be solved with this approach, firstly, how to calculate the fundamental space filling mode of the cladding; and secondly, what core size to choose for the equivalent step index fibre.

The first problem can be solved in a number of ways. For example, we could use MPB for this calculation as it is not a supercell problem and is quite efficient. However, it is still not fast enough on current hardware for the purpose of interactive visualisation. Instead we use a full vectorial solution of Maxwell's equations by solving for the unit cell of the cladding structure with a circular symmetric approximation. Such problems, like the conventional step index fibre, have exact analytical solutions [Sny83]. To illustrate this method, Fig. 1.6 shows the PCF cladding unit cell and the circular symmetric approximation to it. The typical PCF structure is hexagonal, as shown in Fig.1.2(a). The air holes are circular and the unit cells tessellate on hexagonal boundaries. Therefore, in Fig. 1.6 we show just one hexagonal cell. The core circular region is air and the surrounding region is the silica which forms the bridges between the air-holes in the PCF cladding. The relative air-hole size is given by the hole diameter (d) to pitch (Λ) ratio. So the boundary of the hexagon at the mid-point of one side is $\Lambda/2$ from the air-hole centre, as shown.

To approximate this structure with a cylindrical problem, we fit a circle to the hexagonal

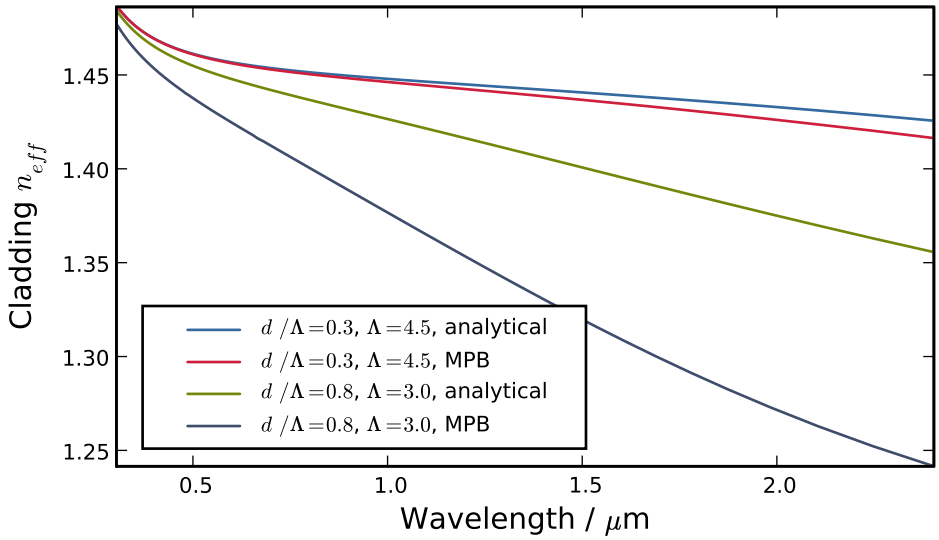
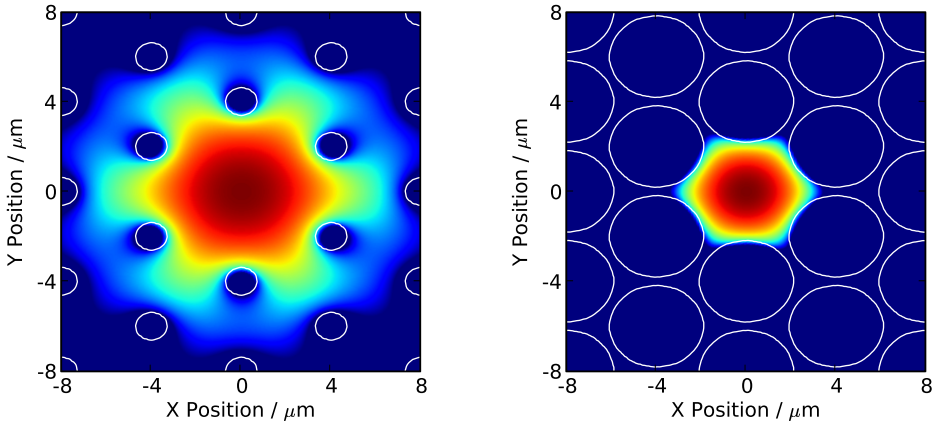


Figure 1.7: A comparison of the effective cladding index between MPB and the vectorial analytic method for two structures.

structure. We can then solve for the fundamental mode of this structure using a variation of the standard methods [Mid00; Sny83]. The one free variable available with this method is the radius of the cell circle used to fit the hexagon. A number of suggestions have been made, including choices which set the cell radius to $\Lambda/2$, the half distance between two air-hole centres [Mid00]; or a choice which makes the total area of silica in the cell the same as that in the hexagonal cell [Li06]. We choose the former as it tended to give a closer fit to full numerical solutions using MPB.

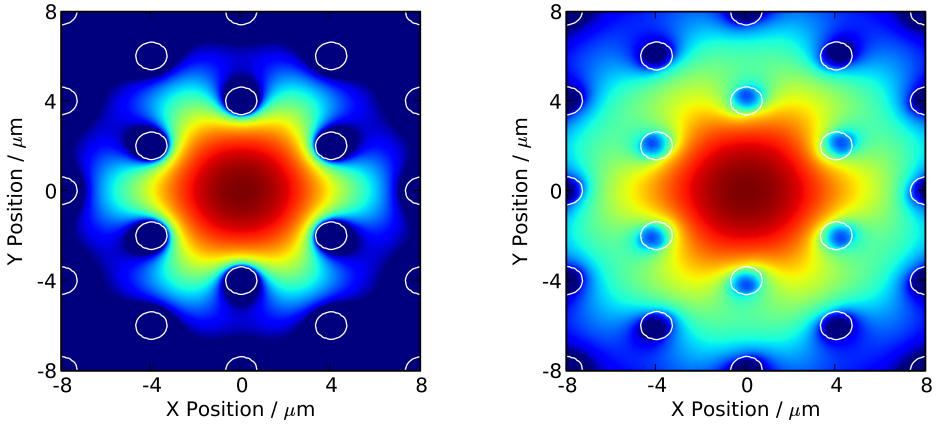
In Fig. 1.7 we compare the effective cladding index of the fundamental space filling mode as calculated with both MPB and the vectorial analytic method for two structures. One structure has a low air filling fraction and large pitch ($d/\Lambda = 0.3$, $\Lambda = 4.5$ μm), the other has a large air filling fraction and a smaller pitch ($d/\Lambda = 0.8$, $\Lambda = 3.0$ μm). For the first structure the agreement of cladding effective index is quite good, but for the tight structure, the agreement is poor, because the circular approximation to the silica lattice becomes less accurate.

Once the effective cladding index is found, the fundamental mode can be solved for using the standard vectorial analysis of a step index fibre [Sny83], with the core size chosen to be 0.625Λ from comparison to full numerical results [Li06]. Although not as precise as MPB, which we use for the majority of dispersion calculations in this thesis, the vectorial analytic method was very useful when developing approximate designs for the PCFs used in the pulse compression experiments.



(a) $d/\Lambda = 0.3$ (b) $d/\Lambda = 0.9$

Figure 1.8: The time-averaged electric field energy density of the fundamental mode of a PCF with $\Lambda = 3$ μm with two air-filling ratios at a wavelength of 1.06 μm. The white circles indicate the air-holes in the PCF structure used to calculate the mode patterns. Colour scale: −30 0 dB.



(a) $\lambda = 0.4$ μm. (b) $\lambda = 2.2$ μm.

Figure 1.9: The time-averaged electric field energy density of the fundamental mode of a PCF with $\Lambda = 3$ μm and $d/\Lambda = 0.3$ at two wavelengths. The white circles indicate the air-holes in the PCF structure used to calculate the mode patterns. Colour scale: −30 0 dB.

Modal properties of PCF

Apart from the propagation constant, the MPB method provides us with access to the transverse magnetic and electric fields of the fibre modes for arbitrary structures. In this subsection we take a brief look at the mode profiles in various circumstances as they can provide insight into the dispersion properties of PCF discussed below.

Fig. 1.8 shows the mode distribution for two PCFs with the same pitch (Λ) but different d/Λ ratios. For the low ratio fibre where the effective index contrast is low, the mode spreads considerably between the cladding holes. In contrast, in the high ratio fibre, the effective index contrast is very high and the mode is tightly confined in the core. Such a PCF will be highly nonlinear and the dispersion properties will resemble those of a silica strand of the same dimensions as the PCF core (see below). These calculations were performed at a wavelength of 1.06 μm. In Fig. 1.9 we contrast the mode patterns for two different wavelengths, 0.4 and 2.2 μm, in the same PCF structure. The mode distribution at 0.4 μm is contained almost entirely in the silica glass region and reasonably well confined to the core with extensions between the first ring of holes. In contrast for 2.4 μm the mode has spread well beyond the first ring of holes and beyond the second ring and also exhibits a large overlap with the air-holes. This change in overlap with wavelength leads to very strong waveguide dispersion.

Dispersion in PCF

By changing the positions, size, shape and material in the PCF structure we can exert a very large control over the PCF dispersion, with the ability to cancel the material dispersion over much of our wavelength range of interest - something not possible with conventional fibres which have relatively small core/cladding refractive index contrast. The unique properties of PCF with respect to dispersion include:

- Shifting the zero dispersion wavelength far shorter than the material dispersion at 1.27 μm and significantly into the visible spectral region as short as 0.55 μm [Kni00].
- Flattening of the dispersion profile over a large wavelength range [Ree02].
- Shifting a second zero dispersion wavelength into our wavelength range of interest, leading to unique phase matching properties.

The first feature, the ability to shift the zero dispersion wavelength, and hence regions of anomalous dispersion into the visible spectral region is perhaps the most celebrated and utilised feature of solid core PCF [Kni00]. It allows for soliton propagation and modulation instability, two of the primary mechanisms for initiating supercontinuum generation, to be achieved at short wavelengths. To illustrate how this works, we shown in Fig. 1.10 the contributions to dispersion in a particular PCF structure. The total dispersion is not actually the simple sum of the material and waveguide dispersion [Sai06], but must be calculated in a self consistent manner (which we do throughout this work), although to a first approximation they both contribute equally. As we saw above, the silica dispersion has a zero crossing at 1.27 μm. For this PCF structure, the waveguide dispersion is strongly

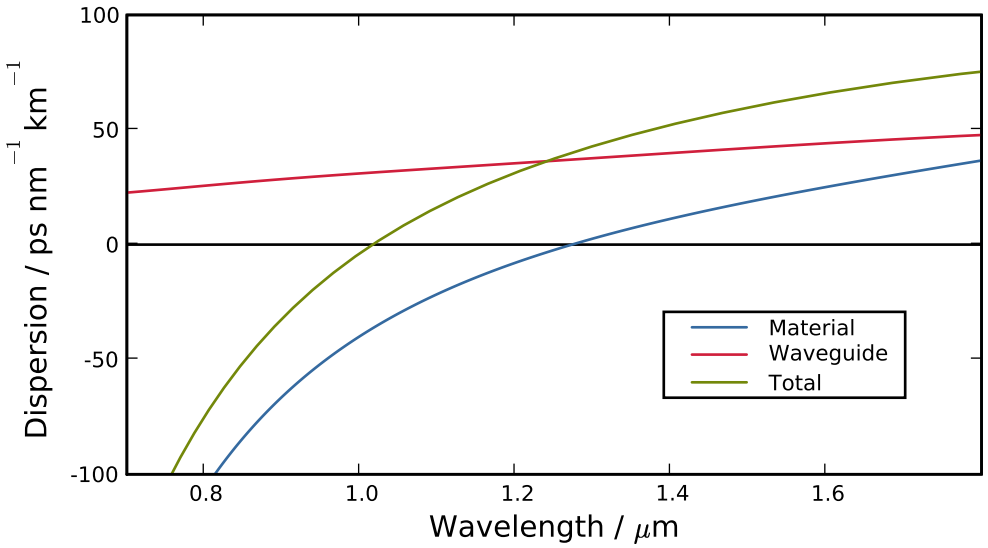


Figure 1.10: The material, waveguide and total group velocity dispersion for a PCF with $\Lambda = 3$ μm and $d/\Lambda = 0.5$.

anomalous across the whole region with the result that it cancels a large portion of the material dispersion and shifts the total zero dispersion wavelength to near 1.0 μm. In conventional optical fibre which is single mode, the waveguide dispersion is always normal and strongly guiding conventional fibres tend to shift the zero dispersion to longer wavelengths instead.

The ultimate limit of tight confinement is when there is no silica glass in the cladding at all and we are simply left with a silica strand. Although such fibres have been used through tapering conventional fibres [Bir00], because of their interesting dispersion and nonlinearity, they are quite impractical and sensitive to the environment. One feature of PCF is that it can be made very similar to this limiting case [Kni00; Sai06]. For example, in Fig. 1.11 we compare the dispersion of a very high air-fill fraction PCF with a silica strand of equivalent core size. It is clear that the dispersion curves are very similar although they diverge somewhat at longer wavelengths as the mode expands into the cladding and is affected by the silica bridges between the air-holes.

The shifting of the zero dispersion is clearly shown in Fig. 1.12 which shows the dispersion curves for PCF structures with the same 3 μm pitch, but increasing air-hole size. As the air-holes get bigger, the effective refractive index contrast becomes larger and so the waveguide dispersion becomes more strongly anomalous and the zero dispersion wavelength shifts to shorter wavelengths. In contrast, for very small air-hole sizes, the dispersion has been flattened with respect to the material dispersion curve and this feature has been utilised to develop ultra-flat dispersion curves.

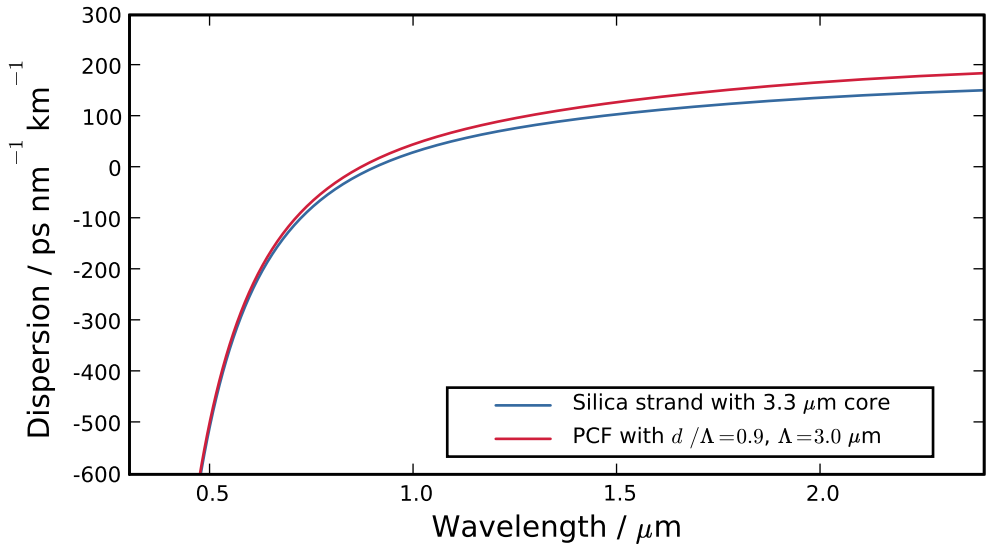


Figure 1.11: A comparison of the group velocity dispersion between a high air-fill fraction PCF and a silica strand in air with the same core size.

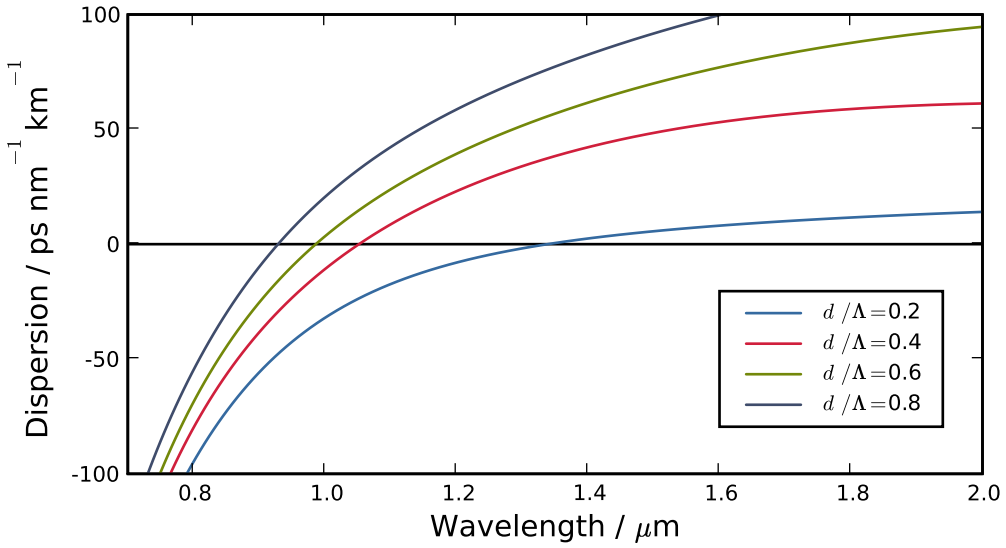


Figure 1.12: The calculated dispersion for PCFs with $\Lambda = 3$ μm and different d/Λ.

In high air-filling structures, like those shown in Fig. 1.13 with $d/\Lambda = 0.9$, decreasing the pitch size leads to the shortest zero dispersion wavelengths achievable. In Fig. 1.13 we have zero dispersion points below 0.6 μm for the tightest structures. Two other features of these curves are apparent. Firstly the maximum dispersion values are quite high, over 170 ps nm^{-1}km^{-1}. Secondly, a second zero dispersion wavelength is introduced. This is

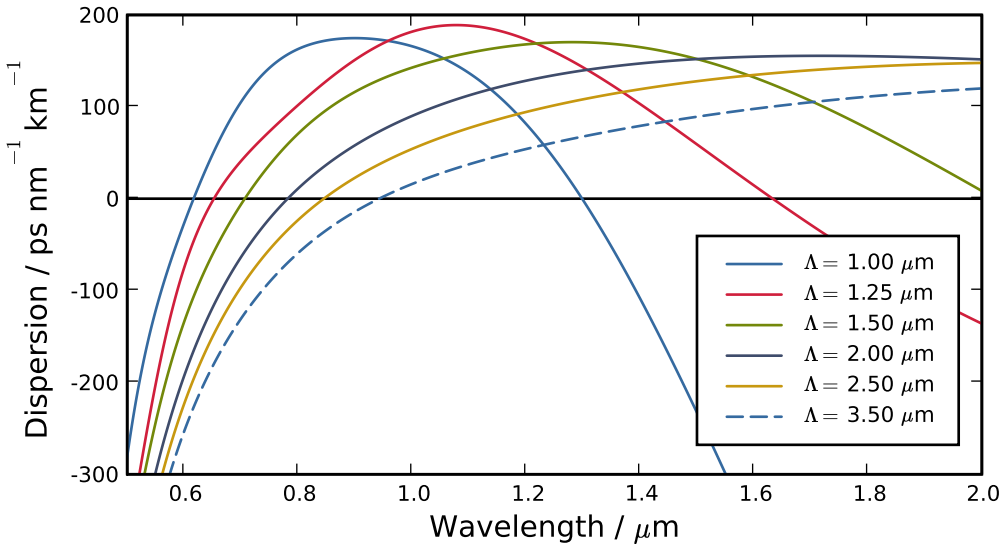


Figure 1.13: The calculated dispersion for PCFs with $d/\Lambda = 0.9$ and the specified pitch.

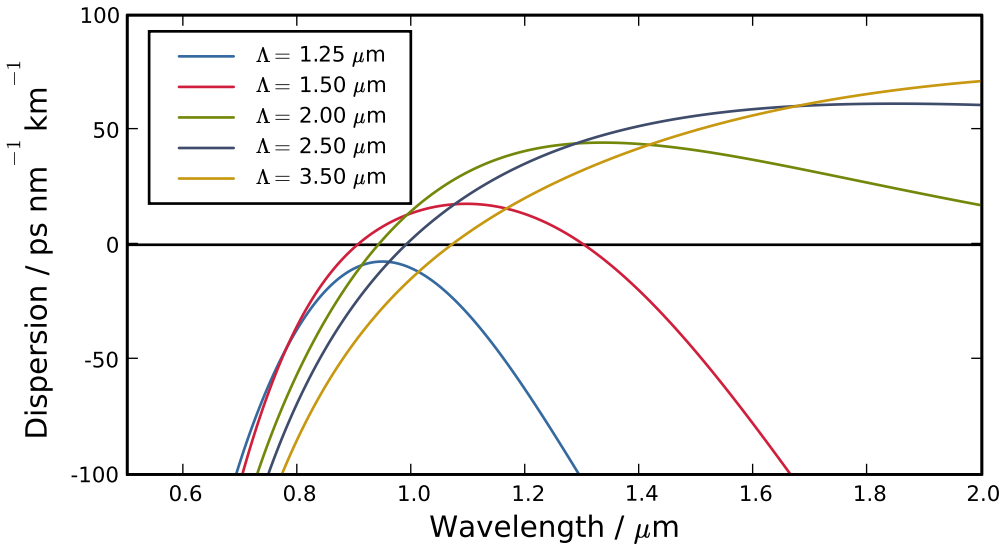


Figure 1.14: The calculated dispersion for PCFs with $d/\Lambda = 0.45$ and the specified pitch.

caused by the waveguide dispersion which is now strongly normal at long wavelengths as the core is too small to contain the field.

In structures which have smaller air-holes like those shown in Fig. 1.14 with $d/\Lambda = 0.45$, decreasing the pitch has a much smaller effect on shifting the first zero dispersion

wavelength, and the overall dispersion values are much lower. However, the reduction in pitch has a stronger effect on the second zero dispersion wavelength, shifting the overall dispersion down, and eventually leading to a fibre with all normal dispersion! The reason for this is the very weak guidance for those parameters and thus normal waveguide dispersion.

Although we have shown this wide variation in dispersion through simply changing the pitch and air-hole diameter, further control can be exercised. For example, one can imagine changing the size of the air holes in each ring of the cladding, creating fibres similar to the conventional depressed cladding and W-profiles [Pol04]. Alternatively, some groups have studied the properties of fibres with square hole arrangements [Bou04]. Finally the material in the holes need not necessarily be air, and fibres with solid and liquid inclusions have been discussed.

1.4.2 Loss

Fused silica glass transmits electromagnetic radiation over a very wide wavelength range from an ultra-violet (UV) absorption edge at about 0.2 μm to an infra-red (IR) absorption edge around 2.5 μm. Within this transmission region, optical fibre loss is limited by Rayleigh scattering, so-called water absorption related to the vibrational absorption of Si-OH bonds (through harmonics at 1.38 μm in particular) and waveguide imperfections. In solid optical fibres, these have effectively been reduced to the limit imposed by Rayleigh scattering, leading to very low loss: less than 0.4 dB/km from at least 1.2 to 1.7 μm with a minimum below 0.2 dB/km at around 1.5 μm.

Photonic crystal fibres have additional losses arising from imperfections on the air-silica interfaces, or fluctuations of the hole sizes [Rus06]. More significantly they exhibit far higher water absorption due to Si-OH bonds at the air-silica interfaces. Loss values over 100s dB/km are common at 1.38 μm and especially affect high air-filling fraction PCFs. In Chapter 2 we study the effect of this loss on continuous wave supercontinuum generation, and ways to overcome it.

Confinement loss is due to the finite number of air-hole rings allowing the evanescent field in the cladding to reach the solid glass outer cladding. This can be a problem at long wavelengths when the waveguide effectively becomes too small to contain the field. In Chapter 4 we calculate the confinement loss for the tapered fibres we used for supercontinuum generation, and also observe how the long wavelength edge of the supercontinuum is curtailed by this loss. In the same chapter we also note the short wavelength bend loss which is unique to PCFs and depressed cladding fibres and also the role of two photon absorption limits to UV supercontinuum generation.

1.4.3 Nonlinearity

In Section 1.3.1 we saw how the linear propagation depends on the linear susceptibility of the material, through the induced polarisation P. For high intensities the material susceptibility can no longer be regarded as linear and higher order contributions must be included. Because silica glass is isotropic it is centro-symmetric (i.e. invariant on inversion in three spatial dimensions) and so χ_2 is zero. Note that it is the amorphous nature of glass that leads to the inversion symmetry even though SiO_2 is itself not centro symmetric. Therefore, the first higher order contribution (which can be found by expanding χ in a Taylor series) is χ_3, the third order susceptibility, and it is nonlinearities arising from this term which we study in this thesis. There are three dominant sources of nonlinearity in silica fibres. The Kerr effect (intensity dependent refractive index), which arises from the nonlinearity of the electronic resonances in silica and which gives rise to self phase modulation, cross phase modulation and four wave mixing; and two stimulated inelastic scattering processes, Raman and Brillouin scattering. Raman scattering originates from the molecular vibrational and rotational resonances in silica and Brillouin scattering from the electrorestriction effect. All of these contributions are included in χ_3. Similarly to the linear susceptibility, χ_3 can be related to a refractive index and an absorption coefficient, except in this case the effect is intensity dependent. The nonlinear refractive index is referred to as n_2 and is taken as $n_2 = 2.74 \times 10^{-20}$ m^{2}W^{-1}, which was determined from an extensive review of measured values [Mil98]. This value includes a fractional contribution from Raman, $f_r = 0.18$, but no contribution from electrorestriction, as we do not study Brillouin scattering in what follows (see Section 1.5.8 as to why). The imaginary part of χ_3 is responsible for multi-photon absorption, which is briefly discussed at the end of Chapter 4, and other effects which result in the transfer of energy to the medium, notably Raman scattering.

The electronic contribution to n_2 can be regarded as instantaneous for pulse durations longer than ~ 10 fs, at the same speed as the linear refractive index. The Raman contribution, however, is delayed, as shown in Fig. 1.15. It is usual to account for this by writing the nonlinear response function as [Sto89; Hol02]:

$$R(t) = (1 - f_r)\delta(t) + f_r h_r(t) \tag{1.11}$$

where $h_r(t)$ is the Raman response shown in Fig. 1.15.

In optical fibres, the intensity is a linear function of power only, because the light is guided in a constant mode shape. Therefore it is usual to define a nonlinear coefficient γ

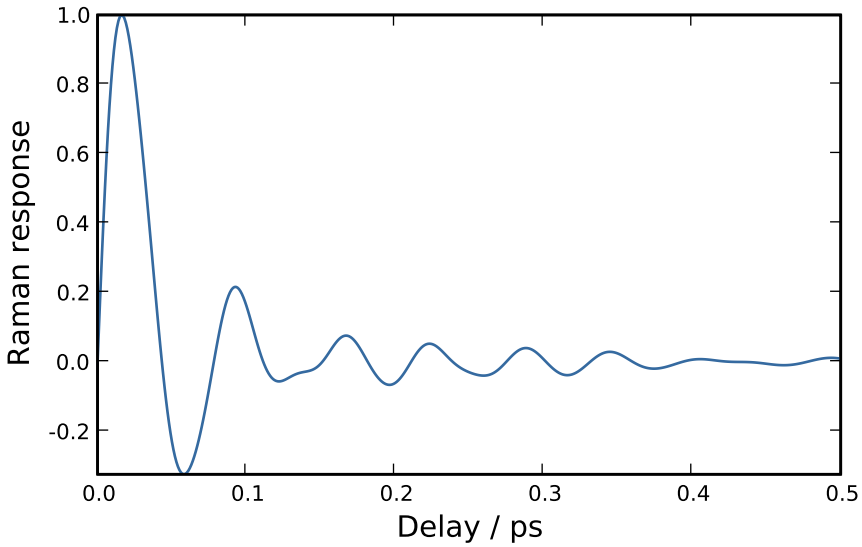


Figure 1.15: The Raman response function $h_r(t)$.

which factors the mode size out from further calculations:

$$\gamma = \frac{2\pi n_2}{\lambda A_{eff}} \tag{1.12}$$

The effective area A_{eff} can be defined a number of ways, in conventional optical fibres, with low index and nonlinearity contrast between the core and cladding the scalar definition is commonly used:

$$A^s_{eff} = \frac{\left(\int_S |\mathbf{E}_m|^2\right)^2}{\int_S |\mathbf{E}_m|^4} \tag{1.13}$$

where S is the fibre cross section and $\mathbf{E}_m$ is the modal electric field distribution (similarly $\mathbf{H}_m$ for the magnetic field). But in PCFs with high refractive index contrast, and significant proportions of the field propagating in air, a full vectorial calculation of the effective area is required [Tzo95], and was used throughout this work:

$$A_{eff} = \frac{\mu_0}{\epsilon_0 n_0^2} \frac{\left(\int_S \mathbf{E}_m \wedge \mathbf{H}_m\right)^2}{\int_{silica} \left[(\mathbf{E}_m \cdot \mathbf{E}_m)^2 + \frac{2}{3}|E_z|^2 \mathbf{E}_m \cdot \mathbf{E}_m + |E_z|^4\right]} \tag{1.14}$$

If the core is significantly smaller than the wavelength, the light is guided mainly outside of the glass and so A_{eff} does not always get smaller as the core shrinks. It should be noted that the effective area is wavelength dependent, sometimes strongly so. For very broadband calculations we must account for this and indicate how we do so below.

1.4.4 Modelling

As part of the work on this thesis a complete code for simulating the propagation of optical pulses through fibres was developed. It was used extensively to design the fibre tapers and understand the supercontinuum mechanisms of our experimental results, and assisted a large part of our analysis. We used a beam propagation method - a modification of the split-step Fourier method. We start by describing the pulse with an envelope equation [Agr01; Blo89; Fra91b; Mam90]:

$$\mathbf{E}(z,t) = E(z,t)\mathbf{E}_m(\omega_0)\exp[-i(\omega t - \beta z)] \tag{1.15}$$

where $E(z,t)$ represents the temporal envelope of the field (i.e. the amplitude of the field neglecting the high frequency oscillation of the carrier). It is complex to allow for the accumulation of phase delay. In practice the modal field distribution $\mathbf{E}_m$ is removed by using γ with A_{eff} evaluated at the centre frequency ω_0, although some adjustment to account for the frequency dependence of γ is required for broadband supercontinuum simulations. The simulations are carried out in a shifted frequency window given by $\Omega = \omega - \omega_0$ where ω_0 is a chosen central frequency. The field is assumed to be zero outside of this window. The envelope $E(z,t)$ is defined by the Fourier transform of the pulse spectrum. We assume that the fibre is single mode and that the light stays linearly polarised, although a large simplification, this assumption works well in practice.

The propagation equation of such an envelope representation of the field through an optical fibre can be described by the generalised nonlinear Schrödinger equation (GNLSE) which has been derived from Eqn. 1.1 in a number of different ways [Blo89; Fra91b; Mam90]. The GNLSE can be written as Eqn. 1.16.

$$\partial_z E = \left(\frac{\alpha}{2} + i\hat{D} + i\hat{N}\right)E, \tag{1.16}$$

where the operators $\frac{\alpha}{2}$, $\hat{D}$, and $\hat{N}$ represent attenuation, dispersion, and nonlinearity respectively, and we have shifted to a frame of reference co-moving with the group velocity: $t = z - \beta_1 t$, and so terms including β_1 are eliminated. The dispersion operator is given by Eqn. 1.17 in the time domain.

$$\hat{D} = \sum_{k\geq 2} \frac{(i)^k \beta_k}{k!}\partial_t^k \tag{1.17}$$

It is more common to solve the dispersion component in the frequency domain, where

the operator is given by:

$$\hat{D}_\omega = \sum_{k\geq 2} \frac{\beta_k}{k!}\Omega^k \tag{1.18}$$

$$= \beta(\omega_0+\Omega) - \beta(\omega_0) - \Omega/V_0 \tag{1.19}$$

and $V_0 = [(d\beta/d\omega)|_{\omega_0}]^{-1}$ is the group velocity at ω_0. The form in Eqn. 1.19 is more accurate and more convenient to use if one has the full β curve of the mode. If the dispersion has been measured, or is estimated from manufacturers information, then Eqn. 1.18 is usually used instead. The attenuation operator is defined by α which is the linear gain or loss, it can be a scalar at $\alpha(\omega_0)$ or a function of frequency, allowing for the modelling of water loss for example.

The nonlinear operator is given by Eqn. 1.20:

$$\hat{N} = \gamma(1 - i\tau_s\partial_t)\int_{-\infty}^{t} R(t')|E(t-t')|^2 dt'. \tag{1.20}$$

In this equation, the response function $R(t)$ represents both the instantaneous and delayed response of silica and was given in Eqn. 1.11 of the previous section. The integral represents a convolution between the nonlinear response and the field intensity. The integration limits run from all previous times to the current time to satisfy causality. As the electronic response is instantaneous, it can be moved out of the convolution resulting in a term $\gamma|E|^2E$ which corresponds to the Kerr effect. The convolution of the Raman component leads to a delayed response for the nonlinear operator. In the frequency domain this amounts to a frequency shift and this term accounts for the Raman soliton shift which we discuss in later sections. The operator $\tau_s\partial_t E$ is responsible for optical shock formation and represents the dispersion of the nonlinearity. By modifying τ_{shock}, which is to first order given by $\frac{1}{\omega_0}$, to include higher order terms, the GNLSE can be used for few cycle optical pulses and can account for the wavelength dependence of A_{eff} [Kib05].

To solve Eqn. 1.16 it is common to use the split-step Fourier method [Agr01; Blo89], which is a pseudospectral method. This entails solving the linear part in the frequency domain (where there is an exact solution) and utilising the Fourier transform to switch to and from the time domain where the nonlinear part is evaluated, this procedure can be written as:

$$E(z+\Delta z) = \exp\left[i\Delta z\hat{N}\right]\mathscr{F}^{-1}\exp\left[\Delta z\left(\frac{\alpha}{2} + i\hat{D}_\omega\right)\right]\mathscr{F}E(z) \tag{1.21}$$

where Δz is the longitudinal step size and $\mathscr{F}$ and $\mathscr{F}^{-1}$ represent the forward and inverse Fourier transforms respectively. The advantage is that the partial derivatives with respect to time in the dispersion operator are replaced simply by multiplications by $i\Omega$ in the frequency domain. However, there can be complications when accounting for the shock

derivative, which must be dealt with as a perturbation [Blo89; Cri04]. Instead, it is also possible to solve Eqn. 1.16 purely in the frequency domain, integrating directly with, for example, a Runge-Kutta method [Fra91b]. This has the additional advantage that the convolution integral in the nonlinear operator (Eqn. 1.20) becomes a simple multiplication and the shock term can be dealt with directly. However, although more accurate, as it deals simultaneously with dispersion and nonlinearity, it can be very inefficient, especially for very large scale problems like supercontinuum generation. Instead, we use a split-step scheme where the linear part is propagated, as per the normal split step, in the frequency domain, by a direct multiplication with $\exp[\Delta z(\frac{\alpha}{2} + i\hat{D}_\omega)]$, but the nonlinear part is directly integrated, also in the frequency domain, using a Runge-Kutta method. This maintains the advantages of the frequency domain formulation, while keeping the efficiency of the split-step method.

After the majority of work described in this thesis was conducted, our propagation code was modified in light of more recent studies on the numerical solution of Eqn. 1.16. In particular, the technique described as the Runge-Kutta in the Interaction Picture method [Hul07], was implemented improving the accuracy and speed of our code. Further work made use of the modified GNLSE as described in [Læg07], which can be integrated directly without a split step technique and can directly include the wavelength dependence of the effective mode area and effective mode index.

Implementation details

The actual implementation of our original scheme, for each step, can be written as follows (the numerical subscripts indicate the progression of the field):

1. Apply the linear operator over the first half of the step ($\Delta z/2$):

$$E_{\omega,1} = \exp\left[\frac{\Delta z}{2}\left(\frac{\alpha}{2} + i\hat{D}_\omega\right)\right] E_{\omega,0}$$

2. Integrate the nonlinear part from $E_{\omega,1}$ at z to $E_{\omega,2}$ at $z + \Delta z$ using a Runge-Kutta method to solve:

$$\partial_z E = i\hat{N}E$$

   where the RHS can be evaluated at each point as follows:

   a) Calculate the time domain field: $E_{t,1} = \mathscr{F}^{-1}E_{\omega,1}$, and intensity: $I_{t,1} = |E_{t,1}|^2$

   b) Calculate the convolution of the intensity and Raman response:

$$R_t = \mathscr{F}^{-1}\left(\mathscr{F}(h_r)\mathscr{F}(I_{t,1})\right)$$

c) Combine the Raman and Kerr effect and apply to $E_{t,1}$:

$$C_\omega = \mathscr{F}\left(\left[(1-f_r)I_{t,1} + f_r R_t\right]E_{t,1}\right)$$

d) Use multiplication by $i\Omega$ in the frequency domain for the shock term and build the nonlinear term:

$$i\hat{N}E_{\omega,1} = i\gamma(1+\tau_s\Omega)C_\omega$$

3. Apply the linear operator over the second half of the step:

$$E_{\omega,0} = \exp\left[\frac{\Delta z}{2}\left(\frac{\alpha}{2} + i\hat{D}_\omega\right)\right]E_{\omega,2}$$

The accuracy of this method is determined by the choice of step size Δz along the fibre length. However if Δz is reduced too low, the simulations take a prohibitively long time. To optimise this we use an adaptive step size algorithm, which monitors the local relative error and adjusts the step size in order to meet a set error goal [Sin03], It should be noted that this does not imply a specific overall error, but the algorithm is fourth order in Δz. A choice of 10^{-8} for the relative local error was used for the simulations in this thesis, and step sizes could be as small as 1 μm. The total error can be observed from the conservation of photon number which is preserved by the GNLSE in the absence of gain or loss [Fra91b; Blo89; Mam90]. In all simulations the photon number was kept to within 5% of the starting value.

It is also important to ensure that the numerical grid used for the simulations is sufficient for the problem. There are two constraints on the grid size, firstly the full temporal width of the grid must accommodate the pump pulse duration and any delay due to group velocity dispersion which may arise. When simulating broadband supercontinua over long fibre lengths, the group delay of the extreme spectrum limits can be up to 100s of picoseconds. Secondly, the temporal grid spacing must be narrow enough to support the frequencies we wish to simulate. Due to the sampling theorem we must choose a grid spacing corresponding to twice our highest frequency [Bra00]. For example, to support wavelengths of 0.35 μm with a central wavelength of 1.06 μm requires a grid spacing Δt smaller than 0.4 fs. Combined, these constraints mean that we have to use grids with up to 2^{19} points to simulate the most broadband supercontinua.

Some of the nonlinear processes involved in supercontinuum formation, notable four wave mixing, require the presence of noise to be initiated. We include this in our model with a phenomenological two photons per mode as described in [Dud06].

We have confirmed the validity of our implementation by checking for correspondence with other published results. These have included: verification against the majority of the very comprehensive results in [Agr01], and the reproduction of the results published in [Fra91b; Blo89]. In addition we have reproduced the supercontinuum simulations of [Dud06] and of [Fro06]. Of course, most importantly, we have found very good agreement with experiment and examples will be shown throughout this thesis.

Visualisation of the results

Numerical results obtained using the method of the previous section do not directly offer the insight gained from analytical results. Instead they are equivalent to obtaining experimental results. The advantages come from the ability to choose arbitrary pump and fibre characteristics, unlike in the laboratory, and then to have perfect diagnostics of what is going on inside the fibre. Of course, the spectrum is still the primary diagnostic, but from the numerical data we can also fully reconstruct the pulse intensity. More significantly we can compute spectrograms, which enable the association of processes simultaneously in time and frequency, allowing for an intuitive visualisation of the nonlinear dynamics. We make extensive use of them in this thesis. It is possible to measure a spectrogram using an XFROG, or one can be recovered from a normal FROG trace [Tre02], but although some supercontinua have been measured with an XFROG [Efi04], the continua spanning the bandwidths which we reproduce in this work are beyond the reach of current experimental techniques.

Mathematically the spectrogram is a windowed Fourier transform defined by:

$$S(t,\omega) = 10\log_{10}\left|\int_{-\infty}^{\infty} E_{ref}(t'-t)E(t')\exp[-i\omega t']dt'\right| \tag{1.22}$$

Here E_{ref} is an envelope of a reference pulse and E is the envelope of the field inside the fibre. If E_{ref} has a duration of t_{ref} then it is possible, by reading the spectrogram, to determine the spectral content of E at time t over a duration of t_{ref}.

1.5 Propagation in optical fibres

In this section we provide an overview of nonlinear fibre optics, concentrating on the effects which are most important to the work in this thesis. In what follows we refer to short wavelengths as blue and long wavelengths as red, to simplify the discussions.

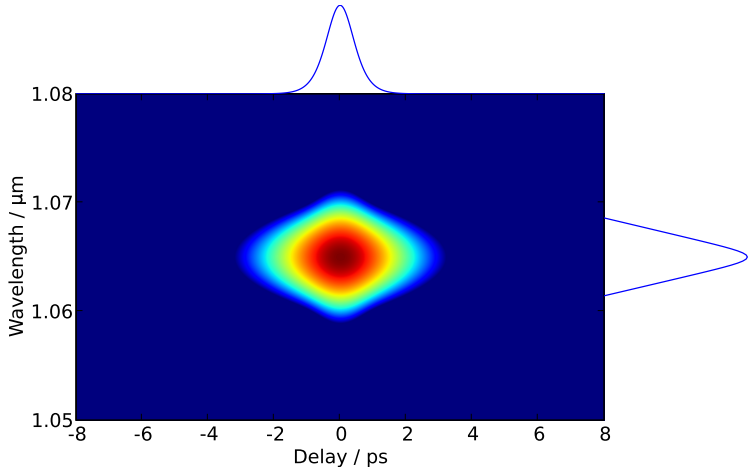
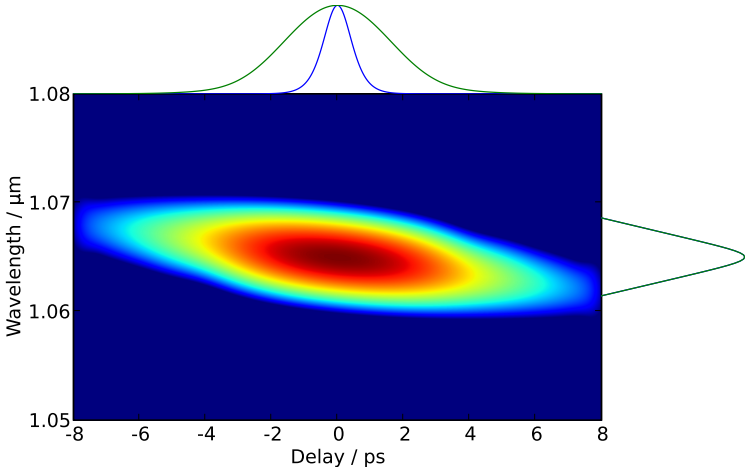


Figure 1.16: The spectrogram of the 1 ps sech^2 input pulse used in the following discussion. Colour scale: −40 0 dB.

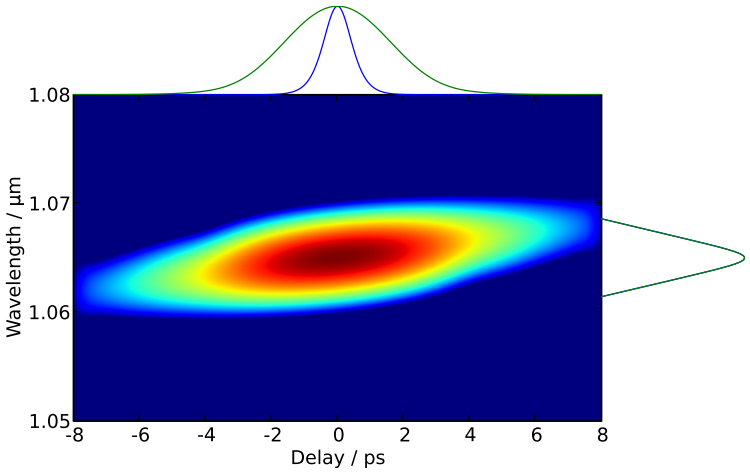
1.5.1 Dispersion

Dispersion is a linear effect, but it is of critical importance in determining the efficiency and character of nonlinear processes. In Section 1.4.1 we saw the origins of dispersion. In this section we simply observe how it affects an optical pulse passing through a fibre. To do this, we consider a 1 ps hyperbolic-secant pulse, with power proportional to sech^2. The spectrogram of this input trial pulse is shown in Fig. 1.16, where we can see that it is initially unchirped.

Dispersion is divided into two regimes: normal and anomalous, where the normal region has positive group velocity dispersion (or negative D), and the anomalous, negative. This means that in the normal dispersion region, low-frequency (red) components travel with higher group velocity than high frequency components. The anomalous region has the opposite characteristic. To visualise this Fig. 1.17 shows the spectrograms of the above mentioned pulse after propagating through a fibre with either normal or anomalous dispersion. In both cases we see that the spectrum is unchanged from the input (which is essential for an energy preserving linear process), but the pulse has broadened in the time domain. The pulse broadening is identical in both the anomalous and normal dispersion regime, for the same dispersion magnitude, but we see from the spectrograms that the chirp is opposite. With high frequencies leading in the anomalous case and trailing in the normal dispersion case.



(a) Normal dispersion.



(b) Anomalous dispersion.

Figure 1.17: Spectrograms of a sech^2 pulse after propagation through normal (a) or anomalous (b) dispersion fibre. Colour scale: −40 0 dB.

1.5.2 Self-phase modulation

If we neglect dispersion, and only consider the Kerr nonlinearity of the fibre then we can observe self and cross phase modulation (SPM and XPM respectively). The time dependent intensity of a pulse causes a corresponding modulation to the local refractive index in the fibre through $n = n_0 + n_2 I$. This in turn causes a time dependent phase delay to the same pulse (for SPM) or a co-propagating pulse (XPM). This amounts to applying a nonlinear chirp across the relevant pulse. Because the pulse intensity always falls to zero away from its centre, the applied chirp is always positive, i.e. the leading edge of the pulse is red shifted and the trailing edge is blue shifted or higher frequency. The spectrogram

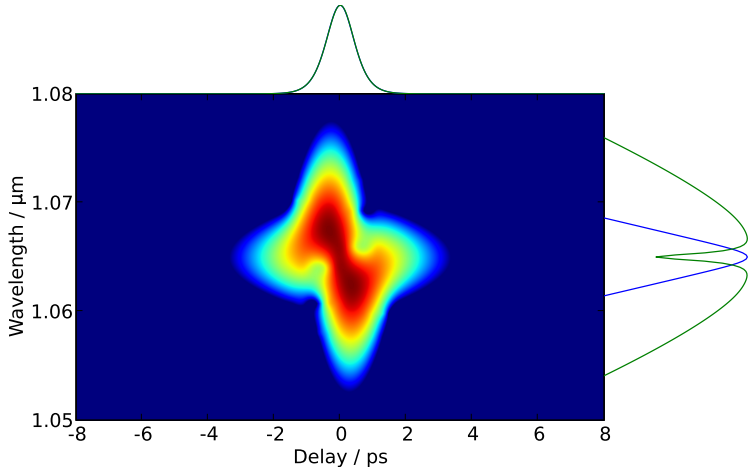


Figure 1.18: The spectrogram of a sech^2 pulse after propagating through nonlinear dispersion-less fibre. Colour scale: −40 0 dB.

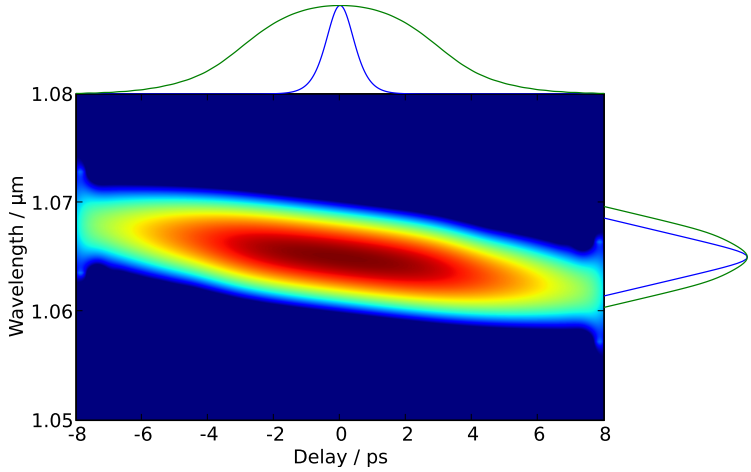


Figure 1.19: The spectrogram of a sech^2 pulse after propagating through nonlinear normally dispersive fibre. Colour scale: −40 0 dB.

shown in Fig. 1.18 shows these features. The time-domain power is unchanged from SPM alone, but the spectrum is broadened symmetrically by the creation of new frequency components.

In general neither the dispersion or nonlinearity of a fibre can be neglected. Therefore it is the interplay of the two which is important. This leads to two regimes of operation which have distinctly different behaviour. In one, SPM and normal dispersion interact. Fig. 1.19 shows the result of propagating the same sech^2 pulse through a nonlinear, normally dispersive fibre. In this case both spectral and temporal broadening occur. The spectral broadening from SPM enhances the temporal broadening from the normal

dispersion (due to the wider spectrum), but the spectral broadening is reduced compared to SPM alone as the dispersion reduces the pulse peak power. However, the resulting chirp is in fact partially linearised which can be understood by noting that a particular frequency shift is present in two parts of the pulse and so these will propagate at the same speed and maintain a fixed separation, therefore, as the pulse as a whole spreads, the proportion which has a nonlinear chirp will decrease. The combination of increased spectral bandwidth and linearised chirp makes such pulses good candidates for temporal compression by anomalously dispersive gratings, for example. This scheme is utilised in Chapter 5.

The second case for interaction between SPM and dispersion occurs in the anomalous dispersion region. The resulting dynamics leads to the generation of solitons.

1.5.3 Solitons

The chirp induced by SPM is opposite to that induced by anomalous dispersion. It is therefore expected that some cancellation can occur. It turns out however, that for a particular set of pulse shapes the cancellation is perfect and no spectral or temporal variation occurs at all – these are called fundamental solitons. The process can be physically understood as follows. The SPM redistributes energy to positive and negative frequency offsets at the trailing and leading sides of the pulse respectively. The effect of anomalous dispersion is to push the energy at these points back towards the centre of the pulse. As dispersion forces this energy towards the centre, the SPM once again redistributes it to the edges of the pulse. Thus a balance can be struck between these two processes. In fact, solitons, are the stable conditions of pulses propagating in the anomalous dispersion region, and other pulse shapes will readjust and converge to the soliton conditions. Solitons are analytic solutions to the NLSE (i.e. the GNLSE in Eqn. 1.16 without higher order dispersion, the shock terms or Raman). The natural soliton shape is the sech^2 pulse we have been using as our input. The envelope field of a soliton is given by:

$$E_{sol}(z,t) = \sqrt{P_0}\text{sech}\left(\frac{t}{\tau_0}\right)\exp\left[iz\frac{\beta_2}{2\tau_0^2}\right] \tag{1.23}$$

where P_0 is the soliton power and τ_0 is the soliton duration. The soliton propagates with an additional phase shift $\frac{\beta_2}{2\tau_0^2}$; using the soliton equation given below in Eqn. 1.24 we see that this phase shift is equal to $\frac{\gamma P_0}{2}$ and is therefore related to the nonlinear refractive index, which modifies the soliton propagation constant. Solitons propagate with a constant phase across the pulse (apart from the carrier frequencies), thus all frequency components of the soliton move with the group velocity of the soliton central frequency. This means that $\beta_{sol}(\omega) \neq \beta(\omega)$; this inequality leads to an interesting resonant coupling

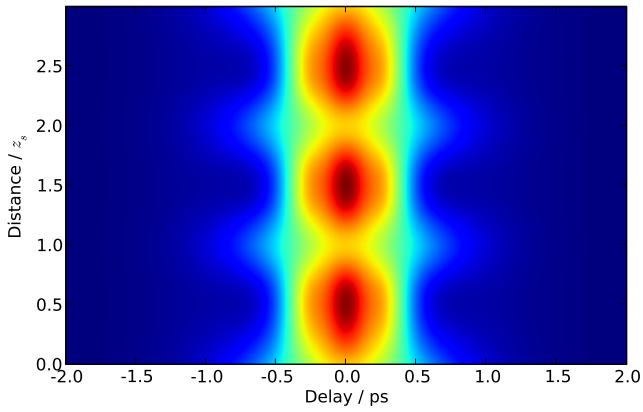


Figure 1.20: The temporal evolution of a 3rd order soliton. Colour scale (linear): 0 1.

with dispersive waves, described in Section 1.5.6. The soliton power, P_0, is given by the soliton equation (also referred to as the soliton condition):

$$N^2 = \frac{\gamma P_0 \tau_0^2}{|\beta_2|} \tag{1.24}$$

where the integer N is the soliton order. For $N = 1$ the soliton is said to be fundamental, and does not show any variation on propagation, except the acquisition of a flat phase. Higher order solitons undergo periodic evolution with an order independent length called the soliton period:

$$z_s = \frac{\pi \tau_0^2}{2|\beta_2|} \tag{1.25}$$

High order solitons are simply a collection of co-propagating fundamental solitons with identical group velocity, but they have, however, different peak powers and durations. There is no binding energy between them and small perturbations can lead to a rapid fissioning of the constituent solitons. In the absence of perturbations, the solitons continue to propagate at a constant group velocity and the periodic evolution emerges due to interference between the constituent solitons which have differing phase velocities. The evolution of an $N = 3$ soliton is illustrated in Figs. 1.20 and 1.21.

As noted above, unlike high order solitons, fundamental solitons are stable against small perturbations and all pulses with the form of Eqn. 1.23 with powers corresponding to $N > 0.5$ evolve into solitons. Even other pulse shapes do, although in both of these cases some energy is shed to non-solitonic, dispersive waves during the adjustment to meet the soliton conditions. By slowly changing the fibre dispersion or amplifying the soliton, the soliton adjusts itself to satisfy the soliton condition Eqn. 1.24. We use this for pulse compression in Chapter 5. Solitons are also robust in the opposite extreme, i.e. very fast

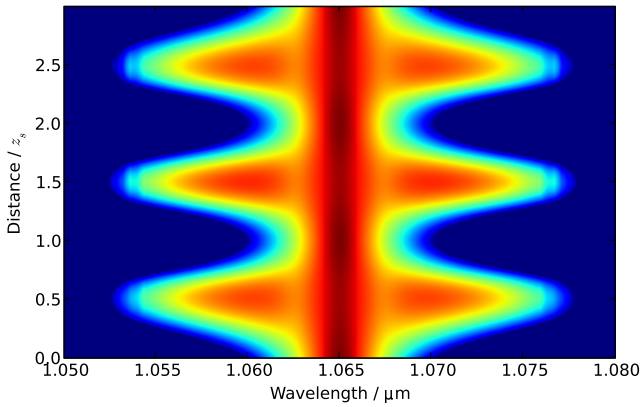


Figure 1.21: The spectral evolution of a 3rd order soliton. Colour scale: −60 0 dB.

changes to dispersion or energy (changes on a scale small compared to z_s). In this case they cannot respond quickly enough and they propagate as if the fibre had characteristics equal to the average the solitons experience over z_s.

Solitons play a critical role in all of the results in this thesis. For CW supercontinuum generation, discussed in Chapter 2, Raman self-scattering of solitons (see Section 1.5.5) is the primary mechanism for the spectral expansion observed. In the visible supercontinua discussed in Chapter 3 the same Raman self-scattering of solitons provides the critical Stokes seed for the four wave mixing processes which create the visible wavelengths. In Chapter 4 the red-shifting solitons trap dispersive waves on the blue/UV edge, and expand the supercontinuum to both longer and shorter wavelengths. Finally in Chapter 5 the stable fundamental soliton condition is used for pulse compression.

1.5.4 Four-wave mixing

Four wave mixing (FWM), including modulation instability (MI), is of central importance to the supercontinuum generation processes we will be discussing later. It allows the generation of new frequency components in spectral regions with no previous spectral overlap with the pump pulse. The process can be understood as a coupling between four waves, through the real part of χ_3. Two of the waves are classified as pumps with frequencies ω_1 and ω_2 and two as the Stokes and anti-Stokes, with frequencies ω_3 and ω_4. Initially the pumps are attenuated and the Stokes and anti-Stokes waves enhanced, though there is a periodic transfer back to the pumps. Due to energy conservation the frequencies are constrained to the following condition:

$$\omega_3 + \omega_4 = \omega_1 + \omega_2. \tag{1.26}$$

In addition, due to momentum conservation between the four interacting photons, the phase mismatch between the pump waves must be zero. This can be expressed by:

$$\Delta k = \beta(\omega_1) + \beta(\omega_2) - \beta(\omega_3) - \beta(\omega_4) + 2\gamma P_0 = 0 \tag{1.27}$$

where the last term, $2\gamma P_0$, accounts for the nonlinear phase shift from the intensity dependent refractive index. In most cases it is assumed that $\omega_1 = \omega 2$, i.e. a degenerate pump, and it is common to expand Δk with a Taylor expansion around the common pump frequency so that the contribution of the lowest order dispersion terms can observed. The FWM process can be seeded from noise, or amplification can occur if a Stokes or anti-Stokes co-propagates with the pump waves. The other Stokes component will be created to conserve energy. If the phase matching condition is perfectly satisfied then FWM exhibits the highest gain of all fibre nonlinearities, except Brillouin scattering which is observed only in a limited number of cases.

In the normal dispersion regime, in PCF, it is relatively straightforward to satisfy Eqn. 1.27, if we pump near the zero dispersion wavelength. Detailed examples of phase matching curves for four wave mixing are provided throughout this thesis when discussing the mechanisms of supercontinuum generation.

Modulational instability

Modulational instability is a feature of propagation in any nonlinear, anomalously dispersive medium and is understood with the formalism of four wave mixing [Sto75; Sto82; Was80]. It only occurs when the pump frequency is in the anomalous dispersion region, where the nonlinear contribution to the phase matching condition is dominant. In the time domain it manifests itself as amplification of noise fluctuations of an otherwise CW or quasi-CW field, with frequencies in the parametric gain sidebands, and therefore the fluctuations experience gain [Tai86; Has80]. More specifically, the NLSE equation which describes soliton propagation can be considered to describe a localised potential originating from the Kerr effect term; solitons form as they are trapped in this potential. As the potential becomes stronger in proportion to the square of the field amplitude, the fluctuations on a CW beam can become self-trapping and evolve towards the fundamental soliton condition with peak powers orders of magnitude higher than the pump powers [Tay92]. Back in the four wave mixing picture, the maximum gain is at frequencies given by [Agr01]:

$$\Omega_{max} = \pm\sqrt{\frac{2\gamma P_0}{|\beta_2|}} \tag{1.28}$$

therefore, high power and nonlinearity, but low dispersion lead to broader sideband separation. The sideband separation determines the period of the resulting soliton pulse train, and as the energy in each period (or modulation cell) mostly contributes to a single soliton, the energy of the resulting solitons also depends on Eqn. 1.28. This fact leads to important considerations when pumping for supercontinuum generation, as modulation instability is the precursor to the Raman-soliton continuum [GN88c], which depends strongly on the soliton energy and is the initial stage of most supercontinua with powerful pump pulses longer than ~ 1 ps. It is central to the work in this thesis. We postpone detailed discussion of this process to Chapter 2, where specific cases are discussed.

1.5.5 Raman scattering

Raman scattering is an inelastic scattering process of photons from vibrational or rotational oscillations of molecules. The resonant frequencies are significantly lower than optical frequencies due to the relatively large mass of the atoms involved. The pump field is absorbed exciting the molecular resonance, mediated by the imaginary part of χ_3, leading to emission of a frequency downshifted signal. The process can be stimulated through a coherent coupling of the pump and Stokes field which works to further enhance the molecular excitation. Significant power transfer to the Stokes field can occur. In principle an anti-Stokes signal can be generated through the absorption of energy from the oscillating molecules, but it is much weaker than the Stokes signal for two reasons: firstly, the molecular excitation must already exist, and secondly, the anti-Stokes process is not phase matched for the collinear case (which is always the case in optical fibre) [Buc04]. In silica glass the molecules are randomly aligned and so the excitation band is smooth and broad (inhomogeneously broadened), over 40 THz wide, with a peak at 13 THz downshift from the pump, as shown in Fig. 1.22. The Raman gain curve is given by the imaginary part of the Fourier transform of the Raman response function $h_r(t)$ shown previously in Fig. 1.15 [Sto89; Hol02].

Significantly, the gain from Raman is available at any wavelength in a fibre because the gain is a function of the pump wavelength and there are no waveguide phase matching requirements. This has led to the wide use of Raman lasers to fill the gaps between gain regions covered by rare earth amplifiers, and the use of Raman for broad and flat amplifiers for telecommunications [Smi06].

Soliton self-Raman scattering

One remarkable property of fundamental solitons is their stability, even in the presence of Raman scattering. It was discovered relatively soon after the first experiments with solitons, that the blue edge of a soliton can pump the red edge, leading to a mean frequency

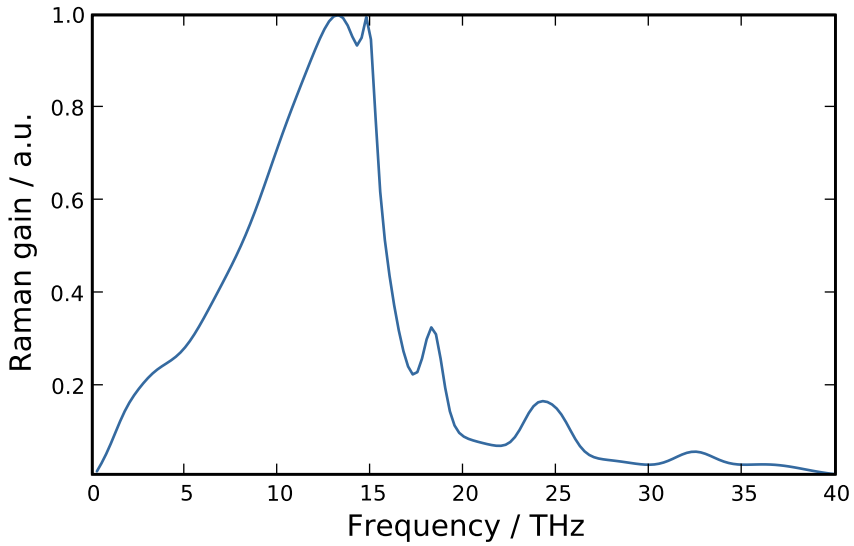


Figure 1.22: The Raman gain curve for fused silica.

shift of the central soliton frequency [Dia85; Gor86; Mit86]. Remarkably, the process is robust, and dispersive waves are not necessarily shed. This process is known by the names of soliton self-frequency shift and self-Raman scattering. The process depends on the peak power of the soliton (for nonlinearity) and the soliton duration, as it is required that the soliton bandwidth is sufficiently broad for the Raman interaction between the spectral edges to occur. From the overlap of the Raman gain spectrum and the soliton spectrum it is possible to derive an equation for the Raman self-scattering frequency shift [Agr01]:

$$\Delta\omega_R(z) = \frac{-8|\beta_2|T_R}{15\tau_0^4}z \tag{1.29}$$

Where $T_R = 3$ fs is the first moment (slope) of the Raman response function given in Fig. 1.15 [Agr01]. The Raman shifting of solitons can lead to higher order soliton fission. More importantly for the work in this thesis, it can lead to the broad spectral expansion of MI induced soliton trains and the above mentioned Raman-soliton continuum. Again, we postpone detailed discussion of this process to Chapter 2.

1.5.6 Soliton fission and dispersive wave generation

Due to the special propagation constant of solitons, which is larger than a linear wave at the same frequency, resonant nonlinear interactions can occur with phase-matched dispersive waves leading to a variety of phenomena. The most studied of these is the excitation of dispersive waves in the normal dispersion region when the soliton propagates

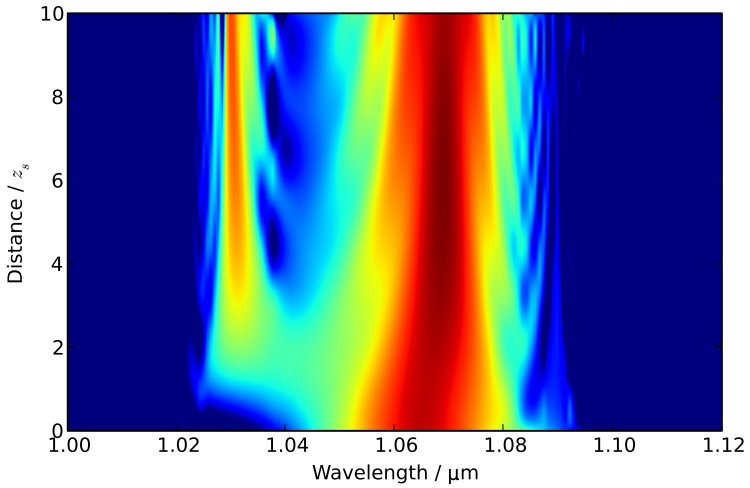


Figure 1.23: The spectral evolution of a fundamental soliton perturbed by third order dispersion, leading to resonant enhancement of a dispersive wave. Colour scale: −30 0 dB.

close to the zero dispersion wavelength [Wai86]. The understanding of these resonant processes can be understood in the framework of four wave mixing [Gor06], but most often alternative pictures are used. For the simplest case, an analogy to Cherenkov radiation can be made, where the fact that the soliton phase velocity is higher than the linear phase velocity causes the transfer of power to linear, dispersive waves [Akh95]. The condition for this to occur is:

$$\beta(\omega_d) = \beta_{sol}(\omega_{sol}) \tag{1.30}$$

where ω_d and ω_{sol} are the dispersive wave and soliton frequencies. It has been shown that for this to be satisfied, ω_d must be in the normal dispersion region [Skr05]. It is also essential that part of the soliton spectrum must overlap with the resonant dispersive wave frequency. These conditions mean that dispersive wave generation from fundamental solitons is generally only observed when the soliton is propagating close to the zero dispersion wavelength. As an example, in Fig. 1.23 we show dispersive wave generation from a fundamental soliton perturbed by high order dispersion, which allows a dispersive wave to satisfy condition Eqn. 1.30. It is apparent that the soliton frequency also shifts to conserve energy, this is known as spectral recoil. The dispersive wave is continuously amplified, but in these conditions can never dominate over the soliton.

For higher order solitons, the spectrum does not need to overlap with the dispersive wave initially because the solitons will temporally compress on propagation and therefore may spectrally overlap as their spectrum expands (or breaths) [Mol83; Sto83]. The dispersive wave amplification will generally occur only once when the high order soliton initially compresses. A significant transfer of power to the dispersive wave can be realised [Lu05].

After this initial event, the constituent fundamental solitons of the higher order soliton shift by differing amounts and therefore fission occurs as they no longer have identical group velocity [Wai86; Dia85]. This prevents further compression events. This fissioning mechanism and amplification of dispersive waves can be utilised to produce broadband supercontinua if an ultra short (less than ~ 500 fs) pump pulse is used in the anomalous dispersion region close to a zero dispersion wavelength [Dud06]. Whether this process occurs, or is prevented by the competing process of MI breakup of the input pulse into fundamental solitons, is determined by the pump pulse and fibre parameters. We discuss this in the following section.

The above soliton fission mechanism was due to higher order dispersion, through the phase matching conditions given in Eqn. 1.30. But any process which shifts the central frequencies of the constituent fundamental solitons by different amounts leads to fission of high order solitons. A key example is fission caused by Raman self-scattering [Hod87], where the fact that the Raman self-frequency shift is determined by the pulse durations leads to the separation of the solitons. Simulation results of this process are presented in Chapter 5 when we discuss the use of higher order solitons for pulse compression.

1.5.7 Supercontinuum generation

A very large body of research has been devoted to understanding the physical processes leading to supercontinuum generation and the dynamics are well understood [Dud06; Gen07]. However, the details are complicated as explanations include the full set of nonlinear processes in fibres, such as self-phase modulation [Cha02], intra-pulse Raman scattering [Dud02a], resonant radiation of solitons [Dud02a; Her02; Cri04], four-wave mixing) [Gen04a; Skr05], modulation instability [Dem05] and cross-phase modulation [Gen04a]. It is important to note that all of these physical processes have been understood for many decades. The main novelty for the extreme supercontinua we are discussing here is the scale and combination of these processes working together.

Soliton fission regime

Perhaps the most widely reported supercontinuum mechanism is that of soliton fission and dispersive wave generation as discussed above. For higher order input pulses the spectral extent of the continuum depends on how broad the soliton expands as it breaths [Cri04]. After the fission event, further interaction between the dispersive radiation and solitons may occur via four-wave mixing [Gor06] and cross-phase modulation [Gen04a]. The resulting supercontinuum can be exceptionally broad (over 1 μm in bandwidth), and can exhibit high degrees of coherence [Cri04; Her02; Ran00b; Dud06]. However, the spectral components are likely to be localised, resulting in a continuum which does

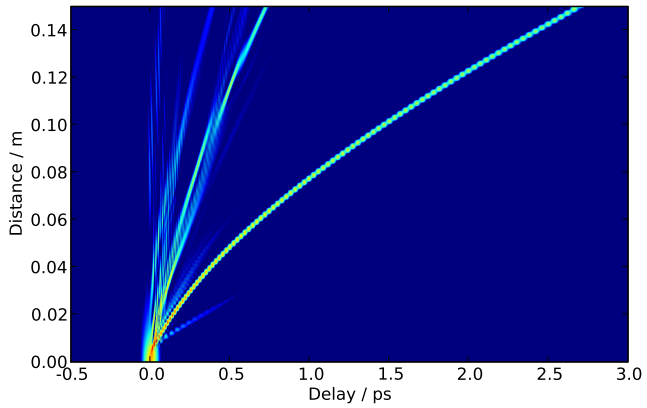


Figure 1.24: Supercontinuum generation by soliton fission - temporal evolution. Colour scale: −20 0 dB.

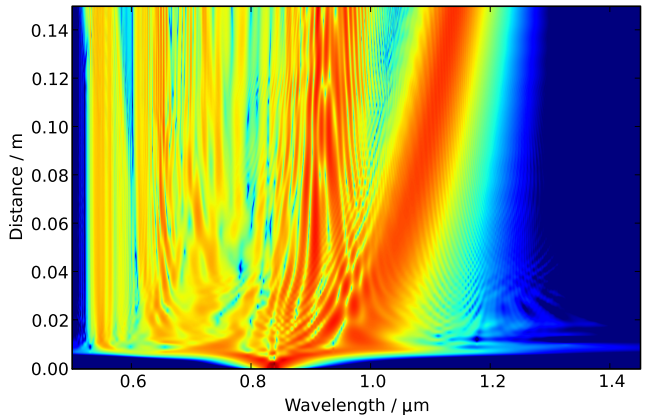


Figure 1.25: Supercontinuum generation by soliton fission - spectral evolution. Colour scale: −60 0 dB.

not have a high degree of smoothness. It is also difficult to use such a continuum to achieve high spectral power as ultra-short (few tens of femtoseconds) pulse sources are not optimal for scaling to high average power. Figs. 1.24 and 1.25 show supercontinuum generation through soliton fission and dispersive wave dynamics. The pump pulse was 50 fs with 10 kW peak power.

Whether soliton fission is likely to be the dominant continuum formation mechanism can be determined from the pulse and fibre parameters. A fibre length scale has been established that estimates the length at which the highest soliton compression (in the time domain) is achieved [Dia86; Dud06]. This is given by Eqn. 1.31.

$$L_{fiss} = \frac{L_D}{N} = \sqrt{\frac{\tau_0^2}{|\beta_2|\gamma P_0}} \tag{1.31}$$

where L_D is the characteristic dispersion length [Agr01]. As the fission process tends to occur at this point, if this length is much shorter than other characteristic length scales then soliton fission will dominate.

Modulation instability regime

The second mechanism of supercontinuum generation is modulation instability as discussed in Section 1.5.4. The phase matching conditions for MI/FWM directly control the extent of supercontinuum bandwidth which can be generated in this regime. After the input field has developed into a train of solitons two main mechanisms are available to broaden the field into a continuum. Firstly intra-pulse Raman scattering of the solitons leads to their red-shift, forming a smooth continuum to longer wavelengths. This is the dominant mechanism in CW pumped supercontinua which are studied in Chapter 2. More significant in the pulse pumped case, with higher peak power, is conventional four wave mixing. If the pump is sufficiently close to the zero dispersion wavelength then the MI side-lobes can develop a strong field in the normal dispersion regime. In this case, FWM can lead to Stokes and anti-Stokes generation at extremely widely separated frequencies due to the phase matching of the waveguide [Har03; Che05; Wad04; And04; Yul04; Bia03]. Continuum formation can then be understood as a cascade of FWM processes, starting with MI, and developing into the normal dispersion region which subsequently lead into a spectral broadening over a very wide frequency range [Dud02b; Wad04; Coe02; Coe01]. As the mechanism is stochastic, small variations between the spectral development between pulses and between the constituent solitons of each pulse lead to a smoothing of the spectrum. As a result supercontinua in this regime are usually very smooth and flat. We consider this process in detail in Section 3.5.2.

The MI continuum process will only occur if the pulse and fibre parameters lead to a breakup of the pump pulse via MI in a shorter fibre length than high order soliton effects and soliton fission occur. A characteristic fibre length scale for MI can be developed based on the length required for MI gain to amplify the background quantum noise to a level where MI has broken the input pulse into ultra-short solitons. This length can be written:

$$L_{MI} = \frac{n_{db}}{20\gamma P_0 \log_e 10} \sim \frac{4}{\gamma P_0} \tag{1.32}$$

where n_{db} is the shift in dB from the peak power level to the background noise. The value of 4 after the second equality is determined from an approximate shot noise level of ~200 dB down. If $L_{MI} \ll L_{fiss}$ then MI will have developed too quickly for soliton fission

to occur and the continuum will form via MI/FWM. This condition can be written as:

$$4^2 \ll \frac{\gamma P_0 \tau_0^2}{|\beta_2|} = N^2 \tag{1.33}$$

Now it is clear that high nonlinearity, high pump power, long pulses and low dispersion all favour the MI mechanism. The second equality in this equation is given by the soliton equation (Eqn. 1.24) and implies that soliton orders much higher than 4 favour the MI/FWM supercontinuum process, in practice the boundary is observed to be around $N = 16$ [Dud06; Gen07]. Therefore it is predominantly ultra-short pump pulses and high dispersion (at the pump wavelength) that lead to the soliton fission mechanism. All of the supercontinuum results reported in this thesis are in the MI initiated supercontinuum regime.

Pumping in the normal dispersion region

Supercontinuum generation has also been observed (in fact was originally observed in optical fibre [Lin76]) when pumping in the normal dispersion region of the fibre. In this case SPM plays the dominant role initially unless the pump is close to the zero dispersion wavelength, in which case FWM processes can contribute significantly. Stimulated Raman scattering is another efficient mechanism of spectral broadening, although in the normal dispersion regime it will lead to a cascade of spectrally isolated Stokes lines. If any of these processes transfer energy into the anomalous dispersion region then soliton dynamics then come into play. In this thesis we concentrate exclusively on pumping in the anomalous dispersion region as this produces the most efficient spectral broadening into a supercontinuum.

1.5.8 Other nonlinear effects

Self steepening

Self steepening arises due to the intensity dependence of the group velocity and is accounted for in the GNLSE by the shock term. For very short optical pulses it leads to a steepening of the tail of the pulse because the central pulse region has a slower group velocity than the front. Self-steepening can also lead to soliton fission: as the soliton re-adjusts to remove the pulse asymmetry, the soliton slows down and as the adjustment required depends on the soliton power, the solitons fission.

Stimulated Brillouin scattering

Stimulated Brillouin scattering is another inelastic scattering process which can occur. The electric field of the pump causes a pressure wave to form in the material through electrorestriction. The resulting modulation in refractive index, moving in the direction of propagation, acts like a Bragg grating and causes back scattering at a frequency downshift (due to the Doppler effect). The process can become stimulated, and is in fact the strongest nonlinear effect in optical fibres. However, it has a very narrow resonance and so the pump power must be within a tight bandwidth. For all of the sources used in this thesis, the power density in the required bandwidth was not significant enough for Brillouin scattering to dominate, and so we do not consider it further.

1.6 A review of early nonlinear fibre optics

Here we provide a brief review of the original work on nonlinear fibre optics and supercontinuum generation. More specific reviews including more recent results are provided in the relevant chapters.

The birth of supercontinuum generation in glass can be traced to the demonstration of SPM [Alf70b] in borosilicate crown glass. Here, 530 nm, picosecond pulses generated spectra ranging from 400 to 700 nm. A thorough investigation into SPM in silica fibres eventually followed [Sto78]. In the same journal issue (and by the same authors) of the paper reporting SPM in glass, four wave mixing (FWM) was demonstrated in borosilicate crown glass [Alf70a]. Degenerate FWM (or three wave mixing) in silica optical fibre was demonstrated a few years later [Sto74], providing a way to generate isolated frequency components at frequencies much further from the pump source than via SPM. This demonstration used phase matching via multiple modes in the fibre. This was followed by CW degenerate FWM [Hil78] which demonstrated the production of several orders of Stokes frequencies at low powers in a single-mode fibre. Further work resulted in the generation of five cascaded orders of FWM from 0.52 to 1.63 μm in a multi-mode fibre with tens of kW pumping at 1.064 μm [Hil80].

Meanwhile, stimulated Raman scattering in optical fibres was demonstrated [Sto72], providing another process that leads to the generation of new spectral components, particularly to the long wavelength side of the pump. In this experiment, a 532 nm frequency doubled Nd:YAG source was used as the pump. Both single pass emission and lasing were observed at 545 nm.

The first use of the word continuum as we use it today: to describe the complex interaction of several nonlinear effects that lead to broad, smooth spectral broadening, was made in the report of a nanosecond, 10 kW pumped source [Lin76]. This source

consisted of a dye-laser emitting 15 nm spectral width, 10 ns pulses, with a 10-20 kW peak power, 1 kW of which was coupled into the fibre. The silica fibre used was 19.5 m long with a core diameter of 7 μm. The broadest generated continuum was between 434 and 614 nm producing a white light emission. The authors claimed that cascaded SRS Stokes generation along with SPM broadening of the Stokes lines was responsible for the smooth spectrum. The first mention of the word supercontinuum appears to be a few years later in [Ger80].

This work was soon followed by a 0.7 to 2.1 μm continuum source pumped at 1.064 μm by a Q-switched Nd:YAG laser [Lin78]. The pulses had a 150 kW peak power and the 315 m fibre was multi-mode with a 33 μm core. The pulses were approximately 20 ns in duration). With 50 kW coupled into the fibre, the spectra generated had clear discrete Stokes lines at 1.12 μm, 1.18 μm and 1.24 μm, subsequent Stokes lines could not be isolated, but a smooth continuum was formed from around 1.3 μm up to 2.1 μm apart from a large dip at 1.4 μm due to the water loss in the fibre. Under higher pumping conditions green emission was observed, but fibre end damage limited experiments. In the same paper continuum generation in single-mode fibres between 0.9 and 1.7 μm was reported, limited mainly by restrictions on coupling efficiency. A few years later, continuum generation over the entire silica window was generated, from 0.3 to 2.1 μm [Fuj80]. The Nd:YAG Q-Switched laser used provided 100 kW peak power pulses which could be coupled with 70% efficiency into a single-mode fibre with a 10 μm core. The authors attributed most of the visible light generation to FWM with the pump light and the Raman generated Stokes light. Although most of the emission was in the fundamental mode, some of the visible light was in higher order modes, which was attributed to sum frequency generation. The authors of these papers did not try to account for the transition from discrete Stokes lines to a broad continuum at longer wavelengths. The actual analysis of what is occurring here required an understanding of soliton propagation and Raman self-scattering. Slightly in anticipation of soliton effects, a paper in 1980 reported continuum formation between 1.15 and 1.6 μm in a single mode optical fibre when pumped with low (tens of Watts) peak powers by an Nd:YAG laser emitting at 1.34 μm (just inside the anomalous dispersion region of solid-core fibres) [Was80]; the critical observation being the absence of discrete Stokes lines.

Solitons in the anomalous dispersion region of optical fibres had been predicted [Zak72; Has73] seven years prior to their demonstration [Mol80], which required optical fibre technology to produce low loss fibres beyond 1.3 μm for anomalous dispersion. Five years later Raman self-scattering (or soliton self-frequency shift) effect was observed [Dia85; Mit86; Tay92], which forms the basis of the Raman-soliton continuum [GN88a; GN88c].

After the considerable effort, during the 1980s, to understand soliton dynamics in fibres

and the resulting nonlinear effects some applications were demonstrated. The generation of wavelength multiplexed sources for telecommunications by filtering solitons at different frequencies from the continuum was demonstrated already in 1987 [Tay87]. Later work used this technique to generate over 100 channels with a 1.9 nm spacing and 10 ps pulse duration from a 170 nm continuum with a few milliWatts average power [Mor93]. Another application was dispersion measurement with a continuum from 1.15 to 1.77 μm, produced from 1.2 kW peak power pulses at 1.55 μm, in a 3 km long dispersion shifted fibre [Mor95a]. An interesting development came when a novel all-fibre Q-switched laser was used to generate a 450 mW supercontinuum spreading from 0.7 to at least 2.0 μm [Che97]. The Q-switch provided 10 kW, 2 ns pulses at 1.06 μm. Raman Stokes lines were observed between 1.1 and 1.3 μm. At longer wavelengths a continuum was formed due to the anomalous dispersion. The short wavelength part of the continuum was over 10 dB down from the long wavelength side. This system was among the first to report fully fibre integrated continuum generation, where no optical alignment or bulk parts were required.

However, a new era of nonlinear fibre optics and supercontinuum generation was born with the development of photonic crystal fibres in 1996 and their subsequent use for nonlinear optics, starting in 1999. The much higher nonlinearity and custom dispersion of these fibres has greatly enhanced our abilities to control and utilise light. Results with PCF are reviewed in the relevant chapters.

1.7 Summary

Optical fibre, particularly photonic crystal fibre allows for very good control of dispersion, and enhanced nonlinearity. This thesis is concerned with utilising PCF to control dispersion and enhance nonlinear optical processes, with a particular focus on supercontinuum generation. We have briefly discussed the guidance properties of optical fibres and PCF, how to calculate the dispersion in PCF and how control of dispersion is achieved. The methods used to model nonlinear pulse propagation in this thesis were also given. The fibre lasers which are used in the experiments we are about to discuss were described. Finally we briefly reviewed the propagation effects emerging from nonlinear fibre optics and gave an overview of their historical discovery.

2 Continuous wave supercontinuum generation

2.1 Introduction

It is remarkable that a broadband supercontinuum, spanning over 1000 nm, can be generated from continuous wave lasers with just a few Watts of pump power. It is made possible only by the use of optical fibre because long interaction lengths at high intensity are required. The physical mechanism for CW continuum generation starts with modulational instability, as do the supercontinua generated from picosecond and nanosecond pump lasers, discussed Chapters 3 and 4. But, the CW case is unique because the efficiency of the initial MI strongly effects all of the subsequent continuum dynamics. This mechanism is fascinating in its own right, but the resulting continuum sources also have many applications. This is due to a number of properties which make them particularly interesting. Some of which include:

Spectral smoothness CW supercontinua are generated from Raman shifted solitons which are formed from noise seeded MI. The averaging of many such solitons with random initial conditions leads to extremely smooth and stable average spectra.

Average power CW lasers have the highest average power available. The resulting supercontinua can therefore have very high average spectral powers: over 10s mW/nm.

Simplicity The experimental requirements for CW supercontinuum generation are extremely simple, and can be compact and robust.

Low noise With the correct pump conditions, CW supercontinua can exhibit relative intensity noise lower than continua pumped with mode locked lasers.

The range of applications for supercontinua were outlined in Chapter 1, of these, CW supercontinua have been particularly useful for: optical coherence tomography (OCT) [Hsi04; Pov05], due to the low noise and high power; the characterisation of devices, such as the measurement of polarisation mode dispersion [GH03]; the detection of

chemical species - where the high average power is particularly useful; and broadband Raman amplification [Smi06].

In this chapter, after a brief literature review, we consider the numerical modelling of CW supercontinuum generation and then detail the physical mechanism. We then report experimental results on the use of speciality low water loss PCF for extended supercontinuum generation from 1 to 2 μm, the effect of the pump spectral bandwidth on the continuum, and the relative intensity noise of both amplified spontaneous emission (ASE) and laser pumped supercontinua. The work in this chapter has been published in a number of papers and conference presentations [Tra05c; Tra05a; Tra05d; Rul08].

2.2 Literature review of experimental results

Supercontinuum generation had been studied for several decades before CW continua were generated. The first report of significant spectral broadening, to which the term supercontinuum could be reasonably applied, was in [Per96]. In this work, an Yb:Er fibre laser was used to pump 2.3 km of Ge doped fibre with 1 W at 1.565 μm. A 100 mW supercontinuum spanning from 1.5 to 1.95 μm was obtained with good spectral power between 1.5 and 1.7 μm. Several years later a 1 W supercontinuum centred at 1.48 μm pumped with a Raman fibre laser was reported [Pra00].

For many years, however, work was mostly focused on the rapidly developing interest in short pulse pumped supercontinua with the dramatic visible supercontinua, some results of which we look at in later chapters. The first CW supercontinuum in PCF was reported in [Avd03]. A 15 W master oscillator power amplifier (MOPFA), ytterbium based source was used to pump a 100 m PCF with a zero dispersion wavelength around 0.86 μm. Approximately 9 W was coupled into the fibre resulting in a 3.8 W continuum with 324 nm bandwidth and a very flat spectrum of $\pm$3.5 dB between 1.09 and 1.375 μm. The resulting spectral power was up to 12 mW/nm. The continuum bandwidth was limited by a dramatic reduction of power after the spectrum reached the water loss region.

In highly nonlinear conventional fibre, new results quickly followed. In [Pra03] higher level pumping of essentially the same setup as in [Pra00] resulted in a 2 W supercontinuum spanning 1.43 to 1.53 μm. In [Nic03] a 4.5 km fibre was pumped with 0.9 W at a wavelength of 1.594 μm leading to a supercontinuum of over 247 nm bandwidth with 210 mW of average power. In [GH03] a 2.1 W fibre Raman laser at 1.455 μm was used to pump a 7 km dispersion shifted fibre, with a zero dispersion at 1.453 μm, resulting in a 207 nm continuum (20 dB level). Another result with a Raman laser was reported in [Abe04], where a 4 W pump at 1.486 μm led to a broad supercontinuum in a highly nonlinear fibre. Modulational instability was clearly observed to start the continuum process. In [Pop04]

either a high power Raman laser at 1.48 μm or a Yb:Er laser at 1.55 μm, depending on the zero dispersion wavelength of the fibre, were used to produce supercontinua spanning from 1.48 to 2.05 μm with up to 10 W of output power. Subsequently, [Cha04] used a tunable fibre laser amplified through a 5 W erbium amplifier to pump 1 km of HNLF at 1.55 μm just above the zero dispersion wavelength. A continuum width of 450 nm was achieved with 2.5 W of output power.

Further work in PCF was reported in [dM04b] with a study of noise characteristics of both laser and ASE pumped supercontinua. The same fibre as in [Avd03] was used. The supercontinuum of 5.5 W average power and over 10 mW/nm spectral power was generated from Yb pump sources at 1.06 μm with up to 10 W pump power. A very low noise was measured for the ASE pumped continuum and much higher noise for the laser pumped continuum, although the continuum spectra were very similar. Again, the supercontinuum was strongly limited by water loss absorption. Autocorrelation measurements were taken of the supercontinuum showing pulse durations ranging from 0.95 to 0.55 ps between 1.15 and 1.32 μm respectively. At 1.06 μm a coherence spike was observed. This source was then used for OCT with < 5 μm axial resolution [Hsi04].

A comparison between normal and anomalous dispersion pump wavelengths was made in [Abe05]. The effect of pump bandwidth on supercontinuum extent was studied in [ML06]. They found that too broad a pump quenched the MI and reduced the continuum and that a too narrow bandwidth also reduced the continuum. However, they used three different source types (laser, ASE, light emitting diode) in their experiments, which may also have affected the results.

Recently, [Abr07] used a 1.315 μm pump to obtain a CW supercontinuum centred around 1.3 μm which is a useful wavelength for OCT. They used 8 W of pump power in 17 km of standard fibres split into four steps with decreasing dispersion to obtain a 260 nm (20 dB level) continuum. They claim that this allows them to benefit from the high order soliton fission dynamics discussed in [Kut05], which was a theoretical paper suggesting that forming high energy solitons in a high dispersion fibre and injecting them into a lower dispersion fibre could lead to soliton fission and a broader continuum development.

This rapid development over the past decade means that broadband and high average power CW supercontinua are now routinely generated in some laboratories and have been used for applications by a number of groups not directly researching nonlinear fibre optics.

2.3 Experimental setup

In this section we review the lasers, fibres and typical setup used for the work in this chapter.

2.3.1 Pump sources

A number of pump sources were used to generate CW or quasi-CW supercontinua. These included three CW pump sources and a nanosecond master oscillator power amplifier for quasi-CW pumping at 1.06 μm.

Two of the CW sources were ytterbium fibre lasers (IPG Photonics). One produced 10 W at 1.0654 μm with a 0.8 nm linewidth, the other produced up to 54.4 W at 1.0705 μm with a 1.15 nm linewidth. Both lasers emitted randomly polarised light, meaning that the polarisation at any point in time is arbitrary and expected to change on a timescale of microseconds for Yb fibre lasers. The third CW source was an amplified spontaneous emission source, also based on ytterbium fibre amplifiers (also IPG Photonics). This source consisted of a number of amplifier gain stages with inter-stage filtering to control the ASE bandwidth. The master oscillator, power fibre amplifier system (MOPFA), used for quasi-CW pumping consisted of a modulated laser diode seed source and a multi-stage amplifier configuration, with inter-stage filtering for ASE suppression. This source was polarisation preserving. A summary of the source parameters is given in Table 2.1.

Source	λ_p [μm]	$\Delta\lambda$ [nm]	P_{max} [W]	Type
CWL1	1.0654	0.8	12	CW Laser
CWL2	1.0705	1.15	54	CW Laser
CWL3	1.064	2.0	150	MOPFA
CWASE	1.065	5.0	23	ASE

Table 2.1: Pump sources used for CW supercontinuum generation; λ_p = pump wavelength, $\Delta\lambda$ = bandwidth, P_{max} = maximum output power.

2.3.2 Fibres

We used a number of fibres to investigate the role of dispersion, nonlinearity and fibre loss profiles in the supercontinuum process. These are summarised in Table 2.2.

The dispersion curves for these fibres are shown in Fig. 2.1. All of the fibres were anomalous at the pump wavelengths used, which is a condition for modulation instability and hence efficient CW supercontinuum generation. They have varying absolute values of dispersion and dispersion slope. The curves of the nonlinear coefficients of these

Fibre	γ_p [W^{-1}km^{-1}]	D_p [ps nm^{-1}km^{-1}]	λ_{zd1} [μm]	λ_{zd2} [μm]	L_{OH} [dB km^{-1}]
CWHF1	44	43	0.86	1.57	1000
CWHF2	11	3	1.05	>1.8	600
CWHF3	44	72	0.83	>1.8	70
CWHF4	34	53	0.88	>1.8	30

Table 2.2: Parameters of the PCFs used for CW supercontinuum generation; γ_p, D_p are respectively the nonlinear coefficient and group velocity dispersion at the pump wavelength, λ_{zd1} and λ_{zd2} are the zero dispersion wavelengths, and L_{OH} is peak water loss at 1.38 μm.

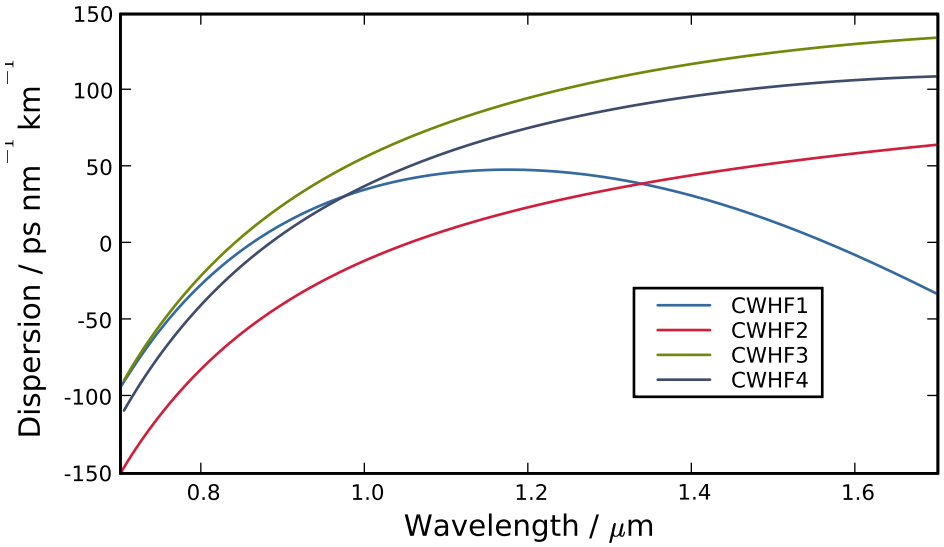


Figure 2.1: ***(numerical)*** The calculated dispersion curves of the CW supercontinuum generation PCFs

fibres, for changing wavelength are shown in Fig. 2.2. All of the fibres exhibit a significant decrease in nonlinearity between 1 and 2 μm.

2.3.3 Benchmark results

Here we present results that reproduce those obtained by [Avd03] and [dM04b], which represented the state of the art when the work on this chapter began. The pump source used was CWL1 and the fibre was 100 m of CWHF1. The experimental setup is shown in Fig. 2.3 and simply consists of the laser spliced directly to the fibre with a splice loss of 0.56 dB.

The early spectral evolution at the output of the PCF for increasing pump power is shown in Fig. 2.4. Although we discuss the mechanism in full detail in Section 2.5, here

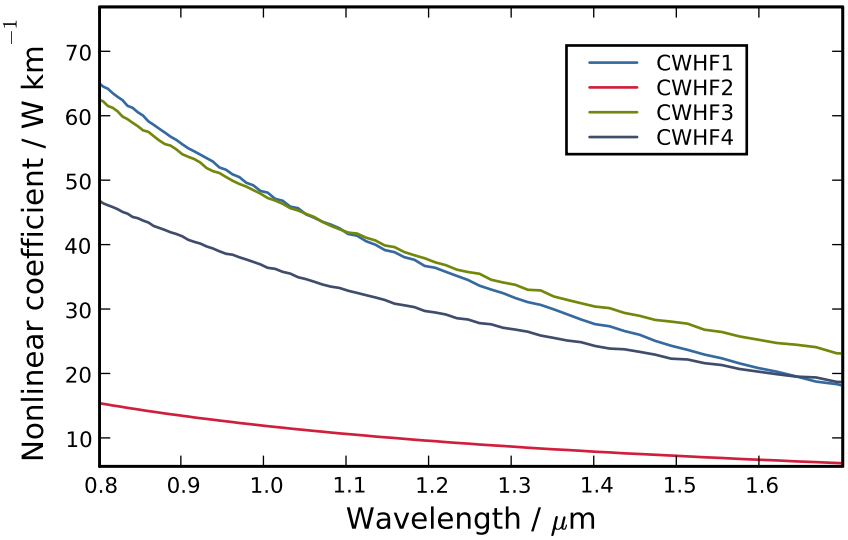


Figure 2.2: ***(numerical)*** The calculated nonlinear coefficient curves of the CW supercontinuum generation PCFs

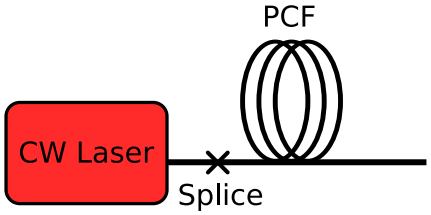


Figure 2.3: The basic experimental setup for CW supercontinuum generation.

we note a few points. The initial broadening is due to MI and for very low powers is symmetrical. The classic MI sidelobes are not clearly observed. This is because the maximum MI gain in CWHF1 at these pump powers (calculated from Eqn. 1.28), is at ~ 1 nm from the pump. Therefore the resulting sidebands are merged with the pump spectrum. With increasing power the MI sidelobes become more prominent and Raman gain causes asymmetry in the spectrum by enhancing the long wavelength edge. Further evolution given in Fig. 2.5 shows the rapid expansion due to Raman self-scattering of the solitons formed through MI. The continuum is limited in CWHF1 by water absorption at 1.38 μm.

2.4 Modelling

Continuous wave supercontinuum generation is a complicated process, therefore numerical modelling of the dynamics can be a valuable tool to help understand the process and

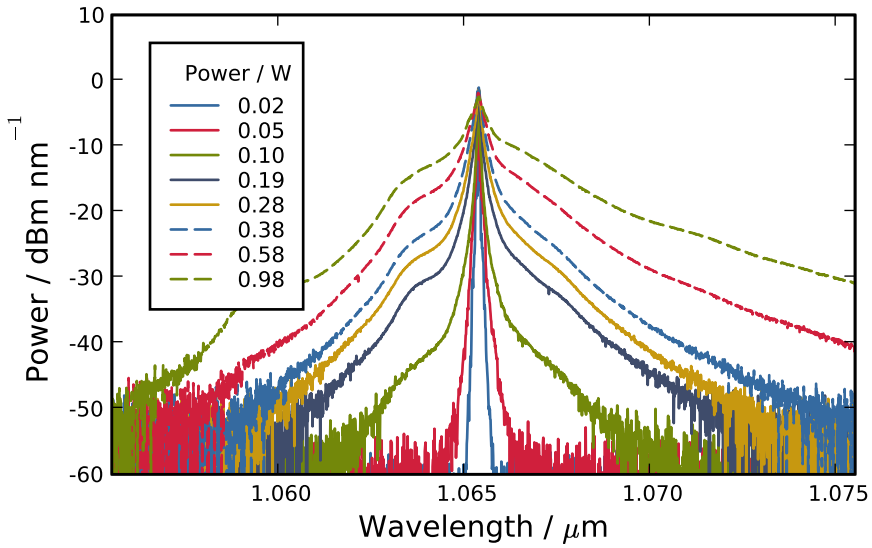


Figure 2.4: ***(experimental)*** The initial spectral broadening of CWL1 in CWHF1 for low pump powers.

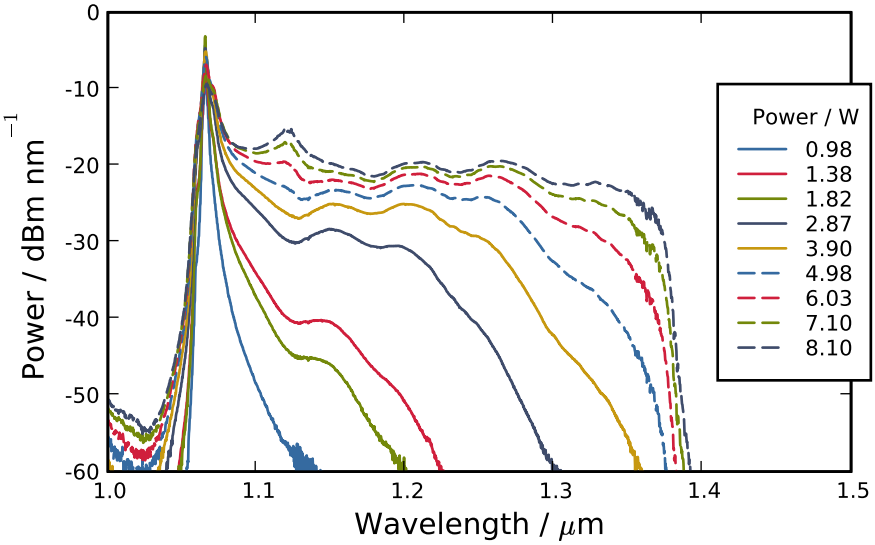


Figure 2.5: ***(experimental)*** The continuum development in CWHF1 for higher power pumping with CWL1.

optimise the choice of experimental parameters. However, modelling CW phenomena is made difficult by the time scales involved. To make the simulations tractable we can only simulate a snapshot of the field as it propagates. We therefore have to carefully choose a time window which contains sufficient information to accurately reproduce experimental observations. A further complication arises due to the absence of a simple diagnostic, such as a FROG, to fully reconstruct a CW field, including its intensity and phase profile,

over significant periods of time, and with sufficient resolution. In general we only have average diagnostics such as average power, the average spectral intensity and the autocorrelation, to determine the field structure. This means that our initial conditions are going to be approximate. In this section, we discuss the various approaches that have been reported to solve these problems and propose a new approach of our own.

The first reported attempt at CW supercontinuum modelling represented the input field as a 400 ps super-Gaussian pulse [Nic03]. This partially solves the temporal griding problem by setting the field to zero at the boundaries of the time window used. This is quickly disrupted with spectral expansion and group velocity dispersion as the field walks out of the initial pulse envelope. The initial conditions included relative intensity noise in the time domain, added in an arbitrary way. The results did not correspond to experiment.

Another approach to the problem utilised a phase-diffusion model, commonly used to model CW lasers [Mus04]. In the time domain, the field is free of amplitude fluctuations but has a random temporal phase with a Gaussian distribution, although the parameters were not chosen to relate to any physical measurable quantities. This leads to a Lorentzian spectrum. The field did not have any applied boundary conditions, so periodic conditions, inherent to the split-step method were used. The results were intended to model the initial modulational instability observed in fibre. Reasonably good spectral agreement with experiment was obtained for low pump powers. In addition, autocorrelations at the output showed agreement, with the MI induced oscillations represented with a coherence spike.

A different approach also neglected temporal amplitude fluctuations and added only quantum noise [Kob05]. Here periodic boundary conditions (due to the split-step algorithm) were used. The simulations resulted in the observation of a characteristic MI spectrum, evolving into a supercontinuum through soliton Raman shifting. Good agreement with experiment was achieved at the maximum pump power levels. Temporal windows ranging from 30 ps to 4 ns were tested, without a visible effect on spectra. This work first introduced the concept of averaging an ensemble of many simulations, as each individual simulation, with a unique set of initial conditions (due to random noise seeding), only represents a very small fraction of what is measured on average by a spectrum analyser. Averaging many such shots leads to a good model of the continuum observed experimentally. The authors of this work noted a very strong dependence of the simulated continuum on pump power input which they did not observe experimentally. Thus they concluded that intensity fluctuations at the input are required to model more closely the power dependence. In what follows we call this the PCW model.

The inclusion of intensity fluctuations to model CW supercontinuum was discussed

in [Van05]. The main theme of this paper was that pump incoherence is the key to CW supercontinuum - something which was well known from previous work on MI induced Raman soliton continua since the 1980s. This model used the measured spectral power of the pump laser and added a random spectral phase to each frequency bin. This process leads to very strong intensity fluctuations in the time domain of the order of the inverse spectral width of the pump (coherence time). The authors supported this by an autocorrelation of the pump source they modelled (a Raman fibre laser), which indicated a 2:1 coherence spike - consistent with 100% intensity fluctuations. Single-shot simulations did not correspond well with the experimental output spectra, and they utilised ensemble averaging like [Kob05]. The larger intensity fluctuations lead to greatly enhanced MI gain and therefore faster continuum initiation compared to a pure CW field input. Periodic boundary conditions were also used in this case with a number of time windows. The authors of this work also claim that changing the time window did not affect the spectral results even though all of the windows were shorter than the walk off time of over 4 ns for the continuum being simulated. In what follows we call this the VB model after [Van05] and also [Bar06] where it was used to model spectral broadening in normally dispersive fibres.

An extension to the phase diffusion model was reported in [Fro06]. This model also neglected intensity fluctuations, but did link the statistics of the Gaussian phase noise to a measurable physical quantity - the bandwidth of the spectrum. The result is a Lorentzian spectral profile with both amplitude and phase noise. However, when they use parameters corresponding to experiments, their results do not agree. If they artificially limited the pump spectral width, then more reasonable results were obtained. We call this model the F model after [Fro06].

A brief review of all of the above models was provided in [Mus07], and the authors asserted that the VB model given in [Van05] (i.e spectral intensity with random spectral phase) gives the best match to experiment.

Although an average CW field is measured, it is unrealistic for a field with multiple longitudinal modes propagating in a nonlinear dispersive medium to remain without intensity fluctuations. As the MI gain and later Raman soliton dynamics depend strongly on the peak power, neglecting such intensity fluctuations will clearly lead to an underestimate of the continuum expansion. This means that a pure CW model, or a phase-diffusion model such as the F model are not suitable. Indeed, the PCW model approximately corresponds to a single frequency laser. On the other hand, the VB model contains intensity fluctuations that may be too strong. This is because it completely ignores any phase relationship between the frequency components, which in reality should exist due to four wave mixing. Such a coupling should work to smooth the intensity fluctuations somewhat. In addition

this model neglects spectral amplitude fluctuations. However, the VB model suffers from a more significant problem. As each frequency bin of the spectrum is given a random spectral phase, the total amount of phase disorder per unit of frequency changes with the selected simulation grid size. This means that, when transferred to the time domain, the degree of intensity fluctuation, (i.e. the peak power), changes with grid size - something that has no basis in physical reality.

We attempted to produce a new model, which was intended to overcome the issues with the current models, by actually simulating a fibre laser cavity. We start from quantum background noise, which is then amplified through a nonlinear dispersive fibre, which represents the fibre laser gain medium. A function simulating the amplitude attenuation and phase characteristics of a broadband high reflector Bragg grating is then applied. The field is then propagated through a fibre identical to the first, i.e. a double pass through the cavity. After this a function representing the output coupler Bragg grating is applied. The reflected field is then passed back into the loop and the transmitted field is taken as the laser output. The reflected field energy is monitored and the amplifier gain is adjusted according to this energy to simulate gain saturation according to Eqn. 2.1.

$$g = \frac{g_0}{1 + \frac{E}{E_{sat}}} \tag{2.1}$$

Where E_{sat}, the saturation energy is chosen to achieve the desired output power of the laser, and g_0 is given the realistic value of 30 dB. The fibre length of the laser was taken as 35 m and the fibre dispersion and nonlinearity that of single mode fibre at 1.06 μm wavelength (Flexcore). The field was propagated around the loop until the average power converged.

For this model we choose to use the periodic boundary conditions inherent to the split-step method, as the consensus from the current literature [Kob05; Van05; Mus07] is that the periodic boundary conditions are not a critical problem as long as a suitably large time window is used. Absorbing boundary conditions would be inferior as the high energy solitons which shift to the longest wavelengths would simply be removed giving an underestimate of the continuum extent. In reality there is a continuous walk-off of red-shifted solitons from earlier times, passing and interacting with the shorter wavelength components, and the periodic conditions maintain this while allowing for a tractable computation window.

2.4.1 A comparison of the CW laser models

The simulated laser spectra from the different models are shown in Fig. 2.6. The CWL model has the distinctive triangular shape common to CW lasers, and as can be seen

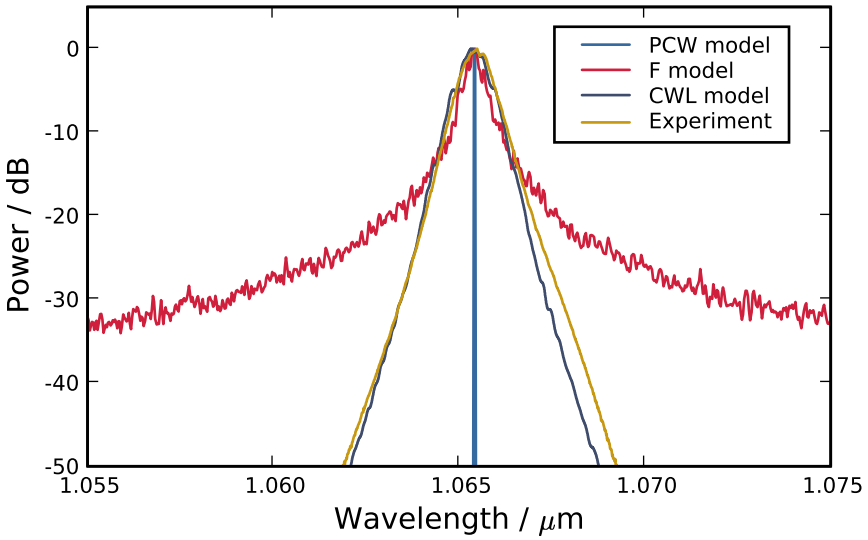


Figure 2.6: The spectra of the PCW, F and CWL models and the experimentally measured spectrum of CWL1. The spectrum of the VB model is normally chosen to be the experimental spectrum. The F and CWL model spectra have been averaged to remove some of the single-shot amplitude fluctuations.

agrees well with experiment. Although smoothed in this figure, it does contain spectral amplitude fluctuations which vary from shot to shot. All of the models contain spectral phase fluctuations. The PCW model has a very narrow and sharp spike at the central laser frequency - similar to a single frequency laser. The F model spectrum contains very significant power outside of the gain region of the fibre, as it has a broad Lorentzian spectral shape. This is not observed experimentally. The VB model is absent from this figure, because the spectrum is chosen arbitrarily. Usually this will simply be the measured spectrum - which means that spectral amplitude fluctuations are neglected.

Fig. 2.7 compares the time domain intensity of the CW pump source models. The CW average power of 6.4 W is indicated for the PCW and F models which do not contain intensity fluctuations. The VB curve indicates the strong intensity fluctuations of the VB model which are clearly the largest, as expected from a random spectral phase. It exhibits high peak powers, up to six times the average CW power, and very short intensity spikes on the order of a few picoseconds for the current parameters. In contrast the CWL model exhibits much smoother fluctuations over longer time scales, as expected, but the degree of smoothing is more than we intuitively predicted. The main advantage of the CWL model is that it is independent of the simulation grid parameters. A comparison of the peak fluctuation power of the CWL and VB models, for different grid frequency resolutions (i.e. increasing time windows) is shown in Fig. 2.8. The CWL model converges whereas the VB model shows a strong grid dependence.

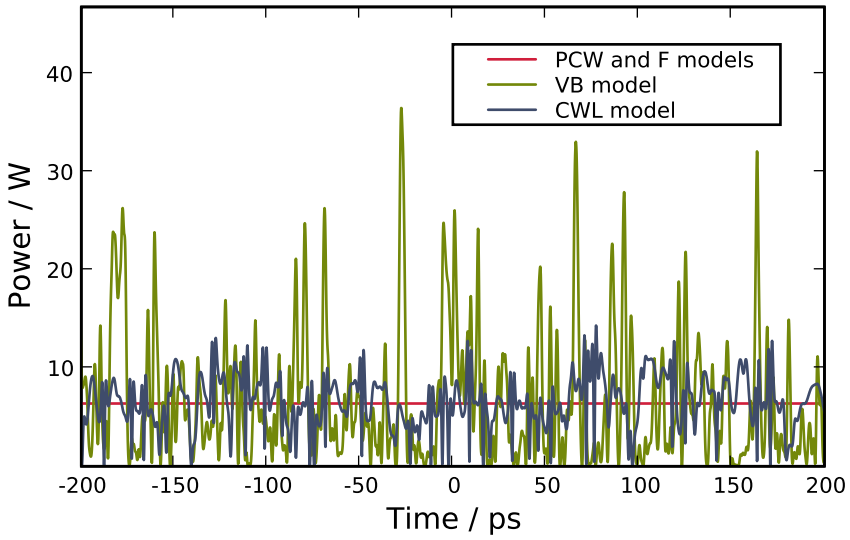


Figure 2.7: ***(numerical)*** The time domain intensity for single shots from the CW continuum pump source models.

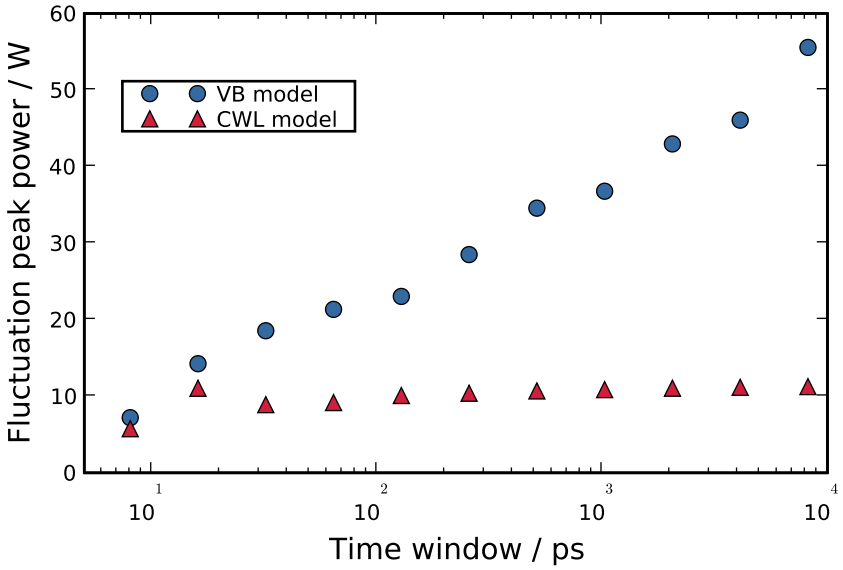


Figure 2.8: ***(numerical)*** Dependence of peak power of time-domain fluctuations on temporal window width (or equivalently, frequency resolution) for the VB and CWL models.

However, the ultimate test of any model is a comparison with experiment. Therefore we simulated the propagation of all four model fields through fibre CWHF1 with parameters corresponding to the experiments presented in Section 2.3.3. Fig. 2.9 shows the results. The VB model is the closest match to experiment. The PCW model leads to very little spectral broadening. The F model leads to a strong Raman Stokes line being formed which

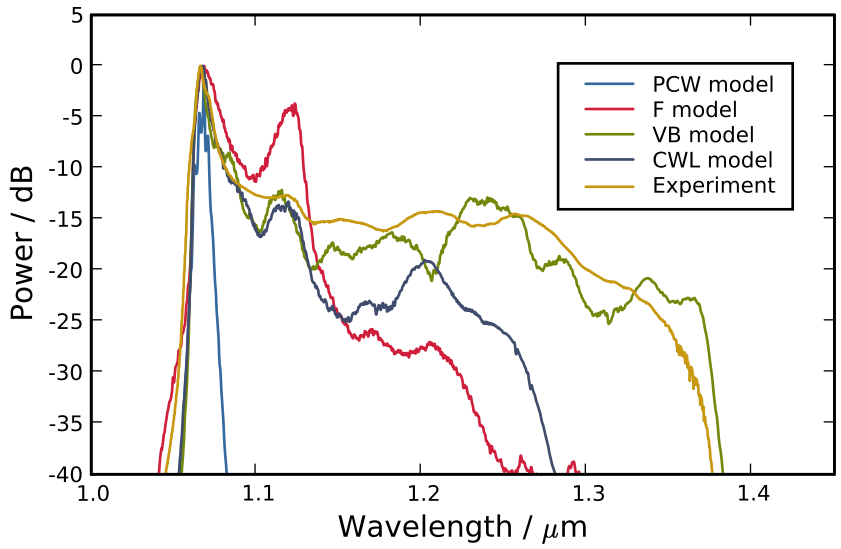


Figure 2.9: The experimental continuum measured for 5.8 W pumping of CWHF1 and the simulated spectra from the PCW, F, VB and CWL models for the experimental conditions averaged over many ensembles.

curtails the continuum extension. This is due to the higher initial spectral power seeding the Raman gain region, and a slower MI initialisation due to the absence of intensity fluctuations. The CWL model does not, unfortunately, agree very well with experiment. It appears that the intensity fluctuations are too small to extend the continuum far enough. One reason for this could be that we iterate around the laser cavity too many times. This is so that the peak power converges to a stable value, typically around 100 iterations. However, for this laser, the expected number of cavity round trips is much smaller. Therefore we are causing too much damping of the intensity fluctuations. Fewer round-trips leads to stronger fluctuations, with the limit of no round trips being equivalent to the VB model. Thus, despite the problems noted above, the VB model is currently the closest match to experimental results and we used it for further studies of the supercontinuum dynamics. Although the pump peak power changes with the choice of grid parameters, the simulated spectrum did not change significantly when increasing the time window by a factor of 4. However, further work needs to be done to improve the CW laser models and remove the unphysical dependence on numerical grid size. One possible approach is to explicitly account for the number of longitudinal modes and then transfer the resulting model to a practical grid size. Alternatively, a recent, more sophisticated treatment, develops analytic techniques to account for the FWM between longitudinal modes of a Raman fibre laser and has been used to quantitatively explain the spectral broadening of the laser [Bab07].

Although the VB model broadly agrees with experiment, it is still not as smooth as the

measured continuum. This is simply due to the number of shots averaged over (in this case 12), increasing this number improves the smoothness. For comparison, a spectrum analyser is likely to average over the equivalent of more than 1000 shots.

2.5 Physical mechanism

The initiation of a continuous wave supercontinuum is due to modulational instability. As discussed in Section 1.5.4 the MI gain and bandwidth depend on the pump power, fibre nonlinearity and dispersion. Therefore the solitons which emerge from the MI process also depend on these parameters. This is significant, because the process which causes the majority of the spectral expansion - soliton self-Raman scattering - depends very strongly on the soliton energy. Careful choice must therefore be made of both the fibre and pump conditions to optimise this process. Further complications arise due to the higher order dispersion and dispersion of the nonlinear parameter, and also due to loss. These we will study in detail. First we shall review the initial supercontinuum stages.

In the anomalous dispersion region of a fibre, solitons are the stable condition of an optical pulse. An arbitrary shaped pulse will evolve to a fundamental soliton shape, shedding excess energy in the process. However, there are two distinct mechanisms for the soliton to emerge. As reviewed in the introduction to this thesis, either a high order soliton will fission to its constituent fundamental solitons, or it will break apart into fundamental solitons through MI, before the fission process can occur. A pure CW field can be viewed as an infinitely high order soliton, and will always break up into solitons if there is nonlinearity and anomalous dispersion. In the case of break up due to MI, because the gain process is noise seeded, the first stable soliton condition which is achieved is that of a fundamental soliton. Therefore MI from fields with no power fluctuations always produces fundamental soliton pulses. However, as the modelling has shown in the previous section, the input CW laser field actually has some significant power fluctuations, which may actually correspond to high order solitons, that may fission before MI has occurred. In Section 1.5.7 of the introduction we showed that the MI dynamics would dominate if the they occurred faster than the fission dynamics, i.e. $L_{MI} \ll L_{fiss}$. If we take a fluctuation of the laser field as a pulse with duration τ_f then it can be shown that this condition is equivalent to:

$$\tau_{cell} \ll \tau_f \tag{2.2}$$

Where τ_{cell} is the modulation cell of MI for the given parameters, which is simply given

by:

$$\tau_{cell} = \frac{2\pi}{\sqrt{2\gamma P_0/|\beta_2|}} \tag{2.3}$$

This is intuitive: if the MI modulations are very short compared to the fluctuations of the laser then the MI evolves as if the field is locally CW. On the other hand, if the MI modulations are comparable to the field fluctuation durations then MI may be quenched and higher order soliton dynamics will occur.

In the previous section we found that the best CW model corresponded to taking the laser spectrum and adding a random phase to each frequency bin. In this model the pulse fluctuation duration is simply the coherence time or $\tau_f = 1/\Delta f$ where Δf is the frequency bandwidth. Therefore pump sources with broader spectra are more likely to lead to the high order soliton condition.

Once the pump field has evolved into a train of solitons, which will have randomly varying energies, the solitons may shift due to Raman self-scattering. To do so they must have a short enough duration so that their bandwidth is broad enough to self amplify through Raman. The self-Raman shift of a soliton can be approximated by Eqn. 1.29 given in Section 1.5.5. From this we see that the Raman shift is dependent on the fourth power of the soliton duration. However, more insight into Raman self-scattering can be gained by considering the soliton energy. We substitute for τ_0 in Eqn. 1.29 using the soliton equation (Eqn. 1.24):

$$E_{sol} = \frac{2|\beta_2|}{\gamma\tau_0}.$$

The result is Eqn. 2.4.

$$\Delta\omega_R(z) = -\frac{T_R\gamma^4 E_{sol}^4}{30|\beta_2|^3}z \tag{2.4}$$

The strong dependence on soliton energy is evident. The dependence on soliton duration (which contains the dependence on spectral bandwidth) is contained in the relation between γ, β_2 and E_{sol}. The soliton energy is reduced as the soliton shifts (the Raman process is inelastic, hence the net frequency shift). We can take account of this fact by including the quantum defect in the energy term; we can also account for the changing dispersion and nonlinearity of the fibre with frequency, by writing Eqn. 2.4 in differential form:

$$\frac{d\omega}{dz} = -\frac{T_R\gamma(\omega)^4[E_{sol}^0\frac{\omega}{\omega_0}]^4}{30|\beta_2(\omega)|^3}, \tag{2.5}$$

where E_{sol}^0 is the starting soliton energy and ω_0 the pump frequency. Eqn. 2.5 can be integrated over z to find the expected location of a soliton propagating through a fibre. All that is required is the initial soliton energy.

The energy of the solitons produced from the MI process can be estimated with good

confidence by using the concept of an energy cell discussed in [Kut05]. The idea is that each modulation cell evolves into one soliton containing the energy available in that cell, so the soliton energy from MI, for pump power P_0, is given by:

$$E_{cell} = \sqrt{2\pi^2|\beta_2|P_0/\gamma}. \tag{2.6}$$

By substituting this equation into Eqn. 2.4 we can get a very approximate estimate for the supercontinuum extent, for a particular set of fibre and pump parameters:

$$\Delta\omega(z) = -\frac{4\pi^4 T_R}{30}\frac{\gamma^2 P_0^2}{|\beta_2|}z \tag{2.7}$$

Eqn. 2.7, contains the familiar optimal conditions for CW continuum generation. For the broadest extent, we need a long fibre length, with high nonlinearity and low dispersion and we should pump with high power. The nonlinearity and pump power dominate unless the dispersion is very small. The fibre length is the least important parameter.

To verify these ideas, we can substitute the values used for the results presented in Section 2.3.3. To do so we must estimate the correct power P_0 to use. As we saw in Section 2.4, the input field has strong power fluctuations, and so using just the average power is insufficient - in this case it predicts a Raman shift to 1.076 μm if the start wavelength is 1.065 μm. From the VB model we can estimate the power fluctuations and thus calculate the expected power in each modulation cell. To do this we use a moving average, with a window the size of the modulation cell τ_{cell}, to obtain P_0 at discrete points within a fixed time period; here we use 4 ns. In reality the cell size varies with power, but only with the square-root of the power and so this is a small effect. From these powers we use Eqn. 2.5 to obtain the distribution of soliton energies at the input to the fibre, shown in Fig. 2.10. The shape of this distribution depends on the pump parameters and in Section 2.6.2 we see how the pump bandwidth is important.

As each soliton energy corresponds to a different Raman shifted wavelength at the output of the fibre, with a fourth order dependence, the shape of the soliton energy distribution strongly affects the resulting continuum spectrum. We can use Eqn. 2.5, to find the distribution of final soliton frequencies from their energies. From the number of solitons at each frequency, their initial energies and the quantum defect of the frequency shift we can obtain an estimate of the power spectrum. Thus we have developed a semi-analytical, statistical model for CW supercontinuum generation. The resulting spectrum for one set of parameters is shown in Fig. 2.11.

The model shows some agreement with the measured supercontinuum spectrum. Although, the inclusion of the dispersion and changing nonlinearity reduced the estimated bandwidth significantly. Therefore another mechanism must be responsible for the extra

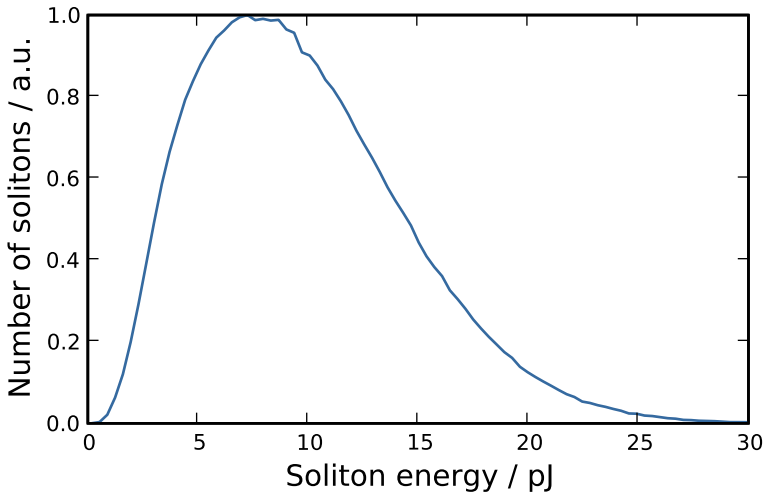


Figure 2.10: ***(numerical)*** The distribution of soliton energies from MI for a 4 ns time window from the VB model of CWL1

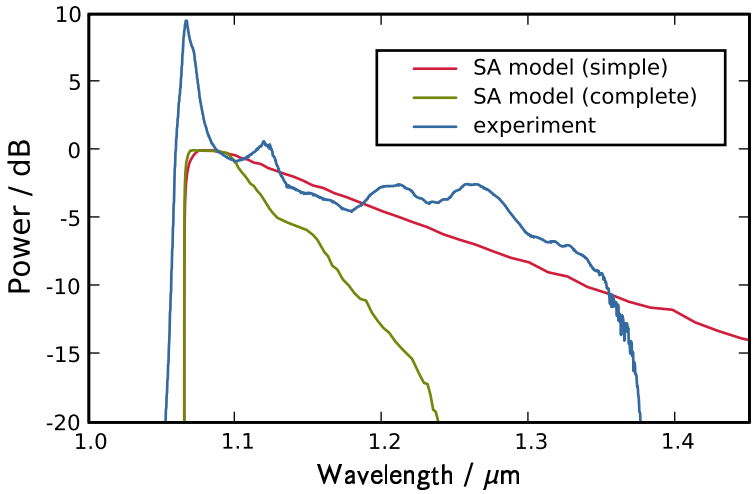


Figure 2.11: ***(numerical)*** The estimated spectrum from the semi-analytical model of CW supercontinuum compared to experiment. The simple model excludes the changing dispersion and nonlinearity with frequency, the complete model includes them. The absolute power level has been adjusted.

spectral expansion. We believe that this is due to inelastic collisions between solitons, which can transmit significant energy from low energy solitons to higher energy solitons through Raman scattering, further exciting the highest energy solitons.

To visualise this process we can use numerical simulations as described in the previous section. Firstly, we can look at the early evolution of the power in the time domain, to observe how the temporal solitons form. Fig. 2.12 shows three slices of the field evolving though the fibre. The top slice shows the input field with time domain power fluctuations

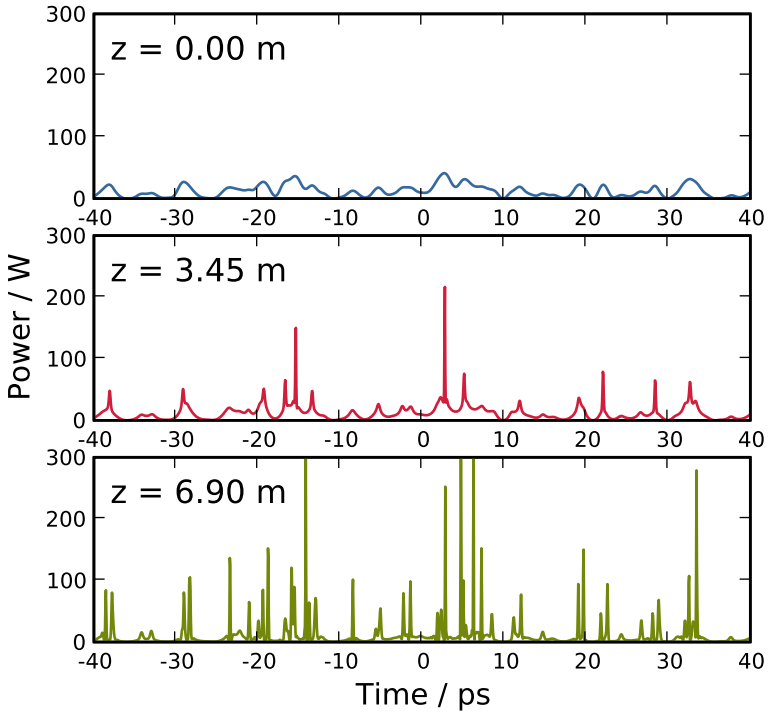
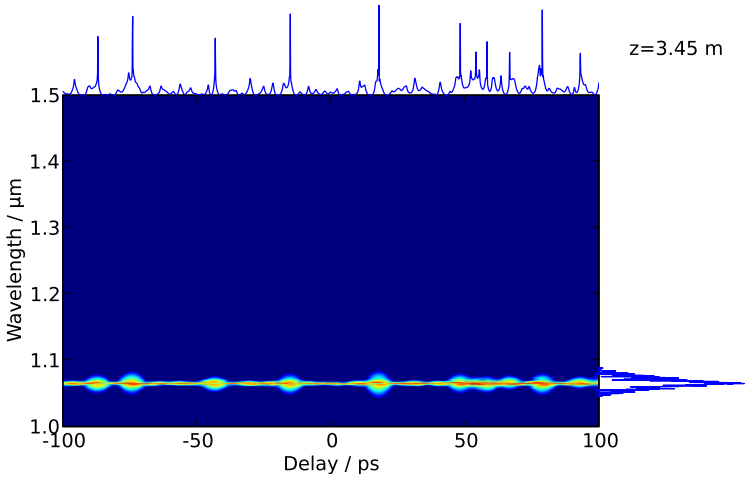


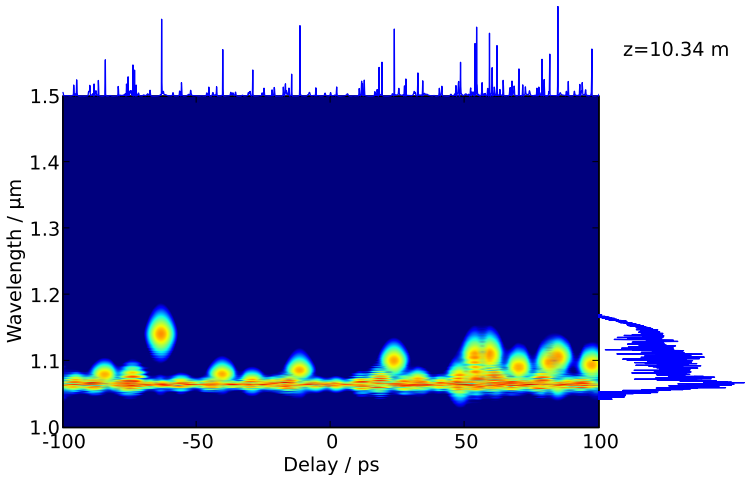
Figure 2.12: ***(numerical)*** Time domain evolution of CW supercontinuum with initial intensity fluctuations.

derived from the VB model. In the second slice, after 3.45 m of propagation we see that MI has caused the emergence of solitons. Here we can clearly see that the solitons form earlier and with higher peak power at the peaks of the input power fluctuations. Note also that the solitons being formed are much shorter in duration than the input power fluctuations. In the last slice we see that more solitons are forming at lower input power regions and we have created a train of solitons with a distribution of energies, such as described above, which will evolve into a smooth continuum. It should be noted that even without input power fluctuations, the solitons formed also have a distribution of energies, as they are still seeded from background noise. However, they will have lower energy than the solitons formed from the input power fluctuations.

Fig. 2.13a shows a spectrogram illustrating the initial break up of the pump field into solitons. In Fig. 2.13b we see how the highest energy solitons have started to shift to longer wavelengths through Raman self-scattering, while new solitons are forming from the remaining pump field. In Fig. 2.14a we see how this process leads to a spreading out of the solitons into a continuum. We should note again that these are single shots of 200 ps duration from a continuous process. The summation of all of these solitons leads to a very smooth spectrum on average. Finally in Fig. 2.14b we see the continuation of this process



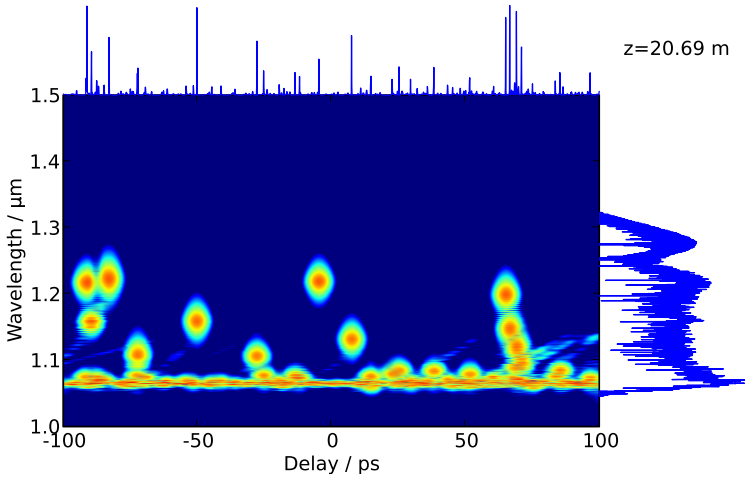
(a) Initial MI breakup into solitons.



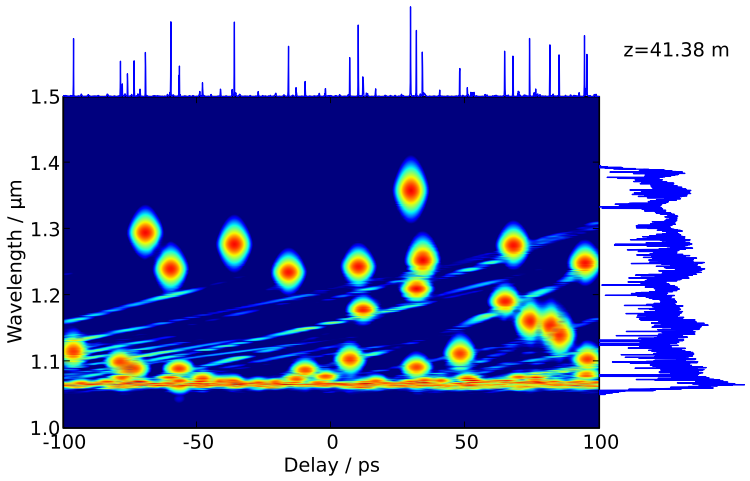
(b) Further MI development and onset of Raman self-scattering.

Figure 2.13: ***(numerical)*** Spectrograms of the initial CW supercontinuum dynamics.

and also clear evidence of soliton collisions. The non-solitonic traces left behind by the solitons is the radiation shed by a pair of solitons after an inelastic collision mediated through the Raman process has occurred. Both solitons involved will have energies which lead to the soliton order N being different from unity and therefore some energy is shed as the soliton adapts. Solitons collide when they overlap in time (i.e. align vertically in these spectrograms) as long as they are close enough spectrally for the Raman process to occur (up to about 40 THz). As the energy transfer is to longer wavelengths, and the most energetic solitons have shifted furthest, the transfer of energy is from low to high energy solitons. Thus the fastest shifting solitons accelerate and collide more often leading to a



(a) Raman self-scattering of the solitons develops.



(b) Energetic solitons scatter furthest and collide most.

Figure 2.14: ***(numerical)*** Spectrograms of the Raman self-scattering of the solitons and soliton collision traces.

cascade. This process can significantly enhance the continuum bandwidth. The role of soliton collisions was also recently discussed in [Fro06], and was originally identified in picosecond pumped supercontinua two decades ago [Isl89a; Isl89b].

Given the accelerating nature of the high energy solitons, why does the continuum not expand forever? Limitations to the continuum bandwidth are caused by at least three mechanisms. Firstly, there is a finite length of fibre, and so the maximum shift is that achieved by the most energetic soliton through the necessarily limited nonlinear medium. Secondly, losses become significant, which reduces the soliton energy and can slow or stop their shift. And lastly, the balance of nonlinearity and dispersion, which maintains the soliton shape can change very significantly and thus broaden the soliton

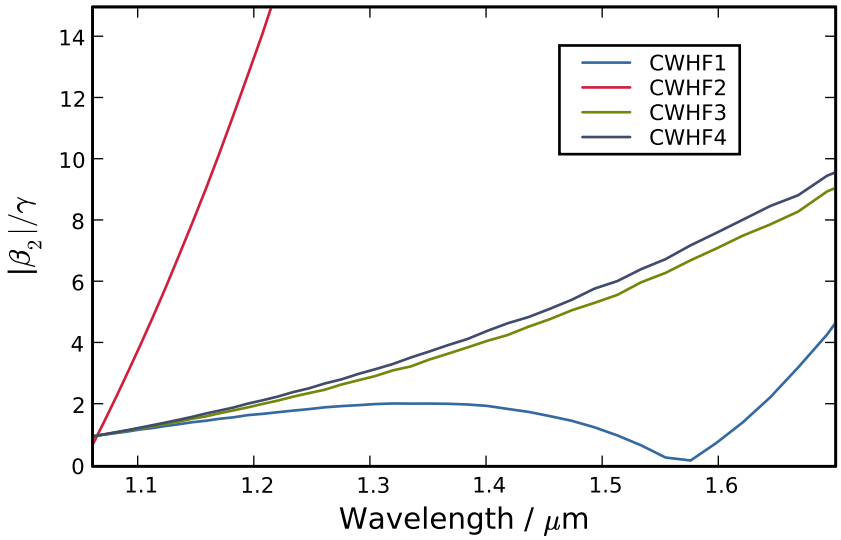


Figure 2.15: ***(numerical)*** The calculated soliton ratio, $|\beta_2|/\gamma$, curves of the CW supercontinuum generation PCFs

temporally so that it no longer has the spectral bandwidth for Raman self-scattering. We saw evidence of this last case in the above example of the semi-analytical model. It can be understood by studying the ratio $|\beta_2|/\gamma$ which is plotted in Fig. 2.15 for the fibres considered in this chapter. The fibre CWHF1, that we have considered so far has a very flat soliton ratio across the spectral region we are interested in. In the absence of other factors, the change of this ratio from 1 at the pump wavelength to around 2 at 1.3 μm will lead to a proportional temporal broadening with a small reduction in frequency shift. Conversely CWHF2 shows a very steep change in soliton ratio with wavelength. This is because the zero dispersion is very close to the pump (see Table 2.2) so the ratio changes from a fractional value to very high values at 1.3 μm. This leads to a halting of the soliton shift, as confirmed in the experimental results in Fig. 2.16. Despite the higher pump power used in CWHF2 the supercontinuum generated in CWHF2 is narrower than that in CWHF1.

Although CWHF1 has good dispersion and nonlinearity profiles for efficient CW supercontinuum generation, it is not optimal because it suffers from very high water loss ~ 600 dB/km around 1.38 μm. This loss can also limit the continuum growth as is clearly seen in Fig. 2.16. In Fig. 2.17 we show the spectrogram at the output of CWHF1. It is clear no solitons have gone beyond ~ 1.38 μm as we would have expected after 100 m when we compare with the growth in the previous spectrograms (Fig. 2.14). Instead, some solitons have very clearly narrowed spectrally, at the extreme limit of the continuum, and stretched in the time domain. This is due to the reduction in soliton energy which halts the Raman

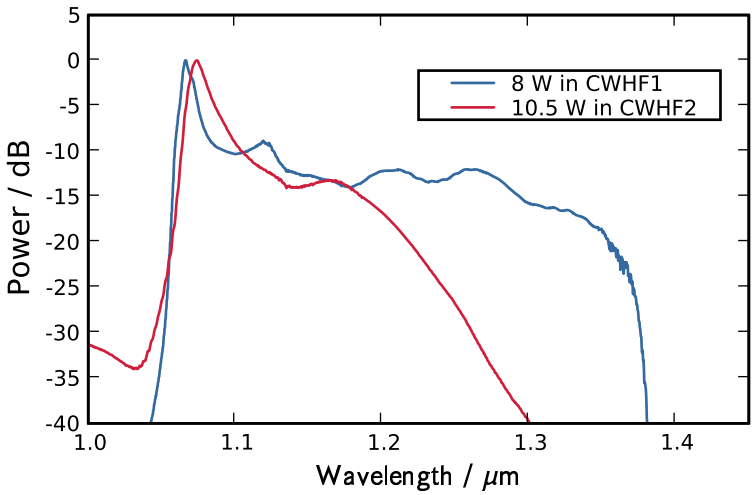


Figure 2.16: ***(experimental)*** Experimental comparison of supercontinuum generation with similar pump powers in CWHF1 and CWHF2. Although CWHF2 is pumped with slightly more power, the continuum is narrower.

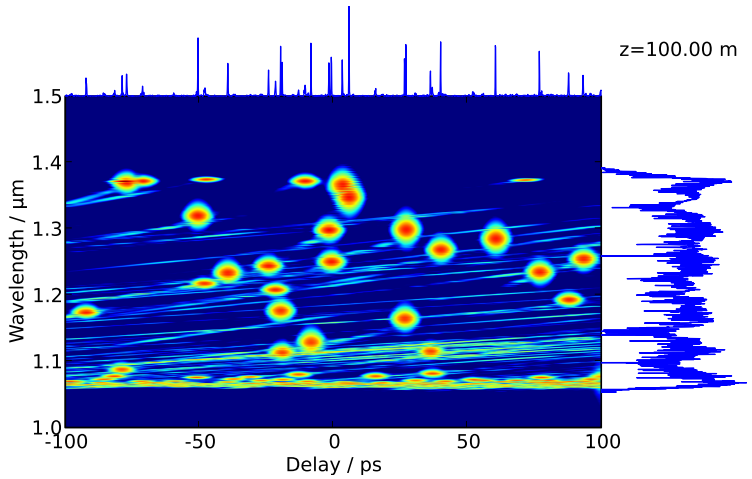


Figure 2.17: ***(numerical)*** Spectrogram of the CW supercontinuum in CWHF1 after 100 m of propagation showing the water loss barrier.

self-scattering. The effect is clearer when observed purely in the spectral domain as shown in Fig. 2.18. One way around the problem with water loss is to pump much shorter fibre lengths thus maximising the nonlinear length in comparison to the loss length of the fibre. However, to do this a much higher pump power is required. While the work for this thesis was carried out, the technology to achieve this was not available. Recently, Burly Cumberland, a colleague in the Femtosecond Optics Group, has achieved such powers by using more advanced splice techniques to obtain up to 50 W CW pump power in a 20 m length of CWHF1. Here we look at some simulated results in this regime. Fig. 2.19

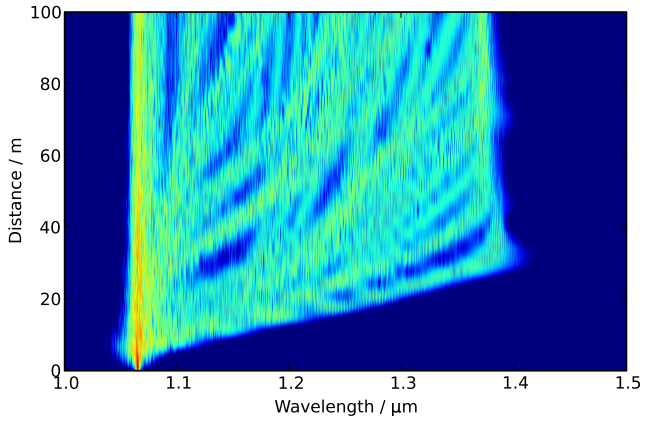


Figure 2.18: ***(numerical)*** Spectral evolution of the supercontinuum along CWHF1 with 8 W pumping.

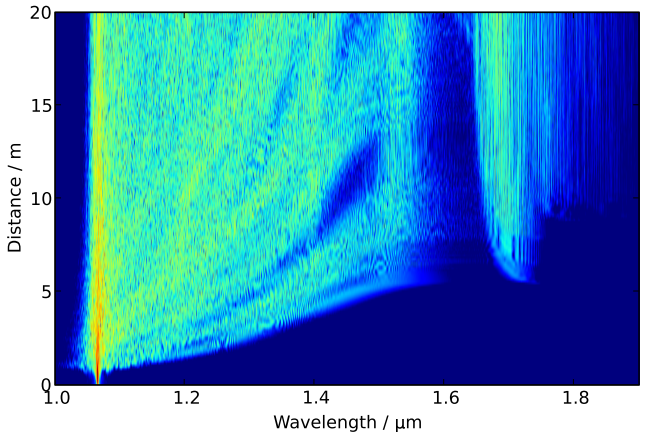


Figure 2.19: ***(numerical)*** Spectral evolution of the supercontinuum along 20 m of CWHF1 with 44 W pumping. Note that the wavelength scale is expanded compared to Fig. 2.18.

shows the spectral evolution along 20 m of CWHF1 for 44 W pump power, using the VB model. The continuum extends well beyond the water loss region, although a change in the soliton trajectories is observable around 1.4 μm. At 1.57 μm the solitons interact with the second zero dispersion wavelength of the fibre. Here the soliton self-frequency shift is halted and dispersive waves are formed beyond the second zero dispersion, around 1.7 μm. This process is more clearly observable, once again, in the spectrogram picture. Fig. 2.20 shows the spectrogram after 20 m of propagation through CWHF1. A large number of high energy solitons are generated at the pump wavelength and Raman shift to form a continuum. After the water loss region at 1.38 μm the solitons are clearly of lower energy, but are still energetic enough to continue shifting. At the second zero dispersion they are prevented from shifting further, but generate dispersive waves in the normally dispersive

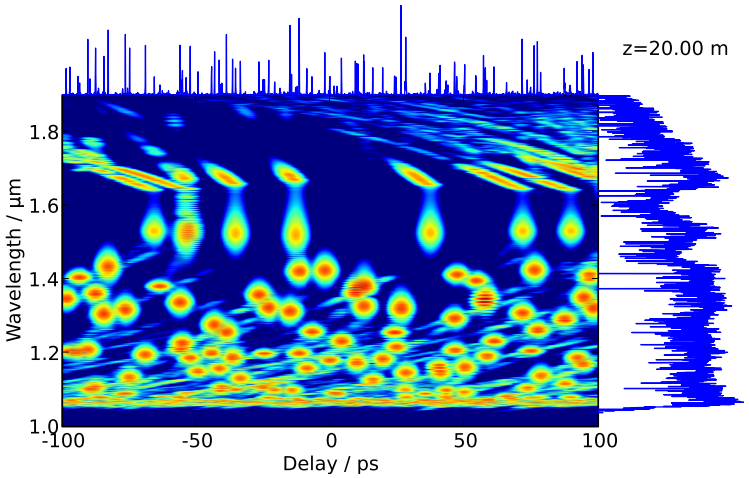


Figure 2.20: ***(numerical)*** Spectrogram of the supercontinuum after 20 m of CWHF1 with 44 W pumping.

region beyond. The dispersive waves are clearly being chirped as they propagate through the fibre.

2.6 Experimental results

2.6.1 Low-water loss PCF

In Section 2.5 we discussed the mechanism of CW supercontinuum generation and the roles of loss and the soliton ratio in limiting the continuum bandwidth. We showed numerical results which reproduce recent experimental developments where very high average power pumping of short lengths of CWHF1 produces an extended continuum. However in that fibre the continuum is limited by a second dispersion wavelength. In this section we look at experiments which used specially fabricated low water loss fibres to generate extended supercontinua with lower power pumps.

The first fibre we used for this purpose was CWHF3. This fibre has a similar nonlinearity to CWHF1, but a higher dispersion value. It also has a larger dispersion slope as evidenced by the stronger increase in the soliton ratio shown in Fig. 2.15. This makes it harder to form a supercontinuum in this fibre. However, the water loss has been reduced by an order of magnitude (in dB/km), to just 70 dB/km by careful manufacturing at Blaze Photonics. The fibre was made using the standard stack and draw process, but special care was taken to reduce water contamination during all of the process steps. The capillaries forming the stack were drawn in a high-purity nitrogen atmosphere from the highest grade of fused silica commercially available. The completed preform stack was then subjected

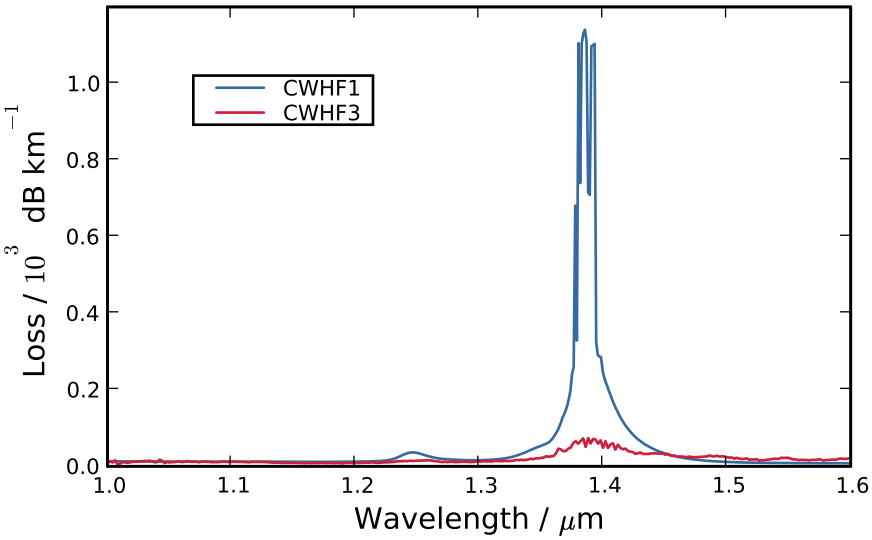


Figure 2.21: ***(experimental)*** Loss spectrum of CWHF1 and CWHF3.

to chemical cleaning and drying in a halogenic atmosphere at over 1000°C to reduce surface contamination and to lower OH^- content in the stack assembly. The resulting fused preforms were again purged with high-purity nitrogen before being drawn to a fibre, and additional care was taken not to reintroduce contaminating water during the fibre draw. The loss spectrum, measured with a supercontinuum source is shown in Fig. 2.21 alongside that of CWHF1.

We pumped CWHF3 with CWL2, achieving up to 26 W in the fibre core. The collimated output of the pump laser was coupled into conventional single mode which was spliced to the PCF via an intermediate mode-matching fibre, leading to a splice loss of just 0.8 dB. The optimal results are shown in Fig. 2.22. The broadest supercontinuum (blue-dashed curve) contained over 15 W of output power for 26 W pump power. The supercontinuum rapidly extends to the water loss region even at the lowest, 15 W, pump power level. Here, the effects of gain competition from the CW Raman Stokes generation process is evident and clear discrete Stokes lines are formed.[1] These arise because CWHF3 has a very high nonlinearity and small amounts of back reflection from the fibre ends and splices can readily cause Raman lasing. The reflections are hard to suppress, even with strong angle-cleaved ends, due to the very high numerical aperture of CWHF3, and other similar PCFs. Nevertheless, despite the lack of flatness due to the Raman lines, the continuum does clearly extend beyond the water loss peak by more than 100 nm.

To confirm the solitonic nature of the continuum experimentally we took autocorre-

[1] Due to this strong Raman response, this fibre was also used to build a Raman laser, though that work is not reported in this thesis [Tra05a].

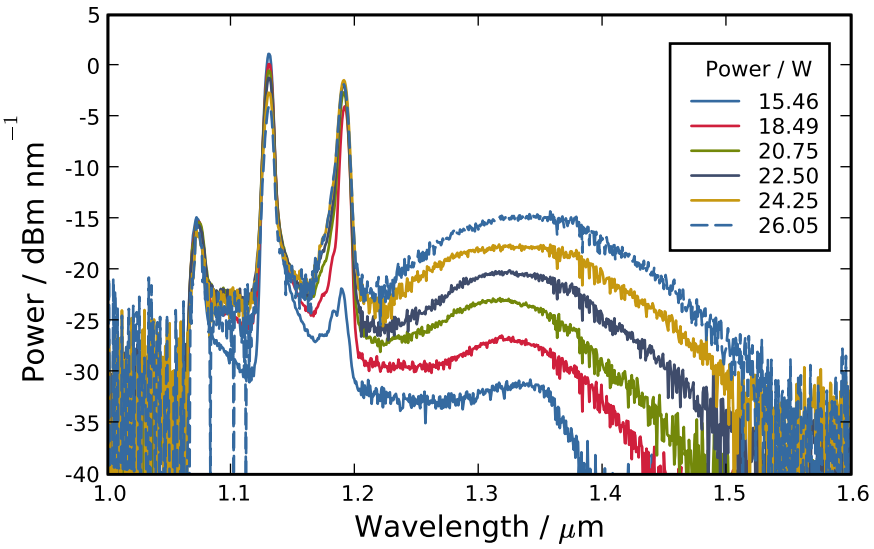


Figure 2.22: ***(experimental)*** The evolution of the supercontinuum in CWHF3.

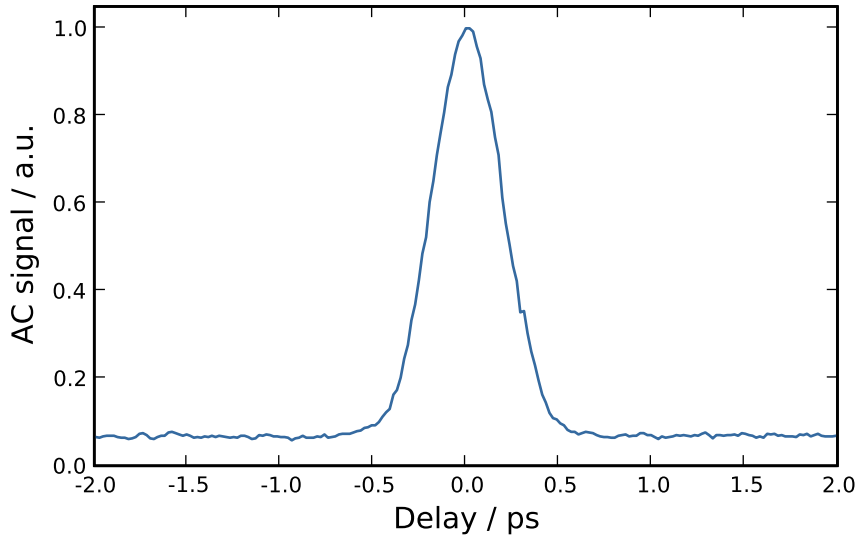


Figure 2.23: ***(experimental)*** The autocorrelation measured at 1.33 μm.

lation measurements of the spectrally filtered supercontinuum, one example of which is given in Fig. 2.23. It shows a soliton of approximately 300 fs with an 8% pedestal. The pedestal changed with wavelength, becoming much larger at shorter wavelengths closer to the pump.

The variation in measured pulse duration with wavelength is shown in Fig. 2.24. It should be noted that these measurements were taken at the end of 100 m of fibre and so the solitons are broadened due to loss. The solitons initially forming the supercontinuum

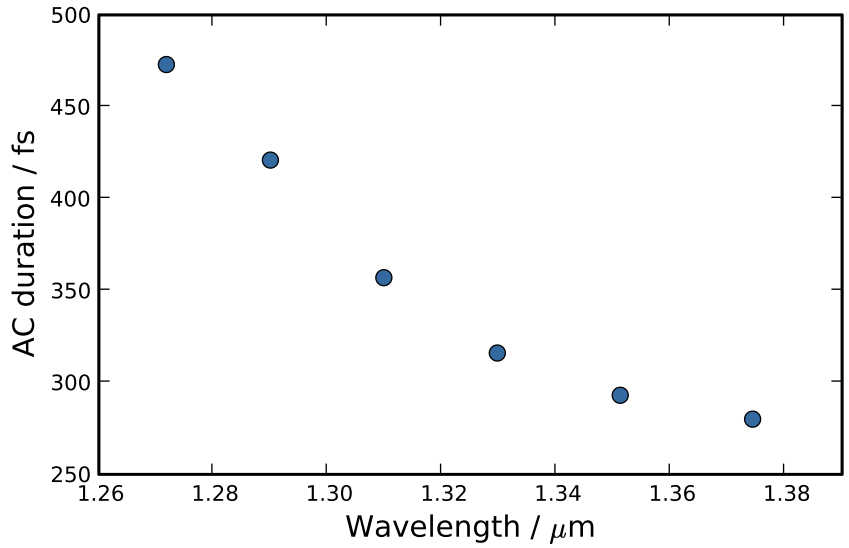


Figure 2.24: ***(experimental)*** Autocorrelation duration for a number of spectral slices from the supercontinuum.

spectrum are necessarily shorter. From the variation in pulse duration it is evident that the solitons decrease in duration at longer wavelengths. This is consistent with the mechanism discussed in Section 2.5 where the shorter, energetic solitons shift furthest.

Although these results are in principle an improvement over those with CWHF1, the supercontinuum was not particularly flat and did not extend as far as we wanted. Even though the flatness can be imposed by filtering, because we have so much average spectral power available, a supercontinuum with intrinsic flatness is preferable. To that end we considered another fibre, CWHF4. This fibre was manufactured by PERFOS and was also produced using the same stack and draw method. The glass used was high purity silica rods and tubes (F300 silica from Heraeus) which were drawn down to a few millimetres with dimensional tolerances better than 1% over 10s of metres. These were then stacked into the desired arrangement and drawn into a preform. PERFOS use chemical cleaning and polishing techniques to avoid the formation of Si-OH liaisons at defect points around the air silica interfaces which are responsible for the high OH related absorption losses. The fibre draw was performed under controlled dry atmosphere conditions in order to avoid extrinsic contamination during this step. PERFOS have managed to achieve OH absorption loss which is independent of the fibre mode field diameter. This indicates that no excess Si-OH liaisons are formed at the air-silica interfaces. The resulting fibre, CWHF4, had a water loss of only 30 dB/km. It had a slightly lower dispersion and nonlinearity at the pump wavelength compared to CWHF3. With improved splice techniques we could pump directly from either the laser CWL2 or the ASE source CWASE. The output of the

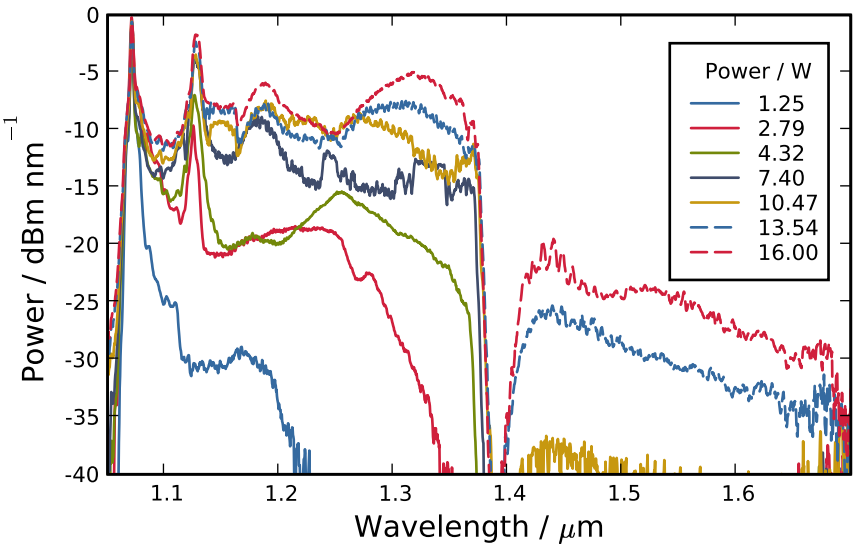


Figure 2.25: ***(experimental)*** Supercontinuum generation in CWHF1 with up to 16 W pump power from CWL2.

laser or ASE source (via an isolator) was spliced directly to an intermediate mode field matching fibre and then to 200 m of the PCF. For comparison we also re-pumped CWHF1 in the same conditions.

The results in CWHF1 are shown in Fig. 2.25. Here we see that although the initial continuum development is very efficient as the fibre parameters at the pump wavelength are good, the water absorption significantly limits the continuum. In contrast, in CWHF4 no such limitation is observed, as shown in Fig. 2.26. In this case, apart from the Raman Stokes lines, the continuum is relatively flat and extends to the edge of the sensitivity of our optical spectrum analyser.

A reduction in the Raman Stokes lines should be possible by splicing the output of the PCF to standard fibre before angle cleaving the end, thus reducing back reflection.

2.6.2 Pump spectral bandwidth dependence

In this section we consider the effect of pump spectral bandwidth on the supercontinuum generation process. We pumped CWHF4 with both CWL2 and CWASE which have a large difference in bandwidth. Previous work has shown that for the same bandwidth ASE and laser pumping produces near identical supercontinua [dM04b]. This means that differences observed in this section must arise from the differing bandwidths. Fig. 2.27 shows the results. The narrow band pumped supercontinuum is flatter and extends significantly further than the broadband pumped continuum.

This difference can be understood by comparing the MI cell duration to the expected

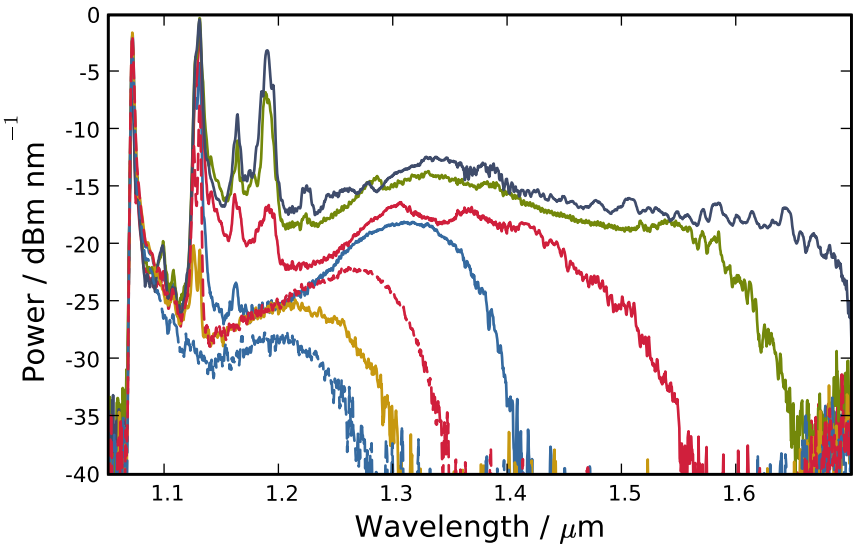


Figure 2.26: ***(experimental)*** Supercontinuum generation in CWHF4 pumped with CWL2. The pump powers were (broader spectra for higher power): 4.1, 4.6, 5.8, 7.7, 10.8, 12.6, 15.7 W

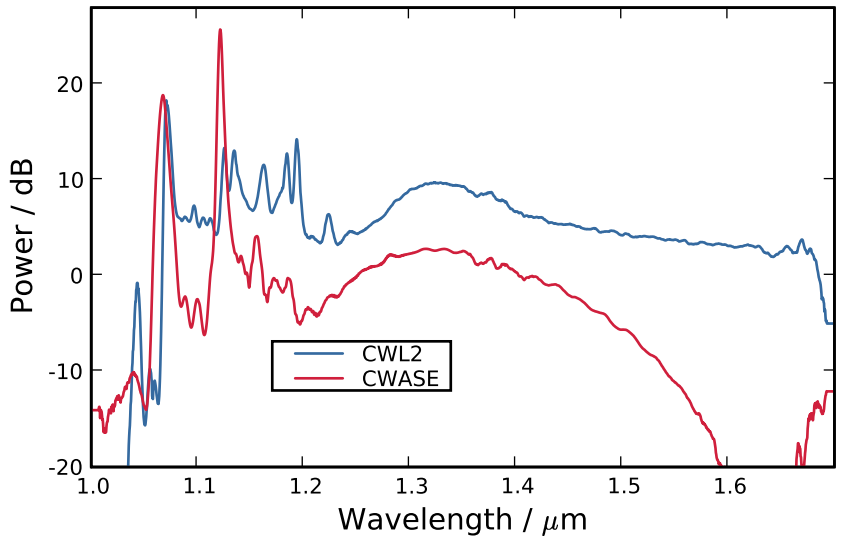


Figure 2.27: ***(experimental)*** Comparison between the supercontinuum obtained in CWHF4 with CWL2 (0.8 nm bandwidth) and CWASE (5 nm bandwidth) pumping with 13 W average power.

modulation period of the pump laser. For example, a pulse with a spectral bandwidth of 0.8 nm will have intensity modulations in the region of 5 ps, whereas a pulse with ten times the bandwidth will have modulations in the region of 0.5 ps. For CWHF4 the MI cell duration is around 1.3 ps. So for the narrow bandwidth pump, the analysis in

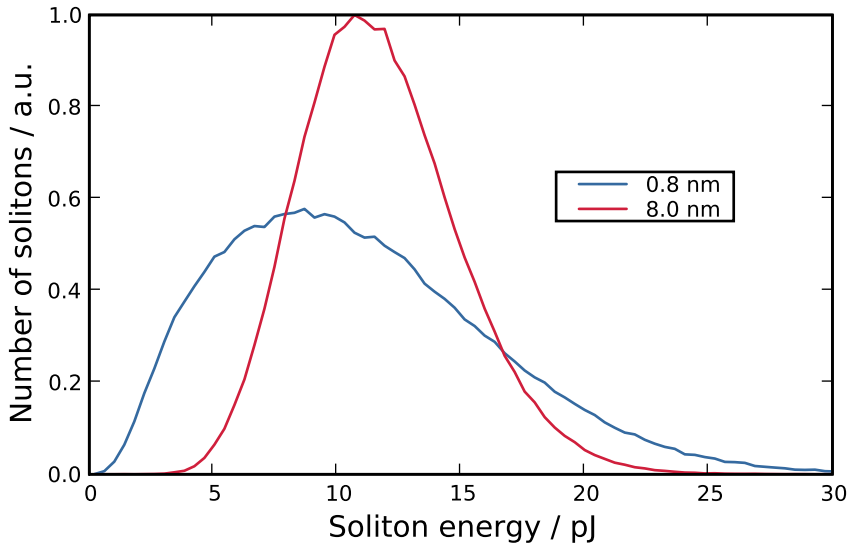


Figure 2.28: ***(numerical)*** Distribution of soliton energies from modulation instability for Gaussian shaped pump spectra with different bandwidths.

Section 2.5 is relevant and a distribution of solitons energies is formed, with some very energetic solitons formed on top of the input pump fluctuations which are several times longer than the MI cell duration. For the broad bandwidth pump, that analysis is not valid. The fluctuation duration is within the modulation cell and the pump bandwidth overlaps significantly with the MI side lobes. The solitons evolve from the input pump fluctuations rather than on (in the time domain) the input fluctuations. This means that the soliton energies will be more uniform without such extreme energetic solitons as in the narrow band case and therefore the continuum bandwidth will be reduced. We can estimate the distribution of soliton energies using the analysis of Section 2.5. Fig. 2.28 shows the distribution of soliton energies for the fibre CWHF1 for a pump field with a Gaussian spectrum. One curve has a bandwidth of 0.8 nm, the other a bandwidth of 8 nm. As noted above, the broadband pump has a narrower (i.e. more uniform) energy distribution, whereas the narrow pump leads to a wider range of energies, a longer tail at the high energy soliton side. The soliton self frequency shift depends on the fourth power of the soliton energy, so this tail becomes very important. To see this we once again estimate the spectrum achieved from these two soliton energy distributions using the same semi-analytical model as before. The resulting continuum spectra are shown in Fig. 2.29. The narrow pumped supercontinuum clearly extends further.

This variation in supercontinuum width with pump spectral bandwidth leads one to the consideration of the optimal pump bandwidth. By estimating the continuum spectrum with the semi-analytical model for different Gaussian pump spectra we can

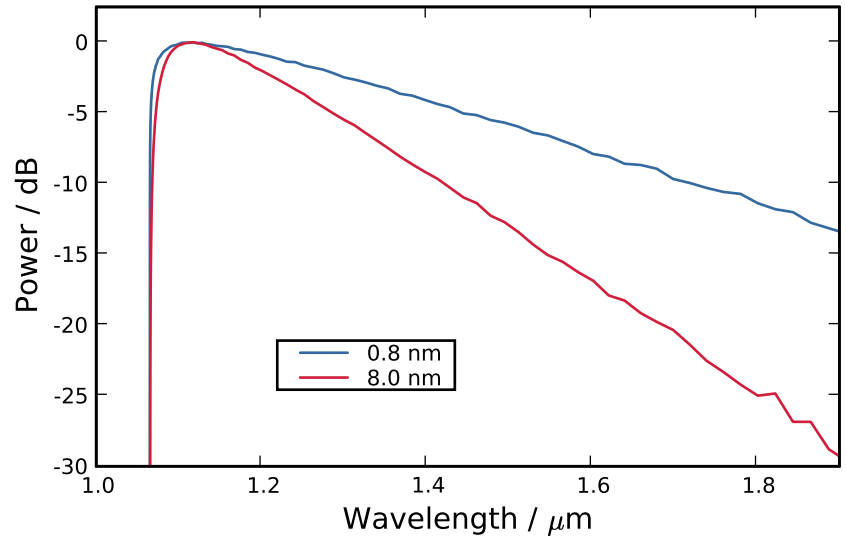


Figure 2.29: ***(numerical)*** Estimated supercontinuum spectra, using the semi-analytical model, for Gaussian shaped pump spectra with different bandwidths.

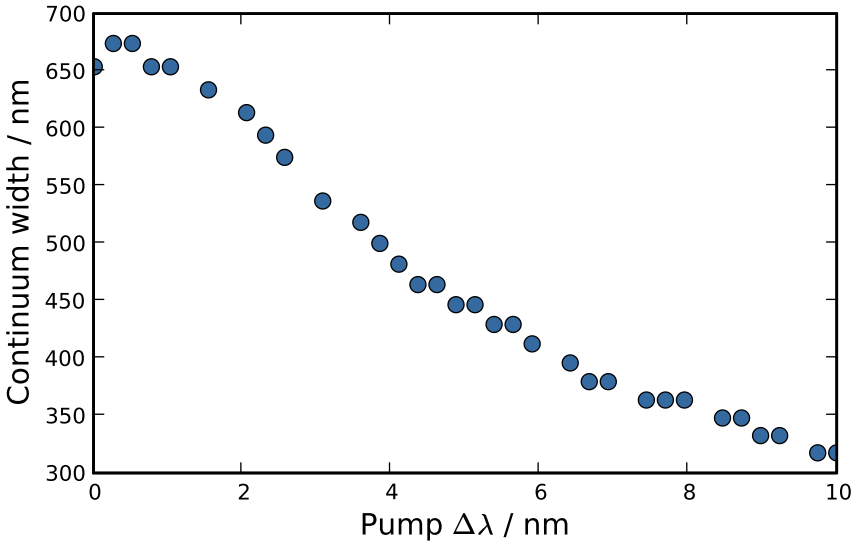


Figure 2.30: ***(numerical)*** Estimated supercontinuum bandwidth using the semi-analytical model, for Gaussian shaped pump spectra with different bandwidths.

produce Fig. 2.30. From this figure it appears that the narrower the pump source, the broader the resulting spectrum. This can be understood in the time domain as discussed above. However, this analysis is in contradiction to some experimental results [ML06], although the setup in that work used different pump types (i.e. laser and LED) to get the bandwidth sources which brings other variables into the analysis. Further, more detailed

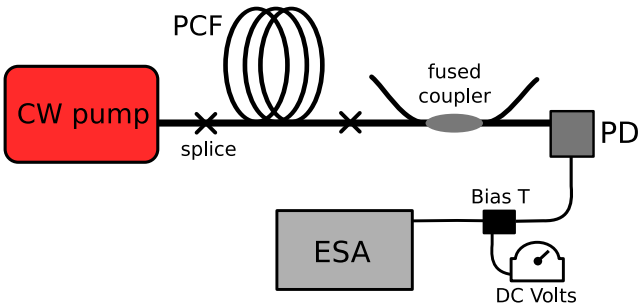


Figure 2.31: Experimental setup for measuring the relative intensity noise in the CW supercontinua. PD = photodiode, ESA = electrical spectrum analyser.

experimental investigation of the influence of pump bandwidth on supercontinuum width is required.

2.6.3 Noise of CW supercontinua

We measured the relative intensity noise of supercontinua produced in CWHF1 pumped with either CWL1 or CWASE. The experimental setup is shown in Fig. 2.31. The supercontinuum at the output of the PCF is passed through a fused fibre coupler selected to filter the pump wavelengths from the supercontinuum. This allows us to monitor the noise of the actual supercontinuum in the absence of the strong pump power. The resulting spectrum was approximately Gaussian with a centre wavelength of 1.23 μm and bandwidth of 150 nm. The power of the continuum is measured with a photodiode with 2 GHz bandwidth. The relative intensity noise is defined as the the time averaged noise power in a 1 Hz bandwidth divided by the DC power [Der98]. To measure this we passed the signal from the photodiode through a bias-T with a 12 GHz bandwidth and DC cut-off at 10 kHz. The DC voltage was measured using a multimeter. The AC signal is passed into an electrical spectrum analyser (ESA) with a frequency range of 10 kHz to 2.2 GHz. The electrical spectrum is measured and from this the electrical power within a 1 Hz bandwidth at a given frequency is measured. This is converted into the equivalent RMS voltage and divided by the DC voltage to obtain the square root of the relative intensity noise (RIN). We also measured the relative intensity noise of the two pump sources alone (without the coupler).

The results are shown in Fig. 2.32. The CWASE pump source has a much lower RIN than the laser pump source. The noise of the pump sources arises from beating between longitudinal modes (in a laser) and between different frequencies outside the laser cavity or for an ASE source. It can be shown [Der98] that the noise of an ASE source is inversely related to its bandwidth, because the DC power increases faster with respect to bandwidth than the beat noise between the extra spectral components. For CWASE the bandwidth

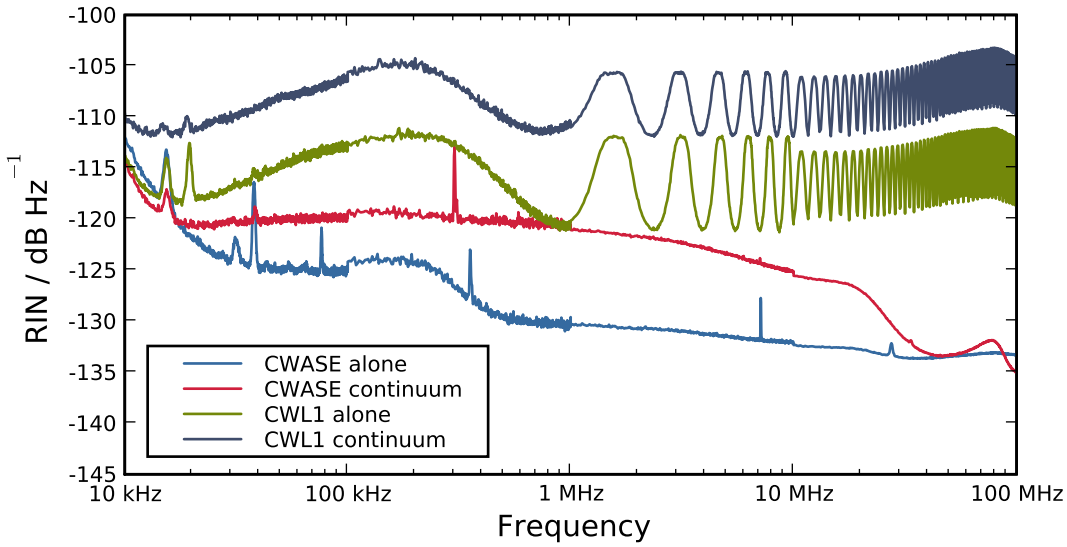


Figure 2.32: ***(experimental)*** The relative intensity noise of the supercontinuum pump sources and the noise of the resulting supercontinua.

was 6 nm or 1.6 THz. Using the estimate from [Der98] this should lead to a RIN of -127 dB/Hz. We measured a RIN of -125 dB/Hz up to 200 kHz and -137 dB/Hz at higher frequencies. The laser source has a much higher RIN due to the longitudinal mode beating and significant oscillations in the RIN spectrum are observed at the cavity frequency. These oscillations are carried through and amplified into the supercontinuum. Due to the higher initial absolute RIN value of the laser, the resulting continuum has a relative intensity noise more than 10 dB higher than the ASE pumped supercontinuum, despite the fact that the relative gain to the continuum noise is lower for the laser pump source. This can be significant for some applications, in particular OCT, where these sources have been used by collaborators [Pov05], and the ASE source has been found to be preferable.

2.6.4 Quasi-CW pumping

We also pumped CWHF3 with the MOPFA source (CWL3). This enabled us to study the supercontinuum dynamics at powers just beyond the reach of our CW lasers from 30 to 150 W. This pump source has a duration of 2 ns, which is well within the quasi-CW regime, i.e. the dynamics are the same as for a CW field as all of the nonlinear processes are much faster than the pulse timescales. Fig. 2.33 shows the results. The spectra for lower pump powers resemble those for the CW pumping described in Section 2.6.1. As the power is increased the spectrum becomes progressively flatter until, apart from the Raman Stokes lines, there is a smooth and flat continuum to the edge of the spectrum analyser sensitivity at 1.75 μm for 60 W pump power. The spectrum is likely to extend to the absorption edge

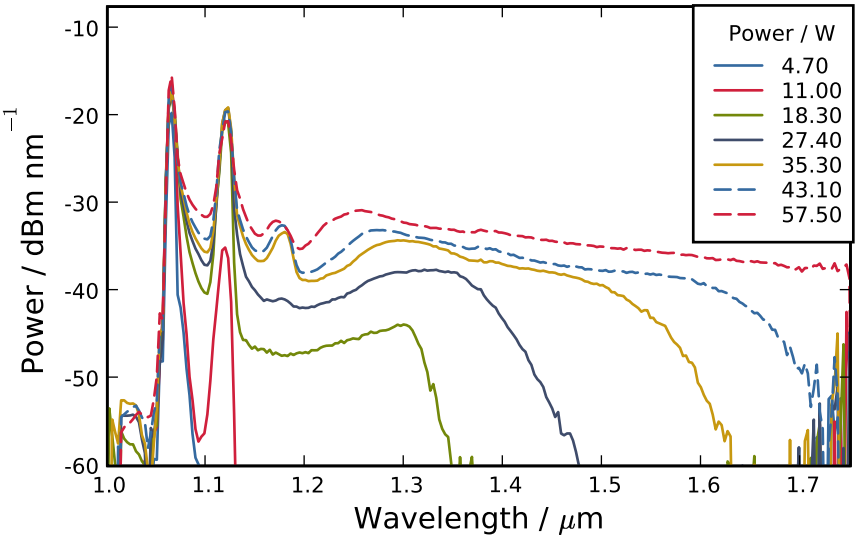


Figure 2.33: ***(experimental)*** Supercontinua generated by pumping CWHF3 with 2 ns pulses with peak powers ranging from 5 to 60 W.

in silica fibres, around 2.2 μm.

This pump regime is interesting because these powers are now easily accessible to true CW lasers. Therefore scaling of the pump power to around 100 W is a real possibility, leading to continua in the few 100 mW/nm regime, spanning from 1 to 2 μm. In addition, these enhanced powers could even generate CW supercontinua to wavelengths in the visible, if the fibre dispersion could be engineered so that one of the initial MI sidelobes overlapped with the normal dispersion region.

2.7 Conclusion

In this chapter we have studied continuous wave supercontinuum generation. After a brief review, we considered the difficulties of numerical modelling of CW fields and attempted to develop a new model for a CW laser pump source. We studied the details of soliton formation from MI and the resulting distribution of soliton energies which leads to the smooth flat spectra associated with CW pumped supercontinua. We then understood the need for soliton collisions to fully account for the experimentally observed spectra. Limitations to the supercontinuum bandwidth were found due to the dispersion and nonlinearity slopes and water peak absorption. The latter was overcome by utilising speciality low water loss fibres, resulting in CW supercontinua with unprecedented bandwidth. We then studied some details relating to the optimal pump bandwidth, the continuum noise and prospects for scaling the pump powers. Further, more detailed, studies on the influ-

ence of pump bandwidth would be interesting along with improvements to the theoretical models. Finally, the possibility of scaling the CW pump power to the 100 W regime is now real and could open up new regimes of supercontinuum generation, perhaps including the generation of wavelengths below 1 μm from a Yb fibre laser, and even into the visible spectral region.

3 Visible supercontinuum generation with picosecond pump pulses in cascaded PCFs

3.1 Introduction

It is possible to generate visible supercontinua simply by pumping a short PCF with a high power, ultra-short laser pulse [Ran00b]. However, few of the the resulting spectra will be particularly flat, and even fewer will have high average spectral power. Moving beyond this simple technique, in what way can we tailor the pulse and fibre properties to engineer desirable features in the supercontinuum? In this chapter, to partially answer this question, we look at the problem of achieving flat and smooth supercontinua across the entire visible spectrum, and doing so with high average spectral power. In particular we look at extending the supercontinua generated by pumping PCFs with a high average power picosecond pump laser at 1.06 μm, across the blue part of the spectrum (0.4 to 0.5 μm).

The outline of this chapter is as follows. First, in Section 3.2 we summarise the literature relevant to this problem. Then, in Section 3.3 we describe the picosecond fibre laser which we use as the pump source in our experiments. In Section 3.4 the experimental setup is described and in Section 3.5 the results achieved when pumping a single PCF are reported. Following this an analysis of the supercontinuum mechanism is reported in Section 3.5.2. The following three sections: 3.6 to 3.8, apply this knowledge to achieve supercontinuum generation with high spectral power into the blue.

3.2 Summary of relevant literature

A broad review of early supercontinuum generation literature was provided in Chapter 1. Here we only consider results which directly pertain to the work of this chapter. In particular, we look at supercontinua, predominantly generated in PCF and pumped around 1.06 μm. It should be noted, however, that the majority of the original supercontinuum

results, and the understanding they provided, were performed by sources outside of these criteria; references to such work are included throughout the chapter where the ideas they developed are directly relevant.

The first use of a practical 1.06 μm source for supercontinuum generation is described in [Che97], where a continuum from 1.0 to beyond 1.75 μm (at the 10 dB level) was reported with an average spectral power of approximately 0.25 mW/nm across the continuum. One unique feature of this source is that the supercontinuum is generated intra-cavity in a Yb fibre laser. Although there is a low spectral power component of this continuum to wavelengths as short as 0.7 μm, no significant spectral power was achieved in the visible spectral range. This can be completely explained by dispersion and phase matching requirements for four wave mixing (FWM) which we will discuss below. Low power and isolated spectral components in the visible did appear and were attributed to second harmonic generation of Raman generated Stokes lines and third harmonic generation of the pump in higher order modes.

Several years passed before a comparable performance was achieved - only after the seminal paper by [Ran00b] did renewed interest in supercontinuum generation occur. Between 2000 and 2003 a large amount of work was published with respect to supercontinuum generation. But only in 2002 was a 1.06 μm source again used. In this case a 7 m length of PCF was pumped with 350 fs pulses to obtain a continuum spanning from 0.4 to 1.7 μm (at 20 dB level) [Pri02a]. Also that year, the same group demonstrated tunable Raman solitons over 1.06 to 1.22 μm [Pri02b], utilising PCFs with anomalous dispersion in this spectral region, to extend the idea first used two decades earlier [GN88b].

In 2003, a high power supercontinuum was also generated from a bulk Nd:glass oscillator pumping a PCF with 10 ps pulses [Sch03]. In that work, supercontinua from 0.5 or 0.64 to 1.8 μm were achieved, depending on the fibre used, with an output power of 5 W. The supercontinua also exhibited excellent flatness. One particular insight from this work was that picosecond pumping produced a flatter continuum, which extended further, than femtosecond pumping in the same fibre. In this case second harmonic generation was also observed to generate isolated frequencies in the visible. Also in 2003, the use of a 10 ps Nd:YVO_4 laser to pump a PCF resulted in a 2.4 W continuum from 0.7 to 1.6 μm [See03].

In 2004 a 0.6 ns Q-switched Nd:YAG laser was used to pump a wide variety of PCFs [Wad04]. A thorough investigation of the interplay between MI and FWM was performed and by choosing the correct fibre either strong direct FWM was achieved (when pumping in the normal dispersion region) producing an anti-Stokes line at 0.7 μm or a supercontinuum (when pumping in the anomalous region) spanning from 0.5 to beyond 1.75 μm. The continuum was again very smooth compared to that produced with femtosecond

pump sources, however, in this case, the spectral power was very low with a total continuum power of less than a few tens of milliWatts. A dual pump scheme was also reported, where a 1.06 μm pump and its second harmonic were used to generate a white-light supercontinuum [Cha04].

In 2005, the same year that the work constituting this chapter was performed, a large number of results were reported. In [Rul05] a supercontinuum spanning from 0.52 to beyond 1.75 μm with an average spectral power of over 1 mW/nm was reported. This result formed the starting point for the work in this chapter. The experimental setup consisted of an all-fibre picosecond laser (described in detail in the next section) which produced up to 8 W average power. In the setup described, a 1.5 W continuum was produced in 60 m of PCF. Other results from 2005 include [Tei05b; Tei05a] which utilised a diode-pumped Nd:YVO_4 picosecond laser or semiconductor saturable absorber mode-locked Yb:glass oscillator to pump tapered conventional optical fibre. The use of tapered conventional fibre had previously been reported with femtosecond pump sources [Bir00]. The resulting supercontinua extended down to just below 0.5 μm but only at the 20 dB level.

Results that have been reported since the work in this chapter was completed include [Tom05] where the use of higher order modes to generate a continuum extending below 0.4 μm was reported. Apart from the entire visible spectrum being 10 dB down from the infra-red spectrum, the visible spectral region was exceptionally flat, but the spectral power was very low and the output limited to higher order modes. In [Rus05] a continuum spanning from 0.65 to 1.75 μm with 1.5 W average power was achieved by compressing amplified 3 ps pulses to 0.4 ps with a grating pair. Interestingly, the uncompressed pulses produced a similar supercontinuum in the same PCF, it is likely that this is because the pulses exiting from the amplifier are positively chirped and will be compressed by the anomalous dispersion of the PCF. A systematic study of the effect of dispersion profiles on the supercontinuum was reported in [Tse06]. The best achieved spectrum extended as short as 0.6 μm with a low spectral power. In [Roy07] a Yb doped PCF was used to simultaneously amplify the pump pulse while the supercontinuum was forming. The resulting continuum was quite flat and spanned from 0.55 to 0.85 μm with 1.5 W which implies a reasonably high spectral power. The use of different PCF structures has also been considered, in one notable example, secondary cores in a PCF were used for enhanced parametric effects based on birefringent phase matching [Dup07]. In a similar vane, multimode PCF structures have also been used for enhanced FWM, leading to supercontinuum generation down to 0.4 μm, although in a region more than 10 dB below the infra-red continuum [Les07].

Although an impressive number of results were reported, some with very high spectral power, none of the experiments generated significant power shorter than 0.5 μm. It was

the purpose of our work to extend a 1.06 μm pumped continua into the blue spectral region, and to do so with high spectral power. The technique used to do this was to cascade multiple PCFs. The results were reported in [Tra05b]. Since this report a different approach, also based on cascaded PCFs was developed [Xio06]. These results are also discussed below. Subsequent to this work a new method for generating supercontinua in tapered PCF was developed with outstanding results. This technique was reported in [Kud06], and forms the content of Chapter 4.

3.3 Pump laser

The pump laser used in this chapter was previously developed by colleagues in the Femtosecond Optics Group [Rul05]. It is an all-fibre setup comprising of a passively mode-locked ytterbium fibre ring laser and a low nonlinearity ytterbium fibre amplifier. It was used as a turn-key source of high peak and average power picosecond pulses for supercontinuum generation and no development work of this source was made by the author. However to fully describe the system used in this chapter this section presents a few details about its construction.

The seed source consisted of an isotropic-fibre loop containing an inline ytterbium fibre amplifier, fibre isolator, two polarisation controllers with a fibre polariser between them and two fused fibre couplers, one for pump input and one as an output coupler. The loop was ~ 3 m long. Passive mode-locking is achieved through nonlinear polarisation evolution with the fibre polariser acting as the discriminating element. The output of the loop was chirped, but by filtering the resulting seed sources had a small RMS time-bandwidth product of 0.66 and a duration of 2.2 ps. The repetition rate was 51 MHz. The seed pulses were amplified through a 1 m long pre-amplifier followed by a 1.5 m large mode area cladding-pumped amplifier. The resulting amplified pulses were approximately 3.3 ps long although measurements at high power were not possible due to the excessive spectral bandwidth which was greater than 40 nm.The amplified peak power was ~ 30 kW from an average power of 8 W. The high average power of this source was one of the key technologies used to achieve the results reported in this chapter as it enabled the generation of very high spectral power supercontinua.

For the modelling of the supercontinuum process we approximated our pump laser as follows. We modelled the seed laser as a bandwidth limited Gaussian shaped pulse with 2.2 ps duration and additional quantum shot noise. We then propagated this field through a system corresponding to the actual amplifier stages. The gain of the fibre amplifier was chosen to amplify the seed pulses to the measured average power. The amplifier stage nonlinearity was estimated as 2 $W^{-1}km^{-1}$ and the dispersion was estimated to be -25 ps

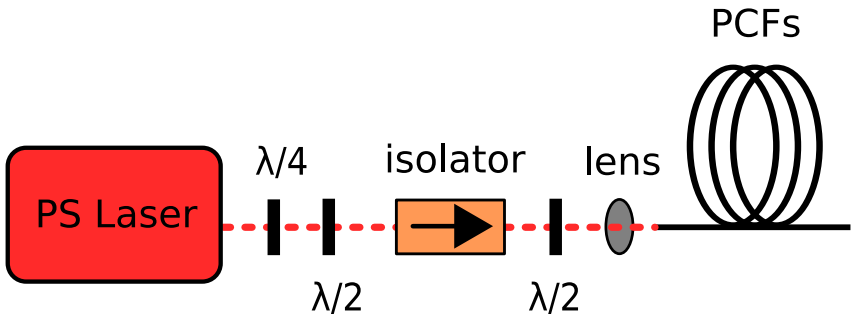


Figure 3.1: Experimental setup for supercontinuum experiments.

$nm^{-1}km^{-1}$ with a dispersion slope of -0.25 ps $nm^{-1}km^{-1}$. In this way, the modelled pump field contained a similar spectrum and nonlinear chirp (broadened by SPM in the final amplifier stages) as the actual pump laser.

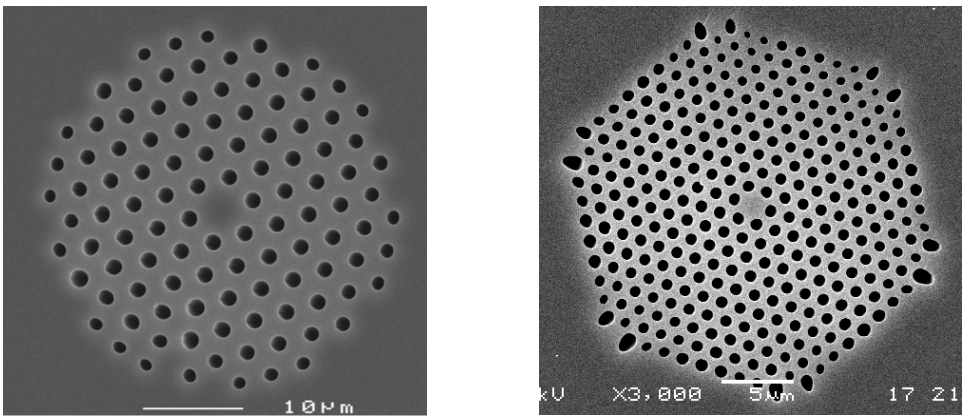
3.4 Experimental setup

The experimental setup for pumping the PCFs is shown in Fig. 3.1. The collimated laser output is passed through a quarter and half wave-plate for polarisation control before passing through a polarisation sensitive isolator. The isolator is required because small back reflections from the cleaved fibre end and splices (when multiple PCFs are used) are strongly amplified in the final stage of the laser amplifier and can cause damage to the laser. The polarisation of the isolated beam is then rotated by a second half wave-plate before being focused into the PCF. Typically 50 to 60% coupling was achieved. The output of the PCF was then measured with a spectrum analyser and thermal power meter.

The polarisation state emitted by the laser changes with output power due to nonlinear polarisation rotation. Therefore at each amplifier current setting, the wave-plates were adjusted to maximise the power incident on the PCF. The final waveplate was then adjusted to maximise the spectral bandwidth of the supercontinuum produced, which showed a small dependence on polarisation for most PCFs used.

3.5 Supercontinuum generation in HF1040

As discussed in Section 3.2 the starting point for this work was a supercontinuum produced by pumping a PCF with a very similar laser as used here. The PCF used was Blaze Photonics SC-5-1040; here it will be called HF1040 as it has a zero dispersion wavelength close 1.04 μm. The structure of this fibre is shown in a scanning electron micrograph (SEM) shown in Fig. 3.2(a). From this figure $\Lambda = 3.36$ μm and $d/\Lambda = 0.47$. These parameters were



(a) HF1040 (b) HF780

Figure 3.2: Scanning electron micrographs of the two most important fibres used in this chapter. Note that the scales are different for the two images. The image of HF1040 is from the Blaze Photonics data sheet, the image of HF780 was taken at Imperial College.

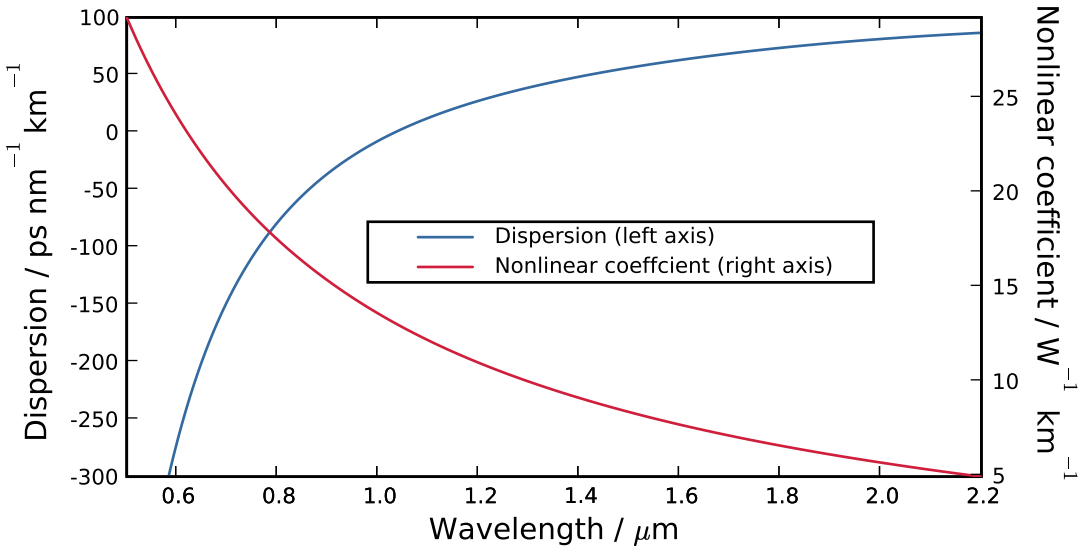


Figure 3.3: ***(numerical)*** Group velocity dispersion and nonlinear coefficient of HF1040.

used with the MPB software (see Section 1.4.1) to calculate the dispersive properties of HF1040. The resulting group velocity dispersion curve is shown in Fig. 3.3 along with the wavelength dependence of the nonlinear coefficient γ. At the pump wavelength of 1.06 μm, the dispersion is 5 ps nm^{-1}km^{-1} and the nonlinearity $\gamma = 13$ W^{-1}km^{-1}. This fibre is suitable for supercontinuum generation with a 1.06 μm pump source due to the

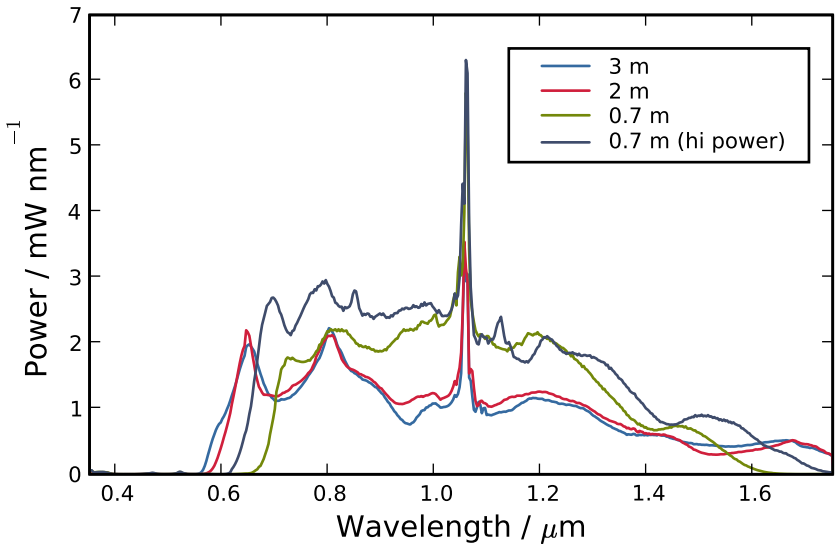


Figure 3.4: ***(experimental)*** Measured spectra at the output of different lengths of HF1040 when pumped at 12.5 kW, except the high power curve which is from 0.7 m of HF1040 pumped with 16 kW.

small anomalous dispersion at the pump wavelength which allows efficient and broad modulation instability to occur. Due to the relatively low air-filling fraction and large core ($\sim 4.9\ \mu$m) it also had a low loss of ~ 2 dB/km at the pump wavelength.

The result described in [Rul05] used up to 65 m of HF1040 to achieve supercontinuum generation down to $\sim 0.52\ \mu$m. In this case the long length was used to extract the widest possible supercontinuum bandwidth with this fibre and pump. The optimal length to use is a balance between nonlinear interaction length and losses, which increase significantly at the short wavelength edge due to scattering. In the work presented in this chapter we use this fibre as a first stage of a multiple fibre approach to supercontinuum generation. Therefore we used much shorter lengths of fibre to achieve higher spectral powers in key wavelength regions between 0.7 and 0.8 μm for reasons described below, rather than trying to obtain the maximum bandwidth. The purpose of the results described in this preliminary section are two-fold. Firstly, the supercontinua achieved are used to pump the secondary PCFs. Secondly, great insight into the supercontinuum generation process is found from these results and was used to design subsequent experiments.

The supercontinuum spectra measured when pumping short lengths of HF1040 with ~ 12 kW peak power pulses are shown in Fig. 3.4. These results are shown on a scale of linear spectral power, and it is clear that with this pump source a very high spectral power of up to 3 mW/nm can be obtained between 0.6 and 1.0 μm. The whole supercontinuum extends from below 0.6 to beyond 1.8 μm. The pump is not completely depleted in these

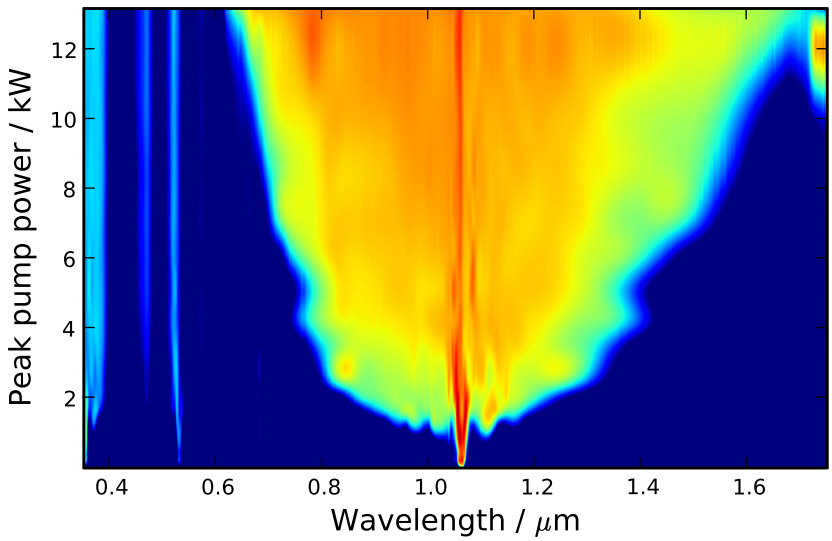


Figure 3.5: ***(experimental)*** Evolution of supercontinuum spectrum with increasing peak pump power in 0.7 of HF1040. Colour scale: −40 0 dBm.

spectra which is a result of the short interaction length. The longer lengths led to broader supercontinua, but at the expense of reducing spectral power in regions closer to the pump. For the shortest length of 0.7 m, the evolution of output spectral power with increasing pump power is shown in Fig. 3.5. Here we see that after an initial spectral broadening suddenly occurring at between 1 and 2 kW pump power, the continuum broadens in proportion to the increasing pump power. Higher level pumping (or using longer lengths) can lead to further broadening (as in [Rul05]), but this is finally limited to the region of 0.5 to 0.6 μm.

The pulse duration measured across the visible spectrum was shorter than 20 ps by measurements with a streak camera; also in [Rul05], the pulse duration at 0.75 μm was found to be 15 ps after several tens of meters of propagation. Therefore we conclude that the pulses do not broaden significantly in the few meters of PCF we have used here.

3.5.1 Supercontinuum mechanism

The following sections cover a detailed analysis of the supercontinuum generation mechanism in HF1040. The aim is to develop design rules to further extend the supercontinuum to the blue.

In Chapter 1 we discussed the two principle supercontinuum generation mechanism; namely soliton fission and dispersive wave dynamics or modulational instability and four wave mixing. By comparing the length scales of these processes we can determine

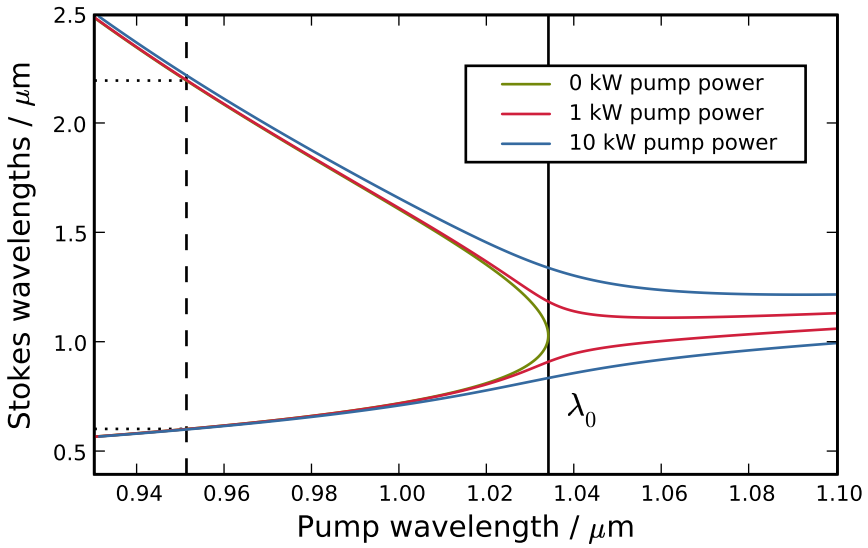


Figure 3.6: ***(numerical)*** Phase matching diagram for pump-degenerate four wave mixing in HF1040 for increasing pump powers. A vertical line from a given pump wavelength crosses the phase matching diagram at two points, from which horizontal lines indicate the Stokes and anti-Stokes phase matched wavelengths. The dashed black lines indicate the shortest phase matched wavelength of 0.6 μm if a long wavelength cut-off of 2.2 μm is assumed. The solid black line indicates the zero dispersion wavelength.

which is dominant in the current situation. From Eqn. 1.32 we find that $L_{MI} < 0.1$ m and from Eqn. 1.31 we find $L_{fiss} = 2.7$ m. Therefore we are firmly within the MI regime. The following subsections deal with the dynamics of modulational instability and four wave mixing, specific to PCFs like HF1040, including the limits to the supercontinuum bandwidth. These physical insights allow us to determine how to further extend the supercontinuum.

3.5.2 Phase matching and gain of MI/FWM

To understand the continuum development in HF1040 as depicted in Fig. 3.5 we have computed the phase-matching diagrams and gain curves for MI and FWM in this fibre. The phase matching diagram is calculated by finding the roots of Eqn. 1.27 under the constraints of Eqn. 1.26, both given in Chapter 1. Fig. 3.6 shows the result for HF1040 when both pump photons are at the same wavelength (pump degenerate). The solid black line indicates the zero dispersion wavelength. The horizontal axis represents the pump wavelength. The figure is read as follows: a vertical line drawn for a given pump wavelength crosses the phase matching curves at two points, the vertical coordinate of

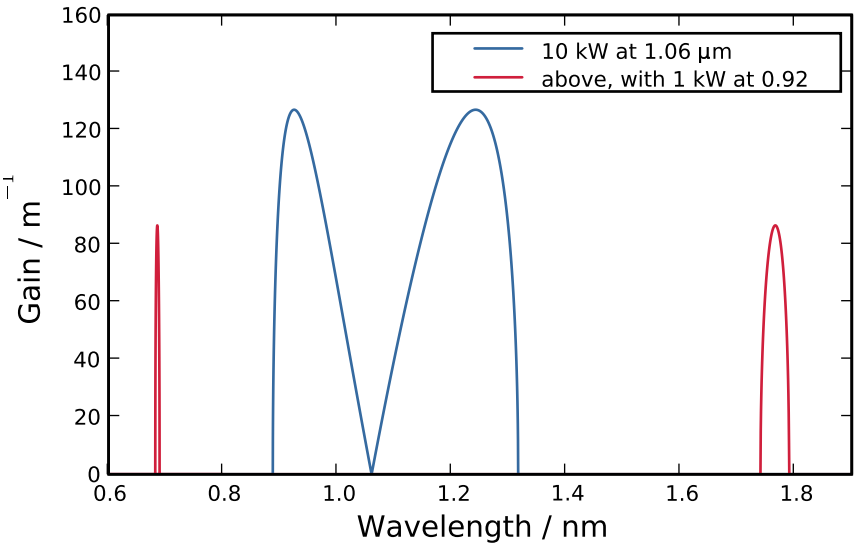


Figure 3.7: ***(numerical)*** FWM gain for two processes. The blue curve is the MI gain for a 10 kW pump at 1.06 μm. The red curve is the gain for a non-pump degenerate FWM process with 10 kW at 1.06 μm and 1 kW at 0.92 μm.

these crossings indicate the Stokes and anti-Stokes wavelengths that phase match for the given pump wavelength. Three curves are drawn for three power levels. At pump wavelengths longer than the zero dispersion wavelength (anomalous dispersion), the phase matching is very strongly power dependent. This is the MI regime. This regime is characterised by relatively small Stokes/anti-Stokes frequency shifts, though for a 10 kW pump, the shift has already extended to 41 THz (anti-Stokes and Stokes wavelengths of 0.92 and 1.24 μm respectively). In the normal dispersion region the phase matched wavelengths are very strongly dependent on the pump frequency, but far less dependent on the pump power; this is due to the dominant contribution of waveguide dispersion to the phase matching curves in this region. Here we see very wide phase matched frequency shifts (for example, the dashed black curve shows phase matching between 0.6 and 2.2 μm, a Stokes shift of 179 THz). Such wide frequency shifts, a unique property of the very strong waveguide dispersion of PCFs have been used to form broadly tunable parametric devices [Hus02; Che05; And04; Sha02; Har03; Won05; Yul04; Bia03].

Fig. 3.7 shows the gain for two FWM processes. The blue curve is the MI gain for a 10 kW pump at 1.06 μm. From this process there is significant gain over a very broad bandwidth (over 80 THz). The peak anti-Stokes gain is at 0.92 μm, which is in the normal dispersion region, and can thus seed conventional FWM processes. If the signal builds up here appreciably, then a second FWM process can occur with one pump photon at 0.92 μm and one at the original pump wavelength of 1.06 μm (note that this is not a pump

degenerate process) The red curve shows the gain for this process. The anti-Stokes and Stokes components of this process are at 0.68 and 1.76 μm respectively. Given the broad bandwidth of the MI gain, a large number of these secondary FWM processes will occur, and because of the large frequency shifts associated with them, and the fact that they will all be at slightly different wavelengths, a broad and smooth supercontinuum can form. The dynamics of this generation process are analysed with the help of numerical simulations in Section 3.5.4. First we look at possible limits to the supercontinuum bandwidth, imposed by the limits of this mechanism.

3.5.3 Limits of supercontinuum generation via FWM

What is the bandwidth limit of supercontinua generated by cascaded FWM? Either the full bandwidth allowed by the phase matching curve will be utilised, and therefore no further spectral expansion by this mechanism can occur, or loss will limit the range of frequencies which can be generated. We can understand this later case by analysing the coupled equations which describe the four wave mixing between the pump (E_1, E_2), Stokes (E_s) and anti-Stokes (E_a) field envelopes [Agr01], given in Eqns. 3.1 to 3.4.

$$\partial_z E_1 = -\frac{\alpha_1}{2}E_1 + i\gamma\Big(|E_1|^2 + 2\sum_{k\neq 1}|E_k|^2\Big)E_1 + i\gamma 2E_2^* E_s E_a e^{i\Delta kz} \tag{3.1}$$

$$\partial_z E_2 = -\frac{\alpha_2}{2}E_2 + i\gamma\Big(|E_2|^2 + 2\sum_{k\neq 2}|E_k|^2\Big)E_2 + i\gamma 2E_1^* E_s E_a e^{i\Delta kz} \tag{3.2}$$

$$\partial_z E_s = -\frac{\alpha_s}{2}E_s + i\gamma\Big(|E_s|^2 + 2\sum_{k\neq s}|E_k|^2\Big)E_s + i\gamma 2E_1 E_2 E_a^* e^{-i\Delta kz} \tag{3.3}$$

$$\partial_z E_a = \underbrace{-\frac{\alpha_a}{2}E_a}_{\text{loss}} + \underbrace{i\gamma\Big(|E_a|^2 + 2\sum_{k\neq a}|E_k|^2\Big)E_a}_{\text{SPM and XPM}} + \underbrace{i\gamma 2E_1 E_2 E_s^* e^{-i\Delta kz}}_{\text{FWM}} \tag{3.4}$$

As indicated in Eqn. 3.4, the first term in each equation accounts for loss, the second for the nonlinear phase shift induced by SPM and XPM and the last for an additional phase shift and gain. The most important fact about these equations is that the gain experienced by the anti-Stokes component depends not only on the pump field, but also directly on the Stokes field. This indicates that strong Stokes attenuation limits the growth at the anti-Stokes side of the continuum. If the Stokes component of a particular phase matched pair is strongly attenuated then the anti-Stokes component will not experience significant gain. This is illustrated in Fig. 3.8 which is produced by numerically solving Eqns. 3.1 to 3.4 for some parameters comparable to the second or third step in a cascaded FWM process. Even if significant power is seeded into the anti-Stokes wave, no significant gain is observed if the Stokes attenuation is high. Now the question is how strong can the Stokes attenuation be, and at which wavelength? There are two sources of loss to long

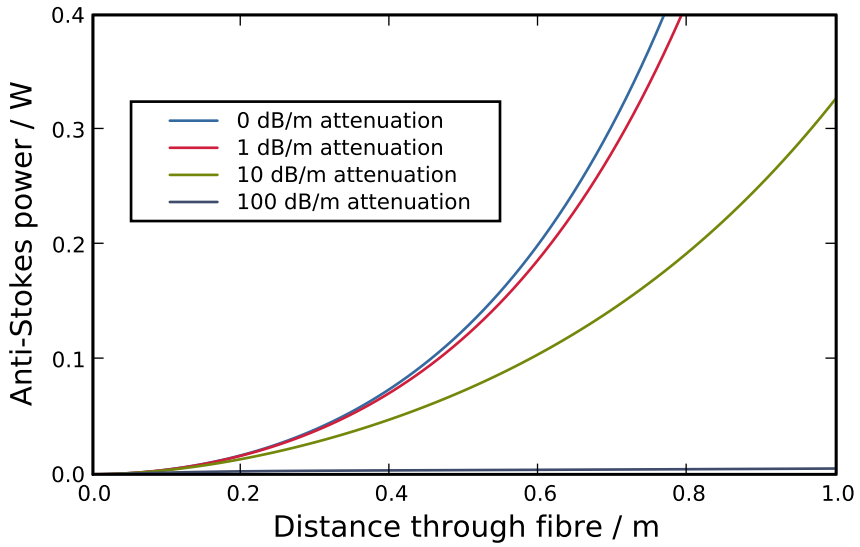


Figure 3.8: ***(numerical)*** Simulated evolution of anti-Stokes power through a fibre in a perfectly phase matched FWM process for different values of attenuation of the Stokes wave. With a pump power of 20 W, anti-Stokes seed power of 0.1 W, no Stokes seed power and nonlinear coefficient of $\gamma = 100\ \mathrm{W^{-1}km^{-1}}$. The attenuation for all waves other than the Stokes was neglected.

wavelengths in PCFs. Waveguide losses can become extremely strong as field confinement decreases, leading to what is known as confinement loss. We analyse this source of loss in Chapter 4, when discussing tapers; using the same techniques we have estimated that for fibres similar to HF1040 the confinement loss is below 1 dB/km for wavelengths shorter than 2.8 μm, therefore it is not relevant here. The other major source of loss is absorption losses, particularly due to water on the air-silica interface. These become particularly significant beyond 2.2 μm. Loss values of well over 100 dB/m are realistic.

Therefore Stokes attenuation will place an upper limit on the supercontinuum bandwidth achievable. For example, considering Fig. 3.6 once again, the dashed black line indicates the pump degenerate FWM process where the Stokes wavelength is at 2.2 μm. This process phase matches with an anti-Stokes component at 0.6 μm. If the Stokes losses beyond 2.2 μm are prohibitively high, then supercontinuum generation to wavelengths shorter than 0.6 μm will not be possible via FWM. In addition, there is a fundamental limit to the anti-Stokes phase matched wavelength, imposed by the fibre dispersion curve. However, the calculations that we have performed indicate that this limit is not reached up to Stokes wavelengths of 3.0 μm, corresponding to an anti-Stokes wavelength of 0.53 μm. But other mechanisms can push the continuum to shorter wavelengths, in particular cross-phase modulation and soliton effects which will be discussed in the next section.

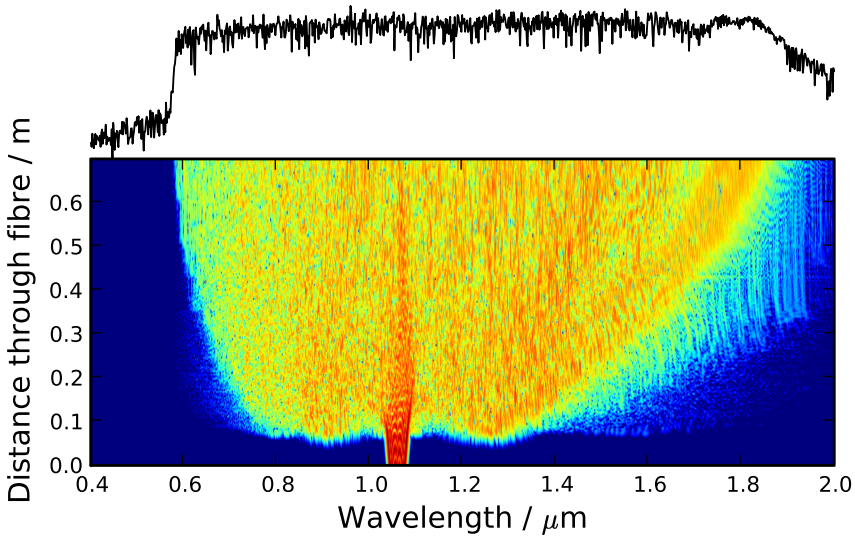


Figure 3.9: ***(numerical)*** Frequency domain results of simulations of 16 kW pulses propagating through 0.7 m of HF1040. Colour scale: −60 0 dB.

Although this analysis is highly simplified, and the process in the actual experiments is likely to be considerably more complicated, the general features of the experimental results in HF1040 are well explained by the ideas discussed above. In particular, the steady expansion of the continuum with increasing power, as shown in the experimental results of Fig. 3.5 fit well within this model. More significantly for the aims of this chapter, the short wavelength limit, understood in terms of Stokes loss and FWM phase matching agrees well with the experimental results.

3.5.4 Simulations of supercontinuum generation in HF1040

The previous sections have given an overview of how MI/FWM has the required characteristics to form supercontinua with our pump and fibre parameters. In this section we look at simulations of the supercontinuum development.

We modelled the pump field as described in Section 3.3, with a reduced power to agree with what was actually coupled into the PCF. The field was then propagated through the 0.7 m of HF1040 using the GNLSE, as described in Section 1.4.4.

Fig. 3.9 shows the simulated spectral evolution for 16 kW pulses propagating through HF1040. The simulations have reproduced the spectral extent and flatness of the experiments remarkably well, given the complexities of the pump pulses. The speckled nature of the spectral density is due to the single shot simulation and would be smoothed out if multiple shots were averaged as is done in a spectrum analyser which has an integration time of around 1 ms. Although these simulations cannot be directly compared to Fig. 3.5

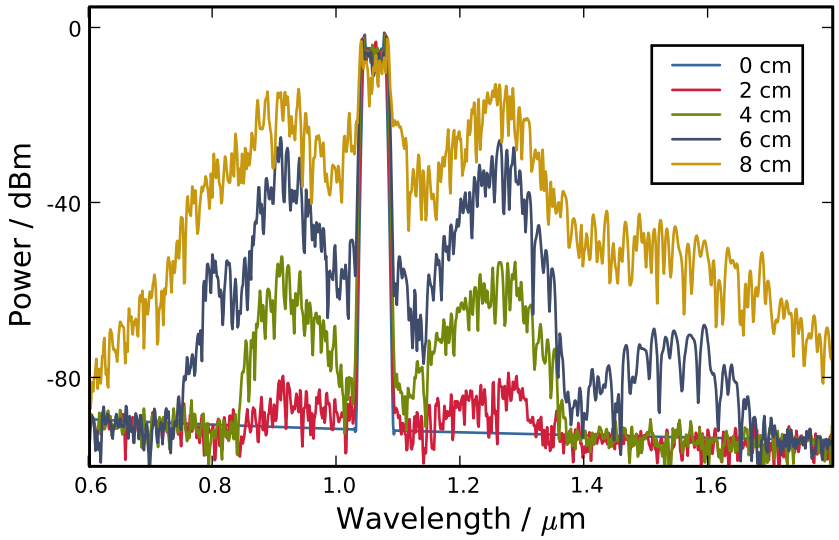


Figure 3.10: ***(numerical)*** The early stages of supercontinuum development in the frequency domain, showing the side lobe development corresponding to the MI gain region. For clarity these data have been smoothed with a 5 nm filter.

which shows the power evolution of the supercontinuum, some correspondence can be observed due to the simplified idea that most nonlinearities respond to a power-length product. The fact that a sudden spectral development followed by a more proportional spectral expansion is observed in both cases adds to the validity of using these results as an aid to understanding the processes involved in the supercontinuum formation.

To that end we now look at the early spectral evolution in the simulations. Fig. 3.10 shows the simulated spectra in the first few centimetres of fibre. Here the MI side-lobes are very clear and correspond well to the MI gain curve shown in Fig. 3.7. After only 8 cm of propagation, the MI side-bands are beginning to reach the same order of magnitude as the pump. Once again, it should be noted that these are single shot spectra.

After about 10 cm of propagation, when the MI sidebands are approximately equal in magnitude as the pump, the input pump pulse in the time domain breaks up into ultrashort sub-pulses. Fig. 3.11 shows a perspective plot of this process. The input peak power was 16 kW. After 15 cm, the peak pulse powers of the sub-pulses formed through MI have exceeded 90 kW. The increased peak power significantly aids the FWM process through higher gain, this is why after the MI formation the FWM based expansion is so explosive. On a more subtle level, the individual fundamental solitons collide with each other - as we discussed in the case of CW supercontinuum generation in Chapter 2. The result of soliton collisions is to transfer energy from the soliton with lowest energy, to the other through inter-pulse Raman scattering [Chi89; Isl89a; Isl89b]. This leads to a compression of the high energy soliton. As the duration of these dominating solitons

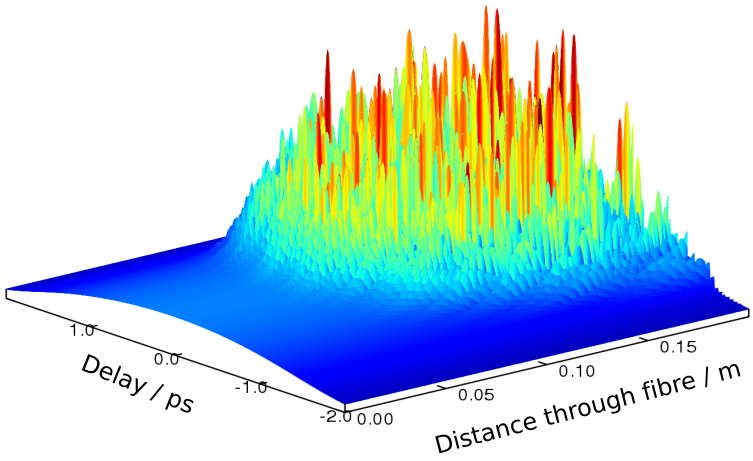


Figure 3.11: ***(numerical)*** The early stages of supercontinuum development in the time domain, showing the breakup of the input pulse into very short and high peak power solitons.

decreases, their spectra broaden, leading to a more efficient intra-pulse Raman scattering. Thus the high-power solitons that form walk to longer wavelengths, and are delayed (through decreasing group velocity at these wavelengths). This process leads to further collisions. The combined result is that several very high energy solitons form out of the original pulse break up. These are very short and have very high power and push the continuum expansion to longer wavelengths through intra-pulse Raman scattering than the pure FWM process would do. Fig. 3.12 shows a plot of the time domain over the whole 0.7 m length of HF1040. After the initial break up has occurred, the curving lines of the high energy solitons can be observed where they collide and shift to longer wavelengths and are further delayed. After 0.3 m of propagation the strongest of these solitons have completely walked off from the original pump pulse.

Apart from pushing the long wavelength edge of the continuum, these solitons can also play a role in extending the short wavelength edge. This can be through several processes mediated by XPM or FWM. To understand these processes we look at spectrograms of the field as it propagates along the fibre. Fig. 3.13 shows spectrograms at 6 locations through the fibre. Fig. 3.13(a) shows the initial pump spectrogram. Here, the SPM caused nonlinear chirp is evident across the pulse. After 0.07 m of propagation, the MI sidelobes appear on either side of the pulse in the frequency axis (Fig. 3.13(b)). After just 0.2 m of propagation the explosive FWM growth is seen, but no significant temporal delay is observed. However, careful examination of Fig. 3.13(c) shows the field splitting in the

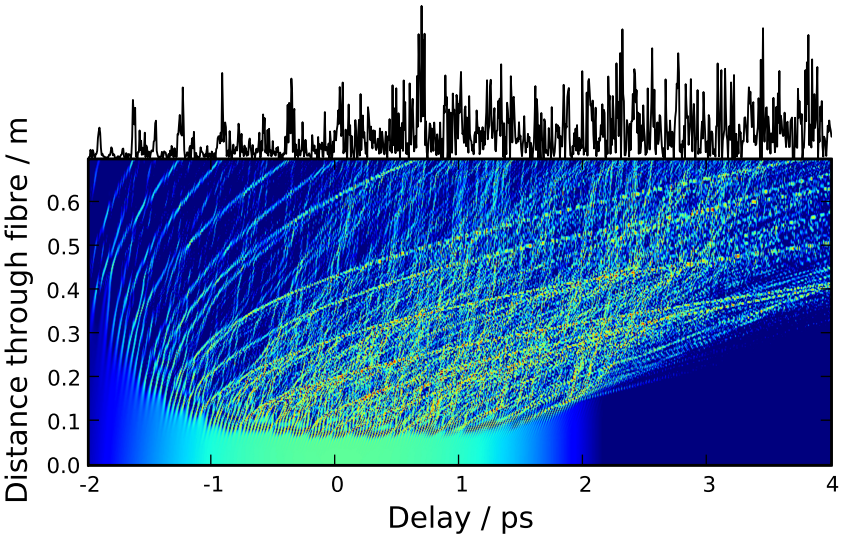
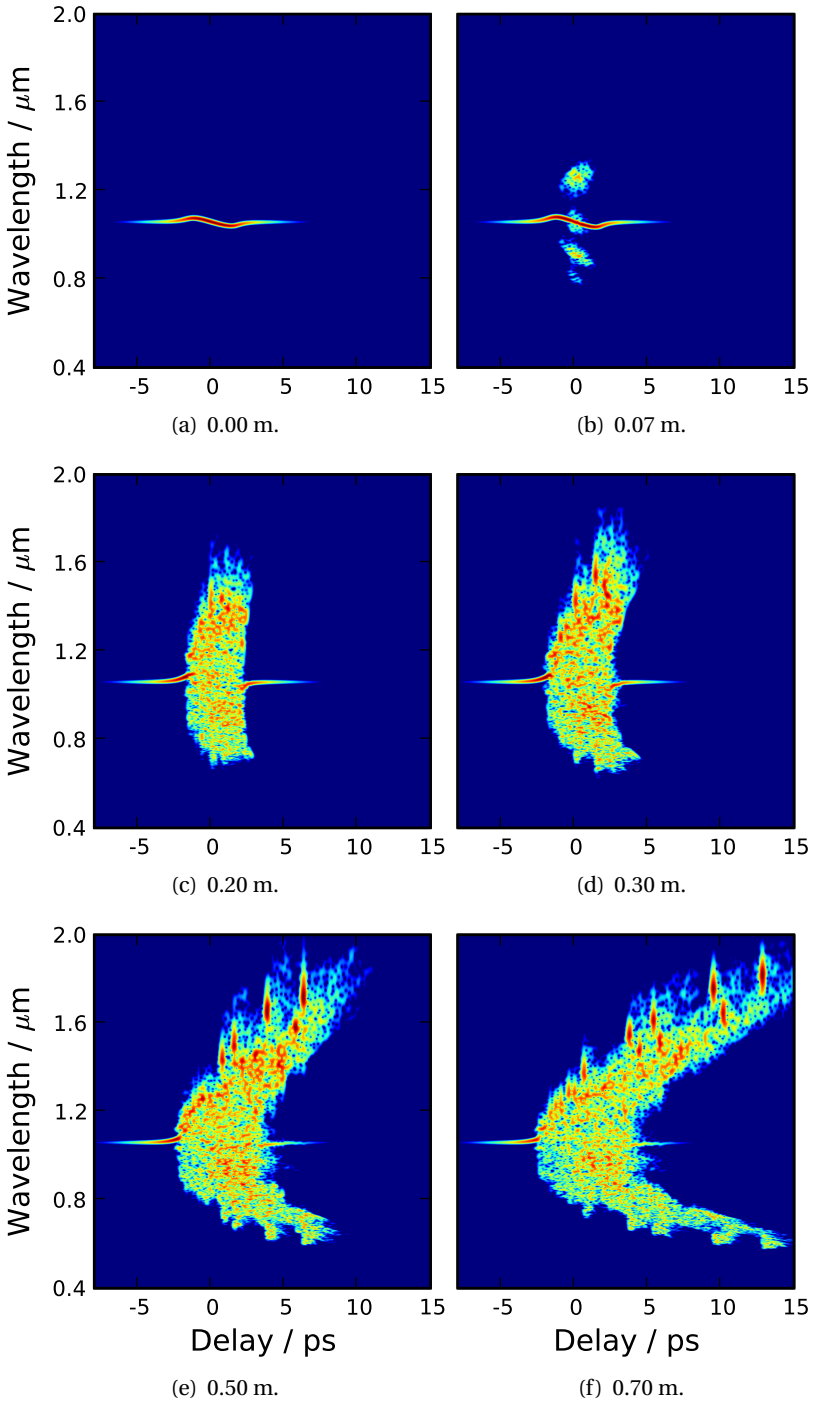


Figure 3.12: ***(numerical)*** Time domain results of simulations of 16 kW pulses propagating through 0.7 m of HF1040. Colour scale: −16 0 dB.

time-axis. In the following frame (Fig. 3.13(d)), several high power solitons can be seen on the long wavelength edge of the pulse and they are beginning to walk off due to group velocity delay (these are clearly evident as the intense, red ellipses). The whole continuum is now shaped as an arc in the time domain due to the changing group velocity across the spectrum. Fig. 3.13(e) shows the spectrogram after 0.5 m. Here the solitons are clearly visible and are significantly delayed. It also becomes clear that a coupling of these solitons to localised parts of the short wavelength edge of the supercontinuum is occurring. These features have been understood as trapping of dispersive radiation by the intense solitons through FWM [Gor06; Skr05], or spectral broadening through XPM [Gen04a]. The effect of these processes is to push the short wavelength edge of the continuum to shorter wavelengths than achievable purely through quasi-CW FWM. We analyse these processes in greater detail in Chapter 4 where they play a more dominant role.

3.6 Pumping fibres with shorter zero dispersion wavelengths

Our analysis in the previous section determined that the blue edge of the supercontinuum was limited by the Stokes losses on the red edge. An obvious first step to overcome this problem is to use fibres where phase matching of the blue spectral components is achieved with shorter Stokes wavelengths, so that the Stokes loss is not so high. Fibres with such characteristics are easily designed, they simply need a shorter zero dispersion



(a) 0.00 m. (b) 0.07 m.

(c) 0.20 m. (d) 0.30 m.

(e) 0.50 m. (f) 0.70 m.

Figure 3.13: ***(numerical)*** Spectrograms of the picosecond pumped field as it develops through HF1040. Colour scale: −40 0 dB.

wavelength. Fig. 3.14 shows the phase matching curve for one such fibre. This fibre has a zero dispersion wavelength around 0.81 μm and we call it HF810. It has parameters $d/\Lambda =$

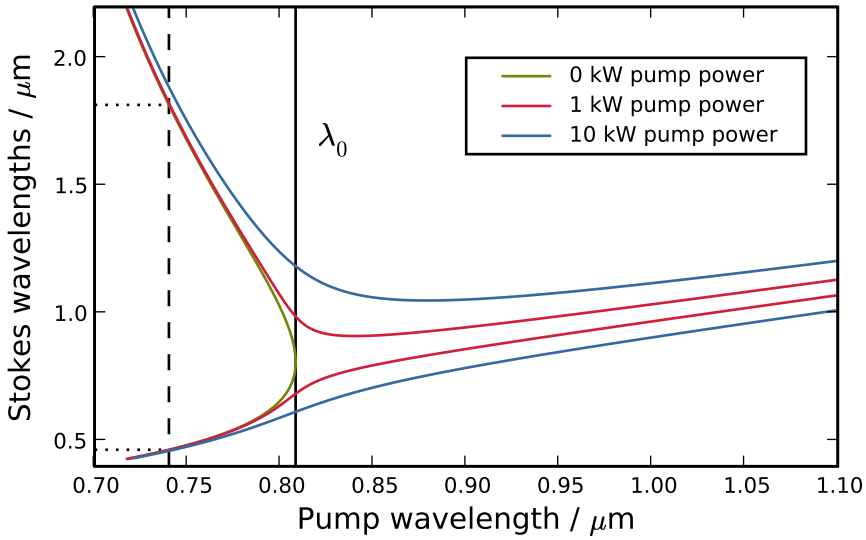


Figure 3.14: ***(numerical)*** Phase matching diagram for pump-degenerate four wave mixing in HF810 for increasing pump powers. A vertical line from a given pump wavelength crosses the phase matching diagram at two points, from which horizontal lines indicate the Stokes and anti-Stokes phase matched wavelengths. The dashed black line indicates the process pumped at 0.74 μm, which phase matches with 1.82 and 0.46 μm.

0.97 and $\Lambda = 4.3$ μm. In this fibre an anti-Stokes wavelength in the blue at 0.46 μm is phase matched with a Stokes wavelength of 1.82 μm when pumped at 0.74 μm. Thus the required Stokes wavelengths are in a relatively low loss region of the fibre and supercontinuum generation to the blue would be expected.

We pumped three fibres which had promising phase matching curves, with zero dispersion wavelengths at 0.66, 0.78 and 0.81 μm respectively; labelled HF660, HF780 and HF810 (HF660 and HF810 were supplied by Blaze Photonics, HF780 was supplied by Crystal Fibre). The pump conditions were identical to the previous results reported above. Fig. 3.15 shows the results achieved at a pump power of approximately 12 kW coupled into the fibres. It is clear that no significant up-conversion to wavelengths shorter than the pump is achieved, while significant power is shifted to longer wavelengths. Although water loss at 1.38 μm curtails the development of the continuum in HF660. The reason for the lack of up-conversion can be understood from the MI side-band locations of these fibres. Referring back to Fig. 3.14, for 10 kW at 1.06 μm, the MI sidelobes are located at 0.97 and 1.17 μm. Thus there is no significant transfer of power to wavelengths shorter than the zero dispersion wavelength of these fibres from a 1.06 μm pump source. Instead, the efficient MI breaks the pulse up into ultrashort solitons, as described before, and these

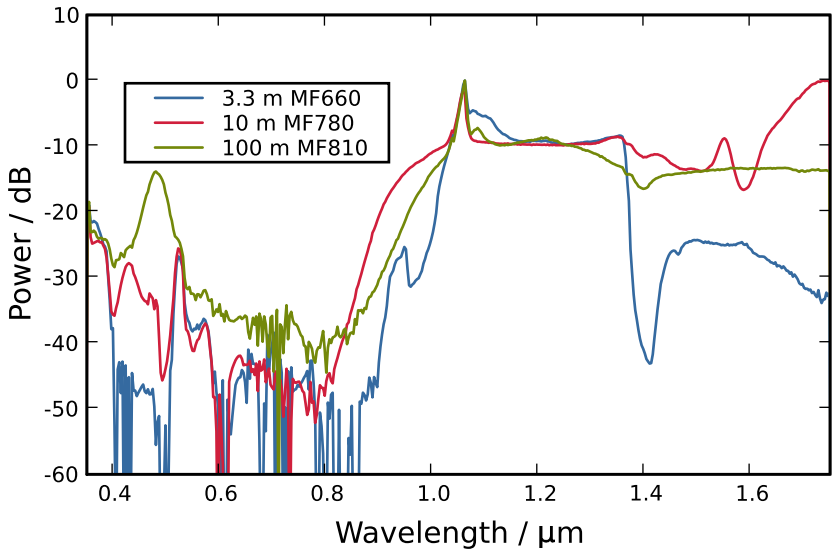


Figure 3.15: ***(experimental)*** Spectrum measured after directly pumping PCFs with shorter zero dispersion wavelengths than HF1040 with the picosecond laser source at ~12 kW pump power.

shift to longer wavelengths through intra-pulse Raman scattering.

3.7 Supercontinuum generation in cascaded PCFs

From the above analysis we knew that HF780 or HF810 should generate a blue supercontinuum if pumped in the correct region of normal dispersion. However, as discussed earlier, we are using a fibre laser at 1.06 μm for the high spectral power it can provide. Noting that the supercontinuum in HF1040 acted to efficiently up-convert our pump laser to wavelengths as short as 0.6 μm, we developed the technique of pumping the second fibre, HF780 with the continuum generated in the first fibre HF1040. Due to the high spectral power between 0.6 and 0.9 μm from the first fibre we expected the cascaded FWM process to continue in the second fibre.

The use of cascaded fibres had previously been reported, but with considerably different aims and outcomes. In [Hor04], cascading was used in a continuum dominated by soliton dynamics (100 fs pump pulses) to obtain a smooth continuum due to the different soliton propagation characteristics in the different fibres. Another report [Nis02b] used hollow capillaries of 300 μm diameter. The technique was based on bulk compression between gas filled capillaries to get larger spectral broadening of 25 fs pulses. In contrast, we use multiple fibres to extend rather than smooth the continuum, and in a very different propagation regime dominated by FWM. Our technique is similar in spirit to the use of

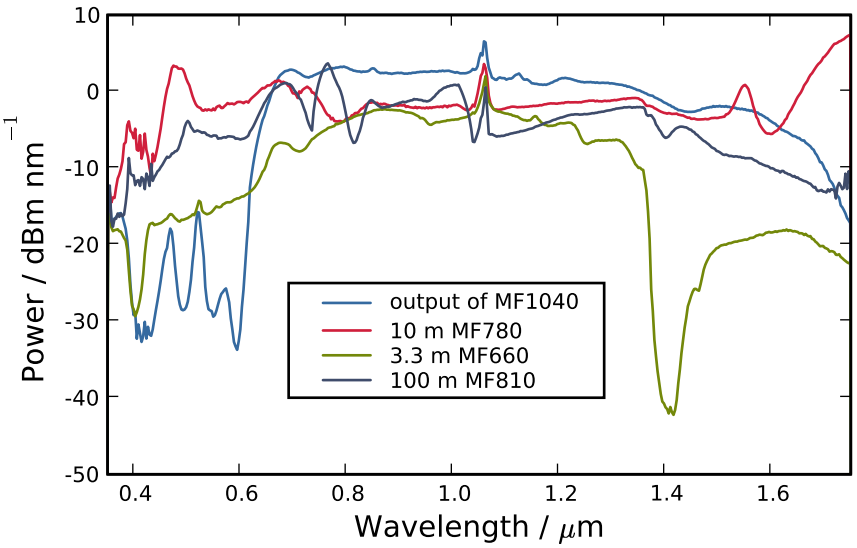


Figure 3.16: ***(experimental)*** Spectrum measured at the output of HF660 and HF810 and HF780 when pumped in the cascaded fibre setup. The pump power to the 0.7 of HF1040 was ~12 kW.

tapered conventional fibres or PCF such as those reported in [Tei05a; Tei05b; Bir00; Lu05], but we have a greater flexibility in fibre length and quality.

Our experimental setup for these experiments was identical to that used above, except the second PCF was spliced directly to HF1040. We discussed in Chapter 1 the difficulties of splicing between PCF. The technique we used, with intermediate mode-field matching fibres resulted in splice losses from HF1040 to our secondary fibres of between 1.0 and 1.8 dB.

The results for pumping HF660, HF810 and HF780 with the output of HF1040 are shown in Fig. 3.16. In all cases we have achieved a continuum which extends below 0.45 μm, which is well across the blue spectral region, in stark contrast to the results in Fig. 3.15. Compared to many previous reports of supercontinuum generation these spectra exhibit remarkable spectral width and relative flatness. However, for HF660 and HF810 the spectral flatness is still only 20 dB, a factor of 100 on a linear scale. This would not be useful for many applications, in addition, the resulting spectral power was quite small, caused both by the roll-off in efficiency of the supercontinuum and losses in the fibres. In contrast, the results with HF780 are considerably smoother, although there is a cut-off on the short wavelength edge around 0.44 μm. In the next section we will find that this is due to the second zero dispersion wavelength in this PCF, which is at 1.56 μm. In fact, evidence of this second zero dispersion point can be seen in Fig. 3.16 where there is a peak in spectral power just before this wavelength, followed by a small dip in the

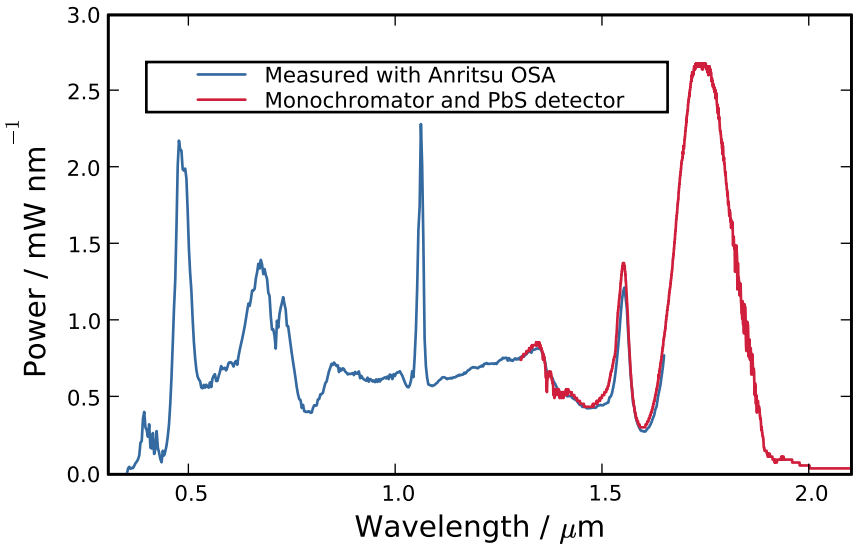


Figure 3.17: ***(experimental)*** Linear spectral power at the output of 10 m of HF780 in the cascaded fibre setup. The blue curve was measured with an Anritsu OSA, the red curve with a grating spectrometer and PbS detector.

spectrum. The peak is due to the gathering of solitons that cannot shift further due lack of anomalous dispersion beyond this point. Beyond the second zero dispersion wavelength, there is another large peak in spectral power due to the dispersive waves formed from the solitons hitting the second zero dispersion wavelength. These features are clearer on a plot of linear spectral power as shown in Fig. 3.17. The first point to note is that even on a linear scale the continuum is reasonably flat; there is considerable spectral power across the whole range between 0.45 and 1.95 μm. In particular there is over 0.5 mW/nm across the visible region with a strong peak of over 2 mW/nm in the blue. As we just noted, on the long wavelength edge there is a very strong peak at 1.74 μm, formed after the second zero dispersion wavelength. These long wavelength measurements were made with a spectrograph and a PbS detector.

Fig. 3.18 shows the evolution of spectral power as the pump power into the cascaded setup with HF780 is increased. We see that the long wavelength edge develops almost immediately as the power increases. The short wavelengths develop only after the long wavelength region is established.

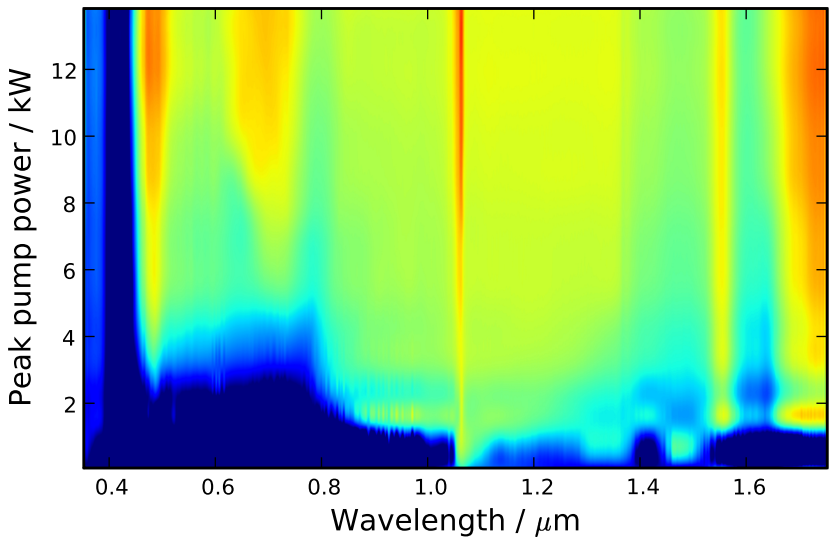


Figure 3.18: ***(experimental)*** Evolution of supercontinuum spectrum with increasing peak pump power in 0.7 m of HF1040 spliced to 10 m HF780. Colour scale: −40 0 dBm.

3.8 Further studies of the cascaded supercontinuum generation

3.8.1 Properties of HF780

Before studying the processes in HF780 any further we must consider the fibre dispersion profile and phase-matching curves. Fig. 3.19 shows the group velocity dispersion curve and nonlinearity of HF780. The dispersion zeros are at 0.78 and 1.57 μm. At the pump wavelength of 1.06 μm, the dispersion is 70 ps nm^{-1}km^{-1} and the nonlinearity is 69 W^{-1}km^{-1}. PCFs with two zero dispersion wavelengths have been studied extensively because they have some unique properties [Fro05; Gae02; And04], including closed phase matching curves. It is only with the very tight confinement and strong waveguide dispersion of small core PCFs that a second zero dispersion wavelength is within the transmission region of silica, as we discussed in Section 1.4.1. Fig. 3.20 shows the full phase matching curve for HF780. Due to the two zero dispersion wavelengths, the curve is closed and phase matching is possible in the anomalous dispersion region without the assistance of nonlinear phase shifts. One interesting point arising from the closed phase matching curves, which will also apply to fibres without two zero dispersion wavelengths in the silica transmission window, is that there is an absolute shortest wavelength which will be phase matched via FWM, regardless of arguments relating to attenuation. Fig. 3.21 shows the phase matching curves around the short zero dispersion wavelength of HF780.

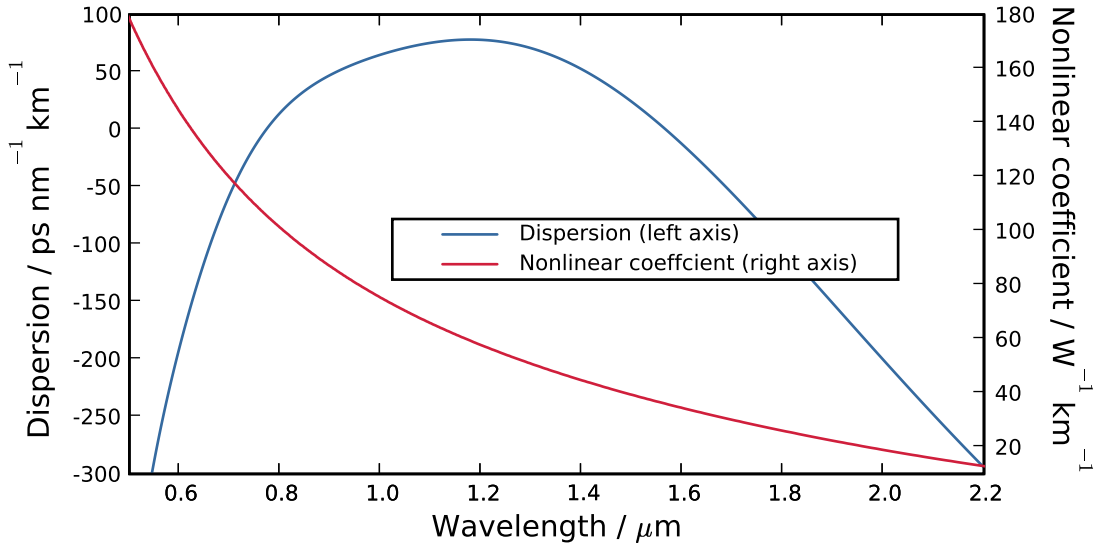


Figure 3.19: ***(numerical)*** Group velocity dispersion and nonlinear coefficient of HF780.

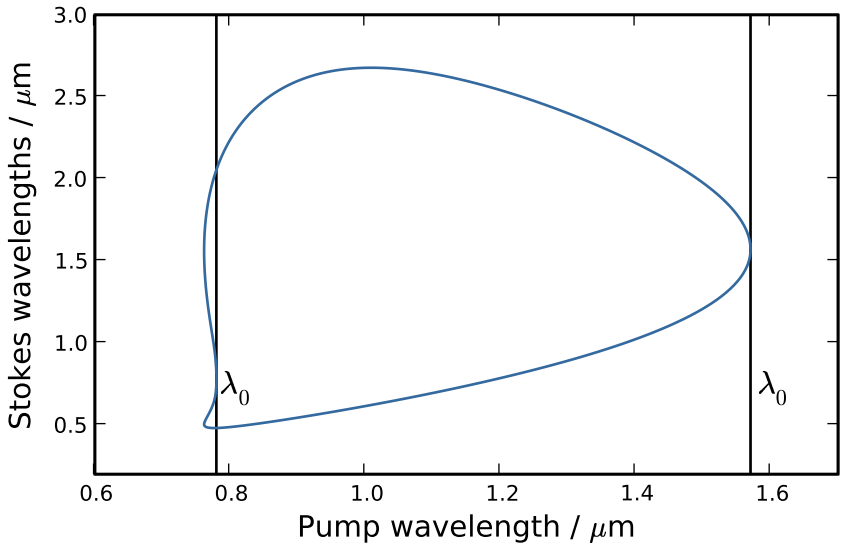


Figure 3.20: ***(numerical)*** Phase matching curve for HF780 with zero pump power.

Using this curve, we can analyse some of the features in the spectra shown in Fig. 3.17. Firstly we note that the blue peak at 0.48 μm is directly phase matched with the peak at 1.74 μm with a pump wavelength of 0.764 μm. The reason that this process is so efficient, above all others, is due to the halting of the soliton shift caused by the second zero disper-

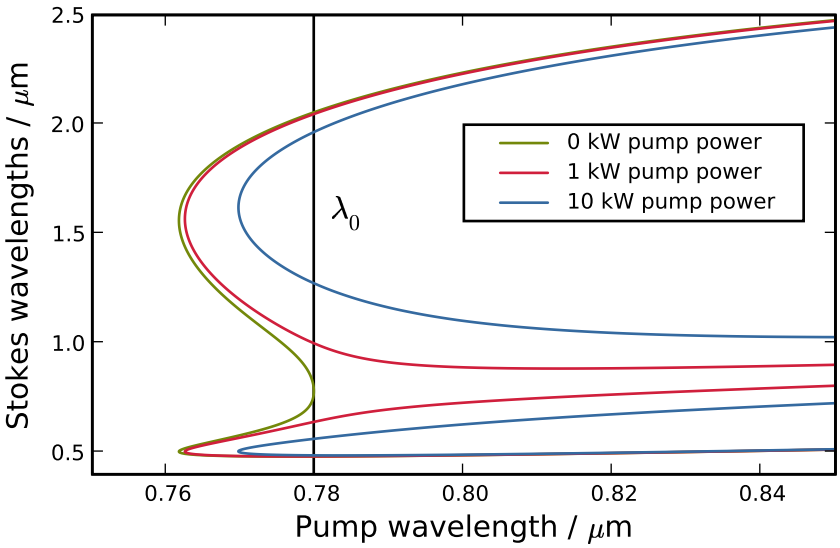


Figure 3.21: ***(numerical)*** Close up of phase matching curve for HF780 showing the region around the short zero dispersion wavelength.

sion wavelength. The interaction of a red-shifting soliton and a second zero dispersion wavelength has been studied extensively [Skr03; Fro05]. It leads to a halting of the soliton red-shift and the generation of a dispersive wave at a fixed resonant wavelength in the normal dispersion region beyond the zero dispersion wavelength. The exact wavelength depends on the fibre dispersion and also on the soliton power. In HF780 the dispersive wave is generated at 1.74 μm. This wavelength region is fixed and the soliton and dispersive wave remain there for further propagation and so it serves as a Stokes source, enhancing the anti-Stokes signal in the blue spectral region.

From Fig. 3.18, it is clear that at low powers (or, approximately equivalently in short fibre lengths at a constant high power), the long wavelength edge is initially formed, including the non-solitonic component around 1.74 μm. After further propagation, the short wavelengths appear suddenly, not gradually as was the case in HF1040. This occurs when the continuum in the first fibre HF1040, has reached the spectral region required for pump wavelengths where FWM phase matching in the second fibre can occur. This is confirmed in Fig. 3.22, where the shorted wavelength in each continuum is plotted against input pump power. At first the continua extend in a similar manner as pump power is increased. However, at around 6 kW of pump power, the continuum from HF1040 reaches wavelengths around 0.78 μm, the region required for FWM to the blue in HF780. At approximately the same power, the blue generation in HF780 occurs, confirming that FWM is a good explanation for this process. We also confirmed that the blue light generated was in the fundamental mode of the fibre by filtering and measuring the far

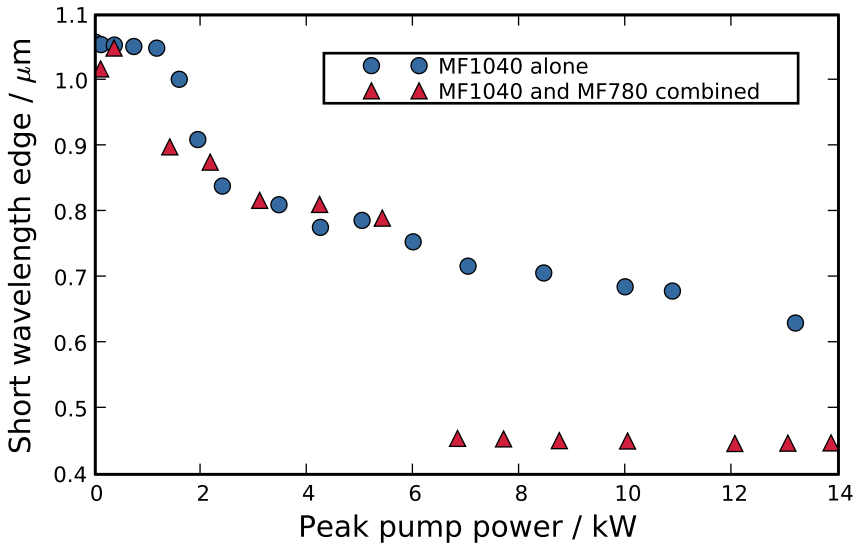


Figure 3.22: ***(experimental)*** Short edge of the supercontinua from 0.7 m of HF1040 (blue circles) and from 0.7 m of HF1040 spliced to 10 m of HF780 (red triangles) with increasing peak pump power.

field pattern, so considering only single-mode FWM processes is valid.

It is worth noting that the intense blue light is a direct result of the second zero dispersion wavelength. If there were no second zero then a smoother continuum would result which may be advantageous. For example, the continuum generated in HF810 (Fig. 3.16) does not have a sharp peak and rolls off smoothly on the blue edge of the spectrum - though it does not have as high spectral power. Alternatively, tailoring of the second zero dispersion point would allow one to selectively enhance certain areas of the visible continuum should this be desired.

3.8.2 Temporal measurements of the cascaded supercontinuum

Apart from spectral power, flatness and extent, another parameter of key interest is pulse duration. Although we were not attempting to generate temporally coherent, or ultrashort supercontinua, the pulse durations at the output are of interest for applications like fluorescence lifetime measurements for example. We measured the temporal duration of filtered pulses from the continuum. The continuum was passed through a grating-based monochromator to filter the light; the spectral bandwidth of the filtered pulses was approximately 4 nm. After the monochromator, the pulses were either measured with a spectrum analyser, or a streak camera.

Fig. 3.23 shows the results of this experiment. It is interesting to note the distinct shape

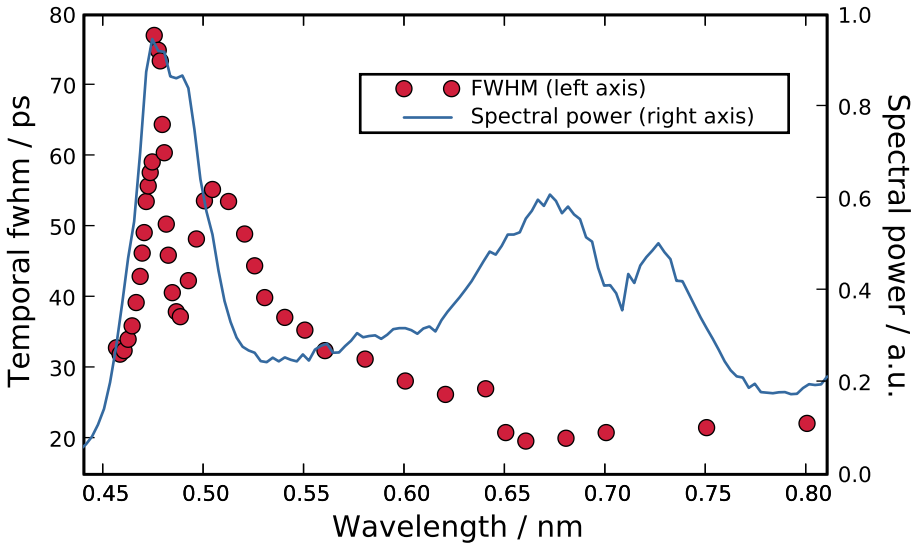


Figure 3.23: ***(experimental)*** FWHM pulse duration measured with a streak camera across the visible spectrum (left axis, red circles), relative spectral power is shown for orientation (right axis, blue line).

of the pulse duration measurements and the fact that it corresponds to certain spectral features. The resolution of the streak camera was 25 ps and for wavelengths longer than 0.8 μm the pulses were shorter in duration than this. This is to be expected, as pulses in the anomalous dispersion region will form solitons and propagate without broadening significantly. The longest pulse duration was 78 ps which is significantly broadened compared to the input pulse duration. This is due to the large dispersion in the blue region of this fibre of over 500 ps nm^{-1}km^{-1} at 0.48 μm. From Fig. 3.18 we can estimate that the continuum forms in a shorter length than the full 10 m we used. If the pulse duration needed to be much shorter, we can shorten the fibre length to mitigate some of the dispersion. The fact that the duration is longest in the region that corresponds to the highest spectral power in the blue is probably due to the fact that these spectral regions form more quickly in the fibre and hence pass through more dispersive fibre before the output. This is confirmed by Fig. 3.24 which shows that the pulse duration at 0.48 μm increases with increasing pump power and we can reasonably expect that at higher peak power the blue spectral region will form earlier in the fibre.

One final point of interest from the streak camera measurements is that of the delay of the pulses. When discussing the spectrograms in Fig. 3.13 we observed the delaying of the long and short edges of the supercontinuum and accounted for it by group velocity delay. To confirm this experimentally we measured the delay against wavelength using the streak camera. Fig. 3.25 shows the results, plotted alongside the group velocity calculated using

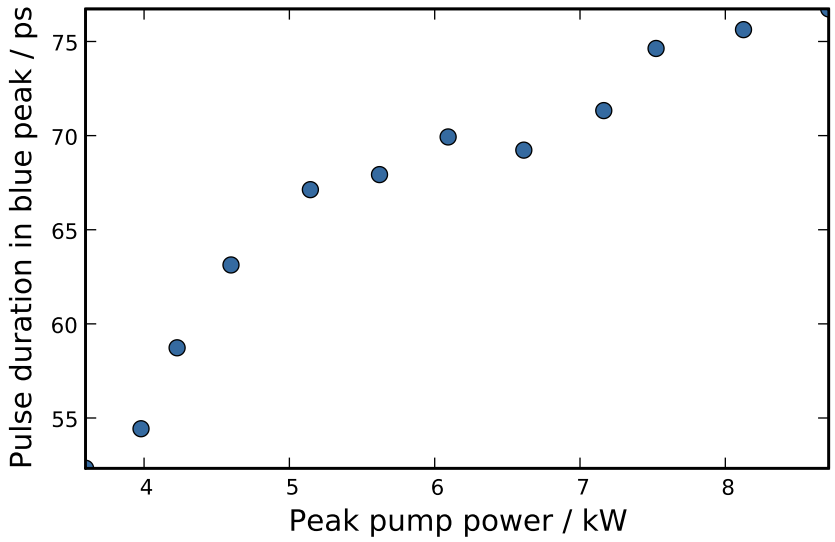


Figure 3.24: ***(experimental)*** Pulse duration at 0.477 μm measured after the monochromator for increasing peak pump powers.

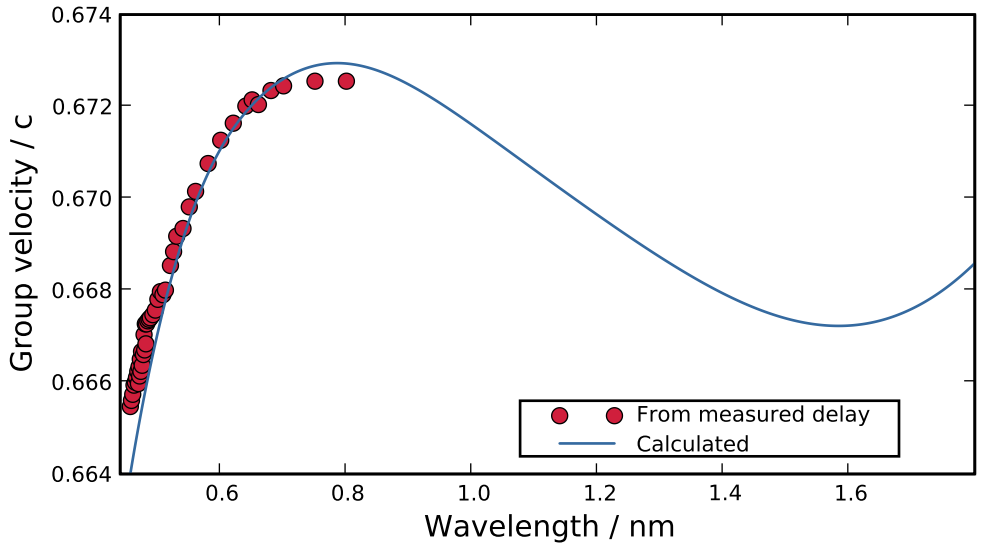


Figure 3.25: Group velocity calculated from streak camera measurements (red circles) and from the calculated propagation constant (blue line), across the visible spectrum.

the MPB software. We see excellent agreement in the measurement region, confirming that linear processes are largely responsible for the delay of different spectral regions of the supercontinuum. From the calculated curve we can also consider group velocity delay between the wavelengths we claim to be active in FWM processes, if the delay is

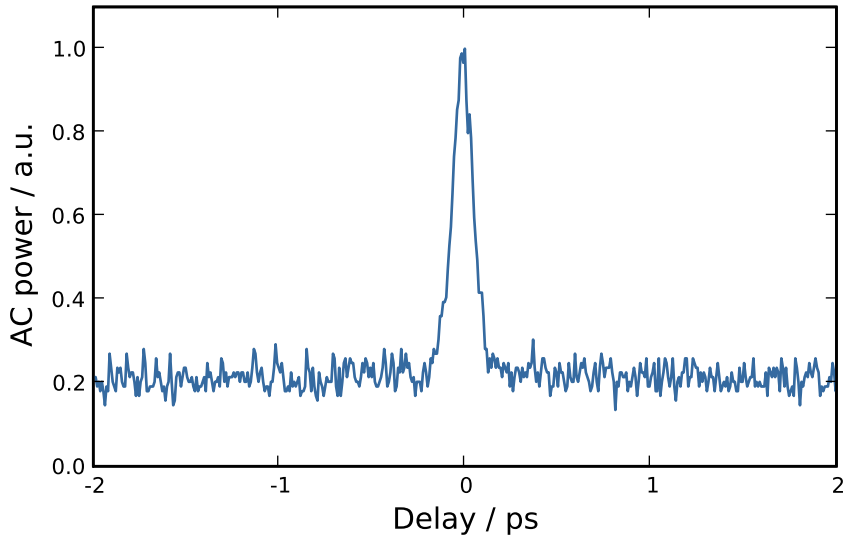


Figure 3.26: ***(experimental)*** Intensity autocorrelation of the continuum around 1.55 μm.

too great then the components will walk off from each other before FWM can occur. We find that the walk off length (the length required for the pulses to walk half-off from each other) for 1.74 and 0.48 μm wavelengths is approximately 0.2 m. This length is easily sufficient for FWM to occur and also indicates that the majority of the 10 m HF780 fibre is not required for the blue generation. Another point of interest is that the wavelength that has exactly the same group velocity delay as the 1.74 μm region is 0.52 μm. This can explain two points. Firstly it explains the second peak in the pulse duration against wavelength curve (around 0.5 μm in Fig. 3.23), this region is matched in group velocity and although efficient conversion does not occur, continuous conversion throughout the fibre can occur. As the 1.74 μm region will be delayed, the generated 0.52 μm will be smeared in the time domain leading to the longer duration of this region. Secondly, it explains the broadening of the blue peak around 0.48 μm. Only the sharpest point is directly phase matched and from the duration measurements can be seen to be generated early in the fibre, but the region just longer than this in wavelength, say 0.49 μm, although not so well phase matched, is matched better in group velocity, so the FWM process has longer to generate the anti-Stokes wavelengths. This leads to the broadening of the blue peak to longer wavelengths. This also agrees with the fact that only the blue edge of the blue peak is long in duration, the red edge of the blue peak is of much shorter duration.

Fig. 3.26 shows an intensity autocorrelation taken at approximately 1.55 μm. This region is anomalously dispersive and hence solitons formed in the initial MI process should exist. Here we see confirmation of this, as after 10 m of propagation the pulse duration is still

less than 100 fs. The high pedestal is due to the non-uniform generation of solitons from pulse to pulse and intra-pulse as they form through MI.

3.9 Recent developments and future enhancements

Since the work described above was carried out, a second approach was developed which also uses a cascaded PCF scheme. In this case the first fibre was designed so that the pump was directly in the normal dispersion regime [Xio06]. In this paper, the pump source was at 1.06 μm but the first fibre had a zero dispersion wavelength of 1.103 μm. This resulted in direct FWM to around 0.742 μm, with relatively little broadening. The 0.742 μm signal was then used to pump a second fibre with a zero at 0.7 μm producing a broad and flat continuum across the visible spectrum. Although in this case the spectral power was not high, using this scheme with the picosecond laser described here, higher powers could be achieved.

However, these results have been completely eclipsed by the development of supercontinuum generation in long tapered PCF. This technique has led to the generation of blue and ultra-violet wavelengths in a very flat supercontinuum with remarkable spectral power. We describe it in detail in the next chapter.

3.10 Conclusion

The use of high average and peak power fibre lasers, with picosecond or nanosecond pulses, to pump PCF allows the development of very high spectral power and spectrally flattened supercontinuum sources. In this chapter we developed a thorough understanding of the visible supercontinuum generation mechanism in the high peak power picosecond pump regime, and using this knowledge developed a method which uses cascaded PCFs to extend 1.06 μm pumped supercontinua to the blue spectral region. The best result spanned from 0.44 to 1.9 μm with 10 dB peak to peak flatness and a total output power of 1.2 W. The idea of changing the fibre parameters in the direction of pulse propagation by cascading PCFs, naturally leads to the idea of PCF tapers, which is discussed in detail in the next chapter.

4 Ultra-violet to mid-infrared supercontinuum generation in tapered PCFs

4.1 Introduction

In this chapter we consider how continuous longitudinal variation of dispersion and nonlinearity along a fibre can be used to further enhance the supercontinuum extent. In the previous chapter we concentrated on the optimisation of dispersion for phase matching of four wave mixing to the blue part of the visible spectrum and achieved this by using two different fibres in a cascade. The work in this chapter was originally inspired by this cascaded approach and was an attempt to make the process continuous in the hope that the efficiency and power transfer would be improved. It was later found that tapered fibres have other more subtle benefits useful for pushing the supercontinuum much further into the UV spectrum than expected from FWM alone.

4.1.1 A review of tapered optical fibres

Tapered fibres add an extra degree of control over both the linear and nonlinear propagation characteristics of a fibre by adding a longitudinal variation of fibre parameters. They were being discussed and analysed as early as 1970 [Sny70]. However their use for controlling propagation characteristics via dispersion and nonlinearity was not discussed until the late 1980s [Taj87]. Subsequent to this a great deal of work went into the design and use of tapered optical fibres, primarily for adiabatic soliton compression, which is the subject of the next chapter.

From the beginning of the work on tapers there have been two techniques to fabricate them – either during manufacture or by post processing the fibre. During manufacture the speed at which the fibre is drawn and other drawing conditions determine the transverse fibre structure; this technique can produce arbitrary long tapers at the expense of loosing control on very short length scales. Subsequent to manufacture, heating of the fibre and stretching can be used to reduce the transverse fibre dimensions; this can be used to

precisely control small tapered regions of fibre. The next two sections briefly review results obtained with these two techniques with a focus on supercontinuum generation.

Post-processed fibre

Heating and stretching fibres to make tapers was first used for mode-matching, fused fibre couplers and other optical components. A detailed model of this tapering process which allows for the design and production of a wide range of taper shapes was given in [Bir92; Ken91]. In [Mar87] it was shown that the fundamental mode was preserved if the tapering process was smooth enough.

Initial use of these short tapers for nonlinear optics utilised the enhanced nonlinearity for SPM [Dum93]. Following this, active devices were made with short tapers by making the evanescent field escaping from the taper waist region overlap with a dye which was used to provide gain [Pen93]. The use of tapered PCF to interface to small core PCF was demonstrated in [Cha01], a particular use of the resulting high dispersion taper was to shift solitons by the self-Raman effect.

For post-processed fibre tapers, PCF has a distinct advantage over normal fibre because it can be manufactured to maintain a stronger outer cladding. With normal fibre, tapered to micron sized cores, the cladding and core of the original fibre become indistinguishable and hence the field is guided purely in the glass, clad by the surrounding air. This makes these devices extremely delicate and sensitive to the environment as a significant fraction of the power is contained in the evanescent field. This feature has been utilised, as noted above, to achieve gain or as environmental sensors. For example, in [Zha04] it was proposed to use tapered fibres passing through carefully selected liquids to tailor the dispersion properties of the fundamental guided mode by carefully selecting the liquid refractive index and taper core size. But this sensitivity to the environment can lead to significant impediment for robust device construction. Post-processed PCF tapers can avoid this if the taper initially has a large air-filling fraction and pressure is maintained during the stretching process. In this case the core can be shrunk while the surrounding silica-air cladding remains intact to provide a protective layer. It should be noted, however, that the dispersive and nonlinear properties are very similar between the two, behaving like a silica strand in air.

The use of tapered standard single mode fibre for supercontinuum generation was actually demonstrated after PCFs had been used [Ran00b], although the technology was available a decade before. In [Bir00; Wad02] a fibre with a short taper transition and very short, 95 mm, waist region was used for continuum generation. In [Wad02] the resulting continuum from a tapered standard fibre is compared to that from a very high air-filled PCF, both with a core diameter of $\sim 2\ \mu$m . They both produced very similar results, a broad

continuum across the visible spectrum, with 200 fs pump pulses at 0.75 to 0.85 μm pump wavelength. Similar tapers were used with 30 fs pump pulses at 1.25 μm [Aki02] generating spectral components into the blue. It should be noted that supercontinuum results with these short tapers are generally achieved with femtosecond scale pulse durations to allow the dispersion lengths to be comparable to the fibre lengths. Longer tapers would be required for picosecond or longer pulse durations. In addition, no deliberate use is made of the transition region, i.e. of the changing fibre conditions. Instead the tapers are used to efficiently pump small core, highly nonlinear fibre, avoiding coupling loss.

In [Har02] tapered standard fibre was used to move the second zero dispersion wavelength to around 1.2 μm and supercontinuum generation was studied around this spectral region. In [Ls04] standard fibres and PCFs were both tapered to sub-micron core diameters. In such structures the nonlinearity is of course very high, but more importantly the dispersion curves are similar to an inverted parabola, i.e. there is a peak value, typically in the visible spectral region around 0.5 to 0.6 μm and the dispersion falls off to either side. Such structures can have interesting phase-matching properties [And04], in particular they allow close phase-matching of processes contained within the visible spectral region, making them interesting for the study of supercontinuum generation. The specific results in [Ls04] lead to a supercontinuum between 0.37 and 0.65 μm. Soon afterwards, tapered microstructured fibres with a sub-wavelength core diameter were used [Fos04]. One important point made in this work is that the effective area of the fundamental mode does not decrease indefinitely with shrinking core size, but will start to expand when the core is much smaller than the wavelength. Thus relentlessly tapering a fibre does not lead to greater nonlinearity. In [Fos04] the optimal taper size for nonlinearity was selected and supercontinuum generation with very low energy pulses achieved. However, the resulting continua were limited by non-optimal dispersion profiles. Care must be taken with tapered fibres as an excessive taper will not be optimal for nonlinear processes to occur. Further work by the same group [Fos05] showed that the effects of waveguide loss due to the large evanescent field significantly alters the supercontinuum spectrum. Following this, [Sum06] showed that a silica strand would effectively stop guiding light when it had a diameter about an order of magnitude smaller than the radiation wavelength.

Refinements to the manufacturing procedure have been made recently. In [Wad05] a technique is described where by pressurising and then heating an existing PCF different air-filling fractions could be obtained; they used this technique to produce a smooth interface from an endlessly single mode fibre to a very small core supercontinuum fibre.

When using extremely short pump pulses, then the changing dispersion in the taper *can* be used to control continuum generation. This was first demonstrated in [Lu05] where dispersion was tailored over millimetre length scales to specifically enhance selected

spectral regions across the visible spectrum. This was achieved by altering the phase-matching conditions for soliton emitted Cherenkov radiation and four wave mixing. On the other hand, [Tei05b] used a single standard fibre with multiple tapered regions to enhance the nonlinear interaction length. This enabled them to use longer pulses (~ 10 ps) to pump the continuum whereas most previous demonstrations had used femtosecond pulses. They did not however, study how using a series of different tapers (with say decreasing core diameter) would enhance the broadening, or utilise the actual changing tapered regions.

Apart from supercontinuum generation, tapered fibres have been investigated in other interesting ways. In [Mäg04] it was studied how the photonic-band gap of a photonic-band gap fibre can be shifted by tapering the PCF structure. In [Ton03] extremely small silica strands were manufactured using a two stage tapering process. Highly uniform 50 nm diameter strands were reported and used to guide light at 0.63 μm. Such small tapers are of no use to supercontinuum generation, but could be very useful in nanophotonic devices or as sensors as they have very large evanescent fields.

Tapers manufactured during fibre drawing

In contrast to the post-processed fibres, fibres tapered at the drawing tower can be as long as the fibre drawing equipment permits – up to tens of kilometres. This allows for slower and more controlled transitions and allows for changing the fibre characteristics as the supercontinuum develops, something only possible with ~10-100 fs pulses with post-processed fibre tapers [Lu05]. This leads to an extra degree of control on the nonlinear processes which can be achieved. The predominant application of such control has been for adiabatic soliton compression which we discuss in detail in the next chapter. But more recently these fibres have been used for supercontinuum generation.

In [Mor97] numerical simulations and experiments showed that by pumping at the central dispersion peak of a double-zero dispersion fibre which is dispersion decreasing, a very flat supercontinuum can be formed. This agreed well with experiments. The mechanism was described as being similar to adiabatic soliton compression where the pulse broadens without acquiring significant chirp. As the dispersion decreases the zero dispersion wavelengths in the fibre move closer together, limiting the region of spectral broadening and thus flattening the spectrum. Work on generating highly stable and coherent supercontinuum has also made use of dispersion decreasing fibre [Tam00; Tam99].

In this chapter we discuss work on using long lengths of tapered PCF fibres manufactured at the drawing tower for efficient supercontinuum generation to the blue/UV wavelengths from a 1.06 μm pump source. At the date of publication [Kud06; Tra06] this

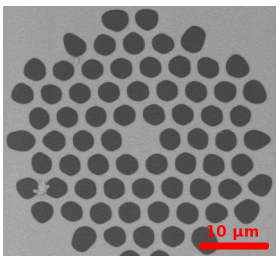


Figure 4.1: Scanning electron micrograph of the input to taper SCT1.

work represented unprecedented spectral power and smoothness for a visible/UV supercontinuum, and tapering PCF at the drawing tower was completely novel – a technique which has subsequently opened new avenues of research.

The work reported in this chapter was done in close collaboration with the Centre for Photonics and Photonic Materials, University of Bath where the PCF tapers were manufactured in response to designs which we proposed. These long lengths of PCF tapers were the first to be manufactured at the drawing tower.

4.2 Manufacturing and taper properties

4.2.1 Manufacturing

Our tapered fibres were drawn directly from a small (3 mm diameter) preform, by adjusting the drawing parameters so as to decrease the outer diameter, while keeping the air-filling fraction in the cladding almost constant. As a result the fibre pitch decreased by the same fraction as the outer diameter, so that the outer diameter measurements acquired during fibre fabrication give an accurate description of the variation of the pitch along the fibre length. We drew a series of tapered fibres, under slightly different drawing conditions.

The detailed taper properties reported here are for the optimal taper for achieving a flat and smooth supercontinuum across the visible spectrum. This taper is labelled SCT1. Several other tapers were produced, providing enhanced UV generation, and results with these are shown in Section 4.3.5. The dispersion and nonlinearity values quoted below are taken from simulations of the fibre structure with the MPB software described in Section 1.4.1.

4.2.2 Properties of the tapers

In this section we review the properties of the tapered PCFs which indicate why such fibre is a good candidate for supercontinuum generation. An SEM image of the input to SCT1 is shown in Fig. 4.1, and Fig. 4.2 shows the variation of pitch of the taper with length. The

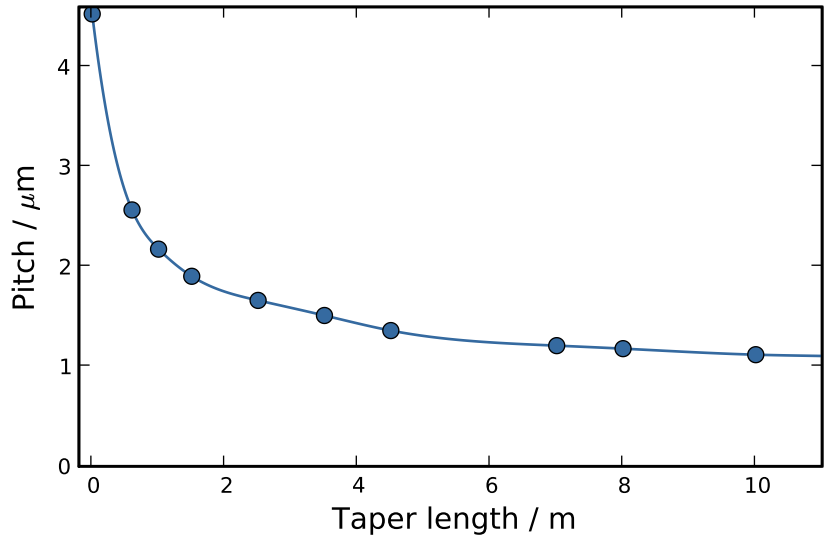


Figure 4.2: ***(experimental)*** The pitch of SCT1 as it changes along the fibre length. Calculated from optical microscope and SEM measurements.

air-filling fraction, parametrised by $d/\Lambda = 0.71$ was constant. The initial change in pitch is quite steep and approximately linear with the fibre length. At the input it is ~ 4.5 μm changing to ~ 2.1 μm at 1 m. At around 0.75-1 m the rate of change of the fibre pitch slows and for further fibre lengths tends towards a constant value of ~ 1.1 μm. The input values correspond quite closely to the fibre HF1040 used as in the initial stage of the cascade in the previous chapter. The second stage of the cascade corresponds to the parameters at a length of approximately 1 m of the taper. These properties show clear advantages over post-processed fibre, which cannot obtain the long transition regions shown here, of over several metres.

In Fig. 4.3 we plot the calculated group velocity dispersion curves of SCT1 at various positions along its length. For the large input pitch at the start of the taper, the zero dispersion is very close to the pump wavelength of 1.06 μm. As the pitch is reduced, the dispersion at the pump wavelength is increased, the zero dispersion wavelength moves shorter and eventually the second zero dispersion wavelength moves into our spectral region of interest. Fig. 4.4 gives a better indication of how the zero dispersion wavelength of the taper decreases with fibre length. It follows the shape of the pitch curve (Fig. 4.2) initially rapidly moving to short wavelengths at the start of the fibre and then levelling off at longer lengths. At 1.5 to 2 m the taper has a zero dispersion which is the same as the second stage of the cascaded fibre setup described in the previous chapter.

The changing dispersion curve directly affects the four wave mixing phase matching curves of the taper. Some examples of the phase matching curves are shown in Fig. 4.5.

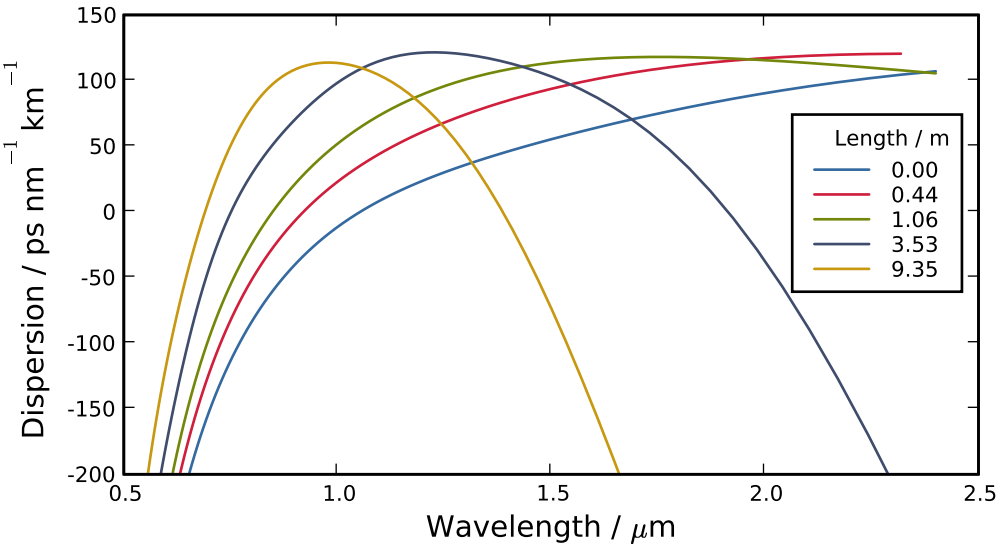


Figure 4.3: ***(numerical)*** The calculated dispersion curves of SCT1 at various lengths through the fibre.

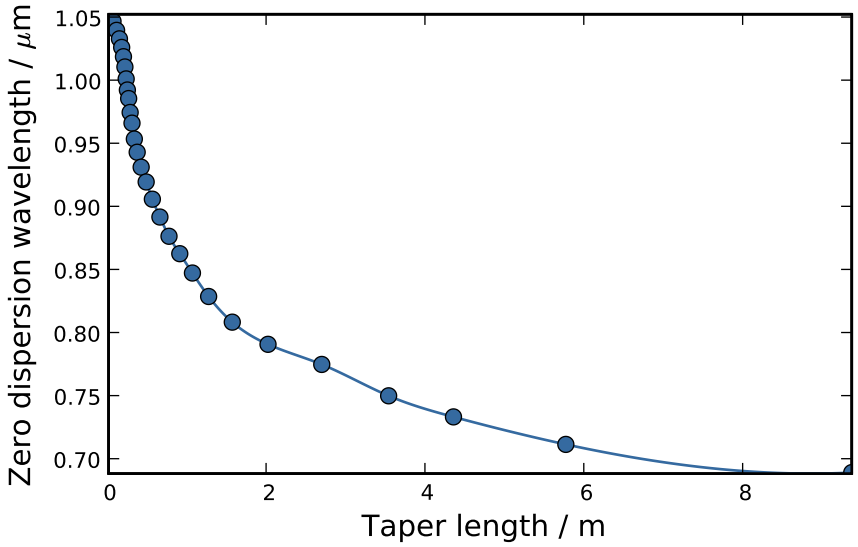


Figure 4.4: ***(numerical)*** The calculated zero dispersion wavelength of SCT1 as it changes along the taper length.

At the input of the taper, the curve is well suited to the initial supercontinuum dynamics. Modulation instability in the low anomalous dispersion will have one sideband generated in the normal dispersion and will then cascade into four wave mixing across a large spectral region from the visible to infrared. As the pulse moves along the taper, however, the phase matching curve changes allowing new four wave mixing processes to occur. At the optimum curve shown (which is after 1 m of taper, this optimum is found from the best

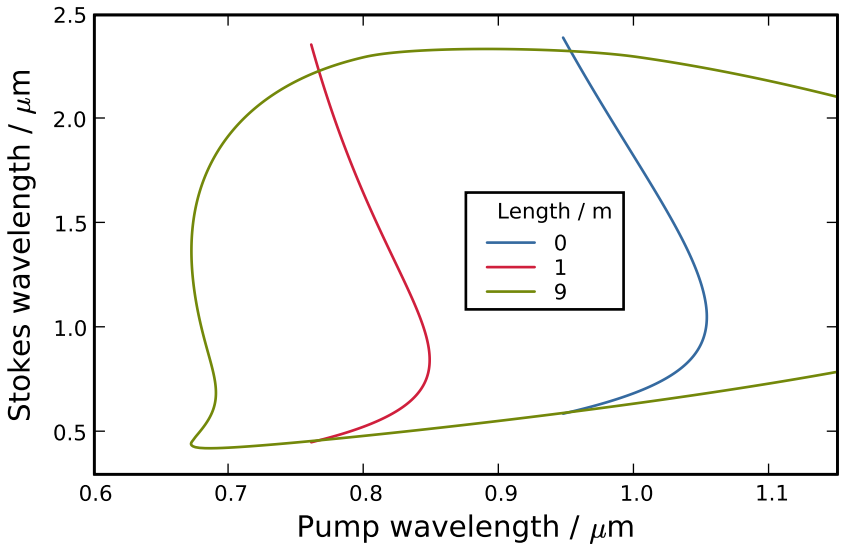


Figure 4.5: ***(numerical)*** Phase matching curves at three lengths through taper SCT1.

supercontinuum extent from the results shown below), the phase matching curve spans from 0.45 to 2.4 μm whereas at the input the curve only stretches as short as 0.6 μm as in HF1040. To see this more explicitly, the shortest phase matched wavelength through four wave mixing is plotted as a function of taper length in Fig. 4.6. Again the shape of this curve is similar to those of the pitch and zero dispersion wavelength. At fibre lengths longer than the optimal curve shown in Fig. 4.5 the second zero starts to move into wavelengths shorter than 2.4 μm and the phase matching curve closes into a loop (see again Fig. 4.5). This enhances the range of pump wavelengths useful for wide frequency separations of four wave mixing, but the approach of the second zero dispersion wavelength will limit the long wavelength edge of the continuum and thus curtail the short wavelength development.

Along with the changing dispersion and phase-matching curves, the reduction in pitch along the fibre increases the nonlinear coefficient as the effective area shrinks. Fig. 4.7 shows the nonlinear coefficient at a wavelength of 1.06 μm as it changes along the taper length. Initially at $\sim 15\,\mathrm{W^{-1}km^{-1}}$ it increases by nearly an order of magnitude by the end of the taper. This will lead to a significant increase in efficiency for the nonlinear processes involved in the supercontinuum generation.

Although the tapers clearly have many advantages compared to constant core fibres, there are some disadvantages due to enhanced losses. Confinement loss at the long wavelength edge becomes increasingly dominant as the pitch is reduced. This can be understood simply: the waveguide becomes too small to contain the field at longer

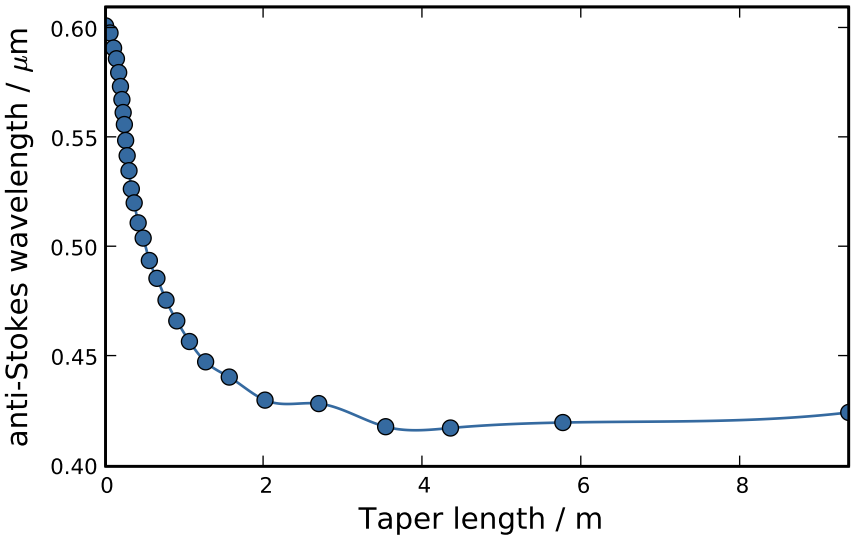


Figure 4.6: ***(numerical)*** The calculated shortest phase-matched wavelength of SCT1 as it changes along the fibre length.

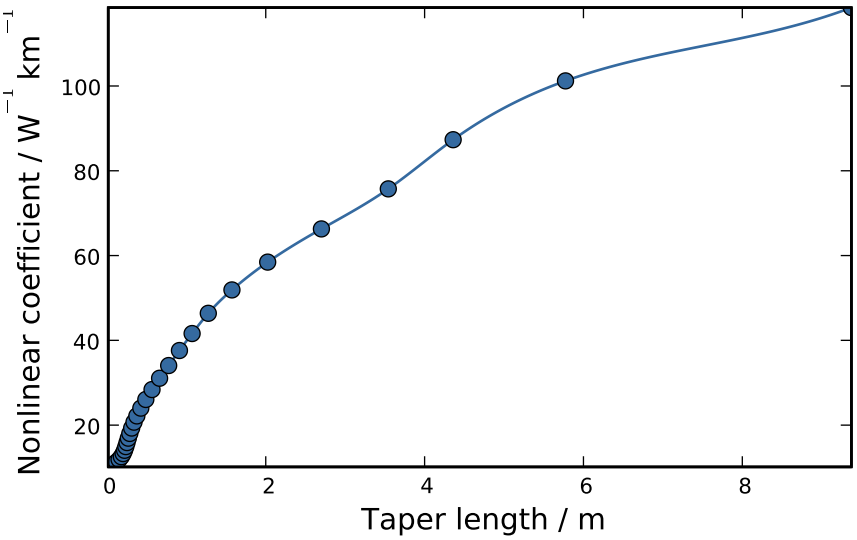


Figure 4.7: ***(numerical)*** The calculated nonlinear coefficient of SCT1 at 1.06 μm as it changes along the fibre length.

wavelengths. The confinement loss of a PCF can be estimated from a model which treats a PCF as a double clad fibre. The microstructured cladding is the inner cladding and the surrounding silica represents the second cladding layer. Following [Kos05] the loss can then be estimated from a pair of analytical equations which depend on the effective index of the guided mode (n_{eff}), the effective index of the fundamental space filling mode (n_{FSM}), the core size and the number of air-hole rings. We solved these equations with

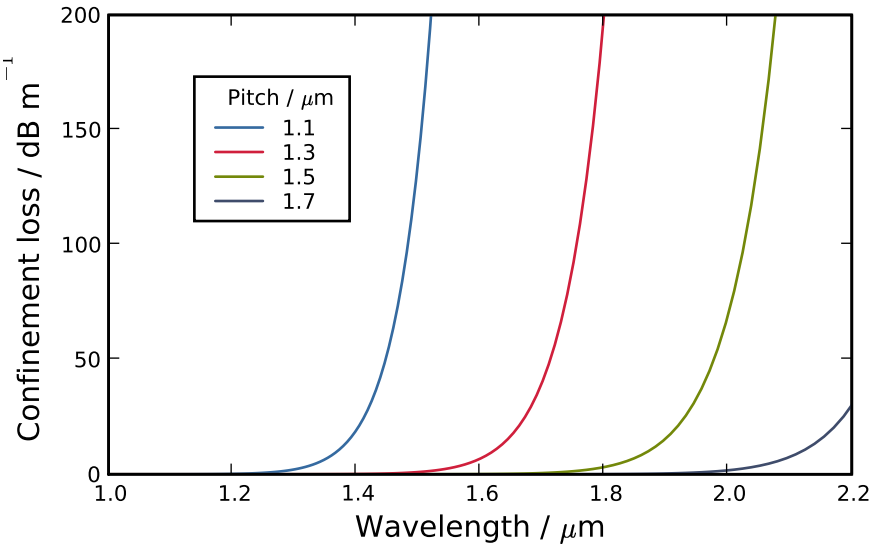


Figure 4.8: ***(numerical)*** The confinement loss from a 4-ring PCF similar in structure to SCT1 ($d/\Lambda = 0.71$ and 4 rings of air-holes), for different pitch sizes.

the values calculated from the analytical method described in Section 1.4.1. The resulting confinement loss curves are shown in Fig. 4.8 for parameters similar to the SCT1 taper ($d/\Lambda = 0.71$ and 4 rings of air-holes) for a number of pitch sizes (1.1, 1.3, 1.5, 1.7 μm). The confinement loss only becomes significant at wavelengths below 2 μm when the pitch is reduced to below approximately 1.5 μm. In out tapers, this is for lengths beyond 4 m. The effect of the long wavelength confinement loss are visible in the results we show below and are one limit to the tapered PCF supercontinuum extent. In addition, PCFs, unlike conventional step-index fibres, can exhibit very significant short wavelength bend loss [Bir97]. A number of analytical models of this process have been developed. In the simplest, the critical bend radius, after which loss becomes significant (and for the bend loss, the cut-off is indeed very steep) is given by another simple analytical equation, also depending on n_{eff} and n_{FSM} [Bir97; Mor03; Sor01]. To visualise the effect of this loss, the critical bend radius is plotted with respect to wavelength for taper SCT1 for a number of pitch sizes in Fig. 4.9. From this figure it is clear that the bend loss at short wavelengths is reduced for smaller pitch sizes. This implies that the tapering process actually limits the effect of bend loss in the blue/UV region, which, from Fig. 4.9 can be significant for bends of a few millimetres in radius for the input pitch sizes. The converse effect is observed for the long wavelength edge and hence additional losses will be incurred there at longer propagation lengths through the taper.

In summary, the tapered PCFs clearly have many features – enhanced nonlinearity, enhanced phase-matching curves for FWM, that change advantageously along the taper

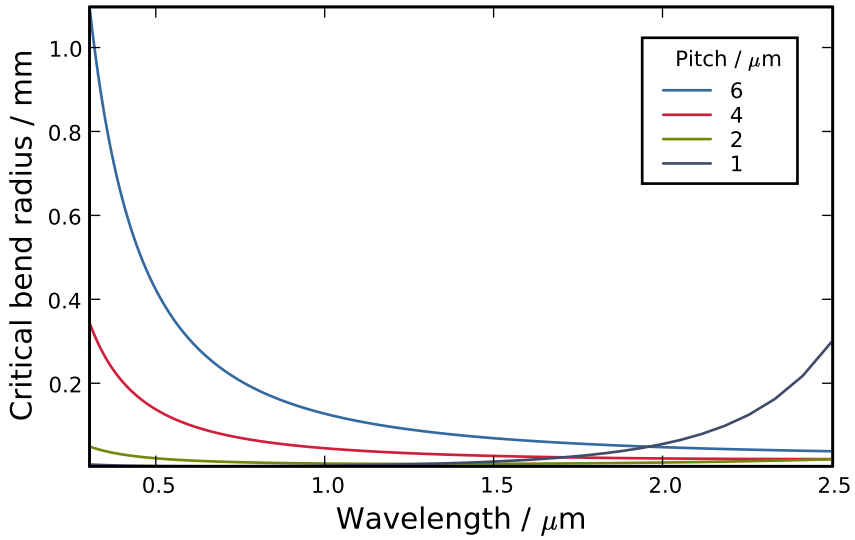


Figure 4.9: ***(numerical)*** The calculated bend loss for taper SCT1 for different pitch sizes.

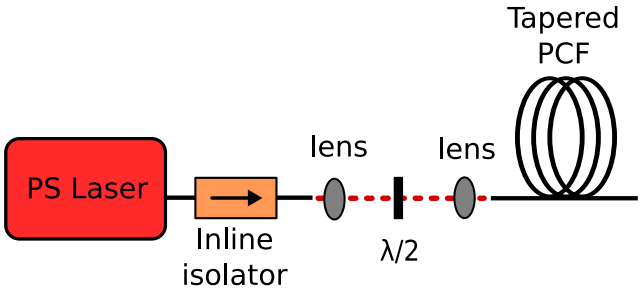


Figure 4.10: Experimental setup used for pumping the tapered PCF for supercontinuum generation.

length – which indicates that they should be considerably better for supercontinuum generation compared to constant core fibres.

4.3 Results and discussion

4.3.1 Experimental setup

Picosecond pumping

The experimental setup used for pumping the supercontinuum is shown in Fig. 4.10. The picosecond laser, which was the same as that used in the previous chapter, was spliced directly to a fibre pigtailed inline isolator which was polarisation insensitive. The isolator had a loss of only ~ 0.5 dB and could handle the full 8 W of power from the

picosecond laser. Therefore higher power was available for pumping the tapered PCF than we had available when studying the cascaded PCFs previously. However, the PCF tapers had a very large cladding diameter at the input end (a result of the procedure used to manufacture them) and therefore it was impossible to splice directly to them. Instead the pump light was coupled out of the isolator pigtail, and then into the taper using two singlet lenses. The lenses were chosen so that the mode field diameters were closely matched at both the output and input coupling. This way, less than 1 dB was lost in this step. The resulting air-gap also allowed us to insert polarisation controlling elements before the taper which we used to check the sensitivity of the supercontinuum process to the polarisation orientation. The average power coupled into the tapers was ~ 5.5 W. The corresponding peak power was ~ 25 kW.

Nanosecond pumping

The nanosecond pump systems was identical to the picosecond system described above except for the pump laser. Instead of the picosecond laser, we used a commercially available nanosecond pulsed fibre laser (IPG Photonics). It is based on a master oscillator power fibre-amplifier configuration making use of an acousto-optic modulator. The system produced 18 ns pulses with peak powers up to ~ 10 kW at a repetition rate of 5 kHz. Unless specifically stated, all of the results shown below are with the picosecond system.

4.3.2 Optimisation of flatness and visible spectral power

As mentioned above, a number of tapers were pumped to achieve a broad and flat supercontinuum across the visible spectral region. The results in this section are just for one taper, discussed above, which produced the best results for this aim.

Fig. 4.11 shows the results of a cutback experiment with taper SCT1 pumped at full power with the picosecond laser source. As noted above, approximately 5.5 W of average power (~ 25 kW of peak power) was coupled into the taper for all of these results. The spectrum rapidly broadens in the first few centimetres of the fibre, followed by a region of gradual expansion. After ~ 1 m of fibre however, gaps start to appear in the spectrum around 0.6 μm, followed by 0.8 μm after 2 m. Later, after around 5 m of propagation evidence of water induced losses at 1.4 μm can be observed and finally the effects of confinement loss can be observed in the long wavelength region at the end of the taper. It is clear then that the early spectral development in the rapidly changing part of the taper produces a very broad supercontinuum, but that several mechanisms cause the spectrum to become less flat with further propagation. Unfortunately these gaps start to appear before the maximum spectral width is achieved and thus one must make a compromise to obtain an ultra-broad spectrum which is still very flat.

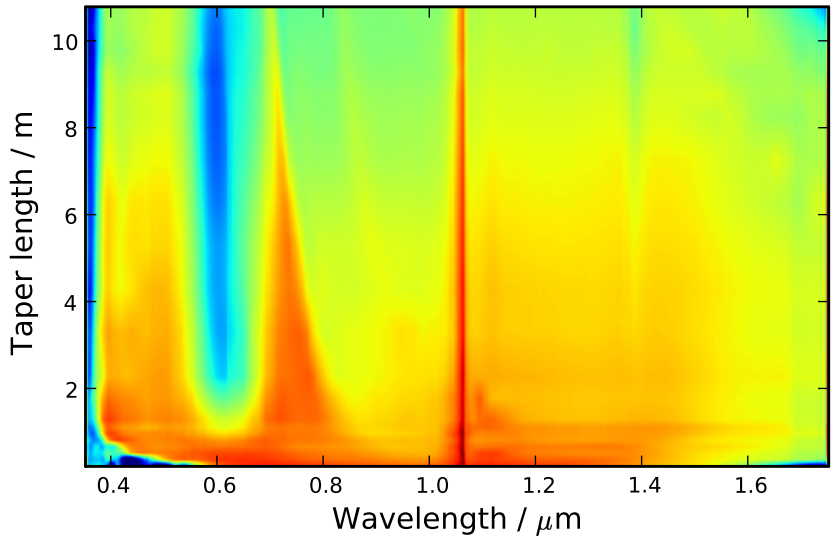


Figure 4.11: ***(experimental)*** Results of the cutback experiment with picosecond pumping of SCT1. The scale is: -30 0 dB.

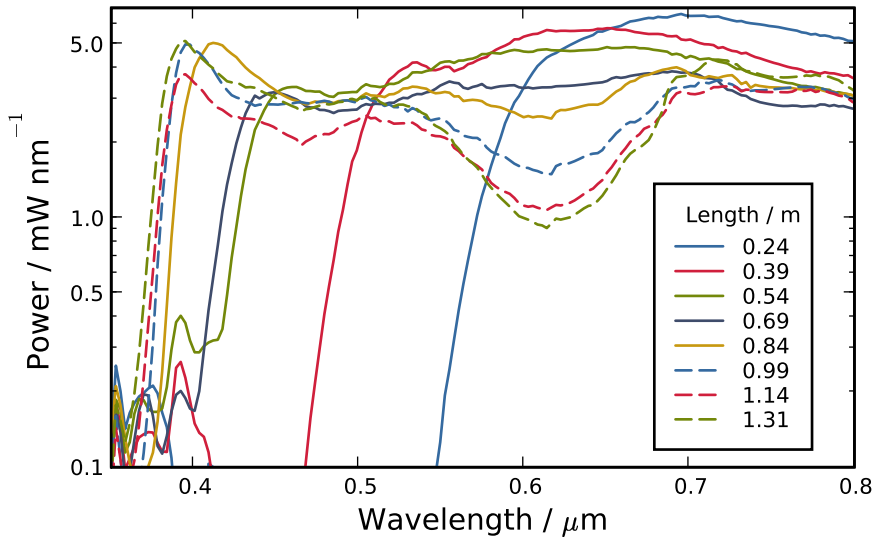


Figure 4.12: ***(experimental)*** The spectral power in the visible part of the supercontinuum for selected spectral slices of the cutback results.

Fig. 4.12 shows close ups of the spectra measured for the visible part of the supercontinuum. The vertical axis is scaled with the measured spectral power. It is apparent that a very high spectral power was achieved across the whole visible spectrum. For the output at 0.84 m the spectral power was above 2 mW/nm across this region. With a peak of 5 mW/nm near 0.4 μm. The total output power of the supercontinuum at this length was over 3.5 W. At the time this work was done, these values represented a large increase over

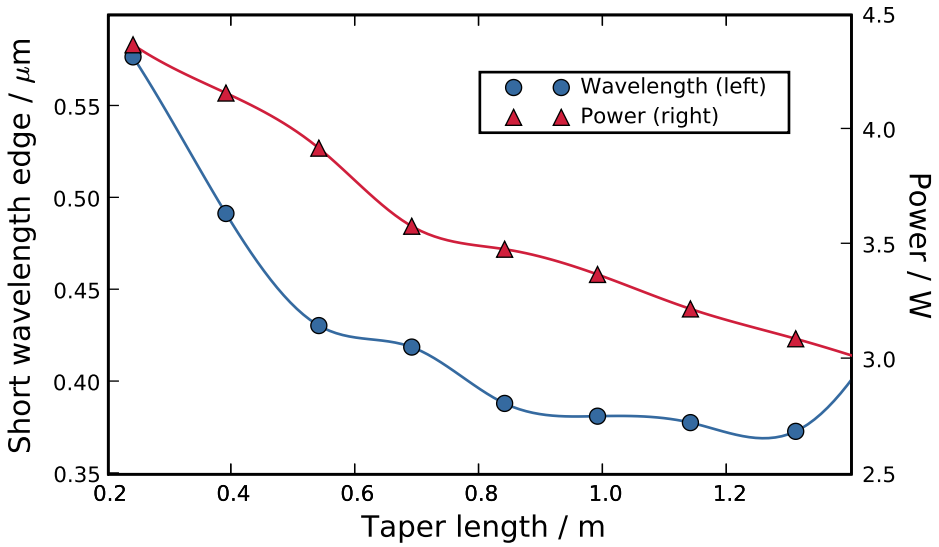


Figure 4.13: ***(experimental)*** The short wavelength edge (-10 dB) as the supercontinuum evolves along the taper SCT1, and the total average output power.

previously obtained results and are still the highest reported in the blue spectral region. As noted above, further propagation induced gaps in the spectrum, visible in the curves of Fig. 4.12 around 0.6 μm. However, the shortest wavelength edge of the continuum extended to below 0.38 μm, a significant improvement over the cascaded fibre setup of the previous chapter. Fig. 4.13 shows how the blue spectral edge evolved along the taper, clearly indicating the flattening of the spectral extension at 0.375 μm. Fig. 4.13 also shows the total output power of the continuum. This drops significantly with increasing fibre length as expected from the spectral gaps mentioned above. But even at the optimum continuum extent the power is still over 3 W. Finally Fig. 4.14 shows a photograph of the taper while it was being pumped – a nice way to visualise the broadening spectrum along the taper length as the scattering turns white. Also evident is the spectral depletion around 0.6 μm as the light scattered at the end of the taper is bluer than the light preceding it. The supercontinuum was measured to have identical spectral content in both polarisation axes and to be independent of the input polarisation angle.

The pulse duration around the wavelength of 0.5 μm was measured using a streak camera to be shorter than the resolution of the camera ($\sim$ 22 ps) as expected from the cumulative dispersion of the taper. Short pulses, below $\sim$ 30 ps are expected across the visible spectrum. Considerably larger temporal spreading would be expected in the blue/UV edge where the dispersion becomes much larger.

The mode profile of the continuum was measured at 0.39 μm and 0.5 μm, by measuring the far field pattern after a bandpass filter. In both cases the continuum was observed to

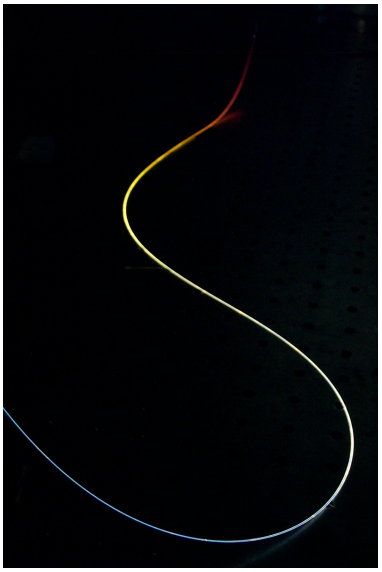


Figure 4.14: ***(experimental)*** The scattering from the taper SCT1 at full pump power.

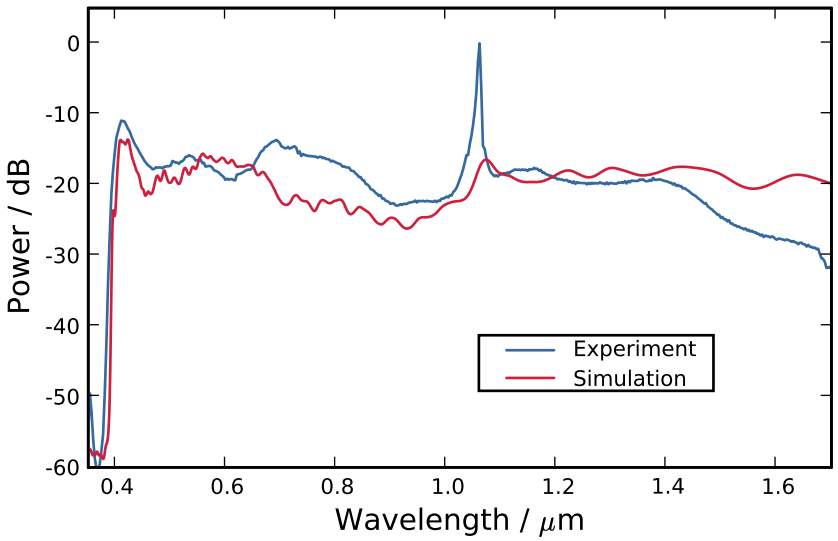


Figure 4.15: Comparison between the experimental and simulated spectrum after propagation through 0.9 m of the taper SCT1.

be in the fundamental fibre mode.

4.3.3 Comparison with simulations

To aid the discussion of the supercontinuum generation mechanism in the following sections we make use of numerical simulations obtained using the techniques described

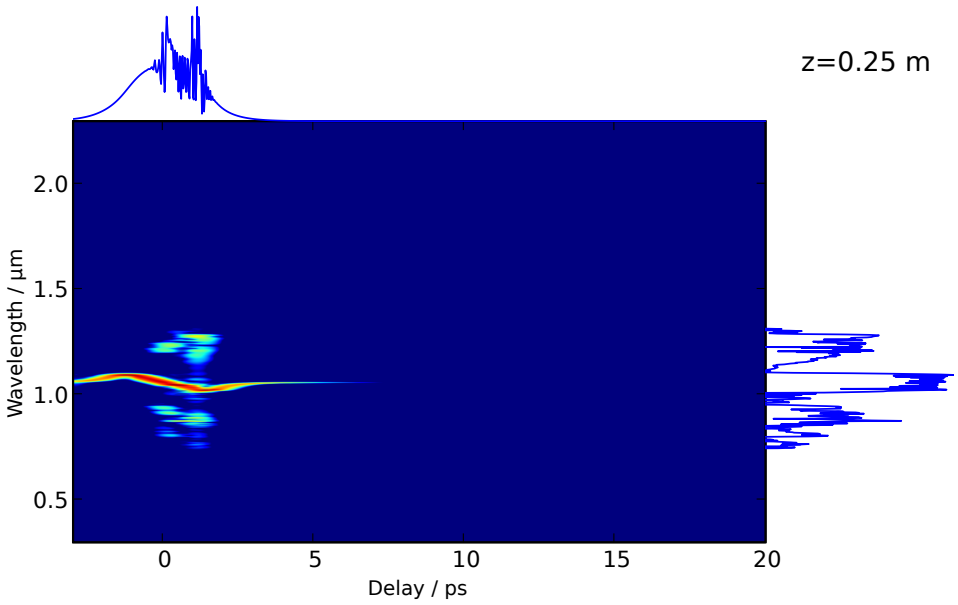
in Section 1.4.4. From an inspection of Fig. 4.15 it is clear that the simulations reproduce the supercontinuum generation results extremely well, considering the bandwidth of the simulated spectrum. Critically, the short wavelength edge of the continuum is reproduced and so we can hope to obtain an insight into the mechanism of generating the shortest wavelength components of the supercontinuum, with an eye to further optimisation. The long wavelength region is less well reproduced which can be readily explained by the fact that loss, particularly the confinement loss of the taper was not included in the simulations. The largest discrepancy concerns the pump depletion; the experimental spectrum shows significant power remaining near the pump wavelength, which is not reproduced in the simulated results. The model of the pump laser was the same as that used in the previous chapter, i.e. a Gaussian pulse is amplified and propagated through fibre which corresponds to the components of the laser – it does not account for amplified spontaneous emission (ASE). The undepleted pump power has a bandwidth of ~ 11 nm and average power of ~ 90 mW which corresponds quite well with ASE emission during the final amplification stage of the pump laser. This can therefore explain the discrepancy. This should not affect the continuum simulation results as the ASE is a continuous background signal which does not interact significantly with the continuum generation process.

To represent the taper in the numerical solution of the generalised nonlinear Schrödinger equation, we must account for the changing dispersion and nonlinearity along its length. This was achieved by using the MPB software to solve for the dispersion and effective area curves (with respect to frequency) at 30 points along the full taper length, accounting for the required adjustment of the pitch at each point. The effective area was found from the electric and magnetic field using the vectorial perturbative approach given in [Tzo95], and described in Section 1.4.3. In the numerical propagation code, the dispersion, nonlinearity and dispersion of the nonlinearity (τ_{shock}) were linearly interpolated between these reference points at each step through the fibre.[1]

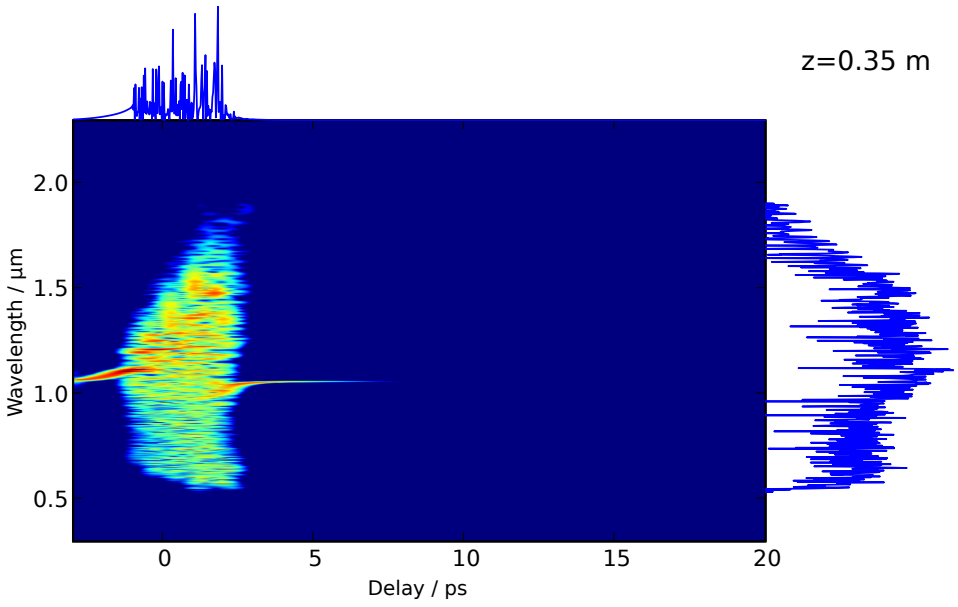
4.3.4 Understanding the results

The initial supercontinuum dynamics are similar to those in the the non-tapered fibres of the previous chapter. MI initiates the continuum and FWM spectrally broadens the continuum in the very early stages. Fig. 4.16 shows spectrograms of these steps. The fibre parameters at the input are similar to HF1040, and so, like in the previous chapter,

[1] Due to the extremely large bandwidth, high power and long length to be simulated, with nonlinearity increasing to values above 100 $W^{-1}km^{-1}$ the code was re-implemented in Fortran and parallel FFT routines utilised to run the simulations in a manageable time frame. They were run on a quad-core system and usually took about 75 hours to complete. The time-base contained 2^{17} points and the adaptive step-size algorithm was used (see Section 1.4.4) with a local relative error goal of 1×10^{-8}.



(a) Initial MI broadening and pulse break-up.



(b) Early spectral expansion due to FWM/MI.

Figure 4.16: ***(numerical)*** Spectrograms of the initial supercontinuum dynamics.

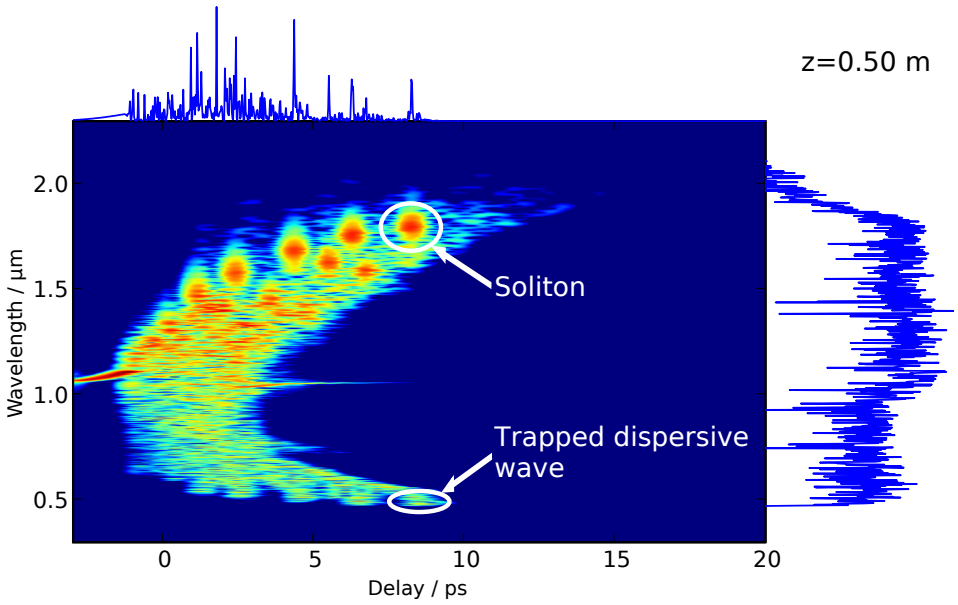
modulation instability dynamics occur much faster than soliton fission for our pump laser. This can be seen in the top graph of Fig. 4.16(a), after 0.25 m of propagation the pump pulse has already broken into many much shorter pulses. This is also clearly accompanied by the MI side lobe development in the spectral domain, visible on the right hand graph

of the same figure. Further propagation leads initially to cascaded four wave mixing as is clearly evident in Fig. 4.16(b) after 0.35 m of propagation. This process has been enhanced by the taper, as the FWM based supercontinuum spans a much larger spectral range than would phase match at the input of the taper.

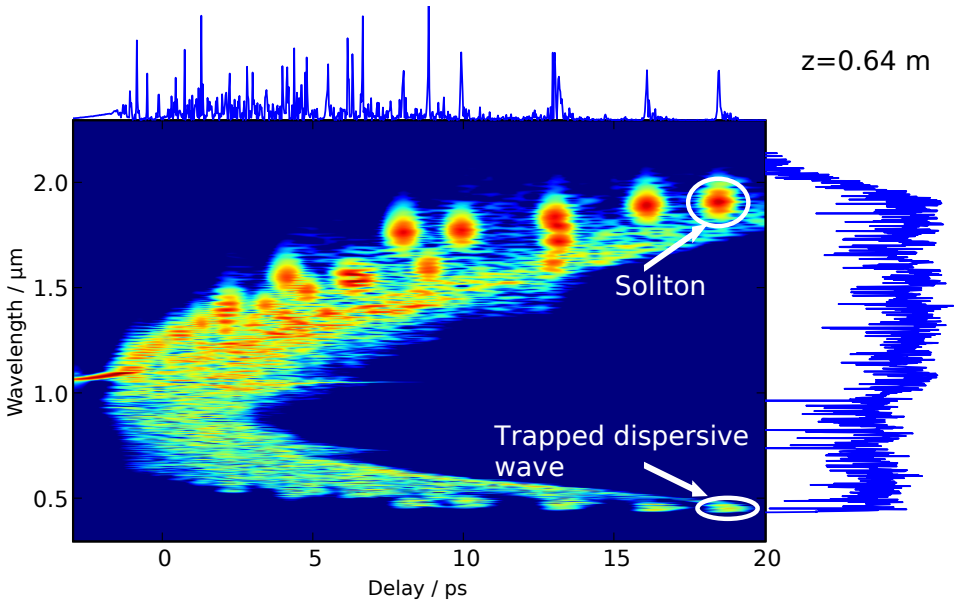
Initially we thought that soliton effects played a relatively minor role in the subsequent propagation as they do in the results of the previous chapter, and that the enhanced cascaded FWM processes enabled by the tapering accounted for the full supercontinuum. However, analysis of the spectral extent achieved and the phase-matching curves of the taper questions this conclusion. In the particular taper we have looked at so far, SCT1, the shortest wavelength achieved is around 0.38 μm. But the FWM phase-matching diagram only stretches to anti-Stokes wavelengths of 0.42 μm. But this is for a length of over 3 m. We see generation to below 0.4 μm in a fibre length which should only phase-match to around 0.58 μm. Thus the supercontinuum is formed to the blue/UV more quickly than the FWM phase-matching curve of the taper has reached that spectral region. It is therefore clear that something else is important to the supercontinuum process.

As discussed briefly in the previous chapter, soliton effects can affect the short wavelength edge of the supercontinuum (and in femtosecond pulse systems where soliton fission dominates the early dynamics, soliton effects are by far the dominant contributors to all of the supercontinuum dynamics). In the constant core fibres we considered previously the soliton effects only slightly enhanced the blue spectral edge. However, in the tapers we have concluded that they play a key role in the UV generation process.

A compelling picture of the dynamics of the dispersive waves on the blue supercontinuum edge is that they are trapped and continuously scattered to shorter wavelengths through a process of intra-pulse FWM [Gor06]. From this point of view, a blue dispersive wave acts as the pump to a FWM process with the high power and temporally localised soliton as the Stokes signal. A new anti-Stokes signal is generated at a small frequency up shift from the original dispersive wave. As the new dispersive wave has a lower group velocity compared to the pump and soliton, it is temporally delayed in the fibre. However, the soliton is continuously down shifted to frequencies with lower group velocities by intra-pulse Raman scattering and hence will also be delayed and eventually pass through the new dispersive radiation. As these processes are continuously occurring the blue dispersive wave can become localised or trapped in the temporal region of the soliton. The process will continue as long as the group velocities are matched and the soliton remains spectrally broad enough for self-Raman scattering. Fig. 4.17 shows spectrograms clearly displaying the dispersive waves trapped by the solitons and Fig. 4.18 shows group velocity curves at various fibre lengths. From this figure we see that as the soliton shifts to longer wavelengths through the Raman effect, its reduced group velocity delays it so that it



(a) Trapping of dispersive waves.



(b) Evolution of the trapped dispersive wave.

Figure 4.17: ***(numerical)*** Spectrograms of the trapped dispersive wave dynamics.

stays close to the dispersive wave which is also slowing as it moves to shorter wavelengths.

Note that the FWM phase matching criteria for the soliton and dispersive wave in this process is different from the purely CW criteria we considered previously because the

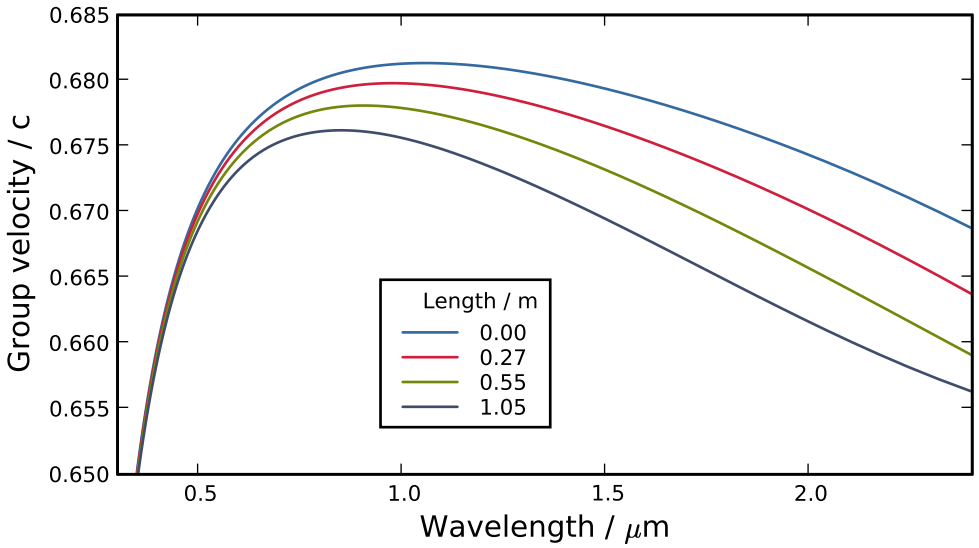


Figure 4.18: ***(numerical)*** Group velocity curves for taper SCT1 at various lengths through the taper.

propagation constant of the frequency components of the soliton must account for the suppression of group velocity dispersion in solitons [Skr05]. One consequence of this is that the soliton (Stokes) and newly generated dispersive wave (anti-Stokes) do not have to be symmetrically separated in frequency about the pump wave.

Further understanding of the trapping of solitons with dispersive waves has recently been developed [Gor07c; Gor07a; Gor07b]. The dispersive wave, which is on the tail of the localised soliton (as is clear from Fig. 4.17), is trapped on one side by the refractive index modulation of the intense soliton (through the nonlinear refractive index). However, the soliton is accelerating (or actually decelerating) due to its constant Raman shift to longer wavelengths (regions of lower group velocity) and thus so is the modulated refractive index which traps the dispersive wave. This understanding led the authors of [Gor07c; Gor07a; Gor07b] to interpret the trapping of the other side of the dispersive wave as being due an inertial force in the frame of reference of the accelerating soliton, drawing an analogy with the inertial force observed by a set of balls in an accelerating box. Of course the inertial force, outside of the soliton reference frame, is simply due to the fact that the decelerating soliton stays close to the dispersive wave which is similarly delayed as it moves to shorter wavelengths. Nevertheless it is an elegant picture of the dynamics.

The understanding of the blue continuum extension, as expressed above, encompasses and extends the explanations previously reported in terms of XPM and FWM by a number of authors trying to understand the soliton trapping of dispersive waves [Gen05; Gen04a; Gen04b; Gor06; Nis02a; Tar03].

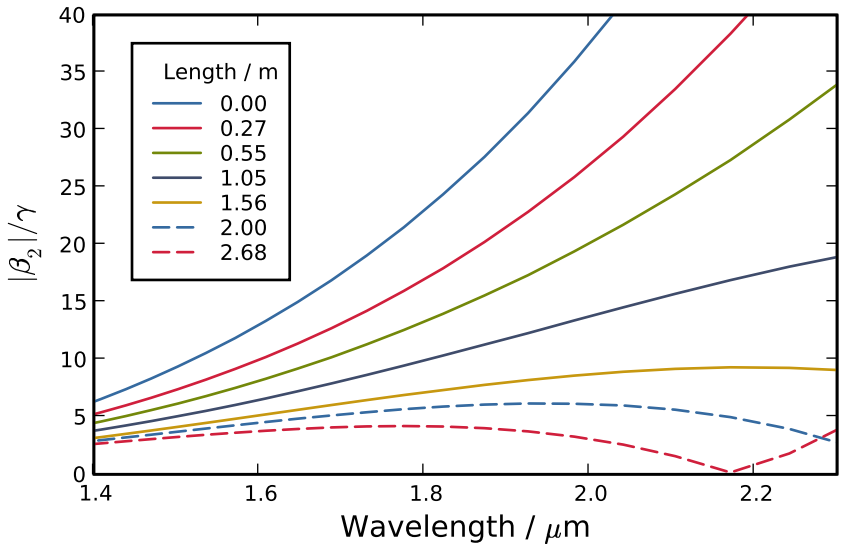


Figure 4.19: ***(numerical)*** Ratio of $|\beta_2|/\gamma$ at various lengths through taper SCT1.

In a non-tapered fibre suitable for visible supercontinuum generation, a soliton formed from MI which is shifting to longer wavelengths through intra pulse Raman scattering will increase in duration due to the increase in dispersion and decrease in nonlinearity at longer wavelengths, because the duration of a soliton of constant energy is directly proportional to the ratio of dispersion to nonlinearity:

$$\tau_0 = \frac{2|\beta_2|}{\gamma E_{sol}} \tag{4.1}$$

Fig. 4.19 shows this ratio at various lengths in the taper SCT1. From this figure, it can be seen that if the fibre characteristics where to stay the same as at the input (i.e. a non-tapered fibre) a soliton would be 7 times longer at 2.0 μm than it was at 1.4 μm. This broadening could easily be sufficient to reduce the soliton bandwidth such that intra-pulse Raman scattering does not occur. This would halt the red-shifting of the soliton and hence the blue shifting of the blue edge of the supercontinuum. However in a tapered fibre, if the pitch is reduced along the length of propagation, then the dispersion at long wavelengths can actually decrease, while the nonlinearity will increase, along the fibre length. Referring again to Fig. 4.19 the soliton duration can remain constant if the taper profile is such that as the soliton red-shifts it walks through a fibre region with a suitable dispersion to nonlinearity ratio for its current wavelength. This can be directly used for soliton compression as we will see in Chapter 5. However, in the present discussion, this fact means that the solitons will remain short, and hence will have sufficient spectral bandwidth for self-Raman scattering to longer wavelengths. In the taper SCT1, analysis of

the results of numerical simulations, which agree very well with the experimental results, show that the solitons maintain a duration of less than ~ 100 fs up to at least 2.1 μm. This is one of the key facts about tapered fibre supercontinuum generation as it means that the soliton trapping of dispersive waves remains efficient and can occur for fibre lengths far exceeding those in constant core fibres.

However, there is another, equally important fact about tapered PCF which also plays a significant role in enhancing the blue/UV supercontinuum edge. In a constant core fibre suitable for supercontinuum generation (i.e. relatively low group velocity dispersion at the pump around 1.06 μm) the group velocity curve has limited matching between long and short wavelength regions. For example, the first curve (z=0 m) shown in Fig. 4.18 represents the group velocity at the input to taper SCT1. Here we see that the group velocity matching cannot be maintained to wavelengths shorter than ~ 0.5 μm. However, tapered fibres can maintain the required conditions at the start of the fibre to initiate supercontinuum generation, while also enhancing the matching of group velocities at shorter wavelengths due to the reduction in pitch and hence change in the dispersion curve (see Fig. 4.18). To see this, Fig. 4.20 shows the group velocity matching curves for various lengths through taper SCT1. As noted above, the curve for the taper input (length=0) does not match to wavelengths significantly short of 0.5 μm. At further lengths through the taper (i.e. as the pitch is reduced), the group velocity matching curve shifts down and shorter wavelengths become matched. For the taper length of 1.06 m, the highly red-shifted solitons would match with dispersive waves as short as 0.38 μm in this taper, in agreement with our experiments. However reducing the pitch too far introduces a minimum group velocity matched wavelength (see last curve in Fig. 4.20). This is to do with the second zero dispersion wavelength, which we will discuss below.

4.3.5 Optimisation of Blue/UV extent

From the above analysis it is clear that to enhance the UV spectral region even further, group velocity matching to the UV wavelengths should be maintained over longer fibre lengths. We can establish an optimal set of fibre parameters to achieve this by considering the group velocity curves over a range of fibre parameters.

Shown in Fig. 4.21 is a density map of the shortest group velocity matched wavelength as a function of the two fibre parameters, pitch and hole diameter to pitch ratio (d/Λ). It is clear that a pitch of around 2 μm gives the shortest matched wavelength almost independently of d/Λ. For larger pitches, the group velocity curve on the long wavelength edge increases, because the field is less confined to the core of the fibre and hence has a larger overlap with air. For smaller pitches, the second zero dispersion wavelength moves down to this spectral region. This means that there is a minimum in the group

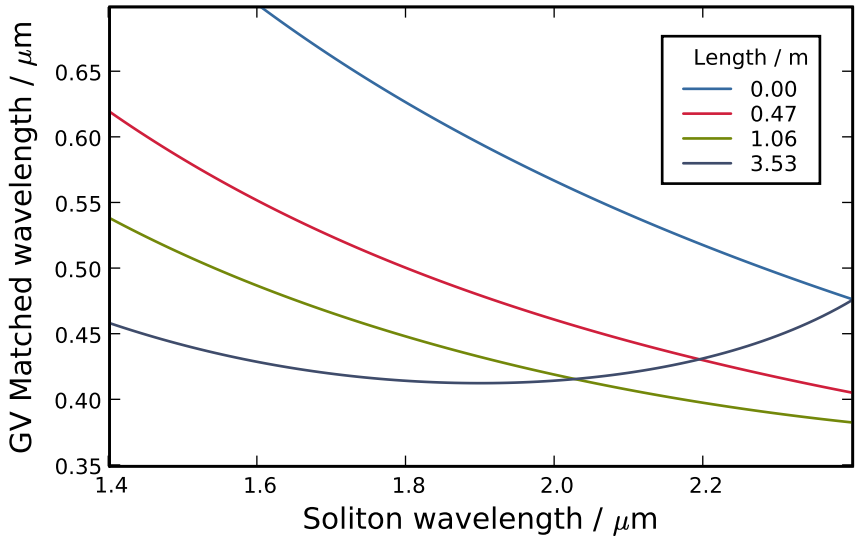


Figure 4.20: ***(numerical)*** Group velocity matching curves for different lengths of taper SCT1.

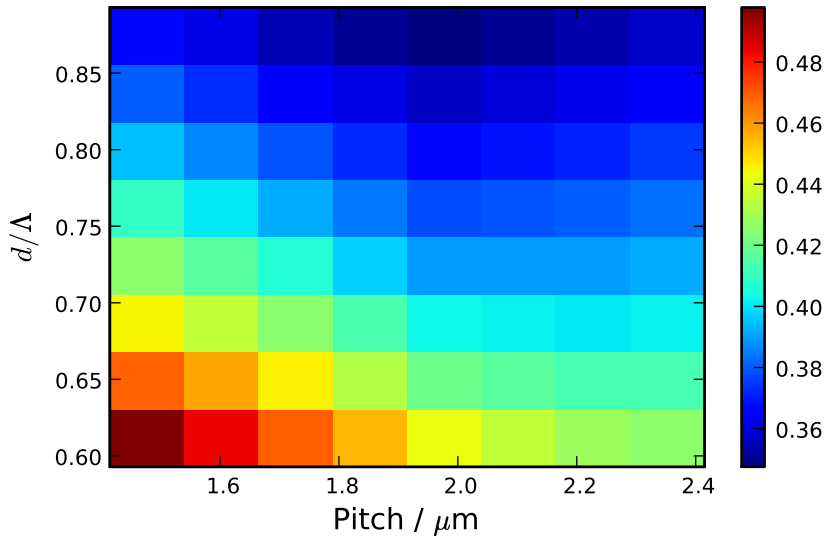


Figure 4.21: ***(numerical)*** Map of the shortest group velocity matched wavelength as a function of pitch and hole diameter to pitch ratio (d/Λ). Darker blue indicates shorter wavelength matching.

velocity curve and hence a limit to how small the group velocity on this long wavelength edge can be, 2 μm appears to be a compromise between these two positions. In terms of the ratio d/Λ, the larger the ratio, the shorter the group velocity matched wavelength becomes. This is because the higher air-filling fraction confines the mode more tightly into the silica core and hence keeps the group velocity at long wavelengths lower. There is,

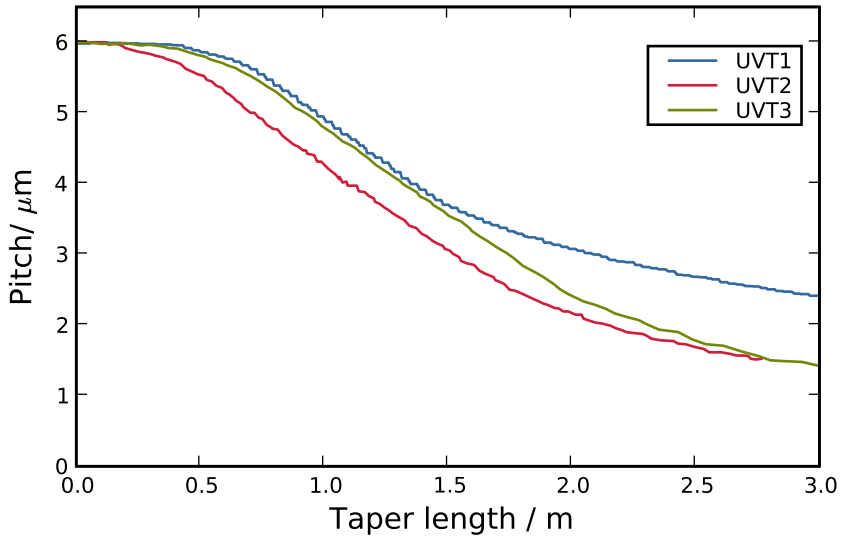
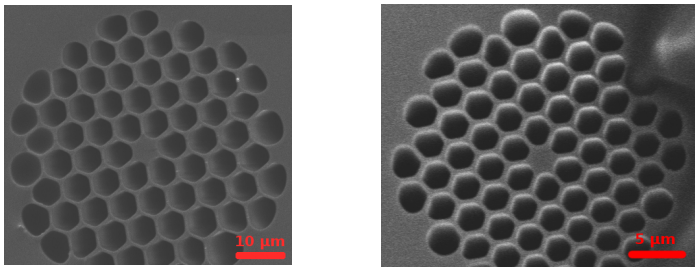


Figure 4.22: ***(experimental)*** The variation of pitch for the three taper samples considered for enhanced UV generation.

however, a practical limit to how large this ratio can be, fibres with $d/\Lambda \sim 0.95$ are readily available. Therefore we can see that the SCT1 taper, with $d/\Lambda = 0.71$, was not optimal for UV generation.

The optimal taper profile is less easy to deduce. We can limit the input fibre characteristics to those which allow highly efficient initial MI/FWM dynamics to occur. The output is defined by the optimal parameters above. But what about the change in between? To properly determine this would require a detailed experimental or numerical study of the soliton dynamics. Once the solitons are formed from the MI and their peak powers and durations known, then it would be possible to determine how they will shift due to intra-pulse Raman scattering and compress due to the changing nonlinearity and dispersion. Of course these two effects will affect each other. But to achieve an optimal design, the group velocity of the dispersive wave must also match that of the soliton as it shifts through the fibre. Thus we have a complicated multi-objective optimisation problem that is non-trivial to solve.

However, we have a limited choice as we are constrained by the manufacturing procedure of the tapers. In essence this means that the taper profiles can have a defined start and end point and defined length, but the shape in between is limited. The shape of three tapers we used to obtain increased UV generation are shown in Fig. 4.22. Here we see that the tapers start and end almost flat and the central region is approximately linear, with smooth transition between the flat end and central linear parts. The three tapers differ significantly only in the end pitch size and the rate of change of pitch with length. In all



(a) Input. (b) Output.

Figure 4.23: Scanning electron micrographs of the input and output of taper UVT1.

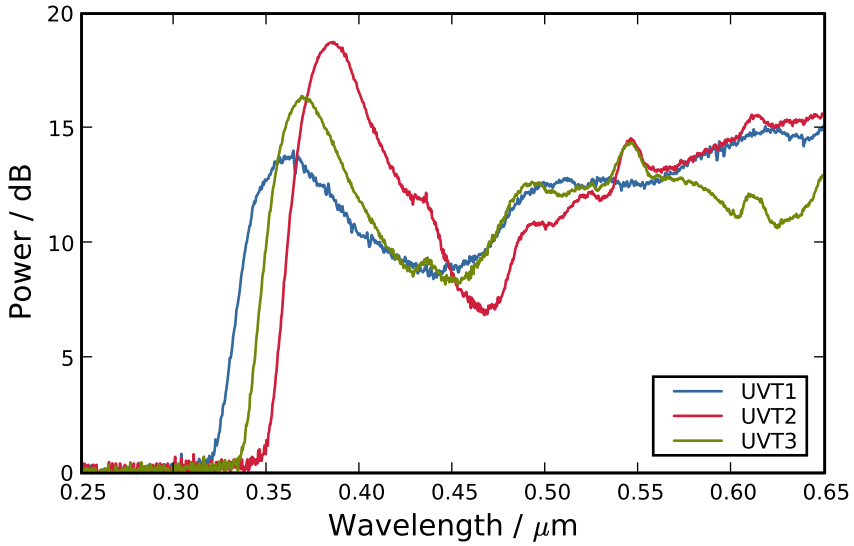


Figure 4.24: ***(experimental)*** The measured spectra after pumping the UV tapers with the full pump power of the picosecond laser.

cases the hole diameter to pitch ratio was d/Λ =0.87 to 0.89 and the start pitches were all 6.0 μm. Fig. 4.23 shows SEM images of the input and output of taper UVT1. Note that these figures are to different scales.

Fig. 4.24 shows the short wavelength edge of the supercontinua achieved with picosecond pumping of these tapers. We can see that significant extension below 0.38 μm is achieved in all three tapers in agreement with the idea that higher air-fill fractions enhances the UV generation. For taper UVT1 the cut-off of the continuum is between 0.33 and 0.34 μm significantly into the UV, far exceeding any previous results with a 1.06 μm pump wavelength. For this taper, the peak at 0.36 μm had a spectral power over 2 mW/nm. This taper had a final pitch value of $\sim$ 2.4 μm (the largest). According to Fig. 4.21 this is still not at the optimum value. Of the other two tapers (UVT2, UVT3) ending with a

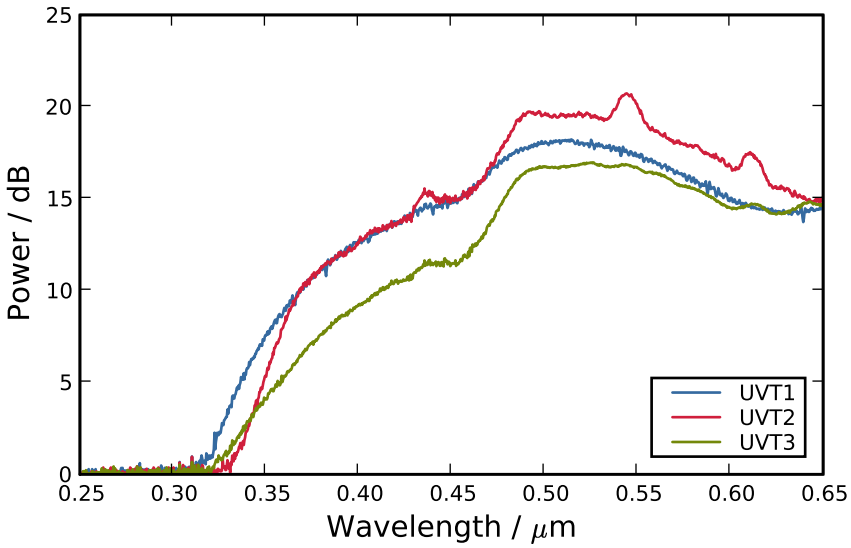


Figure 4.25: ***(experimental)*** The measured spectra after pumping the UV tapers with the full pump power of the nanosecond laser.

pitch at ~ 1.5 μm, UVT3, which was the slowest changing (or maintained a largest pitch for longer) extended further into the UV. The total output power in the supercontinua of UVT1, UVT2 and UVT3 was 3.16, 2.85 and 1.8 W respectively, thus very high spectral power was maintained for these tapers. The supercontinua generated in all three tapers exhibited large peaks at the short wavelengths. This can be explained due to the bunching of trapped dispersive waves at the short limit of the group velocity matching. This indicates that the short wavelength cut-off of these supercontinua was not caused by loss, but by the possible group velocity matched wavelengths of the given fibre structures. This enhancement could be deliberately used to provide increased spectral power in the UV if desired. The observation that the supercontinua are not loss limited leads one to the conclusion that further extension is possible. Thus for a yet higher air-fill fraction in the taper, with a pitch changing from around 6 μm to 2 μm, greater UV generation could be expected.

Fig. 4.25 shows the short wavelength edge of the supercontinua achieved with nanosecond pumping of these tapers. In this case the supercontinuum cut-off is much smoother and less spectral power is concentrated in the UV. It would have been reasonable for one to expect that the nanosecond continuum would shift further because walk-off due to differing group velocities would have been less significant. However, the fact this is not observed is probably because much less peak power was available from the nanosecond source, which is estimated to be ~ 5 kW in comparison to ~ 25 kW for the picosecond pump. Given this disparity in pump peak power, it is actually impressive that the contin-

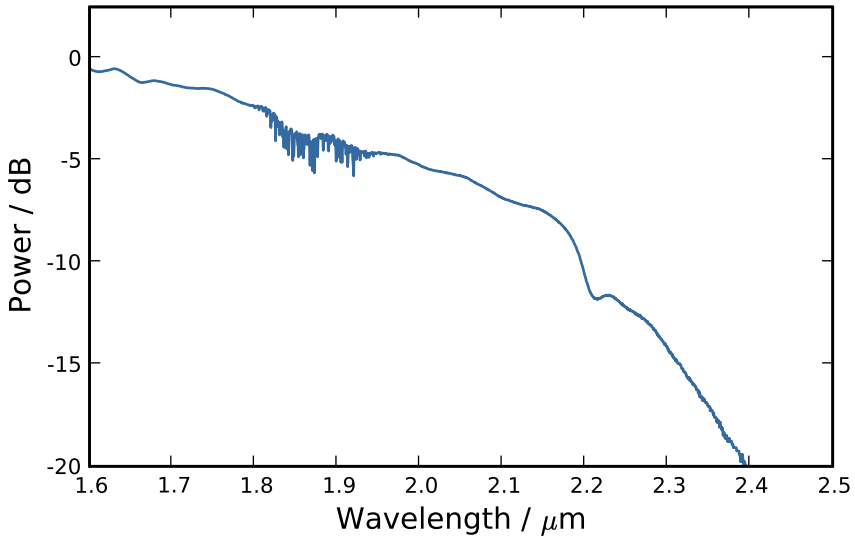


Figure 4.26: ***(experimental)*** The measured long wavelength spectrum of a supercontinuum generated in a taper similar to SCT1 pumped with the picosecond laser.

uum stretches so far and could be expected to perform better than the picosecond source for equivalent peak powers.

4.3.6 Mid-infrared extent

Fig. 4.26 shows the long wavelength spectrum of the supercontinuum generated by picosecond pumping of a taper similar to SCT1. The lines near 1.8 μm are due to water absorption in the spectrometer used and not features of the continuum spectrum. The continuum extends up to 2.4 μm at the -20 dB level, although the -10 dB edge is only at 2.2 μm. This is expected due to the very high losses in silica glass at these wavelengths. The dip just beyond 2.2 μm is probably due to the second dispersion wavelength which will limit self-Raman scattering of solitons to longer wavelengths, the extended spectral power being due to dispersive wave generation in the normal dispersion region beyond this point.

4.4 Limits to short wavelength generation

4.4.1 Limits inherent to the nonlinear processes

We discussed above the optimal fibre structure for group velocity matching of dispersive waves at the shortest wavelength edge. From that analysis, the continuum edge will be limited to around 0.33 to 0.35 μm which we have already reached in the above results.

Given that we have also found the limit to continuous wave four wave mixing, any further extension must be due to different nonlinear mechanisms than those discussed in this thesis.

Harmonic generation and four wave mixing effects mediated through polarisation, or high order mode phase-matching can provide such mechanisms as evidenced by experimental reports. In [Pri03] four wave mixing in higher order modes is cited as the mechanism for UV generation as short as 0.3 μm from a 0.82 μm pump source of 150 fs pulses with low average power. In [Efi03] the generation of high order UV modes through phase-matched processes was reported. Generation as short as 0.26 μm was observed in a discrete spectrum separate from the main continuum with ~80 kW peak pump power. However, even if these new processes could be made efficient and a continuum generated to much shorter wavelengths, loss will ultimately limit the spectrum.

4.4.2 Limits due to loss

Linear loss due to material absorption, Rayleigh scattering, scattering from imperfections in the microstructure and short wavelength bend loss will limit the continuum extent. Although we should note again, that short wavelength bend loss is reduced along with the fibre pitch and so in our tapers is not a significant limiting factor. In fact, the limiting linear loss at short wavelengths will certainly be due to scattering as the wavelength becomes similar in scale to the microstructure imperfections or material imperfections (Rayleigh scattering).

But, for any linear loss a higher pump power and shorter fibre length can be used, i.e. we could make use of the power - length scaling of nonlinear optics. Lengths of the order of a few millimetres have been successfully used. This cannot be utilised indefinitely though. Either practical problems due to extremely short fibre lengths, or excessively high peak powers, or a fundamental limit inherent in the nonlinear mechanisms would eventually be reached and therefore the shortest wavelength achievable will be limited. However, before this point is reached, nonlinear loss mechanisms will place an even more fundamental limit as two-photon absorption also scales with peak input power, severing the power-length scaling.

Two photon absorption (TPA) will start to limit supercontinua at around 0.26 μm twice the band-gap wavelength of silica which has been found to be in the region of 0.13 μm. The two photon absorption is given by:

$$\alpha_{TPA} = \frac{\beta_{TPA} P}{A_{eff}} \tag{4.2}$$

where β_{TPA} is the two-photon absorption coefficient. Therefore as this loss mechanism is

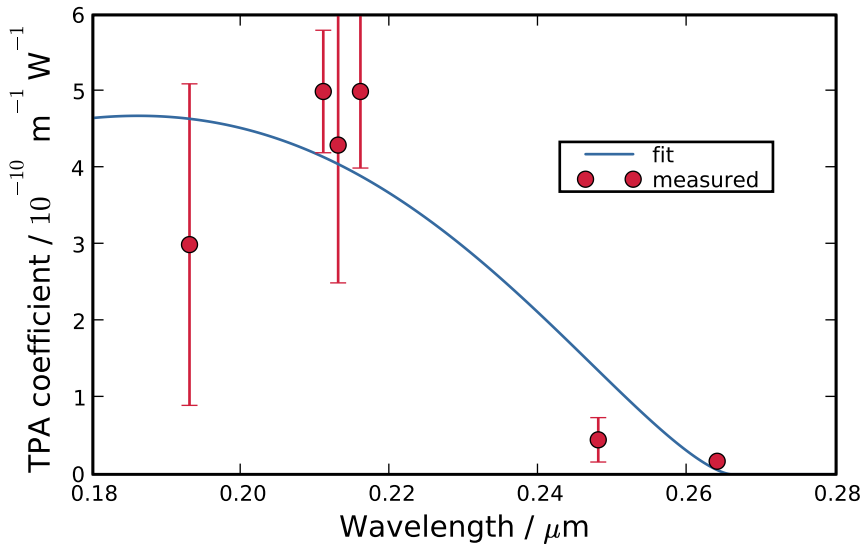


Figure 4.27: Measured values of β_{TPA} (from the literature) with a fit of Eqn. 4.3.

nonlinear, shortening the fibre and increasing the peak power brings no advantage. Thus as the TPA loss increases towards shorter wavelengths there will come a point where no nonlinear process has sufficient gain. A model of two-photon absorption [deS96] defines β_{TPA} to be given by:

$$\beta_{TPA} = a\frac{(b\omega-1)^{\frac{3}{2}}}{(b\omega)^5} \tag{4.3}$$

$$b = \frac{2\hbar}{E_g} \tag{4.4}$$

where a is a fitting parameter, ω is the frequency and E_g is the band-gap of the material (in terms of energy). As is seen from this model, β_{TPA} is very strongly wavelength dependent (as you get closer to the band edge, the absorption increases dramatically). The two photon absorption in silica has been measured multiple times at a variety of wavelengths, Fig. 4.27 shows a fit, based on Eqn. 4.3 to the values from the literature [Sla03]. From these values we can calculate the expected loss in a tapered fibre structure at these wavelengths. Taking the extremely conservative estimate of just 1 mW in a tapered fibre with $A_{eff} = 3.5 \times 10^{-12}$ m^2 (which is an estimate for our tapers) we get the attenuation curve shown in Fig. 4.28 along with Rayleigh scattering. For higher powers, the attenuation increases in proportion to the power. From these estimates it is clear that no significant supercontinuum can be generated below 0.26 μm in silica fibre. This coincides with the extreme limit of the broadening observed in [Efi03] and is shorter than the limit imposed by the currently understood mechanisms of supercontinuum generation.

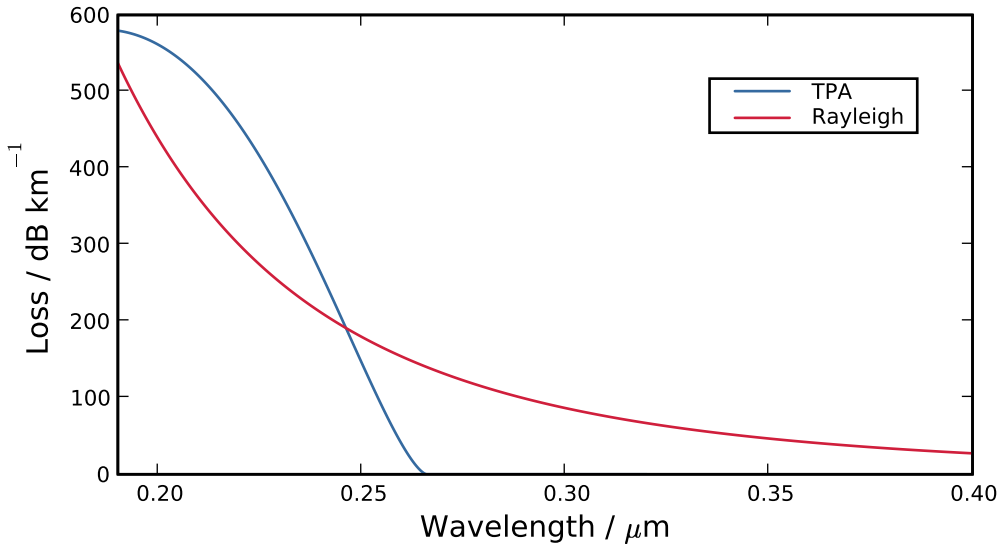


Figure 4.28: ***(numerical)*** Estimated values of Rayleigh and TPA loss at the output end of taper SCT1. The TPA loss is estimated with a peak power of just 1 mW. The TPA loss increases in proportion to the power.

4.5 Conclusion and future development

In conclusion we have demonstrated the first use of tapered PCFs manufactured at the drawing tower. Such a manufacturing technique allows for longer tapers with better control of the dispersive properties along their lengths. We used tapers several meters long, with a constant air-fill fraction and a continuously changing pitch along their lengths, over several meters, for supercontinuum generation to the very short visible and UV wavelengths. By selecting the taper profiles, either a very flat, very high average power supercontinuum from 0.38 to 2.2 μm with a spectral power of over 2 mW/nm across the visible/UV was achieved, or an enhanced UV continuum as short as 0.34 μm was obtained. The mechanism of the blue/UV edge generation was found to be initially four-wave mixing in the zero dispersion decreasing taper followed by trapping of dispersive waves due to high power solitons. As the tapers aid the self-Raman scattering of the solitons by preserving their bandwidth, the taper significantly enhances the dispersive wave trapping process. In addition, as the taper ensures group velocity matching to shorter wavelengths over extended fibre lengths, the blue/UV edge is driven to very short wavelengths. We used tapers which were optimal for this trapping process to further enhance the UV development. Finally fundamental limits to the short wavelength edge, due to linear and nonlinear loss were analysed.

Future directions would include power scaling by engineering the pump source to achieve higher spectral powers, and optimisation of the taper profiles to try and further

enhance the UV continuum edge until the loss limits are reached.

5 Pulse compression in dispersion decreasing PCFs

5.1 Introduction

Optical pulse compression is an important tool for many systems which require pulses much shorter than 1 ps because primary seed lasers, particularly reliable fibre based lasers around 1.06 μm, are often not short enough themselves. One of the most compact and versatile compression schemes is adiabatic soliton compression in long lengths of dispersion decreasing fibre. This technique can guarantee bandwidth limited output while still offering very high compression ratios. Until recently, adiabatic soliton compression had not been demonstrated at wavelengths shorter than $\sim$ 1.3 μm because it requires anomalous group velocity dispersion – as it is a soliton effect – which is unachievable in conventional single-mode optical fibre below this wavelength. In this chapter we make use of dispersion decreasing photonic crystal fibre, made by tapering the PCF structure, to achieve decreasing anomalous dispersion at 1.06 μm and use these fibres to perform adiabatic soliton compression. The ability to taper PCF structures over several tens of meters was developed at the University of Bath as a collaboration on this project. The motivation was to achieve a compact fibre-based compression scheme at 1.06 μm while maintaining high pulse quality.

At the same time as the work in this chapter was being carried out, a theoretical [Hu06] and experimental [Tse06] result with the same goal were reported. In the experimental result, a small compression factor of 2 was demonstrated in a tapered PCF at 1.06 μm in an 8 m fibre.

5.2 Pulse compression techniques with optical fibres

In this section we review the three most important pulse compression techniques which utilise optical fibre. They are all fundamentally based on the same principle. To compress an optical pulse two things must be achieved. First the spectral bandwidth of the pulse must be expanded to accommodate the shorter pulse duration and secondly, the phase

across the expanded spectrum must be made flat, i.e. the pulse must not be chirped (although some degree of pulse compression can, of course, be achieved without fully dechirping the pulse). The expansion of the spectral bandwidth must be achieved through a nonlinear effect, in all of the cases considered here, self-phase modulation is utilised. The removal of the pulse chirp is achieved through dispersive effects.

5.2.1 Fibre-grating compressors

Fibre-grating compressors are based on some of the earliest pulse compression schemes which themselves were based on techniques for chirped radar. A suitably chirped pulse is passed through a delay line (usually a pair of gratings) so that the chirp is exactly cancelled. Usually the chirp must be linear as most gratings are also linear. In original schemes, the optical pulse was chirped through SPM in a nonlinear material. However, only the central portion of the pulse will be linearly chirped in this case. A significant advance was made when it was recognised that the combination of SPM and positive group velocity dispersion (normal dispersion) produced a linear chirp on the pulse. Clearly an optical fibre is perfect for such a task. This setup was first described and used in the early 1980s [Sha82; Gri82]. A second advantage of the fibre scheme is that the chirp is uniform across the spatial distribution of the pulse, which is not the case with the use of SPM in bulk materials. In modern setups the delay line consists of a pair of transmission gratings and the pulse is passed through twice. This ensures that the spatial chirping of the gratings is fully compensated for. By carefully selecting the power of the input pulse, the length of fibre used for the chirping and the separation between the transmission gratings a highly tunable source of bandwidth limited pulses can be produced.

In the first demonstration of a fibre-grating setup 90 fs pulses were passed through 15 cm of fibre and then compressed with a pair of gratings with a 1.6 μm pitch separated by 6.4 cm. This resulted in pulses compressed to 30 fs which was a record at the time [Sha82]. Further results soon followed leading to pulse durations of 90 fs [Nik83], 16 fs [Fuj84], 12 fs [Hal84] and then 8 fs [Kno85].

Significant increases to the overall compression ratio were achieved by using both fibre-grating compressors and then soliton-effect compressors in sequence (see following sections). First 1100 times compression resulting in 90 fs pulses was reported [Tai86], then compression of 90 ps pulses to 33 fs was achieved, a compression ratio of 2700 [GN87].

The power scaling of the system is limited by the onset of Raman scattering in the chirping fibre. The main drawbacks of fibre-grating compressors are the bulk setup, leading to a lack of robustness, and the need to considerably readjust the setup to accommodate different input or output pulse durations. Even so, fibre-grating compressors remain one of the most versatile and primary tools for pulse compression.

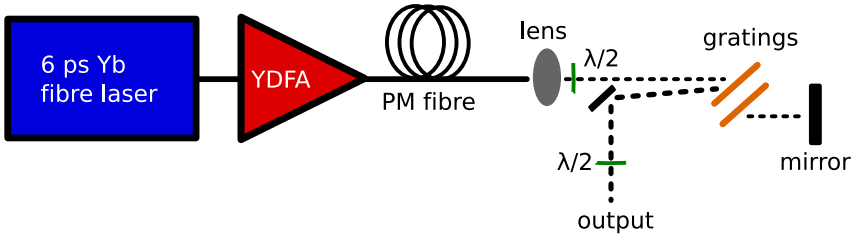


Figure 5.1: Experimental setup for fibre grating compressor. YDFA = ytterbium doped fibre amplifier; PM = polarisation maintaining.

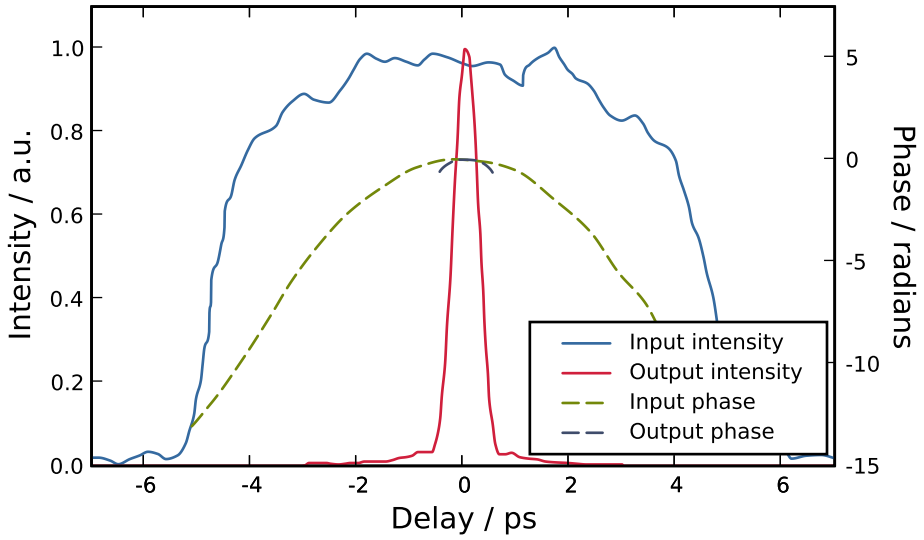


Figure 5.2: ***(experimental)*** Intensity and phase of pulses measured at the input and output of the gratings of the fibre grating compressor.

To illustrate this technique, we consider the pulse source used as the pump in the compression experiments described below. This was, ironically, based on a fibre-grating compressor so that we could optimise the input pulse duration to the dispersion decreasing fibre. This setup was based on a system constructed by my colleagues in the Femtosecond Optics Group [Ken07] and is shown in Fig. 5.1. A semiconductor saturable-absorber, mode-locked fibre laser producing linearly polarised 6 ps pulses was used as the seed source. This was amplified in a low power, polarisation preserving ytterbium fibre amplifier to a power of a few tens of milliWatts. The pulses were then passed through a variable length of normally dispersive polarisation maintaining fibre (~20 m) with a nonlinearity $\sim 5\,\mathrm{W^{-1}km^{-1}}$ and dispersion $\sim -34\,\mathrm{ps\,nm^{-1}km^{-1}}$. The degree and shape of the phase of the output pulses was measured with a FROG (frequency resolved optical gating) setup. Fig. 5.2 shows the result for one optimally adjusted pulse, where the parabolic phase of the input pulse is evident (linear chirp). Due to the dispersion of the fibre stretcher, the

pulses have broadened to 9 ps and the time-bandwidth product increased to 12. These pulses were then double passed through a pair of transmission gratings with a pitch of 0.8 μm and separation optimised for maximum compression (approximately 35 mm). The reflecting mirror was tilted up slightly from the optical axis thus enabling the compressed pulse to be separated. The resulting pulse and phase are also shown in Fig. 5.2. The compressed pulses in this case were 560 fs with a time-bandwidth product of 0.7. The compression ratio achieved was therefore 10 across the whole system.

By adjusting the amplifier power, fibre length and grating separation, the pulse duration at the output can be varied while maintaining a small time-bandwidth product. For the experiments below we used a tuning range of 100 to 900 fs.

5.2.2 Using hollow photonic band-gap PCF for pulse compression

With the introduction of hollow photonic band-gap fibre a new technique for pulse compression became available. This is essentially the same as a fibre-grating compressor, except the delay line is now implemented with a photonic band-gap fibre. Such fibre makes a very good delay line because is has very low nonlinearity and strong anomalous dispersion at the long wavelength band-edge – a fundamental feature of a photonic band-gap. This technique was first demonstrated in the context of chirped-pulse amplification [dM03; dM04c; Lim03] and then also directly for compression [dM04a]. This technique can be implemented in a fully fibre-integrated fashion and hence maintains the benefits of both the fibre-grating compressor and the fibre format.

5.2.3 Soliton effect compressors

Soliton effect compressors (SEC) utilise the propagation of high order solitons. As we reviewed in Section 1.5.3, a high order soliton follows a periodic evolution of temporal splitting, compression and expansion. The pulse compression technique is to simply remove the soliton from the fibre at its point of maximum compression. Essentially the spectral broadening through SPM and chirp cancelling through dispersion occur simultaneously, distributed throughout the fibre.

To illustrate this technique we have run some simulations of the propagation of an $N = 8$ soliton through a fibre, the results are shown in Fig. 5.3. The initial $N = 8$ soliton has a very small amplitude compared to the compressed pulses and hence can barely be seen on the scale of Fig. 5.3. The input pulse compresses to a considerably shorter pulse in a fraction of a soliton length. If the fibre is cut at the optimum location, then large compression factors can be realised. For this numerical example the input pulse of 1 ps is compressed to 157 fs after propagation through $0.03 z_s$ of fibre. A compression factor of over 6.

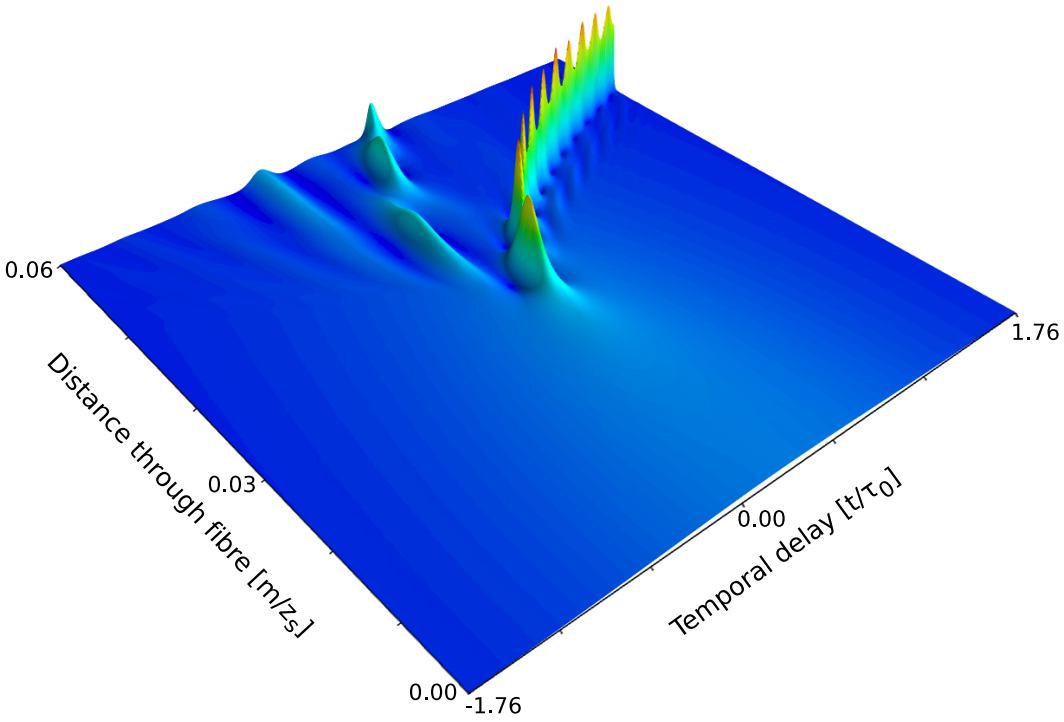


Figure 5.3: ***(numerical)*** A perspective plot of the temporal power of an $N = 8$ soliton through an optical fibre in the time domain.

After this point of maximum compression, however, the high order soliton fissions (see the discussion of soliton fission in Chapter 1 for details of this process). The first ejected soliton starts to be delayed due to a lower group velocity and hence the pulse spreads apart. Further solitons will be emitted and no recompression will occur. Due to this the correct length for a given input power has to be carefully selected, usually by experiment. An approximate guide to the achievable compression and optimum length was given in [Dia86]. The compression factor was determined to be approximately $4.1N$, however this analysis did not take Raman or high order dispersion effects into account and so this is an over estimate, due to the soliton fission process. However the separation of the fissioned soliton through intra-pulse Raman scattering is a useful way to separate the compressed pulse from the pedestal and the remains of the input pulse [Agr90].

It should also be noted that the compressed pulse will not have a sech^2 shape and will tend to have a large pedestal as N is increased. For example, a compression ratio of 60 will lead to up to 80% of the pulse energy moving to the pulse pedestal [Pel97]. As high compression factors require higher N this means that available pulse quality degrades as high pulse compression is achieved.

The first demonstration of soliton effect compression was in 1983 [Mol83]. The idea was

expressed as being a combination of SPM chirp and dispersion compensation, distributed throughout the fibre. A compression ratio of 27 was obtained. A compression to below 19 fs was subsequently reported [Mit87]. Soliton effect compression at 1.06 μm in a PCF was recently demonstrated by my colleagues [Ken05].

5.2.4 Adiabatic soliton compression

Adiabatic soliton compression can be understood by considering the balance between soliton energy and pulse duration and the fibre dispersion and nonlinearity which is described by Eqn. 5.1, which is just a reorganisation of the soliton equation given in Section 1.5.3.

$$\tau_0 = \frac{2N^2|\beta_2|}{\gamma E_s} \tag{5.1}$$

Where $E_s = 2P_0\tau_0$ is the soliton energy, $\tau_0 = 0.568\tau_{FWHM}$ is the soliton duration and and the other symbols have their usual meanings. Fundamental solitons display the remarkable property of being highly stable to small perturbations. The technique of adiabatic soliton compression utilises this fact to compress a soliton by gradually adjusting the parameters in Eqn. 5.1. Note that a fundamental soliton is simply a balance between SPM and dispersion and so the same basic processes, mentioned above, of nonlinearity and dispersion are being utilised to achieve the pulse compression.

Soliton propagation is adiabatic when the fibre parameters such as dispersion and nonlinearity, or the soliton energy (through gain or loss) vary slowly with respect to the soliton length z_s. In this regime the total energy is contained in the soliton, which behaves according to Eqn. (5.1). In this case, it is clear that the soliton duration will change if either the dispersion or the nonlinearity is changed along the fibre. These parameters are changed by varying the core size (tapering) in a conventional fibre or by changing the microstructure parameters in a PCF. It has been shown that the length of the taper and the taper profile are not critical parameters for the soliton compression as long as the adiabatic condition is maintained by using sufficiently long tapers (typically several soliton lengths) [Mos97]. In this case, and neglecting the variation in γ, the input to output pulse duration ratio τ_0/τ_z is equal to the ratio of the input and output dispersion $\beta_2(0)/\beta_2(z)$. In practise, the soliton energy is not constant, due to the attenuation of the fibre. This reduction of soliton energy leads to pulse broadening and so must be compensated for by additional dispersion decrease. In contrast, additional gain increases the soliton energy and pulse compression can be achieved by this mechanism alone, typically using Raman amplifiers which are very well suited to provide the distributed gain required for adiabatic soliton propagation [Gou89; RH00; Guy98]. The compression due to Raman gain is eventually limited by the gain bandwidth.

Fundamental limits to the minimum pulse duration achievable with adiabatic soliton compression result from higher order dispersion (which disturbs the balance between SPM and dispersion) and intra-pulse Raman scattering which will eventually shift the soliton into regions of higher or normal dispersion. Though it should be noted that use has been made of intra-pulse Raman scattering to shift solitons into regions of lower dispersion and hence enhance the compression (even without tapering the fibre) [Mam93].

The technique of adiabatic soliton compression was derived from original ideas developed to solve the problem of soliton spreading through loss in optical communication systems [Taj87]. The original idea was to compensate for the soliton broadening (which arises due to a decrease in soliton energy) by decreasing the dispersion along the fibre length. Further analysis [Kue88; Smi89; Iva92] showed that soliton compression can be achieved by over compensating for the fibre loss with the dispersion decrease, and that decreasing dispersion is equivalent to gain. Many results soon followed [Mam90; Che91; Che92; Che93]. It has also been demonstrated that a continuous decrease in dispersion is not required, but a step-like dispersion profile can be utilised as long as the individual steps are small compared to z_S [Che94a; Che94b].

In standard optical fibre the input to output dispersion ratio is limited by the largest core/cladding refractive index profile. Typically, ratios around 20 are possible [Pel97]. Although 38 times compression has been demonstrated with careful control of the third order dispersion [Tam99]. This ratio can be increased significantly by using PCF as greater control of high order dispersion is possible.

Outside of the adiabatic regime, the soliton will shed energy into non-solitonic radiation leading to spectral and temporal distortion of the pulse and therefore the useful pulse compression achievable will be limited. As the soliton length is proportional to the square of the pulse duration, this dictates that longer tapers are required for compression of longer pulses and hence for high compression ratios.

Although true adiabatic compression is achieved by injecting $N = 1$ solitons it is possible to mitigate the effects of fibre loss and enhance the pulse compression by injecting pulses corresponding to $1 \leq N \leq 2$. This can lead to considerably higher compression ratios without significantly decreasing the pulse quality [Pel97].

5.2.5 Combined adiabatic and soliton effect pulse compression

As noted above, the soliton effect compression of high order solitons and adiabatic compression in a dispersion decreasing fibre can be combined to achieve the higher compression ratios of the former with the higher pulse quality of the later [Kue88; Pel97]. This technique allows one to use shorter fibre lengths, as short as one soliton period, while still obtaining the high pulse quality. It also allows for achieving higher compression ratios

than possible using the decreasing dispersion alone. From the example given in [Pel97] an $N = 1.5$ soliton can achieve twice the compression ratio of pure adiabatic compression, in half the fibre length, emitting only 11% of its energy to non-solitonic radiation. Furthermore, subsequent propagation of the compressed pulse showed it did not significantly change shape and behaved similarly to a fundamental soliton, rather than a high order soliton, even though an $N = 1.5$ soliton would eventually evolve into an $N = 2$ soliton in a constant dispersion fibre. Further increases in the output pulse quality of combined SEC and dispersion decreasing systems can be obtained by using Gaussian rather than the hypersecant shape of a soliton for the input pulse. Simulations suggest that in this case the pedestal is reduced [Pel97]. It should be noted however that the results achieved in a non-adiabatic compression system will not be as high quality as those of a properly adiabatic compression where fundamental soliton propagation is assured [Fat02].

If the fibre length used is relatively short with respect to the soliton length then a dispersion decreasing profile that is slow initially, such as an exponential profile, is optimal. However, for longer fibre lengths the profile shape has no significant effect on the compression which can be achieved.

5.3 Design of dispersion decreasing PCF

5.3.1 Manufacturing technique

The dispersion decreasing PCF, like that used in the previous chapter, was manufactured by J. C. Knight's group at Center for Photonics and Photonic Materials, University of Bath. Refinements were made to the process used for the supercontinuum tapers to gain greater control over the tapering process. These were achieved by more careful control over the stopping of the fibre draw and by variation of the pressure in the fibre air-holes. The result was the ability to produce much longer tapers, with the air-hole size varying independently of the pitch.

5.3.2 Controlling the dispersion in a tapered PCF

As we discussed in the previous chapter, short tapered PCF has been produced either by simultaneous stretching and heating to post-process a fibre [Hum06] or, as for the supercontinuum generation tapers we discussed in Chapter 4, at the drawing tower as the fibre was being drawn [Kud06; Tra06]. However, it is impossible to use these short tapers to achieve high compression ratios or to compress pulses longer than a few hundred femtoseconds because they are not sufficiently long compared to the soliton period. In this chapter we report tapers which are up to 50 m long and which have much lower loss,

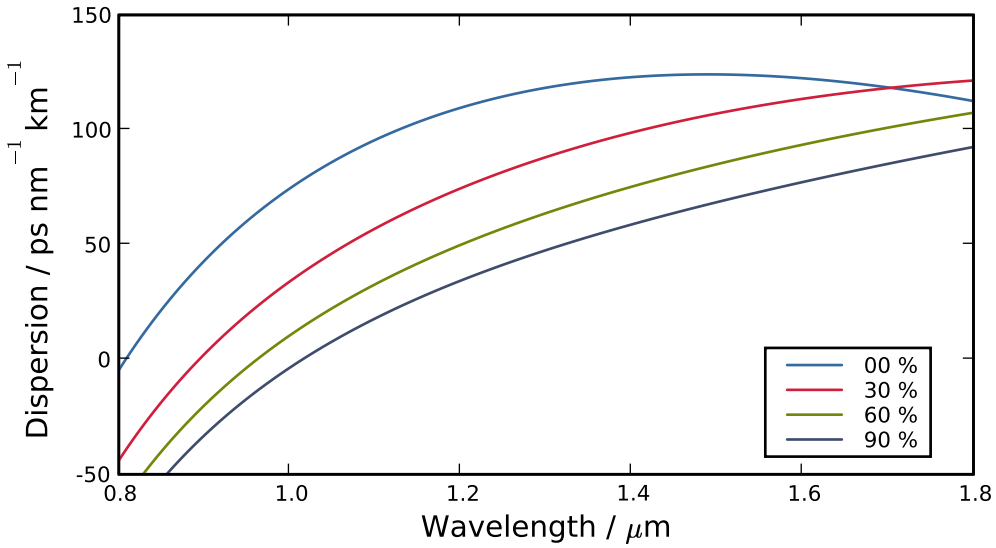


Figure 5.4: ***(numerical)*** The dispersion curves of Taper S1 (d/Λ constant at 0.8, Λ changing from 2 to 4.2 μm) at various lengths along the fibre (shown in percent of the taper length as the actual taper length can vary).

significantly broadening the range of applications for which tapered PCFs can be used.

The fibres used in our compression experiments were produced after extensive numerical modelling with the generalised nonlinear Schrödinger equation to optimise the interplay between the loss, dispersion and nonlinearity. In particular, the change in γ can be very significant and care must be taken to ensure that it increases as the dispersion decreases or some cancelling of the compression effect can occur. The dispersion profiles of the PCFs used in these simulations were calculated using the analytical vector effective-index method for efficiency (see Section 1.4.1). While designing the PCF tapers we concentrated on achieving the correct input/output ratio of dispersion and nonlinearity for pulse compression. We assumed that the taper profiles would be approximately linear.

To illustrate the importance of this interplay we discuss two different tapered PCF structures. The first taper (S1) has a constant air-hole diameter to pitch ratio (d/Λ) while the pitch is increased by a factor of 2. This structure is similar to those we used for supercontinuum generation (though used here in reverse) [Kud06; Tra06]. Fig. 5.4 shows how the dispersion curve evolves along this taper. The zero dispersion wavelength moves to longer wavelengths as the pitch increases and hence the dispersion at the fixed pump wavelength of 1.06 μm decreases. However, as the pitch increases, the effective area also increases and hence the nonlinearity decreases. The effect of this can be to compensate for the dispersion decrease.

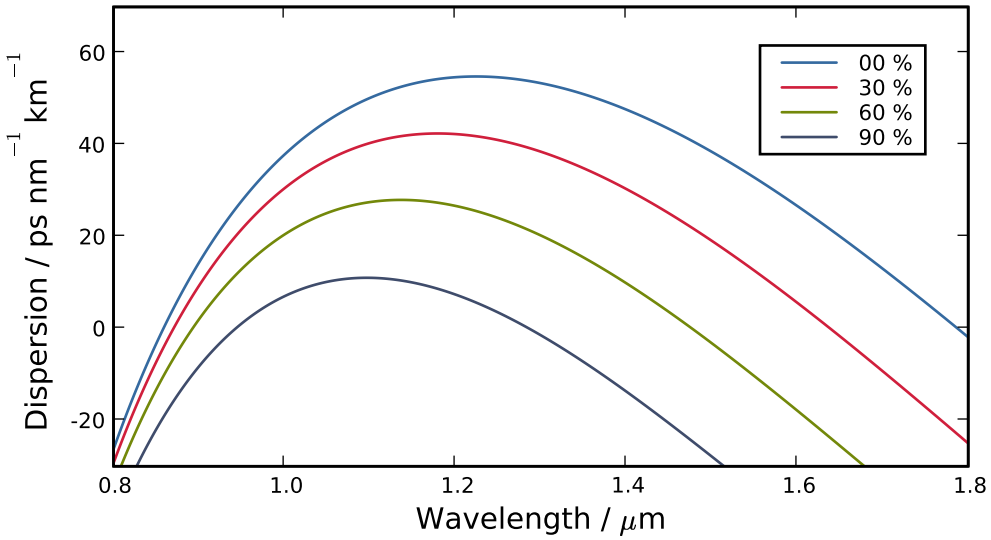


Figure 5.5: ***(numerical)*** The dispersion curves of Taper S2 (d/Λ changing from 0.55 to 0.44 and Λ changing from 1.76 to 1.56 μm).

In the second taper we considered (S2) the air-hole diameter to pitch ratio is reduced by 20% and the pitch is reduced by just over 11%. This structure is similar to that used in the experiments described below. Fig. 5.5 shows how the dispersion curve evolves along this taper. In this case, the dispersion at the pump wavelength decreases as the second zero dispersion wavelength of the fibre moves to shorter wavelengths. But in this taper the pitch is actually reduced and combined with the reduction in the hole diameter, the effective core stays approximately constant and hence so does the nonlinearity.

We simulated the propagation of an $N = 1$ soliton through both of these structures over 6 soliton periods. The results are shown in Fig. 5.6. Fig. 5.6 also shows the comparison of input/output dispersion and nonlinearity along the tapers. From these figures, we see that both have comparable dispersion decrease along the taper, but S1 has a commensurate decrease in nonlinearity whereas S2 has almost constant nonlinearity. The resultant compression ratios are 2 and 8 respectively.

We studied a number of structures within our manufacturing capability and concluded that working around the second zero dispersion wavelength as in taper S2 was the optimal way to achieve compression in a tapered PCF.

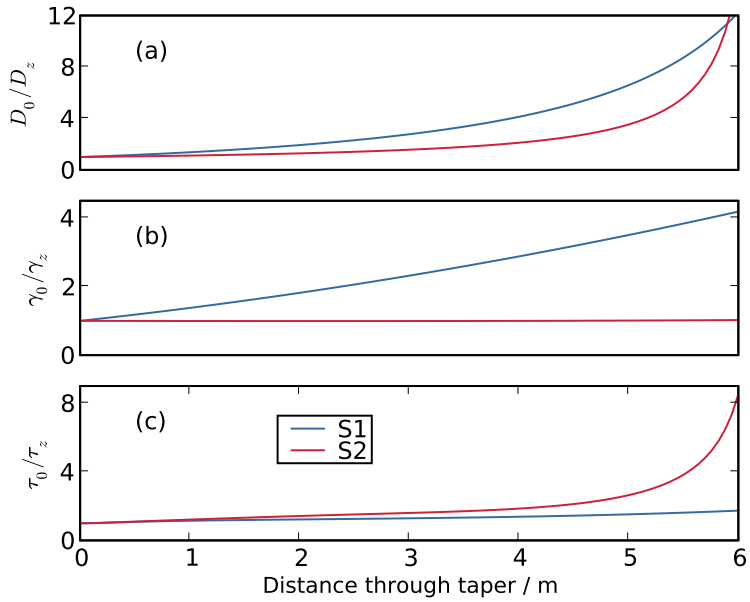


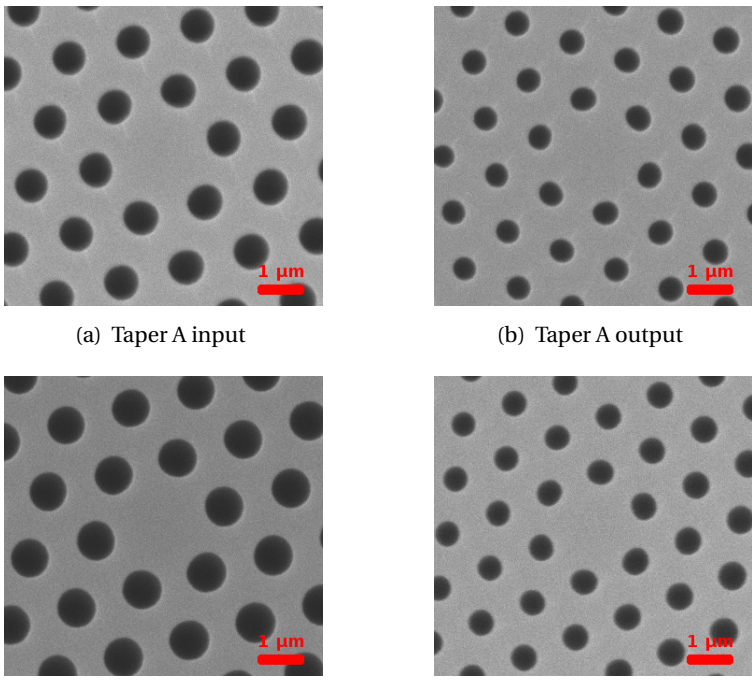
Figure 5.6: ***(numerical)*** Profiles of (a) the dispersion and (b) the nonlinearity along two illustrative tapers S1 (d/Λ constant at 0.8, Λ changing from 2 to 4.2 μm) and S2 (d/Λ changing from 0.55 to 0.44 and Λ changing from 1.76 to 1.56 μm). (c) The simulated pulse compression factors along the tapers. All are shown over a length corresponding to 6 soliton periods. The input pulse duration was τ_{FWHM} = 800 fs and both tapers had a realistic loss of 25 dB/km.

5.4 Experimental results

5.4.1 Properties of the dispersion decreasing PCF

Experiments were carried out with two tapers we label A and B. Fig. 5.7 shows SEM images of the tapers used in this work. Taper A had a pitch changing from Λ = 1.44 to 1.25 μm and a hole diameter to pitch ratio changing from d/Λ = 0.52 to 0.42. Taper B had Λ = 1.48 to 1.20 μm and d/Λ = 0.55 to 0.45.

The dispersion of the fibres was measured using an interferometric technique. A short section (~ 40 mm) of fibre was placed in one arm of a Mach-Zehnder interferometer equipped with a moveable mirror. An optical supercontinuum was used as a light source, and spectral interferograms were recorded for different values of the delay. From this the group delay was obtained, and used to find the group velocity dispersion. Fig. 5.8 shows the measured dispersion curves for the two tapers. Taper A was 17 m long and had a measured dispersion changing from D ~ 33 to~ −5 ps nm^{-1} km^{-1} at 1.06 μm. Taper B was 56 m long and had a measured dispersion varying from D ~ 40 to 10 ps nm^{-1} km^{-1}. In both tapers the attenuation was measured by the cut-back technique to be around 30 dB/km in the spectral range of interest. The nonlinearity of both fibres varies from



(a) Taper A input (b) Taper A output

(c) Taper B input (d) Taper B output

Figure 5.7: Scanning electron micrographs of the input and output ends of the tapers used in the pulse compression experiments.

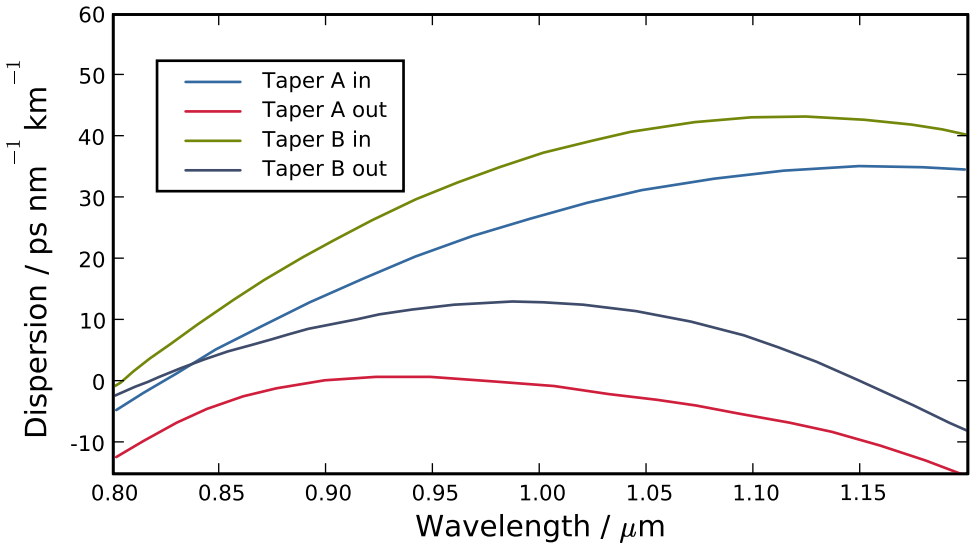


Figure 5.8: ***(experimental)*** The measured dispersion profiles of the tapers

about 40 to 50 W^{-1} km^{-1} with the core diameter varying from 2.2 to 2 μm.

Although the dispersion of Taper A is slightly normal at the output, it is so only for a very

short propagation length at the end of the taper (estimated from the previous cut-back of the taper), therefore we expect it to have only a small influence on the pulse compression process.

5.4.2 Experimental setup

The tapered PCFs were pumped with pulses from the fibre-grating compressor setup shown above in Fig. 5.1. The pulse duration could be varied between 100 and 900 fs. The pulses always had a time-bandwidth product of less than 0.75. They were then injected into the tapers with a coupling efficiency of approximately 60% and the output pulses were analysed using a second-harmonic generation autocorrelator and an optical spectrum analyser. The pulse energy was controlled using a half-wave plate before the polarised transmission gratings. The polarisation of the pulses entering the tapered fibre was adjusted by an additional wave plate. The input pulse durations were optimised for the highest compression ratio in each taper. For Taper A, 655 fs pulses were used; for Taper B, 830 fs pulses were used.

In what follows we often refer to the soliton order N when discussing results, however, this value of N was calculated from the input pulse energy. As the time-bandwidth product of the input pulses and the pulse shape did not perfectly agree with an ideal soliton of 0.31 and hypersecant profile, not all of the energy was used to form the soliton and these values of N are an over estimate.

5.4.3 Results

The results for Taper A are shown in Fig. 5.9 to Fig. 5.12. From Fig. 5.9 the highest order soliton, estimated as $N = 2$, compressed to a pulse of sub 50 fs duration, a compression factor of over 13. The $N = 1$ soliton actually broadened, though this may be due to the inaccuracy in N. Other factors possibly leading to the broadening are loss and the short length of normally dispersive fibre at the taper end. Increasing the pulse energy led to greater pulse compression. It should be noted that the optimal soliton effect compression (SEC) of an N=2 soliton in an optimal fibre length will be a factor of 8 [Dia86], this would occur in a fibre length of 4.7 m and subsequent propagation would degrade the compression. Here we have a suboptimal SEC length and so the decreasing dispersion is clearly significant for obtaining the 13 times compression observed. However, the soliton length $z_s = 11$ m in this taper, and thus the taper length of 17 m is insufficient for adiabatic compression alone. It is the combined effect of SEC and decreasing dispersion which achieves the pulse compression ratio of 13 in this taper. Fig. 5.10 shows a fringe resolved autocorrelation trace of the compressed $N = 2$ soliton. From the good quality 8:1 contrast ratio and smooth wings it is evident that the temporal structure of the compressed pulse

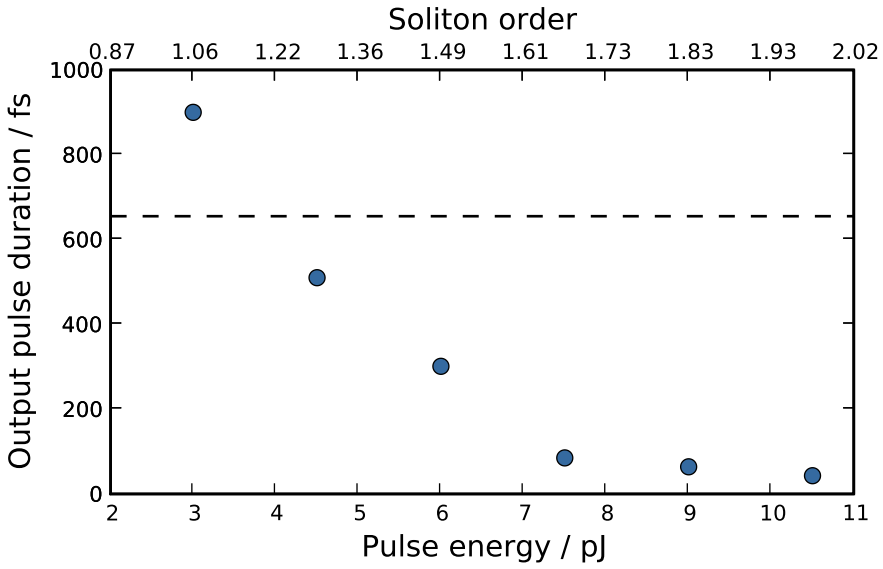


Figure 5.9: ***(experimental)*** Output pulse duration (FWHM) from Taper A for given soliton order (input $\tau_{FWHM} = 655$ fs).

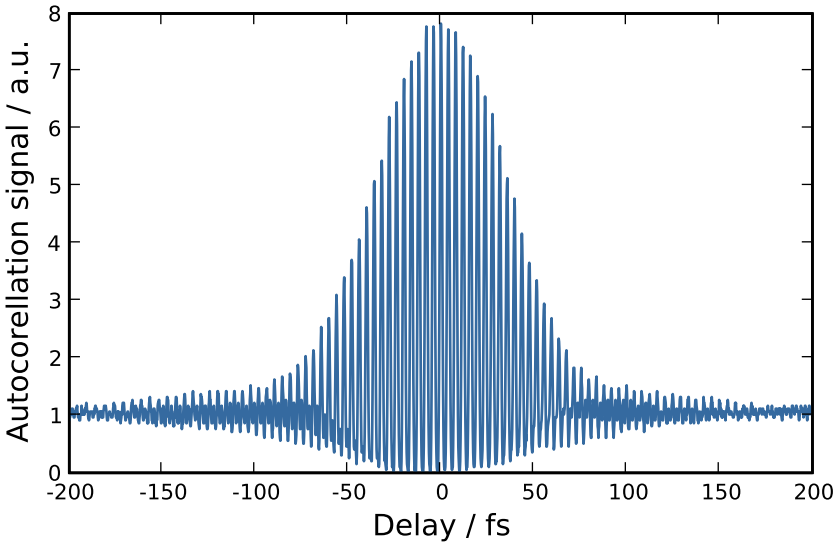


Figure 5.10: ***(experimental)*** Fringe-resolved autocorrelation of the output pulse of Taper A when pumped with a pulse corresponding to $N = 2$.

is good. Fig. 5.11 shows the input and output pulses on the same scale, showing the large compression ratio. We believe that the output pulse duration from Taper A was inhibited slightly by the onset of normal dispersion at the end of the taper. Evidence of this can be seen from the spectra shown in Fig. 5.12 where for the $N = 2$ input, a dispersive wave at long wavelengths is observed. The compressed soliton is actually shifted to shorter

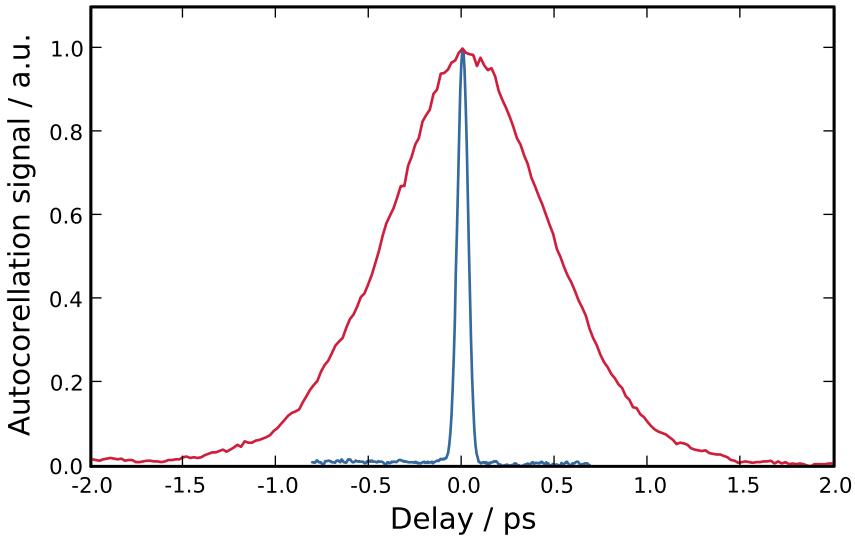


Figure 5.11: ***(experimental)*** Intensity autocorrelation of input and output to Taper A for $N = 2$. Input pulse duration is estimated to be 655 fs, output 43 fs

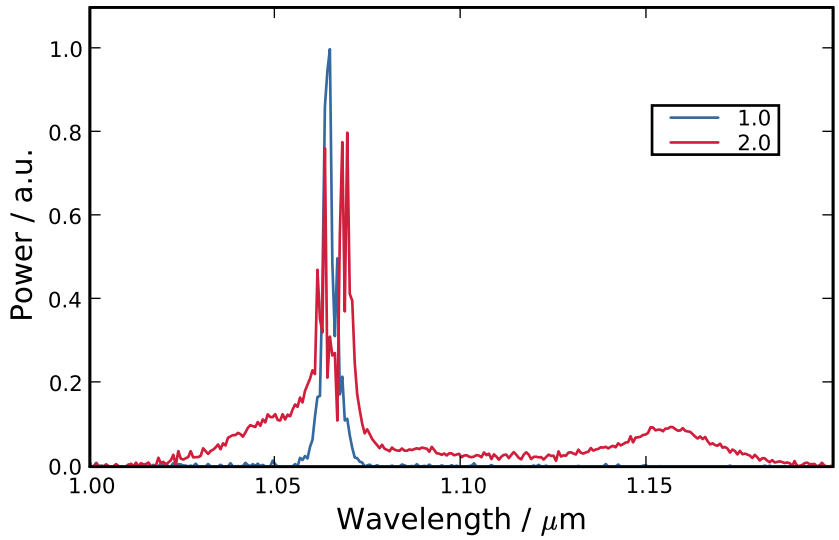


Figure 5.12: ***(experimental)*** Spectra of the output pulses of Taper A at various soliton orders.

wavelengths around 1050 nm and could be filtered from the dispersive components if desired.

The results for Taper B are shown in Fig. 5.13 to Fig. 5.15. From Fig. 5.13 we see that compression to a 55 fs pulse was achieved at the highest pulse input soliton order $N = 2$, this is a compression factor of 15. In contrast to Taper A, an $N = 1$ soliton is compressed by a factor of 3 in this taper and hence the assistance of SEC is not required. In fact at the

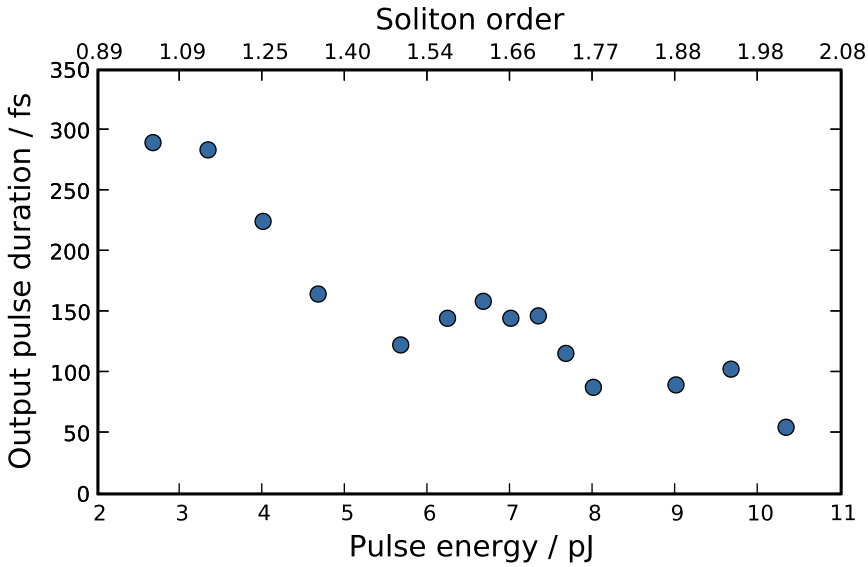


Figure 5.13: ***(experimental)*** Output pulse duration (FWHM) from Taper B for given soliton order (input $\tau_{FWHM} = 830$ fs).

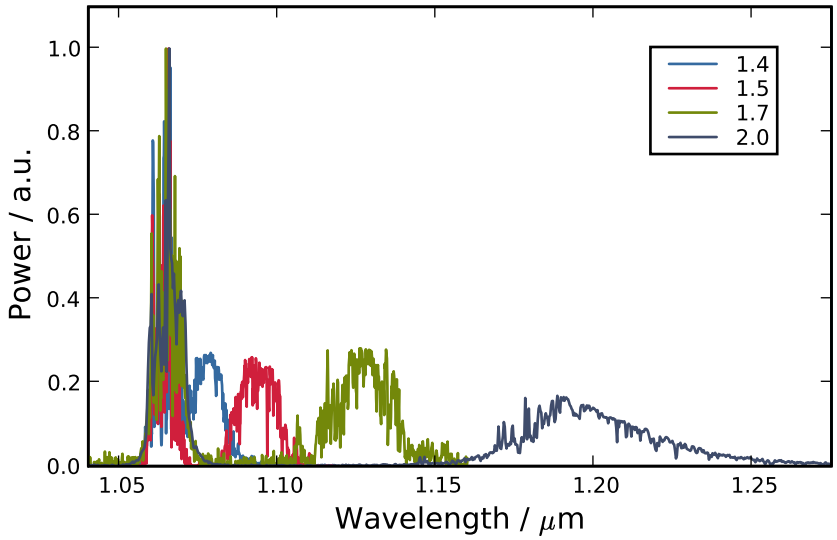


Figure 5.14: ***(experimental)*** Spectra of the output pulses of Taper B at various soliton orders.

pump wavelength the input/output dispersion ratio of this taper is approximately 4 and so, accounting for the inaccuracy in N, we see that we achieve the expected adiabatic compression. This is in contrast to Taper A because the length of Taper B is approximately 3-4 soliton lengths. However, a significant increase in compression is obtained for $N > 1$. The pulse spectra shown for the output of Taper B in Fig. 5.14 indicate soliton self-frequency shifting of the output solitons to longer wavelengths. By considering Fig. 5.8 it is clear

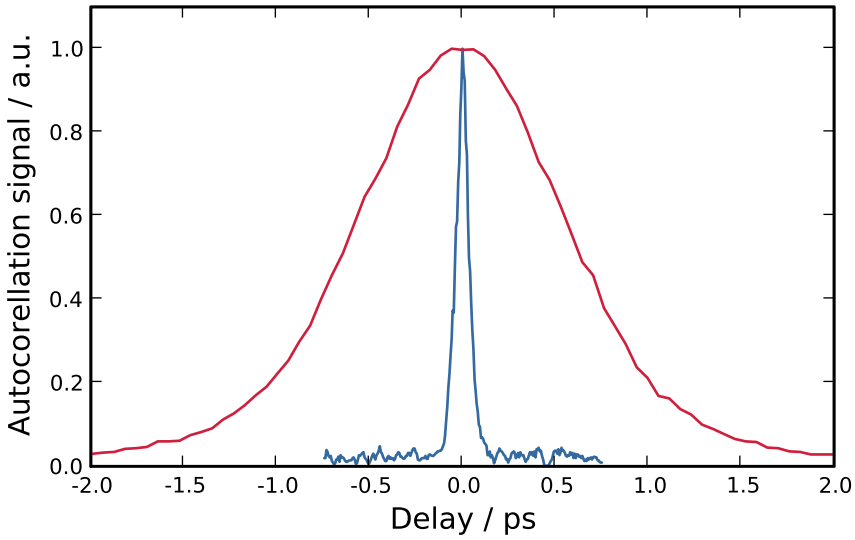


Figure 5.15: ***(experimental)*** Intensity autocorrelation of input and output to Taper B for $N = 2$. Input pulse duration is estimated to be 830 fs, output 55 fs.

that such a shift further decreases the dispersion and hence enhances the compression[1]. This explains why the compression factor is so much higher than that expected from the dispersion ratio at the pump wavelength alone. We should note here that the use of the Raman shift to cause a soliton to compress through decreasing dispersion in a non-tapered fibre has also been observed [Mam93]. From the spectra in Fig. 5.14 we confirmed that the time bandwidth product of the solitons was 0.31. Fig. 5.15 shows the input and output autocorrelations of the $N = 2$ soliton on the same scale.

5.5 Future possibilities

Many improvements can be made to the above experiments. The use of shorter input pulses and longer tapers to more clearly demonstrate the adiabatic compression would be interesting. More significantly, the use of much longer tapers (which depends only on improvements in manufacturing) should allow for the direct compression of the output of the compact SESAM source laser which was used in these experiments. If this can be achieved then a source of 50 fs solitons in 10×10 cm package could be realised.

Other possibilities include the use of dispersion decreasing PCF in a nonlinear loop mirror to achieve pulse compression, as discussed in the introduction to this chapter. Alternatively, correct engineering of the PCF structure could allow for adiabatic soliton compression purely by increasing the nonlinearity of the PCF, γ, while keeping the disper-

[1] Although the dispersion at the very end of the taper is normal at 1.2 μm it will be only for the very end of the taper and hence will not have significantly broadened the output pulses.

sion approximately constant. It may also be possible, by careful PCF design to achieve a decreasing dispersion PCF in the visible spectral region, suitable for pulse compression.

Finally, interesting results could be achieved by moving to the 1.55 μm region and carefully flattening the PCF dispersion to achieve extremely short pulses. Simulations suggest that pulses as short as a single optical cycle could be achieved.

5.6 Conclusion

In conclusion, we have demonstrated pulse compression ratios of over 15 in dispersion decreasing PCF by utilising soliton compression at 1.06 μm. By analysing the PCF dispersion and nonlinearity characteristics we optimised the tapering parameters of PCFs to produce pulses as short as 55 fs from input pulses of 830 fs. This demonstration has proved that the use of PCF tapers can enable high pulse compression ratios through adiabatic soliton compression at wavelengths where it is impossible to use conventional optical fibre. By further reducing the fibre loss and by careful control of the third order dispersion it should be possible to produce even shorter pulses.

6 Conclusion and outlook

In this thesis we have used the ability to tailor the dispersion and nonlinearity of photonic crystal fibres to control and enhance nonlinear effects. The results and analysis we have discussed have contributed to the body of knowledge on supercontinua and demonstrated original and improved techniques for their generation. We have also demonstrated adiabatic soliton pulse compression in spectral regions not previously accessible to this technique.

In particular, in Chapter 2 we made a study of the modelling and physical mechanism involved with continuous wave supercontinuum generation. We found that more detailed models of the pump lasers are required for full agreement between experiment and numerical results. We gained insight by taking a statistical approach to the distribution of soliton energies from MI and the expected spectral shift from self-Raman scattering. From these considerations we could understand the effect of the dispersion slope and change in nonlinearity with wavelength. We also found that the role of soliton collisions was important to the explanation of the full continuum bandwidth. Experimentally, we demonstrated a two-fold increase in CW supercontinuum bandwidth by using specialised low water loss fibres. We also made studies of the continuum noise and the effects of pump bandwidth. Further experiments to understand the dynamics are required. In the near future it should be possible to scale the CW supercontinuum powers up to the 100 W region. Also, by carefully designing the dispersion and pump parameters, it should be possible to generate a visible CW supercontinuum.

In Chapters 3 and 4 we looked in detail at the generation of visible supercontinua with picosecond pump pulses with high average power. In Chapter 3 we found that the pump and fibre parameters placed us in the MI/FWM regime, and we could understand the limits to the supercontinuum extent from the possible FWM phase matched processes allowed in the fibre. It was shown that simply moving the zero dispersion wavelength of the fibre towards the visible was not sufficient to extend the supercontinuum to the blue; but instead a cascaded fibre approach which optimises the initial MI process and later, extends FWM processes to shorter wavelengths was found to work well. In Chapter 4 we demonstrated that taking this technique to its natural limit, by tapering the PCF, produced

significantly enhanced and flatter supercontinua. We experimentally demonstrated over 3.5 W in a supercontinuum spectrum spanning from 0.34 to 2.4 μm. The visible region had less than 3 dB peak to peak variation and over 2 mW/nm spectral power. The initial mechanism was also found to be through MI/FWM leading to a broad visible continuum, but the UV extension was understood to be due to trapping of dispersive waves by high energy solitons. The unique group velocity matching features of the tapers, in addition to their preservation of the soliton bandwidth, enhance this process, enabling the short wavelength extension. This source has already found application to fluorescence lifetime microscopy [Owe07]. Further optimisation of the taper profiles ought to be possible to slightly extend the bandwidth, although two photon absorption will finally limit the process. Average power scaling of the continuum by engineering the pump source to achieve higher spectral powers could also lead to new areas of application.

In Chapter 5 we used completely different PCF tapers for adiabatic soliton compression. These tapers were optimised to preserve nonlinearity while decreasing the group velocity dispersion along their length. Due to this feature we were able to use them to achieve compression ratios of over 15 at 1.06 μm. Pulses as short as 55 fs were achieved from input pulses of 830 fs. By reducing the fibre loss and careful control of the third order dispersion it should be possible to produce even shorter pulses. The particular significance of this result is because conventional fibre cannot be used for adiabatic compression in this wavelength region.

Photonic crystal fibres have enabled the results of this thesis to be achieved. Future work will no doubt make use of new PCF designs – the versatility of these fibres has not been exhausted. For example, although hollow core photonic band-gap fibres have been widely used, especially for dispersion compensation, the use of solid core photonic band-gap fibres has been less widespread. However, these fibres have similar photonic band-gap guidance properties to hollow core fibres, with the associated extreme dispersion properties, while maintaining nonlinearity. Many applications can make use of this feature, for example for nonlinear processes with suppression of effects outside of the band-gap, or phase-matching due to the unique dispersion. Alternatively, the hollow core fibres can be filled with new materials to change their properties. The use of hydrogen filled fibres for enhanced Raman effects has been widely explored [Ben02], but the use of liquids has received little attention. By filling the core or cladding holes with a nonlinear liquid strong enhancement of certain processes could be observed. Also, the dispersion properties of the resulting structure could be more easily tunable as it is easier to change a liquid concentration than re-fabricate a structure [dM07]. The interplay of the dispersion tunability and nonlinear effects of liquid filled PCFs has also been suggested as a new route to supercontinua [Zha06]. Also, the use of liquid crystals may enable electrical

control of fibre properties [Lar03].

Other than new PCF structures, or different material inclusions, it is possible to use completely different glasses to make fibres and PCFs. Much interest has been expressed towards chalcogenide glass fibres and waveguides because of its enhanced nonlinearity and transmission to mid-infrared frequencies [Aso97]. However, its use may be limited by its particular sensitivity to the environment and toxicity. It also has a very unfavourable zero dispersion wavelength. More interesting are fluoride fibres, which have been extensively studied for nearly 30 years [Fra90]. They have zero dispersion wavelengths around 1.6 μm and transmission deep into the mid-infrared. The emerging high power thulium fibre laser technology is well suited to generate supercontinua or other nonlinear processes beyond 2-3 μm in these fibres. Other types of fibre have been suggested or used including tellurite [Pri07], and sapphire [Yin08].

Apart from the specific fibre structures or materials, nonlinear fibre optics in general is moving in new directions. Most of the basic processes have been well understood for some time. The more complicated emergent processes such as supercontinuum generation, which have been intensively studied over the past decade, are also now reasonably understood. Even so, new phenomena are being uncovered or re-discovered from previous generations (as supercontinuum itself was). For example there has been a revival of interest in soliton spectral tunnelling [Ser93; Kib07]. Another recent excitement has been about so called rogue waves in supercontinuum generation, with analogies to tidal waves in the ocean [Sol07]. These appear to simply be statistical fluctuations of the soliton generation process from MI, as we analysed in Chapter 2, but the conclusions and cross discipline input is novel. Other examples of such cross fertilisation include the reference to gravity like potentials when discussing soliton trapping, as we noted in Chapter 4 [Gor07b], and more recently, stimulating ideas relating nonlinear fibre optics with Hawking radiation from black holes [Phi08].

As with all research, many of these new analogies and ideas or fibre types and designs will prove incorrect or unsuccessful; but some will work. Nonlinear fibre optics in novel types of fibres is a vibrant and active field. This thesis has provided some examples of what can be achieved, but there is much more to do.

List of publications

Journal papers

1. Travers, J.C., Popov, S.V. & Taylor, J.R. “Efficient continuous-wave holey fiber Raman laser.” *Appl. Phys. Lett.*, 87 (2005) p. 031106.

2. Travers, J.C., Kennedy, R.E., Popov, S.V., Taylor, J.R., Sabert, H. & Mangan, B. “Extended continuous-wave supercontinuum generation in a low-water-loss holey fiber.” *Opt. Lett.*, 30 (2005) pp. 1938.

3. Travers, J.C., Popov, S.V. & Taylor, J.R. “Extended blue supercontinuum generation in cascaded holey fibers.” *Opt. Lett.*, 30 (2005) pp. 3132.

4. Kudlinski, A., George, A.K., Knight, J.C., Travers, J.C., Rulkov, A.B., Popov, S.V. & Taylor, J.R. “Zero-dispersion wavelength decreasing photonic crystal fibers for ultraviolet-extended supercontinuum generation.” *Opt. Express*, 14 (2006) pp. 5715.

5. Cumberland, B.A., Travers, J.C., Kennedy, R.E., Popov, S.V. & Taylor, J.R. “2 W/nm peak-power all-fiber supercontinuum source and its application to the characterization of periodically poled non-linear crystals.” *Opt. Commun.*, 277 (2007) pp. 134.

6. Travers, J.C., Stone, J.M., Rulkov, A.B., Cumberland, B.A., George, A.K., Popov, S.V., Knight, J.C. & Taylor, J.R. “Optical pulse compression in dispersion decreasing photonic crystal fiber.” *Opt. Express*, 15 (2007) pp. 13203

7. Rulkov, A.B., Ferin, A.A., Travers, J.C., Popov, S.V. & Taylor, J.R. “Broadband, low intensity noise CW source for OCT at 1800 nm.” *Opt. Commun.*, 281 (2008) pp. 154.

Conference papers

1. Cumberland, B.A., Travers, J.C., Kennedy, R.E., Popov, S.V. & Taylor, J.R. “Application of a 2W/nm All-Fiber Supercontinuum Source to the Characterization of Nonlinear

Crystals." *Conference on Lasers and Electro-Optics*, (2006) JThC53.

2. Cumberland, B., Ferin, A., Rulkov, A.B., Travers, J.C., Popova, S.V. & Taylor, J.R. "Non-linear optics and frequency conversion - fiber lasers in IR, VIS and UV (INVITED)." *Fiber Lasers IV: Technology, Systems, and Applications, Lase 2007, Photonics West*, (2007).

3. Cumberland, B.A., Travers, J.C., Popov, S.V., Taylor, J.R., O. I. Medvedkov and, S.A.V. & Dianov, E.M. "2.1 μm CW Raman Source in GeO2 Fiber." *Conference on Lasers and Electro-Optics*, (2007) CML7.

4. Cumberland, B., Travers, J.C., Popov, S.V. & Taylor, J.R. "High-Power Continuous Wave Supercontinuum." *Fiber Lasers V: Technology, Systems, and Applications, Lase 2008, Photonics West*, (2008).

5. Ferin, A., Rulkov, A., Travers, J., Popov, S. & Taylor, J. "Broadband, low intensity noise source for optical coherence tomography at 1.8¿ m." *Conference on Lasers and Electro-Optics*, (2007) JTuA45.

6. Kennedy, R.E., Rulkov, A.B., Travers, J.C., Popov, S.V., Gapontsev, V.P. & Taylor, J.R. "High power, completely fiber integrated super-continuum sourcesn (INVITED)." *Fiber Lasers II: Technology, Systems, And Applications, Lase 2005, Photonics West*, (2005).

7. Kennedy, R., Popov, S., Rulkov, A., Travers, J. & Taylor, J. "High power fibre integrated sources." *IET Seminar Digest: High Power Diode Pumped Lasers and Systems*, (2006).

8. Popov, S., Travers, J., Rulkov, A., Cumberland, B. & Taylor, J. "Versatile all-fibre lasers for bio-imaging applications (INVITED)." *Ultrafast Optics VI, Applications of High Field Short Wavelength Sources XII*, (2007).

9. Povazay, B., Bizheva, K., Gasparoni, S., Hermann, B., Unterhuber, A., Sattmann, H., Drexler, W., Pflug, R., Anger, E., Reitsamer, H., Ahnelt, P., Travers, J., Popov, S., Taylor, J. & Gapontsev, V. "Ultrahigh resolution, functional OCT with all-fiber broadband Raman-continuum light-source." *Conference on Lasers and Electro-Optics*, (2005) JThE34.

10. Stone, J., George, A., Knight, J., Travers, J., Cumberland, B., Rulkov, A., Popov, S. & Taylor, J. "Pulse compression at 1.06 μm in dispersion decreasing photonic crystal fibre." *Non-linear Photonics*, (2007) NThB2.

11. Travers, J.C., Popov, S.V. & Taylor, J.R. "Extension of Supercontinuum Generation to the Blue in Cascaded Holey Fibers." *Advanced Solid State Photonics*, (2005) WA2.

12. Travers, J.C., Popov, S.V. & Taylor, J.R. "High efficiency continuous-wave holey-fiber Raman laser." *Conference on Lasers and Electro-Optics*, (2005) CMV2.

13. Travers, J.C., Popov, S.V., Taylor, J.R., Sabert, H. & Mangan, B.J. "CW-Pumped, High Power, Extended Supercontinuum Generation in Low Water-Loss PCF." *Advanced Solid State Photonics*, (2005) TuC6.

14. Travers, J.C., Rulkov, A.B., V.Popov, S. & Taylor, J. "High brightness polychromatic visible generation in photonic crystal fibers with picosecond Yb pumping." *Conference on Lasers and Electro-Optics*, (2005) CWA3.

15. Travers, J., Popov, S., Taylor, J., Sabert, H. & Mangan, B. "Extended bandwidth CW-pumped infra-red supercontinuum generation in low water-loss PCF." *Conference on Lasers and Electro-Optics*, (2005) CFO4.

16. Travers, J., Popov, S., Taylor, J., Sabert, H. & Mangan, B. "CW-Pumped, High Power, Extended Supercontinuum Generation in Low Water-Loss PCF." *Advanced Solid-State Photonics*, (2005).

17. Travers, J.C., Cumberland, B.A., Popov, S.V., Taylor, J.R., Traynor, N. & Monteville, A. "Pump Format Influence on Noise Characteristics and Spectral Extent of CW Continuum Generation in New Low-water-loss Holey Fibers." *Conference on Lasers and Electro-Optics*, (2006) CMGG5.

18. Travers, J.C., Rulkov, A.B., Popov, S.V. & Taylor, J.R. "Fibre-Integrated High-Power Blue-Enhanced Continuum Source." *Conference on Lasers and Electro-Optics*, (2006).

19. Travers, J., Rulkov, A., Popov, S., Taylor, J., Kudlinski, A., George, A. & Knight, J. "Dispersion-Decreasing PCF for Blue-UV Supercontinuum Generation." *Conference on Lasers and Electro-Optics*, (2006) CPDA11.

20. Travers, J.C., Cumberland, B.A., Rulkov, A.B., Popov, S.V., Taylor, J.R., Stone, J.M., George, A.K. & Knight, J.C. "Pulse Compression in Dispersion Decreasing Photonic Crystal Fiber." *Conference on Lasers and Electro-Optics*, (2007) CFK1.

21. Travers, J., Rulkov, A., Cumberland, B., Popov, S. & Taylor, J. "Non-linear applications of microstructured optical fibres (INVITED)." *International Conference on Materials for Advanced Technologies*, (2007)

22. Travers, J., Rulkov, A., Popov, S., Taylor, J., Kudlinski, A., George, A. & Knight, J. "Multi-Watt Supercontinuum Generation from 0.3 to 2.4 μm in PCF Tapers." *Conference on Lasers and Electro-Optics*, (2007) CFK1.

References

[Abe04] A. K. Abeeluck, C. Headley and C. G. Jørgensen. "High-power supercontinuum generation in highly nonlinear, dispersion-shifted fibers by use of a continuous-wave Raman fiber laser". *Opt. Lett.*, **29** (2004) pp. 2163.

[Abe05] A. Abeeluck and C. Headley. "Continuous-wave pumping in the anomalous-and normal-dispersion regimes of nonlinear fibers for supercontinuum generation". *Opt. Lett.*, **30** (2005) pp. 61.

[Abr07] L. Abrardi, S. Martin-Lopez, A. Carrasco-Sanz, P. Corredera, M. L. Hernanz and M. Gonzalez-Herraez. "Optimized All-Fiber Supercontinuum Source at 1.3$ mu hbox {m}$ Generated in a Stepwise Dispersion-Decreasing-Fiber Arrangement". *J. Lightwave Technol.*, **25** (2007) pp. 2098.

[Agr90] G. P. Agrawal. "Effect of intrapulse stimulated Raman scattering on soliton-effect pulse compression in optical fibers". *Opt. Lett*, **15** (1990) pp. 224.

[Agr01] G. P. Agrawal. *Nonlinear Fiber Optics*. Academic Press (2001).

[Akh95] N. Akhmediev and M. Karlsson. "Cherenkov radiation emitted by solitons in optical fibers". *Phys. Rev. A*, **51** (1995) pp. 2602.

[Aki02] D. A. Akimov, A. A. Ivanov, M. V. Alfimov, S. N. Bagayev, T. A. Birks, W. J. Wadsworth, P. S. Russell, A. B. Fedotov, V. S. Pivtsov, A. A. Podshivalov and A. M. Zheltikov. "Two-octave spectral broadening of subnanojoule Cr: forsterite femtosecond laser pulses in tapered fibers". *Appl. Phys. B*, **74** (2002) pp. 307.

[Alf70a] R. R. Alfano and S. L. Shapiro. "Emission in the Region 4000 to 7000 Å Via Four-Photon Coupling in Glass". *Phys. Rev. Lett.*, **24** (1970) pp. 584.

[Alf70b] R. R. Alfano and S. L. Shapiro. "Observation of self-phase modulation and small-scale filaments in crsytals and glasses". *Phys. Rev. Lett.*, **24** (1970) pp. 592.

[And04] T. Andersen, K. Hilligsøe, C. Nielsen, J. Thøgersen, K. Hansen, S. Keiding and J. Larsen. "Continuous-wave wavelength conversion in a photonic crystal fiber with two zero-dispersion wavelengths". *Opt. Express*, **12** (2004) pp. 4113.

[Aso97] M. Asobe. "Nonlinear Optical Properties of Chalcogenide Glass Fibers and Their Application to All-Optical Switching". *Opt. Fiber Technol.*, **3** (1997) pp. 142.

[Avd03] A. V. Avdokhin, S. V. Popov and J. R. Taylor. "Continuous-wave, high-power, Raman continuum generation in holey fibers". *Opt. Lett.*, **28** (2003) pp. 1353.

[Bab07] S. A. Babin, D. V. Churkin, A. E. Ismagulov, S. I. Kablukov and E. V. Podivilov. "Four-wave-mixing-induced turbulent spectral broadening in a long Raman fiber laser". *J. Opt. Soc. Am. B*, **24** (2007) pp. 1729.

[Bar06] B. Barviau, S. Randoux and P. Suret. "Spectral broadening of a multimode continuous-wave optical field propagating in the normal dispersion regime of a fiber". *Opt. Lett.*, **31** (2006) pp. 1696.

[Ben02] F. Benabid, J. C. Knight, G. Antonopoulos and P. S. J. Russell. "Stimulated Raman Scattering in Hydrogen-Filled Hollow-Core Photonic Crystal Fiber". *Science*, **298** (2002) p. 399.

[Bia03] F. Biancalana, D. V. Skryabin and P. S. J. Russell. "Four-wave mixing instabilities in photonic-crystal and tapered fibers". *Phys.Rev. E*, **68** (2003) p. 46603.

[Bir92] T. A. Birks and Y. W. Li. "The shape of fiber tapers". *J. Lightwave Technol.*, **10** (1992) pp. 432.

[Bir97] T. A. Birks, J. C. Knight and P. S. J. Russell. "Endlessly single-mode photonic crystal fiber". *Opt. Lett.*, **22** (1997) pp. 961.

[Bir00] T. A. Birks, W. J. Wadsworth and P. S. J. Russell. "Supercontinuum generation in tapered fibers". *Opt. Lett.*, **25** (2000) pp. 1415.

[Bja03] A. Bjarklev, J. Broeng and A. S. Bjarklev. *Photonic Crystal Fibres*. Kluwer Academic Publishers (2003).

[Blo89] K. J. Blow and D. Wood. "Theoretical Description of Transient Stimulated Raman-Scattering in Optical Fibers". *IEEE J. Quantum Electron.*, **25** (1989) pp. 2665.

[Bou04] A. H. Bouk, A. Cucinotta, F. Poli and S. Selleri. "Dispersion properties of square-lattice photonic crystal fibers". *Opt. Express*, **12** (2004) pp. 941.

[Bra00] R. N. Bracewell. *The Fourier transform and its applications*. McGraw Hill (2000).

[Buc04] J. A. Buck. *Fundamentals of Optical Fibers*. Wiley-Interscience (2004).

[Cha01] J. K. Chandalia, B. J. Eggleton, R. S. Windeler, S. G. Kosinski, X. Liu and C. Xu. "Adiabatic coupling in tapered air-silica microstructured optical fiber". *IEEE Photonic. Tech. L.*, **13** (2001) pp. 52.

[Cha02] P. A. Champert, S. V. Popov and J. R. Taylor. "Generation of multiwatt, broadband continua in holey fibers". *Opt. Lett*, **27** (2002) pp. 122.

[Cha04] P. A. Champert, V. Couderc, P. Leproux, S. Février, V. Tombelaine, L. Labonté, P. Roy, C. Froehly and P. Nérin. "White-light supercontinuum generation in normally dispersive optical fiber using original multi-wavelength pumping system". *Opt. Express*, **12** (2004) pp. 4366.

[Che91] S. V. Chernikov and P. V. Mamyshev. "Femtosecond Soliton Propagation in Fibers with Slowly Decreasing Dispersion". *J. Opt. Soc. Am. B*, **8** (1991) pp. 1633.

[Che92] S. V. Chernikov, D. J. Richardson, E. M. Dianov and D. N. Payne. "Picosecond Soliton Pulse Compressor Based on Dispersion Decreasing Fiber". *Electron. Lett.*, **28** (1992) pp. 1842.

[Che93] S. V. Chernikov, E. M. Dianov, D. J. Richardson and D. N. Payne. "Soliton Pulse-Compression in Dispersion-Decreasing Fiber". *Opt. Lett.*, **18** (1993) pp. 476.

[Che94a] S. V. Chernikov, J. R. Taylor and R. Kashyap. "Comb-Like Dispersion-Profiled Fiber for Soliton Pulse-Train Generation". *Opt. Lett.*, **19** (1994) pp. 539.

[Che94b] S. V. Chernikov, J. R. Taylor and R. Kashyap. "Experimental Demonstration of Step-Like Dispersion Profiling in Optical-Fiber for Soliton Pulse Generation and Compression". *Electron. Lett.*, **30** (1994) pp. 433.

[Che97] S. V. Chernikov, Y. Zhu, J. R. Taylor and V. P. Gapontsev. "Supercontinuum self-Q-switched ytterbium fiber laser". *Opt. Lett*, **22** (1997) pp. 298.

[Che05] A. Y. H. Chen, G. K. L. Wong, S. G. Murdoch, R. Leonhardt, J. D. Harvey, J. C. Knight, W. J. Wadsworth and P. S. J. Russell. "Widely tunable optical parametric generation in a photonic crystal fiber". *Opt. Lett.*, **30** (2005) pp. 762.

[Chi89] S. Chi and S. F. Wen. "Raman cross talk of soliton collision in a lossless fiber". *Opt. Lett.*, **14** (1989) pp. 1216.

[Coe01] S. Coen, A. H. L. Chau, R. Leonhardt, J. D. Harvey, J. C. Knight, W. J. Wadsworth and P. S. J. Russell. "White-light supercontinuum generation with 60-ps pump pulses in a photonic crystal fiber". *Opt. Lett*, **26** (2001) pp. 1356.

[Coe02] S. Coen, A. H. L. Chau, R. Leonhardt, J. D. Harvey, J. C. Knight, W. J. Wadsworth and P. S. J. Russell. "Supercontinuum generation by stimulated Raman scattering and parametric four-wave mixing in photonic crystal fibers". *J. Opt. Soc. Am. B*, **19** (2002) pp. 753.

[Cre99] R. F. Cregan, B. J. Mangan, J. C. Knight, T. A. Birks, P. S. Russell, P. J. Roberts and D. C. Allan. "Single-Mode Photonic Band Gap Guidance of Light in Air." *Science*, **285** (1999) pp. 1537.

[Cri04] I. Cristiani, R. Tediosi, L. Tartara and V. Degiorgio. "Dispersive wave generation by solitons in microstructured optical fibers". *Opt. Express*, **12** (2004) pp. 124.

[Dem05] A. Demircan and U. Bandelow. "Supercontinuum generation by the modulation instability". *Opt. Commun.*, **244** (2005) pp. 181.

[Der98] D. Derickson. *Fiber optic test and measurement.* Prentice Hall PTR (1998).

[deS96] R. deSalvo, A. A. Said, D. J. Hagan, E. W. Van Stryland and M. Sheik-Bahae. "Infrared to ultraviolet measurements of two-photon absorption and n_2 in wide bandgap solids". *IEEE J. Quantum Electron.*, **32** (1996) pp. 1324.

[Dia85] E. M. Dianov, A. Y. Karasik, P. V. Mamyshev, A. M. Prokhorov, V. N. Serkin, M. F. Stelmakh and A. A. Fomichev. "Stimulated-Raman conversion of multisoliton pulses in quartz optical fibers". *JETP Lett.*, **41** (1985) p. 294.

[Dia86] E. M. Dianov, Z. S. Nikonova, A. M. Prokhorov and V. N. Serkin. "Optimal compression of multi-soliton pulses in optical fibers". *Sov. Tech. Phys. Lett*, **12** (1986) pp. 311.

[dM03] C. J. S. de Matos, J. R. Taylor, T. P. Hansen, K. P. Hansen and J. Broeng. "All-fiber chirped pulse amplification using highly-dispersive air-core photonic bandgap fiber". *Opt. Express*, **11** (2003) pp. 2832.

[dM04a] C. J. S. de Matos, S. V. Popov, A. B. Rulkov, J. R. Taylor, J. Broeng, T. P. Hansen and V. P. Gapontsev. "All-Fiber Format Compression of Frequency Chirped Pulses in Air-Guiding Photonic Crystal Fibers". *Phys. Rev. Lett.*, **93** (2004) p. 103901.

[dM04b] C. J. S. de Matos, S. V. Popov and J. R. Taylor. "Temporal and noise characteristics of continuous-wave-pumped continuum generation in holey fibers around 1300 nm". *Appl. Phys. Lett.*, **85** (2004) p. 2706.

[dM04c] C. J. S. de Matos and J. R. Taylor. "Multi-kilowatt, all-fiber integrated chirped-pulse amplification system yielding 40× pulse compression using air-core fiber

and conventional erbium-doped fiber amplifier". *Opt. Express*, **12** (2004) pp. 405.

[dM07] C. J. S. de Matos, C. M. B. Cordeiro, E. M. dos santos, J. S. K. Ong, A. Bozolan and C. H. B. Cruz. "Liquid-core, liquid-cladding photonic crystal fibers". *Opt. Express*, **15** (2007) pp. 11207.

[Dud02a] J. Dudley, X. Gu, L. Xu, M. Kimmel, E. Zeek, P. O'Shea, R. Trebino, S. Coen and R. S. Windeler. "Cross-correlation frequency resolved optical gating analysis of broadband continuum generation in photonic crystal fiber: simulations and experiments". *Opt. Express*, **10** (2002) pp. 1215.

[Dud02b] J. M. Dudley, L. Provino, N. Grossard, H. Maillotte, R. S. Windeler, B. J. Eggleton and S. Coen. "Supercontinuum generation in air-silica microstructured fibers with nanosecond and femtosecond pulse pumping". *J. Opt. Soc. Am. B*, **19** (2002) pp. 765.

[Dud06] J. M. Dudley, G. Genty and S. Coen. "Supercontinuum generation in photonic crystal fiber". *Reviews of Modern Physics*, **78** (2006) pp. 1135.

[Dum93] P. Dumais, F. Gonthier, S. Lacroix, J. Bures, A. Villeneuve, P. G. J. Wigley and G. I. Stegeman. "Enhanced self-phase modulation in tapered fibers". *Opt. Lett*, **18** (1993) pp. 1996.

[Dun04] C. Dunsby, P. M. P. Lanigan, J. McGinty, D. S. Elson, J. Requejo-Isidro, I. Munro, N. Galletly, F. McCann, B. Treanor, B. Onfelt, D. M. Davis, M. A. A. Neil and P. M. W. French. "An electronically tunable ultrafast laser source applied to fluorescence imaging and fluorescence lifetime imaging microscopy". *J. Phys.D*, **37** (2004) pp. 3296.

[Dup07] P. Dupriez, F. Poletti, P. Horak, M. N. Petrovich, Y. Jeong, J. Nilsson, D. J. Richardson and D. N. Payne. "Efficient white light generation in secondary cores of holey fibers". *Opt. Express*, **15** (2007) pp. 3729.

[Efi03] A. Efimov, A. J. Taylor, F. G. Omenetto, J. C. Knight, W. J. Wadsworth and P. S. J. Russell. "Nonlinear generation of very high-order UV modes in microstructured fibers". *Opt. Express*, **11** (2003) pp. 910.

[Efi04] A. Efimov, A. J. Taylor, F. G. Omenetto, A. V. Yulin, N. Y. Joly, F. Biancalana, D. V. Skryabin, J. C. Knight and P. S. J. Russell. "Time-spectrally-resolved ultrafast nonlinear dynamics in small-core photonic crystal fibers: Experiment and modelling". *Opt. Express*, **12** (2004) pp. 6498.

[ET03] M. Ere-Tassou, C. Przygodzki, E. Fertein and H. Delbarre. "Femtosecond laser source for real-time atmospheric gas sensing in the uv-visible". *Opt. Commun.*, **220** (2003) pp. 215.

[Fat02] F. K. Fatemi. "Analysis of nonadiabatically compressed pulses from dispersion-decreasing fiber". *Opt. Lett*, **27** (2002) pp. 1637.

[Fer00] A. Ferrando, E. Silvestre, J. J. Miret, P. Andres and M. V. Andres. "Donor and acceptor guided modes in photonic crystal fibers". *Opt. Lett.*, **25** (2000) pp. 1328.

[Fos04] M. A. Foster and A. L. Gaeta. "Ultra-low threshold supercontinuum generation in sub-wavelength waveguides". *Opt. Express*, **12** (2004) pp. 3137.

[Fos05] M. A. Foster, J. M. Dudley, B. Kibler, Q. Cao, D. Lee, R. Trebino and A. L. Gaeta. "Nonlinear pulse propagation and supercontinuum generation in photonic nanowires: experiment and simulation". *Appl. Phys. B*, **81** (2005) pp. 363.

[Fra90] P. W. France (editor). *Fluoride Glass Optical Fibres.* Blackie (1990).

[Fra91a] P. W. France (editor). *Optical Fibre Lasers and Amplifiers.* Blackie (1991).

[Fra91b] P. L. Francois. "Nonlinear Propagation of Ultrashort Pulses in Optical Fibers - Total Field Formulation in the Frequency-Domain". *J. Opt. Soc. Am. B*, **8** (1991) pp. 276.

[Fre98] A. Freiberg, J. A. Jackson, S. Lin and N. W. Woodbury. "Subpicosecond pump-supercontinuum probe spectroscopy of LH2 photosynthetic antenna proteins at low temperature". *J. Phys. Chem. A*, **102** (1998) pp. 4372.

[Fro05] M. H. Frosz, P. Falk and O. Bang. "The role of the second zero-dispersion wavelength in generation of supercontinua and bright-bright soliton-pairs across the zero-dispersion wavelength". *Opt. Express*, **13** (2005) pp. 6181.

[Fro06] M. H. Frosz, O. Bang and A. Bjarklev. "Soliton collision and Raman gain regimes in continuous-wave pumped supercontinuum generation". *Opt. Express*, **14** (2006) pp. 9391.

[Fuj80] Y. Fujii, B. S. Kawasaki, K. O. Hill and D. C. Johnson. "Sum-frequency light generation in optical fibers". *Opt. Lett.*, **5** (1980) pp. 48.

[Fuj84] J. G. Fujimoto, A. M. Weiner and E. P. Ippen. "Generation and measurement of optical pulses as short as 16 fs". *Appl. Phys. Lett.*, **44** (1984) p. 832.

[Gae02] A. Gaeta. "Nonlinear propagation and continuum generation in microstructured optical fibers". *Opt. Lett*, **27** (2002) pp. 924.

[Gap05] V. Gapontsev, D. Gapontsev, N. Platonov, O. Shkurikhin, V. Fomin, A. Mashkin, M. Abramov and S. Ferin. "2 kW CW ytterbium fiber laser with record diffraction-limited brightness". In *Conference on Lasers and Elctro-Optics Europe*. IEEE, Munich, Germany (2005), p. 508.

[Gen04a] G. Genty, M. Lehtonen and H. Ludvigsen. "Effect of cross-phase modulation on supercontinuum generated in microstructured fibers with sub-30 fs pulses". *Opt. Express*, **12** (2004) pp. 4614.

[Gen04b] G. Genty, M. Lehtonen, H. Ludvigsen and M. Kaivola. "Enhanced bandwidth of supercontinuum generated in microstructured fibers". *Opt. Express*, **12** (2004) pp. 3471.

[Gen05] G. Genty, M. Lehtonen and H. Ludvigsen. "Route to broadband blue-light generation in microstructured fibers". *Opt. Lett.*, **30** (2005) pp. 756.

[Gen07] G. Genty, S. Coen and J. M. Dudley. "Fiber supercontinuum sources (Invited)". *J. Opt. Soc. Am. B*, **24** (2007) pp. 1771.

[Ger80] J. I. Gersten, R. R. Alfano and M. Belic. "Combined stimulated raman scattering and continuum self-phase modulations". *Phys. Rev. A*, **21** (1980) pp. 1222.

[GH03] M. González-Herráez, S. Martín-López, P. Corredera, M. L. Hernanz and P. R. Horche. "Supercontinuum generation using a continuous-wave Raman fiber laser". *Opt. Commun.*, **226** (2003) pp. 323.

[GN87] A. S. Gouveia-Neto, A. S. Gomes and J. R. Taylor. "Generation of 33 fsec pulse at 1.32, um through a high-order soliton effect in a single-mode optical fiber". *Opt. Lett*, **12** (1987) p. 395.

[GN88a] A. S. Gouveia-Neto, M. E. Faldon and J. R. Taylor. "Temporal and spectral evolution of femtosecond solitons in the region of the zero-group velocity dispersion of a single-mode optical fiber". *Opt. Commun.*, **69** (1988) pp. 173.

[GN88b] A. S. Gouveia-Neto, A. S. L. Gomes and J. R. Taylor. "Femto soliton Raman generation". *IEEE J. Quantum Electron.*, **24** (1988) pp. 332.

[GN88c] A. S. Gouveia-Neto, A. S. L. Gomes and J. R. Taylor. "Pulses of Four Optical Cycles from an Optimized Optical Fibre/Grating Pair/Soliton Pulse Compressor at 1·32 μm". *J. Mod. Opt.*, **35** (1988) pp. 7.

[Gor86] J. P. Gordon. "Theory of the soliton self-frequency shift". *Opt. Lett*, **11** (1986) pp. 662.

[Gor06] A. V. Gorbach, D. V. Skryabin, J. M. Stone and J. C. Knight. "Four-wave mixing of solitons with radiation and quasi-nondispersive wave packets at the short-wavelength edge of a supercontinuum". *Opt. Express*, **14** (2006) pp. 9854.

[Gor07a] A. V. Gorbach and D. V. Skryabin. "Bouncing of a dispersive pulse on an accelerating soliton and stepwise frequency conversion in optical fibers". *Opt. Express*, **15** (2007) pp. 14560.

[Gor07b] A. V. Gorbach and D. V. Skryabin. "Light trapping in gravity-like potentials and expansion of supercontinuum spectra in photonic-crystal fibres". *Nature*, **1** (2007) pp. 653.

[Gor07c] A. V. Gorbach and D. V. Skryabin. "Theory of radiation trapping by the accelerating solitons in optical fibers". *Physical Review A*, **76** (2007) 053803.

[Gou89] A. S. Gouveianeto, P. G. J. Wigley and J. R. Taylor. "Soliton Generation through Raman Amplification of Noise Bursts". *Opt. Lett.*, **14** (1989) pp. 1122.

[Gri82] D. Grischkowsky and A. C. Balant. "Optical pulse compression based on enhanced frequency chirping". *Appl. Phys. Lett.*, **41** (1982) p. 1.

[Guy98] M. J. Guy, S. V. Chernikov and J. R. Taylor. "Lossless transmission of 2 ps pulses over 45 km of standard fibreat 1.3 μm using distributed Raman amplification". *Electron. Lett.*, **34** (1998) pp. 793.

[Hal84] J. M. Halbout and D. Grischkowsky. "12-fs ultrashort optical pulse compression at a high repetition rate". *Appl. Phys. Lett.*, **45** (1984) p. 1281.

[Har01] I. Hartl, X. D. Li, C. Chudoba, R. K. Ghanta, T. H. Ko, J. G. Fujimoto, J. K. Ranka and R. S. Windeler. "Ultrahigh-resolution optical coherence tomography using continuum generation in an air–silica microstructure optical fiber". *Opt. Lett.*, **26** (2001) pp. 608.

[Har02] J. M. Harbold, F. O. Ilday, F. W. Wise, T. A. Birks, W. J. Wadsworth and Z. Chen. "Long-wavelength continuum generation about the second dispersion zero of a tapered fiber". *Opt. Lett*, **27** (2002) pp. 1558.

[Har03] J. D. Harvey, R. Leonhardt, S. Coen, G. K. L. Wong, J. C. Knight, W. J. Wadsworth and P. S. J. Russell. "Scalar modulation instability in the normal dispersion regime by use of a photonic crystal fiber". *Opt. Lett.*, **28** (2003) pp. 2225.

[Has73] A. Hasegawa and F. Tappert. "Transmission of stationary nonlinear optical pulses in dispersive dielectric fibers. i. anomalous dispersion". *Appl. Phys. Lett.*, **23** (1973) pp. 142.

[Has80] A. Hasegawa and W. F. Brinkman. "Tunable coherent IR and FIR sources utilizing modulational instability". *IEEE J. Quantum Electron.*, **16** (1980) pp. 694.

[Hec04] J. Hecht. *City of Light: The Story of Fiber Optics*. Oxford University Press, USA (2004).

[Her02] J. Herrmann, U. Griebner, N. Zhavoronkov, A. Husakou, D. Nickel, J. C. Knight, W. J. Wadsworth, P. S. J. Russell and G. Korn. "Experimental Evidence for Supercontinuum Generation by Fission of Higher-Order Solitons in Photonic Fibers". *Phys. Rev. Lett.*, **88** (2002) p. 173901.

[Hil78] K. O. Hill, D. C. Johnson, B. S. Kawasaki and R. I. MacDonald. "cw three-wave mixing in single-mode optical fibers". *J. Appl. Phys.*, **49** (1978) pp. 5098.

[Hil80] K. O. Hill, B. S. Kawasaki, Y. Fujjii and D. C. Johnson. "Efficient sequence-frequency generation in a parametric fiber-optic oscillator". *Appl. Phys. Lett.*, **36** (1980) pp. 888.

[Hod87] W. Hodel and H. Weber. "Decay of femtosecond higher-order solitons in an optical fiber induced by Raman self-pumping". *Opt. Lett*, **12** (1987) pp. 924.

[Hol90] M. J. Holmes, F. P. Payne and D. M. Spirit. "Matching fibres for low loss coupling into fibre amplifiers". *Electron. Lett.*, **26** (1990) pp. 2102.

[Hol00] R. Holzwarth, T. Udem, T. W. Hänsch, J. C. Knight, W. J. Wadsworth and P. S. J. Russell. "Optical Frequency Synthesizer for Precision Spectroscopy". *Phys. Rev. Lett.*, **85** (2000) pp. 2264.

[Hol02] D. Hollenbeck and C. D. Cantrell. "Multiple-vibrational-mode model for fiber-optic Raman gain spectrum and response function". *J. Opt. Soc. Am. B*, **19** (2002) pp. 2886.

[Hor04] T. Hori, J. Takayanagi, N. Nishizawa and T. Goto. "Flatly broadened, wideband and low noise supercontinuum generation in highly nonlinear hybrid fiber". *Opt. Express*, **12** (2004) pp. 317.

[Hsi04] P. L. Hsiung, Y. Chen, T. H. Ko, J. G. Fujimoto, C. J. S. de Matos, S. V. Popov, J. R. Taylor and V. P. Gapontsev. "Optical coherence tomography using a continuous-wave, high- power, raman continuum light source". *Opt. Express*, **12** (2004) pp. 5287.

[Hu06] J. Hu, B. S. Marks, C. R. Menyuk, J. Kim, T. F. Carruthers, B. M. Wright, T. F. Taunay and E. J. Friebele. "Pulse compression using a tapered microstructure optical fiber". *Opt. Express*, **14** (2006) pp. 4026.

[Hul07] J. Hult. "A Fourth-Order Runge-Kutta in the Interaction Picture Method for Simulating Supercontinuum Generation in Optical Fibers". *J. Lightwave Technol.*, **25** (2007) pp. 3770.

[Hum06] G. Humbert, W. J. Wadsworth, S. G. Leon-Saval, J. C. Knight, T. A. Birks, P. S. J. Russell, M. J. Lederer, D. Kopf, K. Wiesauer, E. I. Breuer and D. Stifter. "Supercontinuum generation system for optical coherence tomography based on tapered photonic crystal fibre". *Opt. Express*, **14** (2006) pp. 1596.

[Hus02] A. V. Husakou and J. Herrmann. "Supercontinuum generation, four-wave mixing, and fission of higher-order solitons in photonic-crystal fibers". *J. Opt. Soc. Am. B*, **19** (2002) pp. 2171.

[Isl89a] M. N. Islam, G. Sucha, I. Bar-Joseph, M. Wegener, J. P. Gordon and D. S. Chemla. "Broad bandwidths from frequency-shifting solitons in fibers". *Opt. Lett*, **14** (1989) pp. 370.

[Isl89b] M. N. Islam, G. Sucha, I. Bar-Joseph, M. Wegener, J. P. Gordon and D. S. Chemla. "Femtosecond distributed soliton spectrum in fibers". *J. Opt. Soc. Am. B*, **6** (1989) pp. 1149.

[Iva92] L. M. Ivanov, P. P. Branzalov and L. I. Pavlov. "Efficient compression of fundamental solitons in fibres with decreasing dispersion". *Opt. Quantum. Electron.*, **24** (1992) pp. 565.

[Joh87] S. John. "Strong localization of photons in certain disordered dielectric superlattices". *Phys. Rev. Lett.*, **58** (1987) pp. 2486.

[Joh01] S. G. Johnson and J. D. Joannopoulos. "Block-iterative frequency-domain methods for Maxwell's equations in a planewave basis". *Opt. Express*, **8** (2001) pp. 173.

[Jon00] D. J. Jones, S. A. Diddams, J. K. Ranka, A. Stentz, R. S. Windeler, J. L. Hall and S. T. Cundiff. "Carrier-Envelope Phase Control of Femtosecond Mode-Locked Lasers and Direct Optical Frequency Synthesis". *Science*, **288** (2000) pp. 635.

[Jr.64] W. H. Jr., E. Snitzer and H. Osterberg. "Optical energy transmitting devices and method of making same". *US Patent* (1964) pp. 3,157,726.

[Kai73] P. Kaiser, E. A. J. Marcatili and S. E. Miller. "A new optical fiber". *Bell Syst. Tech. J*, **52** (1973) pp. 265.

[Kan05] H. Kano and H. Hamaguchi. "Near-infrared coherent anti-stokes raman scattering microscopy using supercontinuum generated from a photonic crystal fiber". *App. Phys. B*, **80** (2005) pp. 243.

[Kao86] K. C. Kao and G. A. Hockham. "Dielectric-fibre surface waveguides for optical frequencies". *IEE proceedings. Part J. Optoelectronics*, **133** (1986) pp. 191.

[Kel99] P. V. Kelkar, F. Coppinger, A. S. Bhushan and B. Jalali. "Time-domain optical sensing". *Electron. Lett.*, **35** (1999) pp. 1661.

[Ken91] R. P. Kenny, T. A. Birks and K. P. Oakley. "Control of optical fibre taper shape". *Electron. Lett.*, **27** (1991) pp. 1654.

[Ken05] R. E. Kennedy, S. V. Popov and J. R. Taylor. "Compact fully fibre integrated source of 100 fs pulses at 1.1 mu m based on compression in holey fibre". *Electron. Lett.*, **41** (2005) pp. 234.

[Ken07] R. E. Kennedy, A. B. Rulkov, S. V. Popov and J. R. Taylor. "High-peak-power femtosecond pulse compression with polarization-maintaining ytterbium-doped fiber amplification". *Opt. Lett.*, **32** (2007) pp. 1199.

[Kib05] B. Kibler, J. M. Dudley and S. Coen. "Supercontinuum generation and nonlinear pulse propagation in photonic crystal fiber: influence of the frequency-dependent effective mode area". *Appl. Phys. B*, **81** (2005) pp. 337.

[Kib07] B. Kibler, P. A. Lacourt, F. Courvoisier and J. M. Dudley. "Soliton spectral tunnelling in photonic crystal fibre with sub-wavelength core defect". *Electron. Lett.*, **43** (2007) pp. 967.

[Kni96] J. C. Knight, T. A. Birks, P. S. Russell and D. M. Atkin. "All-silica single-mode optical fiber with photonic crystal cladding". *Opt. Lett.*, **21** (1996) pp. 1547.

[Kni98] J. C. Knight, T. A. Birks, P. S. J. Russell and J. P. de sandro. "Properties of photonic crystal fiber and the effective index model". *J. Opt. Soc. Am. A*, **15** (1998) pp. 748.

[Kni00] J. C. Knight, J. Arriaga, T. A. Birks, A. Ortigosa-Blanch, W. J. Wadsworth and P. S. J. Russell. "Anomalous dispersion in photonic crystal fiber". *IEEE Photonic. Tech. Lett.*, **12** (2000) pp. 807.

[Kno85] W. H. Knox, R. L. Fork, M. C. Downer, R. H. Stolen, C. V. Shank and J. A. Valdmanis. "Optical pulse compression to 8 fs at a 5-kHz repetition rate". *Appl. Phys. Lett.*, **46** (1985) p. 1120.

[Kob05] S. M. Kobtsev and S. V. Smirnov. "Modelling of high-power supercontinuum generation in highly nonlinear, dispersion shifted fibers at CW pump". *Opt. Express*, **13** (2005) pp. 6912.

[Koe64] C. J. Koester and E. Snitzer. "Amplification in a fiber laser". *Applied Optics*, **3** (1964) pp. 1182.

[Kos05] M. Koshiba and K. Saitoh. "Simple evaluation of confinement losses in holey fibers". *Opt. Commun.*, **253** (2005) pp. 95.

[Kud06] A. Kudlinski, A. K. George, J. C. Knight, J. C. Travers, A. B. Rulkov, S. V. Popov and J. R. Taylor. "Zero-dispersion wavelength decreasing photonic crystal fibers for ultraviolet-extended supercontinuum generation". *Opt. Express*, **14** (2006) pp. 5715.

[Kue88] H. H. Kuehl. "Solitons on an axially nonuniform optical fiber". *J. Opt. Soc. Am. B*, **5** (1988) pp. 709.

[Kuh02a] B. Kuhlmey, T. White, G. Renversez, D. Maystre, L. C. Botten, C. M. de Sterke and R. C. McPhedran. "Multipole method for microstructured optical fibers. II. Implementation and results". *J. Opt. Soc. Am. B*, **19** (2002) pp. 2331.

[Kuh02b] B. T. Kuhlmey, R. C. McPhedran, C. M. de Sterke, P. Robinson, G. Renversez and D. Maystre. "Microstructured optical fibers: whereâĂŹs the edge?" *Opt. Express*, **10** (2002) pp. 1285.

[Kut05] J. N. Kutz, C. Lyngå and B. J. Eggleton. "Enhanced Supercontinuum Generation through Dispersion-Management". *Opt. Express*, **13** (2005) pp. 3989.

[Læg04] J. Lægsgaard and A. Bjarklev. "Reduction of coupling loss to photonic crystal fibers by controlled hole collapse: a numerical study". *Opt. Commun.*, **237** (2004) pp. 431.

[Læg07] J. Lægsgaard. "Mode profile dispersion in the generalised nonlinear Schrödinger equation". *Opt. Express*, **15** (2007) pp. 16110.

[Lar03] T. T. Larsen, A. Bjarklev, D. S. Hermann and J. Broeng. "Optical devices based on liquid crystal photonic bandgap fibres". *Opt. Express*, **11** (2003) pp. 2589.

[Les07] C. Lesvigne, V. Couderc, A. Tonello, P. Leproux, A. Barthelemy, S. Lacroix, F. Druon, P. Blandin, M. Hanna and P. Georges. "Visible supercontinuum generation controlled by intermodal four-wave mixing in microstructured fiber". *Opt. Lett.*, **32** (2007) pp. 2173.

[Li06] Y. Li, C. Wang, Y. Chen, M. Hu, B. Liu and L. Chai. "Solution of the fundamental space-filling mode of photonic crystal fibers: numerical method versus analytical approaches". *Appl. Phys. B*, **85** (2006) pp. 597.

[Lim03] J. Limpert, T. Schreiber, S. Nolte, H. Zellmer and A. Tünnermann. "All fiber chirped-pulse amplification system based on compression in air-guiding photonic bandgap fiber". *Opt. Express*, **11** (2003) pp. 3332.

[Lim04] J. Limpert, A. Liem, M. Reich, T. Schreiber, S. Nolte, H. Zellmer, A. Tünnermann, J. Broeng, A. Petersson and C. Jakobsen. "Low-nonlinearity single-transverse-mode ytterbium-doped photonic crystal fiber amplifier". *Opt. Express*, **12** (2004) pp. 1313.

[Lin76] C. Lin and R. H. Stolen. "New nanosecond continuum for excited-state spectroscopy". *Appl. Phys. Lett.*, **28** (1976) p. 216.

[Lin78] C. Lin and V. T. Nguyen. "Wideband near-i.r. continuum (0.7-2.1 μm) generated in low-loss optical fibres". *Electron. Lett.*, **14** (1978) pp. 822.

[Ls04] S. G. Leon-saval, T. A. Birks, W. J. Wadsworth, P. S. J. Russell and M. W. Mason. "Supercontinuum generation in submicron fibre waveguides". *Opt. Express*, **12** (2004) pp. 2864.

[Lu05] F. Lu, Y. Deng and W. H. Knox. "Generation of broadband femtosecond visible pulses in dispersion-micromanaged holey fibers". *Opt. Lett.*, **30** (2005) pp. 1566.

[Mäg04] E. Mägi, P. Steinvurzel and B. Eggleton. "Tapered photonic crystal fibers". *Opt. Express*, **12** (2004) pp. 776.

[Mam90] P. V. Mamyshev and S. V. Chernikov. "Ultrashort-Pulse Propagation in Optical Fibers". *Opt. Lett.*, **15** (1990) pp. 1076.

[Mam93] P. V. Mamyshev, P. G. J. Wigley, J. Wilson, G. I. Stegeman, V. A. Semeonov, E. M. Dianov and S. I. Miroshnichenko. "Adiabatic compression of SchrÃűdinger solitons due to the combined perturbations of higher-order dispersion and delayed nonlinear response". *Phys. Rev. Lett.*, **71** (1993) p. 73.

[Mar87] D. Marcuse. "Mode conversion in optical fibers with monotonically increasing core radius". *J. Lightwave Technol.*, **5** (1987) pp. 125.

[Max73] J. Maxwell. *A Treatise on Electricity and Magnetism.* Clarendon Press (1873).

[Mea85] R. J. Mears, L. Reeke, S. B. Poole and D. N. Payne. "Neodymium-doped silica dingle-mode fibre laser". *Electron. Lett.*, **21** (1985) pp. 738.

[Mid00] M. Midrio, M. P. Singh and C. G. Someda. "The space filling mode of holey fibers: An analytical vectorial solution". *J. Lightwave Technol.*, **18** (2000) pp. 1031.

[Mil98] D. Milam. "Review and Assessment of Measured Values of the Nonlinear Refractive-Index Coefficient of Fused Silica". *Appl. Opt*, **37** (1998) pp. 546.

[Mit86] F. M. Mitschke and L. F. Mollenauer. "Discovery of the soliton self-frequency shift". *Opt. Lett.*, **11** (1986) pp. 659.

[Mit87] F. M. Mitschke and L. F. Mollenauer. "Ultrashort pulses from the soliton laser". *Opt. Lett.*, **12** (1987) pp. 407.

[ML06] S. Martin-Lopez, A. Carrasco-Sanz, P. Corredera, L. Abrardi, M. L. Hernanz and M. Gonzalez-Herraez. "Experimental investigation of the effect of pump incoherence on nonlinear pump spectral broadening and continuous-wave supercontinuum generation". *Opt. Lett.*, **31** (2006) pp. 3477.

[Mol80] L. F. Mollenauer, R. H. Stolen and J. P. Gorden. "Experimental observation of picosecond pulse narrowing and solitons in optical fibers". *Phys. Rev. Lett.*, **45** (1980) pp. 1095.

[Mol83] L. F. Mollenauer, R. H. Stolen, J. P. Gordon and W. J. Tomlinson. "Extreme Picosecond Pulse Narrowing by Means of Soliton Effect in Single-Mode Optical Fibers". *Opt. Lett.*, **8** (1983) pp. 289.

[Mor93] T. Morioka, K. Mori and M. Saruwatari. "More than 100-wavelength-channel picosecond optical pulse generation from single laser source using supercontinuum in optical fibers". *Electron. Lett.*, **29** (1993) pp. 862.

[Mor95a] K. Mori, T. Morioka and M. Saruwatari. "Ultrawide spectral range group-velocity dispersion measurement utilizing supercontinuum in an optical-fiber pumped by a 1.5 mu-m compact laser source". *IEEE T. Instrum. Meas.*, **44** (1995) pp. 712.

[Mor95b] T. Morioka, K. Uchiyama, S. Kawanishi, S. Suzuki and M. Saruwatari. "Multi-wavelength picosecond pulse source with low jitter and highoptical frequency stability based on 200 nm supercontinuumfiltering". *Electron. Lett.*, **31** (1995) pp. 1064.

[Mor97] K. Mori, H. Takara, S. Kawanishi, M. Saruwatari and T. Morioka. "Flatly broadened supercontinuum spectrum generated in a dispersiondecreasing fibre with convex dispersion profile". *Electron. Lett.*, **33** (1997) pp. 1806.

[Mor03] N. A. Mortensen and J. R. Folkenberg. "Low-loss criterion and effective area considerations for photonic crystal fibres". *J. Opt. A*, **5** (2003) pp. 163.

[Mos97] A. Mostofi, H. Hatami-Hanza and P. L. Chu. "Optimum dispersion profile for compression of fundamental solitons in dispersion decreasing fibers". *IEEE J. Quantum Electron.*, **33** (1997) pp. 620.

[Mus04] A. Mussot, E. Lantz, H. Maillotte, T. Sylvestre, C. Finot and S. Pitois. "Spectral broadening of a partially coherent CW laser beam in single-mode optical fibers". *Opt. Express*, **12** (2004) pp. 2838.

[Mus07] A. Mussot, M. Beaugeois, M. Bouazaoui and T. Sylvestre. "Tailoring CW supercontinuum generation in microstructured fibers with two-zero dispersion wavelengths". *Opt. Express*, **15** (2007) pp. 11553.

[Nic03] J. W. Nicholson, A. K. Abeeluck, C. Headley, M. F. Yan and C. G. Jorgensen. "Pulsed and continuous-wave supercontinuum generation in highly nonlinear, dispersion-shifted fibers". *Appl. Phys. B*, **77** (2003) pp. 211.

[Nik83] B. Nikolaus and D. Grischkowsky. "90-fs tunable optical pulses obtained by two-stage pulse compression". *Appl. Phys. Lett.*, **43** (1983) p. 228.

[Nis02a] N. Nishizawa and T. Goto. "Characteristics of pulse trapping by ultrashort soliton pulse in optical fibers across zerodispersion wavelength". *Opt. Express*, **10** (2002) pp. 1151.

[Nis02b] M. Nisoli, G. Sansone, S. Stagira, C. Vozzi, S. De Silvestri and O. Svelto. "Ultra-broadband continuum generation by hollow-fiber cascading". *Appl. Phys. B*, **75** (2002) pp. 601.

[OB00] A. Ortigosa-Blanch, J. C. Knight, W. J. Wadsworth, J. Arriaga, B. J. Mangan, T. A. Birks and P. S. J. Russell. "Highly birefringent photonic crystal fibers". *Opt. Lett.*, **25** (2000) pp. 1325.

[Owe07] D. M. Owen, E. Auksorius, H. B. Manning, C. B. Talbot, P. A. A. De beule, C. Dunsby, M. A. A. Neil and P. M. W. French. "Excitation-resolved hyperspectral fluorescence lifetime imaging using a UV-extended supercontinuum source". *Opt. Lett.*, **32** (2007) pp. 3408.

[Pas95] H. M. Pask, R. J. Carman, D. C. Hanna, A. C. Tropper, C. J. Mackechnie, P. R. Barber and J. M. Dawes. "Ytterbium-doped silica fiber lasers: versatile sources for the1-1.2 μm region". *IEEE J. Sel. Topics in Quantum Electron.*, **1** (1995) pp. 2.

[Pas97] R. Paschotta, J. Nilsson, A. C. Tropper and D. C. Hanna. "Ytterbium-doped fiber amplifiers". *IEEE J. Quantum Electron.*, **33** (1997) pp. 1049.

[Pel97] M. D. Pelusi and H. F. Liu. "Higher order soliton pulse compression in dispersion-decreasing optical fibers". *IEEE J. Quantum Electron.*, **33** (1997) pp. 1430.

[Pen93] G. J. Pendock, H. S. MacKenzie and F. P. Payne. "Dye lasers using tapered optical fibers". *Appl. Opt.*, **32** (1993) p. 5236.

[Per96] P. Persephonis, S. V. Chernikov and J. R. Taylor. "Cascaded CW fibre Raman laser source 1.6-1.9 μm". *Electron. Lett.*, **32** (1996) pp. 1486.

[Phi08] T. G. Philbin, C. Kuklewicz, S. Robertson, S. Hill, F. Konig and U. Leonhardt. "Fiber-optical analogue of the event horizon". *arXiv*, **3** (2008) p. 0711.4797.

[Pol04] F. Poli, A. Cucinotta, S. Selleri and A. H. Bouk. "Tailoring of flattened dispersion in highly nonlinear photonic crystal fibers". *IEEE Photonic. Tech. L.*, **16** (2004) pp. 1065.

[Poo85] S. B. Poole, D. N. Payne and M. E. Fermann. "Fabrication of low-loss optical fibres containing rare-earth ions". *Electron. Lett.*, **21** (1985) pp. 737.

[Pop04] S. V. Popov, J. R. Taylor, A. B. Rulkov and V. P. Gapontsev. "Multi-watt, 1.48-2.05 μm range CW Raman-soliton continuum generation in highly-nonlinear fibres". *Conference on Lasers and Electro-Optics*, **2** (2004).

[Pov05] B. Povazay, K. Bizheva, S. Gasparoni, B. Hermann, A. Unterhuber, H. Sattmann, W. Drexler, R. Pflug, E. A. Anger, H. Reitsamer *et al.* "Ultrahigh Resolution, Functional OCT with All-Fiber Broadband Raman-Continuum Light-Source". *Quantum Electronics and Laser Science Conference*, **3** (2005).

[Pra00] M. Prabhu, N. S. Kim and K. Ueda. "Ultra-broadband CW supercontinuum generation centered at 1483.4 nm from Brillouin/Raman fiber laser". *Jpn. J. Appl. Phys*, **39** (2000) pp. 291.

[Pra03] M. Prabhu, A. Taniguchi, S. Hirose, J. Lu, M. Musha, A. Shirakawa and K. Ueda. "Supercontinuum generation using Raman fiber laser". *Appl. Phys. B*, **77** (2003) pp. 205.

[Pri02a] J. Price, W. Belardi, T. Monro, A. Malinowski, A. Piper and D. Richardson. "Soliton transmission and supercontinuum generation in holey fiber, using a diode pumped Ytterbium fiber source". *Opt. Express*, **10** (2002) pp. 382.

[Pri02b] J. H. V. Price, K. Furusawa, T. M. Monro, L. Lefort and D. J. Richardson. "Tunable, femtosecond pulse source operating in the range 1.061. 33 um based on an Yb 3+-doped holey fiber amplifier". *J. Opt. Soc. Am. B*, **19** (2002) pp. 1286.

[Pri03] J. H. V. Price, T. M. Monro, K. Furusawa, W. Belardi, J. C. Baggett, S. Coyle, C. Netti, J. J. Baumberg, R. Paschotta and D. J. Richardson. "UV generation in a pure-silica holey fiber". *Appl. Phys. B*, **77** (2003) pp. 291.

[Pri07] J. H. V. Price, T. M. Monro, H. Ebendorff-Heidepriem, F. Poletti, P. Horak, V. Finazzi, J. Y. Y. Leong, P. Petropoulos, J. C. Flanagan, G. Brambilla *et al.* "Mid-IR supercontinuum generation from non-silica microstructured optical fibers". *IEEE J. Sel. Top. Quantum Electron.*, **13** (2007) pp. 738.

[Ran00a] J. K. Ranka, R. S. Windeler and A. J. Stentz. "Optical properties of high-delta air silica microstructure optical fibers". *Opt. Lett.*, **25** (2000) pp. 796.

[Ran00b] J. K. Ranka, R. S. Windeler and A. J. Stentz. "Visible continuum generation in air-silica microstructure optical fibers with anomalous dispersion at 800 nm". *Opt. Lett*, **25** (2000) pp. 25.

[Ree02] W. Reeves, J. C. Knight, P. S. J. Russell and P. Roberts. "Demonstration of ultra-flattened dispersion in photonic crystal fibers". *Opt. Express*, **10** (2002) pp. 609.

[RH00] P. C. Reeves-Hall, S. A. E. Lewis, S. V. Chenikov and J. R. Taylor. "Picosecond soliton pulse-duration-selectable source based on adiabatic compression in Raman amplifier". *Electron. Lett.*, **36** (2000) pp. 622.

[Roy07] A. Roy, P. Leproux, P. Roy, J. L. Auguste and V. Couderc. "Supercontinuum generation in a nonlinear Yb-doped, double-clad, microstructured fiber". *J. Opt. Soc. Am. B*, **24** (2007) pp. 788.

[Rul05] A. B. Rulkov, M. Y. Vyatkin, S. V. Popov, J. R. Taylor and V. P. Gapontsev. "High brightness picosecond all-fiber generation in 525-1800nm range with picosecond Yb pumping". *Opt. Express*, **13** (2005) pp. 377.

[Rul08] A. B. Rulkov, A. A. Ferin, J. C. Travers, S. V. Popov and J. R. Taylor. "Broadband, low intensity noise CW source for OCT at 1800nm". *Opt. Commun.*, **281** (2008) pp. 154.

[Rus03] P. S. J. Russell. "Photonic crystal fibers". *Science*, **299** (2003) pp. 358.

[Rus05] M. Rusu, A. Grudinin and O. Okhotnikov. "Slicing the supercontinuum radiation generated in photonic crystal fiber using an all-fiber chirped-pulse amplification system". *Opt. Express*, **13** (2005) pp. 6390.

[Rus06] P. S. J. Russell. "Photonic-crystal fibers". *J. Lightwave Technol.*, **24** (Dec. 2006) pp. 4729.

[Sai06] K. Saitoh, M. Koshiba and N. A. Mortensen. "Nonlinear photonic crystal fibres: pushing the zero-dispersion towards the visible". *New Journal of Physics*, **8** (2006) p. 207.

[Sch03] T. Schreiber, J. Limpert, H. Zellmer, A. Tunnermann and K. P. Hansen. "High average power supercontinuum generation in photonic crystal fibers". *Opt. Commun.*, **228** (2003) pp. 71.

[See03] M. Seefeldt, A. Heuer and R. Menzel. "Compact white-light source with an average output power of 2.4 W and 900 nm spectral bandwidth". *Opt. Commun.*, **216** (2003) pp. 199.

[Ser93] V. N. Serkin, V. A. Vysloukh and J. R. Taylor. "Soliton spectral tunnelling effect". *Electron. Lett.*, **29** (1993).

[Sha82] C. V. Shank, R. L. Fork, R. Yen, R. H. Stolen and W. J. Tomlinson. "Compression of Femtosecond Optical Pulses". *Appl. Phys. Lett.*, **40** (1982) pp. 761.

[Sha02] J. E. Sharping, M. Fiorentino, P. Kumar and R. S. Windeler. "Optical parametric oscillator based on four-wave mixing in microstructure fiber". *Opt. Lett*, **27** (2002) pp. 1675.

[Sin03] O. V. Sinkin, R. Holzlohner, J. Zweck and C. R. Menyuk. "Optimization of the split-step Fourier method in modeling optical-fiber communications systems". *J. Lightwave Technol.*, **21** (2003) pp. 61.

[Skr03] D. V. Skryabin, F. Luan, J. C. Knight and P. S. J. Russell. "Soliton Self-Frequency Shift Cancellation in Photonic Crystal Fibers". *Science*, **301** (2003) pp. 1705.

[Skr05] D. V. Skryabin and A. V. Yulin. "Theory of generation of new frequencies by mixing of solitons and dispersive waves in optical fibers". *Phys. Rev. E*, **72** (2005) p. 016619.

[Sla03] S. A. Slattery and D. N. Nikogosyan. "Two-photon absorption at 211 nm in fused silica, crystalline quartz and some alkali halides". *Opt. Commun.*, **228** (2003) pp. 127.

[Smi89] K. Smith and L. F. Mollenauer. "Experimental-Observation of Adiabatic-Compression and Expansion of Soliton Pulses over Long Fiber Paths". *Opt. Lett.*, **14** (1989) pp. 751.

[Smi06] S. Smirnov, J. D. Ania-Castanon, T. J. Ellingham, S. M. Kobtsev, S. Kukarin and S. K. Turitsyn. "Optical spectral broadening and supercontinuum generation in telecom applications". *Opt. Fiber Technol.*, **12** (2006) pp. 122.

[Sni61a] E. Snitzer. "Optical maser action of Nd^{+3} in a barium crown glass". *Phys. Rev. Lett.*, **7** (1961) pp. 444.

[Sni61b] E. Snitzer. "Proposed fiber cavities for optical masers". *J. Appl. Phys.*, **32** (1961) pp. 36.

[Sny70] A. W. Snyder. "Coupling of Modes on a Tapered Dielectric Cylinder". *IEEE T. Microw. Theory.*, **18** (1970) pp. 383.

[Sny83] A. W. Snyder and J. D. Love. *Optical Waveguide Theory*. Chapman and Hall, London (1983).

[Sol07] D. R. Solli, C. Ropers, P. Koonath and B. Jalali. "Optical rogue waves." *Nature*, **450** (2007) pp. 1054.

[Sor01] T. Sorensen, J. Broeng, A. Bjarklev, E. Knudsen and S. Libori. "Macro-bending loss properties of photonic crystal fibre". *Electron. Lett.*, **37** (2001) pp. 287.

[Sto72] R. H. Stolen, E. P. Ippen and A. R. Tynes. "Raman Oscillation in Glass Optical Waveguide". *Appl. Phys. Lett.*, **20** (1972) pp. 62.

[Sto73] J. Stone and C. A. Burrus. "Neodymium-doped silica lasers in end-pumped fiber geometry". *Appl. Phys. Lett.*, **23** (1973) pp. 388.

[Sto74] R. H. Stolen, J. E. Bjorkholm and A. Ashkin. "Psase-matched three-wave mixing in silica fiber optical waveguides". *Appl. Phys. Lett.*, **24** (1974) pp. 308.

[Sto75] R. Stolen. "Phase-matched-stimulated four-photon mixing in silica-fiber waveguides". *IEEE J. Quantum Electron.*, **11** (1975) pp. 100.

[Sto78] R. H. Stolen and C. Lin. "Self-phase-modulaion in silica opical fibers". *Physical Review A*, **17** (1978) pp. 1448.

[Sto82] R. H. Stolen and J. E. Bjorkholm. "Parametric amplification and frequency conversion in optical fibers". *IEEE J. Quantum Electron.*, **18** (1982) pp. 1062.

[Sto83] R. H. Stolen, L. F. Mollenauer and W. J. Tomlinson. "Observation of pulse restoration at the soliton period in optical fibers". *Opt. Lett.*, **8** (1983) pp. 186.

[Sto89] R. H. Stolen, J. P. Gordon, W. J. Tomlinson and H. A. Haus. "Raman Response Function of Silica-Core Fibers". *J. Opt. Soc. Am. B*, **6** (1989) pp. 1159.

[Sum06] M. Sumetsky. "How thin can a microfiber be and still guide light?" *Opt. Lett.*, **31** (2006) pp. 870.

[Tai86] K. Tai, A. Hasegawa and A. Tomita. "Observation of modulational instability in optical fibers". *Phys. Rev. Lett.*, **56** (1986) pp. 135.

[Taj87] K. Tajima. "Compensation of Soliton Broadening in Nonlinear Optical Fibers with Loss". *Opt. Lett.*, **12** (1987) pp. 54.

[Tam99] K. R. Tamura and H. Nakazawa. "Femtosecond soliton generation over a 32-nm wavelength range usinga dispersion-flattened dispersion-decreasing fiber". *IEEE Photonic. Tech. L.*, **11** (1999) pp. 319.

[Tam00] K. R. Tamura, H. Kuhota and M. Nakazawa. "Fundamentals of stable continuum generation at high repetitionrates". *IEEE J. Quantum Electron.*, **36** (2000) pp. 773.

[Tar03] L. Tartara, I. Cristiani and V. Degiorgio. "Blue light and infrared continuum generation by soliton fission in a microstructured fiber". *Appl. Phys. B*, **77** (2003) pp. 307.

[Tay87] J. R. Taylor, A. S. L. Gomes and A. S. Gouveia-Neto. "Radiation pulse generation". *European Patent Application* (1987) p. 88302981.

[Tay92] J. R. Taylor. *Cambridge Studies in Modern Optics; Optical Solitons - Theory and Experiment.* Cambridge University Press, Cambridge, UK (1992).

[Tei05a] J. Teipel, D. Türke, H. Giessen, A. Killi, U. Morgner, M. Lederer, D. Kopf and M. Kolesik. "Diode-pumped, ultrafast, multi-octave supercontinuum source at repetition rates between 500 kHz and 20 MHz using Yb: glass lasers and tapered fibers". *Opt. Express*, **13** (2005) pp. 1477.

[Tei05b] J. Teipel, D. Türke, H. Giessen, A. Zintl and B. Braun. "Compact multi-Watt picosecond coherent white light sources using multiple-taper fibers". *Opt. Express*, **13** (2005) pp. 1734.

[Tom05] V. Tombelaine, C. Lesvigne, P. Leproux, L. Grossard, V. Couderc, J. L. Auguste, J. M. Blondy, G. Huss and P. H. Pioger. "Ultra wide band supercontinuum generation in air-silica holey fibers by SHG-induced modulation instabilities". *Opt. Express*, **13** (2005) pp. 7399.

[Ton03] L. Tong, R. R. Gattass, J. B. Ashcom, S. He, J. Lou, M. Shen, I. Maxwell and E. Mazur. "Subwavelength-diameter silica wires for low-loss optical wave guiding". *Nature*, **426** (2003) pp. 816.

[Tra05a] J. C. Travers, S. V. Popov and J. R. Taylor. "Efficient continuous-wave holey fiber Raman laser". *Appl. Phys. Lett.*, **87** (2005) p. 031106.

[Tra05b] J. C. Travers, S. V. Popov and J. R. Taylor. "Extended blue supercontinuum generation in cascaded holey fibers". *Opt. Lett.*, **30** (2005) pp. 3132.

[Tra05c] J. C. Travers, S. V. Popov and J. R. Taylor. "Extended CW supercontinuum generation in a low water-loss Holey fiber". *Opt. Lett*, **30** (2005) p. 3132.

[Tra05d] J. C. Travers, S. V. Popov and J. R. Taylor. "High efficiency continuous-wave holey-fiber Raman laser". *Conference on Lasers and Electro-Optics* (2005) p. CMV2.

[Tra06] J. C. Travers, A. B. Rulkov, S. V. Popov, J. R. Taylor, A. Kudlinski, A. K. George and J. C. Knight. "Dispersion-Decreasing PCF for Blue-UV Supercontinuum Generation". In *Conference on Lasers and Elctro-Optics*. Optical Society of America, Long Beach, CA, USA (2006), p. CPDA11.

[Tre02] R. Trebino. *Frequency-Resolved Optical Gating: The Measurement of Ultrashort Laser Pulses*. Kluwer Academic Publishers (2002).

[Tse06] M. L. V. Tse, P. Horak, J. H. V. Price, F. Poletti, F. He and D. J. Richardson. "Pulse compression at 1.06 mu m in dispersion-decreasing holey fibers". *Opt. Lett.*, **31** (2006) pp. 3504.

[Tzo95] V. P. Tzolov, M. Fontaine, N. Godbout and S. Lacroix. "Nonlinear self-phase-modulation effects: a vectorial first-order perturbation approach". *Opt. Lett*, **20** (1995) pp. 456.

[Van05] F. Vanholsbeeck, S. Martin-Lopez, M. González-Herráez and S. Coen. "The role of pump incoherence in continuous-wave supercontinuum generation". *Opt. Express*, **13** (2005) pp. 6615.

[Wad02] W. J. Wadsworth, A. Ortigosa-Blanch, J. C. Knight, T. A. Birks, T. Man and P. Russell. "Supercontinuum generation in photonic crystal fibers and optical fiber tapers: a novel light source". *J. Opt. Soc. Am. B*, **19** (2002) pp. 2148.

[Wad04] W. J. Wadsworth, N. Joly, J. C. Knight, T. A. Birks, F. Biancalana and P. S. J. Russell. "Supercontinuum and four-wave mixing with Q-switched pulses in endlessly single-mode photonic crystal fibres". *Opt. Express*, **12** (2004) pp. 299.

[Wad05] W. J. Wadsworth, A. Witkowska, S. Leon-Saval and T. A. Birks. "Hole inflation and tapering of stock photonic crystal fibres". *Opt. Express*, **13** (2005) pp. 6541.

[Wai86] P. K. A. Wai, C. R. Menyuk, Y. C. Lee and H. H. Chen. "Nonlinear pulse propagation in the neighborhood of the zero-dispersion wavelength of monomode optical fibers". *Opt. Lett.*, **11** (1986) pp. 464.

[Was80] K. Washio, K. Inoue and S. Kishida. "Efficient large-frequency-shifted three-wave mixing in low dispersion wavelength region in single-mode optical fibre". *Electron. Lett.*, **16** (1980) p. 658.

[Won05] G. K. L. Wong, A. Y. H. Chen, S. G. Murdoch, R. Leonhardt, J. D. Harvey, N. Y. Joly, J. C. Knight, W. J. Wadsworth and P. S. J. Russell. "Continuous-wave tunable optical parametric generation in a photonic-crystal fiber". *J. Opt. Soc. Am. B*, **22** (2005) pp. 2505.

[Xio06] C. Xiong, A. Witkowska, S. G. Leon-Saval, T. A. Birks and W. J. Wadsworth. "Enhanced visible continuum generation from a microchip 1064nm laser". *Opt. Express*, **14** (2006) pp. 6188.

[Yab87] E. Yablonovitch. "Inhibited Spontaneous Emission in Solid-State Physics and Electronics". *Phys. Rev. Lett.*, **58** (1987) pp. 2059.

[Yab89] E. Yablonovitch and T. J. Gmitter. "Photonic band structure: The face-centered-cubic case". *Phys. Rev. Lett.*, **63** (1989) pp. 1950.

[Yin08] S. S. Yin, J. Kim, C. Zhan, J. An, J. Lee, P. Ruffin, E. Edwards, C. Brantley and C. Luo. "Supercontinuum generation in single crystal sapphire fibers". *Opt. Commun.*, **281** (2008) pp. 1113.

[Yul04] A. V. Yulin, D. V. Skryabin and P. S. J. Russell. "Four-wave mixing of linear waves and solitons in fibers with higher-order dispersion". *Opt. Lett.*, **29** (2004) pp. 2411.

[Zak72] V. E. Zakharov and A. B. Shabat. "Exact theory of two-dimensional self-focusing and one-dimensional self-modulation of waves in nonlinear media(Differential equation solution for plane self focusing and one dimensional self modulation of waves interacting in nonlinear media)". *JETP Lett.*, **34** (1972) pp. 62.

[Zha04] R. Zhang, J. Teipel, X. Zhang, D. Nau and H. Giessen. "Group velocity dispersion of tapered fibers immersed in different liquids". *Opt. Express*, **12** (2004) pp. 1700.

[Zha06] R. Zhang, J. Teipel and H. Giessen. "Theoretical design of a liquid-core photonic crystal fiber for supercontinuum generation". *Opt. Express*, **14** (2006) pp. 6800.

[Zol05] F. Zolla, G. Renversez, A. Nicolet, B. Kuhlmey, S. Guenneau and D. Felbacq. *Foundations Of Photonic Crystal Fibres.* Imperial College Press (2005).